

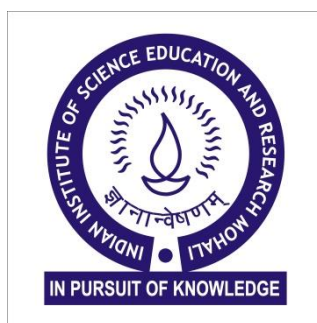
**CONFORMATIONS AND HYDROGEN BONDED INTERACTIONS IN
PROPARGYL SYSTEMS:**

A Matrix Isolation Infrared and Computational Study

*A thesis submitted in partial fulfillment of requirements
for the degree of Doctor of Philosophy*

**By
Jyoti Saini
PH14033**

**Research Advisor
Prof. K. S. Viswanathan**



**Department of Chemical Sciences
Indian Institute of Science Education & Research Mohali
Sector-81, Knowledge City, S.A.S. Nagar, Mohali-140306 Punjab, India**

May 2019

CERTIFICATE

I hereby certify that the thesis titled “**Conformations and Hydrogen Bonded Interactions in Propargyl Systems: A Matrix Isolation Infrared and Computational Study**” submitted for the degree of Doctor of Philosophy by Ms. Jyoti Saini is the record of research work carried out by her during the period August 2014 to March 2019 under my guidance and supervision and further state that this work has not formed the basis for the award of any degree, diploma or a fellowship to any other University or Institute. I further state that this work in this thesis was carried out independently by Ms. Jyoti Saini. In my capacity as the supervisor of the candidate's PhD thesis work, I certify that the above statements are true to the best of my knowledge.

Place: Mohali
Date : 16th May, 2019



Prof. K.S. Viswanathan
(Research Supervisor)

DECLARATION

The work presented in this thesis has been carried out by me under the guidance of Prof. K. S. Viswanathan at the Indian Institute of Science Education and Research Mohali. This work has not been submitted in part or in full for a degree, diploma or a fellowship to any other University or Institute. Whenever contributions of others are involved, every effort has been made to indicate this clearly, with due acknowledgement of collaborative research and discussions. This thesis is a bonafide record of original work done by me and all sources listed within have been detailed in the bibliography.

Place: Mohali
Date : 16th May, 2019

Jyoti Saini

ACKNOWLEDGEMENTS

I am extremely thankful to my PhD supervisor Prof. K. S. Viswanathan, Department of Chemical Science (DCS), IISER Mohali. At the time during my PhD journey, when I completely lost belief in my abilities and gave up, he encouraged and motivated me. He is a role model to me. It is because of him as a guide, I am able to finish my PhD since he cares so much for my research work and career, and completely devoted his time for the discussions related to work, different projects, multiple iterations on manuscripts, we submitted and lastly the chapters of this thesis, and provided me with valuable suggestions and improvements as early as he can. He has given me enough freedom to work in an independent manner to explore new ideas, at the same time he has always been there to guide me through the problems when I sought help during experimental and computational work. His humble, patient, friendly and understanding nature made working with him enjoyable. Besides research work, I have also learnt important lessons in life from his rational thinking. I am really lucky to work under his guidance and proud to be his student.

My Doctoral committee members Dr. P. Balanarayan and Dr. S. Venkataramani, have provided their constant assessment and evaluation of my work from time to time. I am grateful to the former Director Prof. N. Sathyamurthy, IISER Mohali for the experimental and computational facilities. I also wish to thank MHRD for the fellowship, liq. N₂ facility and the Head of department HOD of Chemistry, Dr. S. A. Babu. The entire IISER Mohali, particularly, the DCS has helped me in completion of the work in some way or the other. I especially want to thank Dr. R. Vijayanand and his lab members who provided me with the chemical (propargyl alcohol), neighbour lab members of Dr. S. Venkataramani (Academic block 2) and Dr. S. Singh (Academic block 1) from whom I borrowed liq. N₂ when in need during

experiments. I also heartily thank Mrs. Moumita Rana, for introducing me to the Fityk software for spectral deconvolution, Prashant and Naveen in installing GAMESS.

The matrix isolation group Dr. Kanupriya, Dr. Ginny and Pankaj with whom I have spent a lot of time working together in lab, I wish to thank them for all the help throughout my work. The hot nozzle assembly used in few experiments was designed by Pankaj. The other lab members: Jai, Himanshi, Dipali and Shivangi, Dr. Anamika and BS-MS final year students and summer students who worked in our lab. My gratefulness to Dr. Bishnu Prasad Kar who helped in setting up of matrix isolation facility in IISER Mohali and my BS-MS senior Mr. Gaurav, from whom I learnt Gaussian and the experimental procedure. I am also thankful to Mrs. Chitra Viswanathan.

I would like to thank my best friend Alok Kumar who has been there for me through good and bad times and my closest friend Akansha Sharma. I am also thankful to Dr. Srinivas Doddipatla, Dr. Kanupriya Verma who have always boosted confidence in me, helped and guided me and my other friends - Sumit Mishra, Akanksha Gautam, Ravi, Nitish, Rajeev Jiju, Dr. Sudha, Shikha Di and Dr. Chandrakala.

Most importantly, I am thankful to my mother, Mrs. Raj Dulari Saini, for all the love, care, support and motivation throughout the work, and my very loving, caring, understanding father Mr. Deep Kamal Saini who has full faith in my abilities and always supported me to follow my dreams and ambitions in life. I am also grateful to my brother Abhishek Saini, for his encouragement. Lastly, I really thank God for always showing me the path whenever I felt stuck and blessing me with this precious life.

Jyoti Saini

CONTENTS

	Page no.
List of Figures	i
List of Tables	iii
List of Abbreviations	vi
Synopsis	vii
CHAPTER 1 INTRODUCTION	1
1.1 Scope of Present Work	8
References	11
CHAPTER 2 EXPERIMENTAL AND COMPUTATIONAL DETAILS	
2.1 Introduction	15
2.2 Matrix Isolation Infrared Setup	18
2.3 Hot Nozzle Source	22
2.4 Supersonic Expansion	23
2.5 Computational Details	24
References	31
CHAPTER 3 PROPARGYL ALCOHOL CONFORMATIONS AND ITS HYDROGEN BONDED COMPLEXES WITH WATER	
3.1 Introduction	33
3.2 Experimental Details	34
3.3 Computational Details	35
3.4 Results- Conformations of PA	36
3.4.1. Experimental	36
3.4.2. Computational	37
3.5 Discussions - Conformations of PA	40
3.5.1. Vibrational Assignments	40
3.5.2. AIM Analysis	41
3.5.3. NBO Analysis	42
3.6 Results- PA-H ₂ O Complexes	45
3.6.1. Experimental	45
3.6.2. Computational	46

3.7	Discussion - PA-H ₂ O Complexes	50
	3.7.1. Vibrational Assignments in the N ₂ matrix	50
	3.7.2. Vibrational Assignments in the Ar matrix	53
	3.7.3. AIM Analysis	53
	3.7.4. NBO Analysis	54
	3.7.5. LMO-EDA Analysis	54
3.8	Does a Hydrogen Bonded Complex with Dual Contacts exhibit Synergism?	55
3.9	Conclusions	56
	References	59
CHAPTER 4	HYDROGEN BONDED COMPLEXES BETWEEN PROPARGYL ALCOHOL AND METHANOL	
4.1	Introduction	61
4.2	Experimental Details	61
4.3	Computational Details	62
4.4	Results	62
	4.4.1. Experimental	63
	4.4.2. Computational	65
4.5	Discussion	70
	4.5.1. Vibrational assignments in N ₂ matrix	70
	4.5.2. Vibrational assignments in Ar matrix	77
	4.5.3. AIM analysis	78
	4.5.4. NBO analysis	78
	4.5.5. LMO-EDA analysis	81
4.6	Comparison of PA-MeOH Complex studies with PA-H ₂ O system	82
4.7	PA-DEE Complexes	85
4.8	Conclusions	87
	References	90
CHAPTER 5	CONFORMATIONS OF PROPARGYL AMINE AND ITS HYDROGEN BONDED COMPLEXES	
5.1	Introduction	91
5.2	Experimental Details	92
5.3	Computational Details	93

5.4	Results-PAm Conformers	94
	5.4.1. Experimental	94
	5.4.2. Computational	94
5.5	Discussion- PAm Conformers	97
	5.5.1. Vibrational Assignments	97
	5.5.2. Heated Nozzle Experiments	98
	5.5.3. Supersonic Experiments	99
	5.5.4. AIM Analysis	99
	5.5.5. NBO Analysis	100
5.6	Results- PAm-H ₂ O Complexes	103
	5.6.1. Experimental	103
	5.6.2. Computational	103
5.7	Discussion- PAm-H ₂ O Complexes	107
	5.7.1. Vibrational Assignments	107
	5.7.2. AIM Analysis	110
	5.7.3. NBO Analysis	111
	5.7.4. LMO-EDA Analysis	112
	5.7.5. Comparison of PAm-H ₂ O Complex studies with PA-H ₂ O system	113
5.8	Results- PAm-MeOH Complexes	114
	5.8.1. Experimental	114
	5.8.2. Computational	116
5.9	Discussion- PAm-MeOH Complexes	117
	5.9.1. Vibrational Assignments	117
	5.9.2. AIM Analysis	119
	5.9.3. NBO Analysis	120
5.10	PAm-DEE Complexes	121
5.11	Conclusions	122
	References	125
CHAPTER 6	DIMER STUDIES IN THE PROPARGYL SYSTEMS	
6.1	Introduction	126
6.2	Experimental Details	127
6.3	Computational Details	128

6.4	Results-PA Homodimer	129
	6.4.1. Experimental	129
	6.4.2. Computational	130
6.5	Discussion- PA Homodimer	133
	6.5.1. Vibrational Assignments	133
	6.5.2. AIM analysis	139
	6.5.3. NBO Analysis	141
	6.5.4. A Discernible trend in the Complexes of PA-H ₂ O, PA-MeOH and PA Dimer?	142
6.6	Results- PA-PAm dimers	144
	6.6.1. Experimental	144
	6.6.2. Computational	145
6.7	Results- PAm Homodimers	149
	6.7.1. Computational	149
6.8	Conclusions	152
	References	155
CHAPTER 7	CONCLUSIONS	156
	LIST OF PUBLICATIONS	162

LIST OF FIGURES

Fig. No.	Figure Caption	Page no.
2.1	Home-built Matrix Isolation Infrared Spectroscopy Setup	19
2.2	a) Cryostat and Matrix Isolation cell and b) Gas Injection System	20
2.3	Hot Nozzle Source assembly used	23
2.4	Supersonic assembly used (a) IOTA ONE Pulse Driver and (b) Supersonic Solenoid Valve	23
3.1	Schematic diagram of Conformers of PA.	33
3.2	Infrared spectra of PA in N ₂ matrix, over the regions 3750-2850 cm ⁻¹ , 1420-1370 cm ⁻¹ , 1060-1020 cm ⁻¹ and 690-620 cm ⁻¹ , a) Recorded at 12 K after deposition of PA (sample to matrix ratio 3:1000) and b) Spectra of (a) after annealing the matrix at 27 K.	37
3.3	Infrared spectra of PA in Ar matrix over the regions 3800-3200 cm ⁻¹ and 1070-1010 cm ⁻¹ , a) recorded at 12 K after deposition of PA (sample: matrix ratio 1.5:1000) and b) Spectra of (a) after annealing the matrix at 32 K.	39
3.4	Plot of Uncorrected energy of different structures of PA (in Hartrees) with the change in dihedral angle CCOH (in degrees) at the MP2 level using 6-311++G(d,p) and aug-cc-pVDZ basis sets.	40
3.5	Correlation diagram showing the relative change in energies (in kcal/mol) of the gauche and trans conformer of PA, when orbital interactions were systematically deleted at the M06-2X/aug-cc-pVDZ level.	44
3.6	Infrared spectra of PA-H ₂ O in N ₂ matrix over the regions 3750-3250 cm ⁻¹ and 1060-1020 cm ⁻¹ , of A) PA: H ₂ O: N ₂ (0.8: 1.0:1000) at 12 K, B) PA: H ₂ O: N ₂ (0.8: 1.0:1000) annealed at 27 K, C) PA: H ₂ O: N ₂ (0.8: 0.0: 1000) annealed at 27 K, D) PA: H ₂ O: N ₂ (0.0: 0.5: 1000) annealed at 27 K, E) PA: H ₂ O: N ₂ (3.0: 0.4:1000) annealed at 27 K.	46
3.7	Infrared spectra of PA-H ₂ O in Ar matrix over the regions 3800-3200 cm ⁻¹ and 1070-1010 cm ⁻¹ , of A) H ₂ O: Ar (5:1000) annealed at 32 K, B) PA: Ar (5:1000) annealed at 32 K, C) PA: H ₂ O: Ar (5:5:1000) at 12 K, D) PA: H ₂ O: Ar (5:5:1000) annealed at 32 K, E) PA: H ₂ O:Ar (5:10:1000) annealed at 32 K, F) PA: H ₂ O: Ar (10:5:1000) annealed at 32 K.	47
3.8	Optimized geometries of the complexes of gauchePA and water, computed at the MP2/aug-cc-pVDZ level	48
3.9	Optimized geometries of the complexes of transPA with water, with their uncorrected interaction energies, computed at the MP2/aug-cc-pVDZ level.	50
3.10	Charge density topologies for the different structures of gauchePA-H ₂ O complexes computed at the MP2/aug-cc-pVDZ level.	53
3.11	Optimised geometries of the transPA-water complexes 5 and 8, with their O...H bond length, O-H...O bond angle and interaction energies, computed at the MP2/aug-cc-pVDZ level	55
4.1	Matrix isolation infrared spectra showing the monomers (PA and MeOH) and the PA-MeOH complexes, in the N ₂ matrix.	64
4.2	Matrix isolation infrared spectra of PA codeposited with CH ₃ OH over the regions 3460-3410 cm ⁻¹ and 1065-1015 cm ⁻¹ , with PA:CH ₃ OH in (A) N ₂ matrix (3:3:1000) annealed at 27 K and (B) Ar matrix (10:5:1000) annealed at 32 K.	66
4.3	Different optimized gauchePA-MeOH complexes computed at the MP2/aug-cc-pVDZ level, with their hydrogen bonded interactions indicated by dashed line.	67

4.4	Experimental IR spectrum of PA:MeOH:N ₂ (3:3:1000) annealed and computed spectra of PA-MeOH complexes 1, 1A, 1' and 1'A with their respective scaled wavenumbers.	73
4.5	Matrix Isolation Infrared spectra of PA:CD ₃ OD:N ₂ (6:1:1000) shown over the regions 3480-3410 cm ⁻¹ (O-H stretch region of PA) and 2710-2620 cm ⁻¹ (O-D stretch region of CD ₃ OD). The spectrum was recorded after annealing the matrix.	75
4.6	AIM analysis for PA-MeOH complexes at MP2/aug-cc-pVDZ level.	79
4.7	PA-MeOH complexes 1, 4' and 6 computed at MP2/aug-cc-pVDZ level, with their uncorrected interaction energies in kcal/mol.	85
4.8	Optimized structures of PA-DEE complexes at the MP2/aug-cc-pVDZ level.	86
5.1	Conformers of propargyl alcohol and propargyl amine for comparison.	91
5.2	Infrared spectrum over the spectral range 3800-2900 and 1300-520 cm ⁻¹ of PAm:N ₂ (0.5: 1000) recorded after (A) depositing the matrix at 12 K (B) annealing the matrix, at 27 K.	95
5.3	Optimized structures of gg- and gt- PAm conformers with some important dihedral angles (in degrees), computed at the MP2/aug-cc-pVDZ level.	97
5.4	Correlation diagram showing relative energies (kcal/mol) of gg and gt PAm, when orbital interactions were systematically deleted at M06-2X/aug-cc-pVDZ level.	102
5.5	Infrared spectra of PAm : H ₂ O: N ₂ in the regions 3750-3650, 3425-3250 and 1000-900 cm ⁻¹ annealed at 27 K (A) 1: 0: 1000 (B) 0: 0.2 : 1000 (C) 0.5: 0.2 : 1000 (D) 1: 0.8 : 1000 (E) 1: 0.2 : 1000 (F) 2.5: 0.2 : 1000 (G) 2.5: 0.2 : 1000. Spectrum F is recorded at 12 K.	104
5.6	Optimized structures of various hydrogen bonded complexes of gg and gt PAm with H ₂ O and their uncorrected, ZPE corrected and BSSE corrected interaction energies, computed at MP2/aug-cc-pVDZ level.	105
5.7	Electron density topologies for various ggPAm-H ₂ O complexes at MP2/aug-cc-pVDZ level.	111
5.8	Matrix isolation infrared spectra in the spectral range 3750-3625, 3440-3240, 1070-1010 and 970-910 cm ⁻¹ , for PAm:MeOH:N ₂ a) 1.0:0.0:1000 annealed b) 0.0:1.5:1000 annealed c) 0.5:1.5:1000 annealed d) 1.0:1.5:1000 annealed e) 0.5:3.0:1000 annealed f) 1.0:3.0:1000 at 12 K and g) 1.0:3.0:1000 annealed.	115
5.9	Optimized geometries for ggPAm-MeOH complexes at MP2/aug-cc-pVDZ level.	116
5.10	AIM analysis of ggPAm-MeOH complexes at the MP2/aug-cc-pVDZ level.	120
5.11	Optimized structures of PAm-DEE complexes at the MP2/aug-cc-pVDZ level.	122
6.1	Matrix isolation infrared spectra of PA over the regions 3750-3400 cm ⁻¹ and 1060-1020 cm ⁻¹ , with (a) PA:N ₂ (0.8:1000) at 12 K, (b) PA:N ₂ (0.8:1000), (c) PA:N ₂ (3:1000), (d) PA:N ₂ (10:1000). Spectra of (b), (c) and (d) were recorded after annealing the matrix at 27 K.	130
6.2	Optimized structures of different PA homodimers having both PA subunits in gauche conformation, computed at the MP2/aug-cc-pVDZ level.	131
6.3	Electron density topologies for different PA homodimers at MP2/aug-cc-pVDZ level with their bond, ring and cage critical points.	132
6.4	Gaussian peak fitted infrared spectrum of PA:N ₂ (10:1000) annealed at 27 K over the region 3500-3390 cm ⁻¹ . The experimental intensities are the areas under the respective features. The computed intensities given in km mol ⁻¹ , obtained at the M06-2X/6-311++G(d,p) level of theory.	138
6.5	Electron density topologies for different PA-PAm dimers at MP2/aug-cc-pVDZ level with their bond, ring and cage critical points.	147
7.1	Global minima PA-H ₂ O complexes 1 and 1* computed at MP2/aug-cc-pVDZ level.	157

LIST OF TABLES

Table No.	Table Caption	Page No.
3.1	Experimental (N_2 matrix at 12 K) and scaled computed wavenumbers (cm^{-1}) at MP2/aug-cc-pVDZ level for the gauche and trans conformers of PA and their vibrational assignments.	38
3.2	Uncorrected and Zero-point energy (ZPE) corrected stabilization energies for PA conformers computed at different levels of theory.	39
3.3	NBO analysis showing the energies obtained after deletion of the different delocalization interactions in PA conformers at M06-2X/aug-cc-pVDZ level.	42
3.4	NBO results listing some of the significant geminal, vicinal and remote delocalization interactions, their donor and acceptor orbitals and the second order perturbation energies, $E(2)$, in PA conformers, calculated at M06-2X/aug-cc-pVDZ level.	43
3.5	Uncorrected, ZPE corrected and BSSE corrected interaction energies (in kcal/mol) for PA- H_2O complexes computed at the M06-2X and MP2 level using 6-311++G(d,p) and aug-cc-pVDZ basis sets. Single point calculations at CCSD(T)/aug-cc-pVDZ level are also shown. Interaction energies using the CBS limit are also computed at MP2 and CCSD(T) levels.	49
3.6	Some important geometrical parameters for different PA- H_2O complexes computed at the MP2/aug-cc-pVDZ level.	49
3.7	Experimental and scaled computed vibrational wavenumbers (cm^{-1}) for PA, H_2O , D_2O , the different PA- H_2O and PA- D_2O complexes in N_2 matrix at MP2/aug-cc-pVDZ level.	51
3.8	AIM analysis showing the charge densities ρ_b and Laplacian $\nabla^2\rho_b$ at the bond critical point for various gauchePA-water complexes at MP2/aug-cc-pVDZ level. The values of ρ_b , $\nabla^2\rho_b$, $G(r_c)$ and $V(r_c)$ are expressed in a.u. and E_{HB} in kcal/mol.	54
3.9	LMO-EDA energy decomposition analysis for various PA- H_2O complexes computed at the MP2/aug-cc-pVDZ level.	54
4.1	Some of the important geometrical parameters for different PA-MeOH complexes computed at MP2/aug-cc-pVDZ level.	68
4.2	Uncorrected ΔE_{RAW} , zero-point energy corrected ΔE_{ZPC} and BSSE corrected ΔE_{BSSE} interaction energies (in kcal/mol) for different PA-MeOH complexes at M06-2X and MP2 methods using 6-311++G(d,p) and aug-cc-pVDZ basis sets. Uncorrected interaction energies are also computed with MP2 and CCSD(T) methods at the CBS limit, using optimized geometries at MP2/aug-cc-pVDZ level.	69
4.3	Experimental (in N_2) and computed scaled vibrational features (in cm^{-1}) for the PA, MeOH and PA-MeOH complexes 1, 1A, 1' and 1'A.	70
4.4	Computed scaled vibrational features (in cm^{-1}) for the PA, MeOH and higher energy PA-MeOH hydrogen bonded complexes at MP2/aug-cc-pVDZ level.	71
4.5	Experimental (in N_2) and computed scaled vibrational features for the PA, CD_3OD , CD_3OH and hydrogen bonded complexes 1, 1A, 1' and 1'A of PA- CD_3OD and PA- CD_3OH at the MP2/aug-cc-pVDZ level.	76
4.6	Experimental (in Ar matrix) and computed scaled vibrational features (in cm^{-1}) for the PA, MeOH and PA-MeOH hydrogen bonded complexes 1, 1A, 1' and 1'A.	77
4.7	Electron density, Laplacian, local electronic kinetic and potential energy density and hydrogen bonded energy E_{HB} values for gauchePA-MeOH complexes at the MP2/aug-cc-pVDZ level. Values for <i>trans</i> PA-MeOH complex 6 have also been shown.	80

4.8	NBO analysis showing the significant orbital interactions between the donor and acceptor orbitals among the two subunits in PA-MeOH complexes 1, 1A, 1' and 1'A, their corresponding second order perturbation energies $E(2)$ in kcal/mol, difference in energy between donor and acceptor orbitals $E(j)-E(i)$ and the off-diagonal NBO Fock matrix element $F(i,j)$, computed at the MP2/aug-cc-pVDZ level.	81
4.9	LMO-EDA results on PA-MeOH complexes at MP2/aug-cc-pVDZ level.	82
4.10	Uncorrected, ZPE corrected and BSSE corrected interaction energies for PA-DEE complexes computed at the MP2 level using 6-311++G(d,p) and aug-cc-pVDZ basis sets. Uncorrected interaction energies at CCSD(T)/aug-cc-pVDZ level have also been shown.	86
4.11	Computed scaled wavenumbers (in cm^{-1}) with their vibrational mode assignments for PA-DEE complexes at MP2/aug-cc-pVDZ level.	87
5.1	Experimental (N_2 matrix) and computed scaled vibrational wavenumbers (cm^{-1}) at MP2/aug-cc-pVDZ level for the PAm conformers.	96
5.2	The Uncorrected (ΔE_{RAW}) and ZPE corrected (ΔE_{ZPE}) relative energies of PAm conformers, gg and gt, computed at different levels of theory.	98
5.3	NBO analysis of significant geminal, vicinal and remote interactions in PAm conformers with their second order perturbation energies, $E(2)$, computed at the M06-2X/aug-cc-pVDZ level.	101
5.4	NBO results listing the energies obtained after deletion of different delocalization interactions in PAm conformers at M06-2X/aug-cc-pVDZ level of computation.	102
5.5	Some important geometrical parameters for different ggPAm- H_2O complexes computed at MP2/aug-cc-pVDZ level, showing bond lengths (in \AA), bond angles and dihedral angles (in degrees).	106
5.6	Interaction energies RAW/ZPE/BSSE (in kcal/mol) for different PAm- H_2O complexes calculated at M06-2X, MP2 and CCSD(T) level using aug-cc-pVDZ basis set and CBS limit.	107
5.7	Experimental (in N_2 matrix) and computed scaled wavenumbers (cm^{-1}) at MP2/aug-cc-pVDZ level for different vibrational modes in PAm- H_2O complexes.	108
5.8	AIM analysis showing electron density $\rho_b(r_c)$, laplacian $\nabla^2\rho_b(r_c)$, local electronic kinetic energy density $G(r_c)$, local electronic potential energy density $V(r_c)$ values, in atomic units, for different hydrogen-bonded interactions in ggPAm- H_2O complexes computed at MP2/aug-cc-pVDZ level.	110
5.9	NBO analysis on ggPAm- H_2O complexes, showing the significant interactions between the donor and acceptor orbitals and their corresponding second order perturbation energies $E(2)$ in kcal/mol, difference in energy between acceptor and donor orbitals $E(j)-E(i)$ and $F(i,j)$ values given in atomic units, computed at MP2/aug-cc-pVDZ level.	111
5.10	LMOEDA analysis for ggPAm- H_2O complexes computed at MP2/aug-cc-pVDZ level.	113
5.11	Interaction energies (Raw/ZPE/BSSE corrected) in kcal/mol for PAm-MeOH complexes at different levels of theory.	117
5.12	Some important geometrical parameters for different ggPAm-MeOH complexes computed at MP2/aug-cc-pVDZ level, showing bond lengths (in \AA), bond angles and dihedral angles (in degrees).	117
5.13	Experimental (in N_2 matrix) and computed scaled wavenumbers (cm^{-1}) at MP2/aug-cc-pVDZ level for different vibrational modes in PAm-MeOH complexes.	118
5.14	AIM analysis for PAm-MeOH complexes at MP2/aug-cc-pVDZ level.	120
5.15	NBO analysis for PAm-MeOH complexes at MP2/aug-cc-pVDZ level.	121

5.16	Uncorrected, ZPE corrected and BSSE corrected interaction energies in kcal/mol, for PAM-DEE complexes computed at the MP2 level using 6-311++G(d,p) and aug-cc-pVDZ basis sets. Uncorrected interaction energies at CCSD(T)/aug-cc-pVDZ level have also been shown.	122
6.1	Important geometrical parameters of the PA-dimers having both subunits in the gauche conformation, showing bond lengths (Å) and bond angles (degrees), computed at the MP2/aug-cc-pVDZ level.	134
6.2	Interaction energies for different PA homodimers given as uncorrected (ΔE_{RAW}), ZPE corrected (ΔE_{ZPC}) and BSSE corrected (ΔE_{BSSE}) energies at various levels of theory. Uncorrected energies at CCSD(T) level have also been shown, using 6-311++G(d,p), aug-cc-pVDZ and complete basis set (CBS) limit.	135
6.3	Experimental (in N ₂ matrix) and computed scaled vibrational wavenumbers at the M06-2X/6-311++G(d,p) level for PA-dimers 1 and 5, given in cm ⁻¹ .	136
6.4	Calculation showing the estimates of concentration of the PA homodimers 1 and 5 in the matrix.	140
6.5	Electron density $\rho_b(r_c)$, Laplacian $\nabla^2\rho_b(r_c)$, local electronic kinetic energy density $G(r_c)$, local electronic potential energy density $V(r_c)$ and hydrogen bond energy E_{HB} values for different hydrogen bonded interactions in the PA homodimers having both PA subunits in gauche conformation, at MP2/aug-cc-pVDZ level.	141
6.6	NBO analysis showing the significant orbital interactions between the donor and acceptor orbitals in the two PA subunits, their corresponding second order perturbation energies, $E(2)$, difference in energy between acceptor and donor orbitals $E(j)-E(i)$ and $F(i,j)$ computed at MP2/aug-cc-pVDZ level for PA homodimers 1 and 5.	142
6.7	Correlation between the structures of PA-H ₂ O, PA-MeOH and PA-dimers, with their interaction energies $\Delta E_{\text{RAW}}/\Delta E_{\text{ZPC}}/\Delta E_{\text{BSSE}}$, in kcal/mol, at the MP2/aug-cc-pVDZ level.	143
6.8	Optimized structures of PAM-PA complexes with their interaction energies computed at the MP2/aug-cc-pVDZ level.	145
6.9	Some of the important geometrical parameters including bond lengths (in Å), bond angles and dihedral angles (in degrees) in PA-PAM complexes computed at MP2/aug-cc-pVDZ level.	148
6.10	Vibrational scaled computed wavenumbers for PA-PAM dimer 1 at the MP2/aug-cc-pVDZ level.	148
6.11	AIM analysis for PA-PAM dimers computed at MP2/aug-cc-pVDZ level, with their electron density $\rho_b(r_c)$, Laplacian $\nabla^2\rho_b(r_c)$, local electronic kinetic energy density $G(r_c)$ and local electronic potential energy density $V(r_c)$ given in atomic units and hydrogen bond energy E_{HB} values in kcal mol ⁻¹ .	149
6.12	Optimized structures of PAM homodimers with their interaction energies computed at the MP2/aug-cc-pVDZ level.	150
6.13	AIM analysis for ggPAM homodimers computed at MP2/aug-cc-pVDZ level, with their electron density $\rho_b(r_c)$, Laplacian $\nabla^2\rho_b(r_c)$, local electronic kinetic energy density $G(r_c)$ and local electronic potential energy density $V(r_c)$ given in atomic units and hydrogen bond energy E_{HB} values in kcal mol ⁻¹ .	151
6.14	Some important geometrical parameters including bond lengths (in Å), bond and dihedral angles (in degrees) for ggPAM homodimers computed at MP2/aug-cc-pVDZ level.	152

LIST OF ABBREVIATIONS

BSSE	Basis Set Superposition Error
AIM	Atoms in Molecules
ESP	Electrostatic Potential
PA	Propargyl Alcohol
PAm	Propargyl Amine
NBO	Natural Bond Orbital
LMO-EDA	Localized Molecular Orbital-Energy Decomposition Analysis
MP2	Møller-Plesset Second order Perturbation
FWHM	Full Width at Half Maximum
ZPC	Zero point Correction
BCP	Bond Critical Point
NAO	Natural Atomic Orbital
NHO	Natural Hybrid Orbital
CBS	Complete Basis set
CCSD(T)	Coupled-Cluster with Single, Double and Perturbative Triple Excitations
M06-2X	Minnesota Global Hybrid Functional with 54% HF Exchange
PhAc	Phenylacetylene
DEE	Diethylether

SYNOPSIS

Chapter 1: Introduction

Non-covalent interactions are known to play a very important role in many physical, chemical and biochemical phenomena. One such interaction is the hydrogen bonding interaction, which has typical interaction energies in the range of ~1 kcal/mol to ~40 kcal/mol. The large range of interaction energies provides the hydrogen bonds, the ability to associate and dissociate quickly at ambient temperatures and hence provide flexibility to the supramolecular architecture. The very strong hydrogen bonds have interaction energies of 15 - 40 kcal/mol such as in $(\text{FHF})^-$, which has interaction energy of ~ 39 kcal/mol. The O-H...O, N-H...O or O-H...N systems fall under strong hydrogen bonds, with interaction energies in the range 4-15 kcal/mol. Weak hydrogen bonds involving proton donors such as C-H or S-H and acceptors such as π systems, have stabilization energies 1-4 kcal/mol.

Investigating these weak hydrogen bonds both experimentally and computationally has been an active area of study. Experimental techniques such as infrared, nuclear magnetic resonance spectroscopy, X-Ray diffraction, and calorimetry have been extensively used. In particular, infrared spectroscopy has been a very popular tool, since it provides information on the non-covalent interactions present in weakly bound complexes. The presence, nature and strengths of hydrogen bonded interactions are determined from the magnitude and direction (red or blue) of shifts in the vibrational features of the submolecules in the complex, relative to those observed in the uncomplexed molecules. To obtain a good estimate of the shifts, it is essential to have spectral features with small linewidths. Towards this end, matrix isolation spectroscopy and supersonic expansion techniques have been used, because of the small linewidths that these techniques offer. While the supersonic jet technique traps the system in the lowest energy, i.e. the global minimum structures, matrix isolation spectroscopy

allows for trapping both the global and local minima structures, thus offering a better perspective of the potential energy landscape.

The motivation of this work is to study the two systems containing propargyl group, the propargyl alcohol and propargyl amine. Both these molecules have multiple hydrogen bonding sites. With an O-H or N-H group, an acidic $\equiv\text{C-H}$ group and a π system, these offer a wide spectrum of structures from $n-\sigma^*$ to H- π contacts. Using matrix isolation spectroscopy, we set out to observe different hydrogen bonded complexes of propargyl alcohol and propargyl amine with a variety of precursors. Before studying the complexes, we also addressed the problem of conformers in propargyl alcohol and propargyl amine. We have also recognized a common thread running between the structures of the various complexes, which one can exploit to predict the structures of higher complexes.

Chapter 2: Experimental and Computational Details

Matrix isolation experiments were carried out at ~ 12 K. N_2 or Ar were used as matrix gases in our experiments. The FTIR spectra were recorded at 12 K, after deposition, in the spectral range of $4000-400\text{ cm}^{-1}$, with resolution of 0.5 cm^{-1} . The matrix was then warmed at temperatures 27 K for N_2 (or 32 K for Ar), kept at this temperature for 1 hr and then recooled to 12 K and again recorded the spectra.

Gaussian 09 suite of programs was used to optimize different structures at the M06-2X and MP2 methods using 6-311++G(d,p) and aug-cc-pVDZ basis sets. Interaction energies were calculated at all these levels. Single point calculations were also done at CCSD(T)/aug-cc-pVDZ level. Interaction energies were also computed at the MP2 and CCSD(T) methods using CBS limit. NBO, AIM and LMO-EDA analysis were done to identify and characterize different hydrogen bonding interactions.

Chapter 3: Conformations of Propargyl Alcohol and its Complexes with Water

In this chapter, we have revisited the study on conformations of propargyl alcohol (PA), which arise from the internal rotation of C-OH group in PA. This resulted into two conformations: the gauche and the trans form. The gauche form was 1.54 kcal/mol more stable than the trans form as reported at CCSD(T)-F12/VDZ-F12 level of theory. The greater stability of gauche form was proposed to be due to presence of intramolecular hydrogen bonding between -OH group and π electrons.

We have studied PA in an effort to understand its conformational preference using matrix isolation infrared spectroscopy and computations. Our experiments, when PA was deposited in N₂ matrix, showed the features of gauche PA conformer, corroborated by computations performed at the MP2/aug-cc-pVDZ level. There was no experimental evidence of the trans PA conformer in the matrix.

The conformational preference in PA was then explored through an NBO analysis, followed by deletions of different orbital interactions at the M06-2X/aug-cc-pVDZ level, to understand the basic factors for conformational preferences. It was found that when only the vicinal interactions were deleted, retaining the other orbital interactions, the energy of both conformers increased significantly together with an inversion in their conformational ordering, suggesting that the gauche form now became less stable than trans conformer. It therefore implied that the vicinal interactions played important role in the stabilization of gauche PA over trans form. Earlier work had indicated that intramolecular hydrogen bonding interactions, determined the conformational preference. However, our AIM results did not support this explanation, as indicated by the absence of bond critical point corresponding to such interactions.

PA provides multiple sites for weak non-covalent interactions; hence complexes of PA with different precursors gives rise to multiple isomeric forms which were studied. We

studied for the first time, the 1:1 hydrogen bonded complexes of gauche PA with water, using matrix isolation infrared spectroscopy and computations. FTIR spectra of PA with H₂O in N₂ matrix together with computations indicated the formation of global minimum complex, which involved an O-H...O contact between the O-H group of PA and oxygen atom of H₂O, and another an O-H... π contact between the O-H group of H₂O and π electron density of PA. The cyclic geometry of complex was confirmed by the AIM theory, showing a ring critical point, consistent with the dual interactions, O-H...O and O-H... π contacts. The convincing evidence for formation of this complex in our experiments, was the large red shift of 174.7 cm⁻¹ in the O-H stretching vibration of PA subunit. NBO analysis revealed a strong electron delocalization between the lone pair on oxygen atom of H₂O and the σ^* orbital of O-H bond in PA. Three other complexes were also located as local minima, however we did not observe features corresponding to their formation in matrix. LMO-EDA analysis on all the computed PA-H₂O complexes, showed electrostatic and exchange energy as the major contributors to the total interaction energy. Isotopic calculations further confirm our vibrational assignments.

It was also recognized that in the global minimum structure, where dual interactions were present, the two precursors adopt a geometry that is not necessarily the one that was found when each of the interactions: O-H...O and O-H... π , were present individually. This result in antagonism, where the optimum geometries when individual interactions were present, were in fact sacrificed when forming the dual interaction complex.

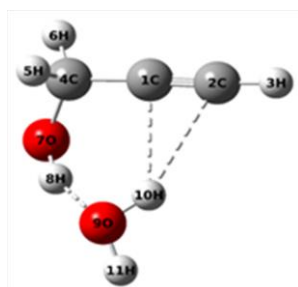


Fig S.1. Global minimum PA-H₂O complex computed at the MP2/aug-cc-pVDZ level.

Chapter 4: Propargyl Alcohol Complexes with Methanol

This chapter includes the study of gauche PA complexes with methanol (MeOH). When PA and MeOH were codeposited in matrix, features corresponding to the formation of two nearly isoenergetic global minima complexes 1 and 1A were observed. Both these complexes were bound by an O-H...O and an O-H... π contact, with O-H...O being the dominant interaction as revealed from AIM. They differ only in the orientation of methyl group in MeOH subunit. Nine other computed complexes, less stable than complexes 1 and 1A were not observed in the matrix.

Antagonistic behaviour was shown by PA-MeOH complexes 1 and 1A, similar to what was noticed in the global minimum PA-H₂O complex. The primary O-H...O interaction in complexes 1 and 1A of PA-MeOH was stronger and showed correspondingly larger red shift in the O-H stretch mode of PA subunit than in PA-H₂O. It implies that PA-MeOH complexes were more stable relative to PA-H₂O complexes. From the gas phase basicity values of MeOH and H₂O, it was found that the strength of O-H...O interaction was greater for PA-MeOH complexes, with lower value of ΔpK_a .

As opposed to PA-H₂O system in which it was not possible to distinguish between the two nearly isoenergetic complexes experimentally, the PA-MeOH complexes 1 and 1A showed discernible differences in their O-H and C-O stretching vibrations, which renders them to be separately identified in our matrix experiments.

We also computed the complexes of PA with diethylether (DEE), which manifests the formation of elusive n- σ^* complex, having a dominant O-H...O interaction. While in PA-H₂O and PA-MeOH complexes, the O-H... π interaction is the secondary interaction; in the PA-DEE this interaction is completely suppressed.

Chapter 5: Conformers of Propargyl Amine and its Complexes with Water and Methanol

In this chapter, a relatively poor proton donor NH_2 group containing propargyl system, propargyl amine (PAm) has been studied experimentally and computationally. IR spectra of matrix isolated PAm indicated to the presence of computed gg conformer in which both N-H bonds were gauche to the acetylenic π cloud in PAm. This form was 1.42 kcal/mol more stable than the gt PAm conformer at MP2/aug-cc-pVDZ level.

Similar to PA conformers, NBO analysis and subsequent deletions of different orbital interactions indicated that the vicinal interactions were responsible for ggPAm to be lower in energy than gt form, however the extent of stabilization achieved from vicinal interactions in PAm conformers was relatively less than in PA conformers.

In the codeposition experiments, features corresponding to the 1:1 hydrogen bonded complex between PAm and H_2O were observed in the matrix. These features were then assigned to the global minimum complex in which PAm served as a proton acceptor to the O-H group in H_2O , forming an O-H \cdots N interaction, which is different from the PA systems. NBO analysis revealed strong delocalization from the lone pair on nitrogen atom in PAm to the σ^* orbital of O-H bond in H_2O molecule. It must be noted that a similar complex in PA- H_2O system, was however, computed as a local minimum.



Fig. S.2. The experimentally observed global minimum PAm- H_2O complex computed at the MP2/aug-cc-pVDZ level.

Two other less stable PAm- H_2O complexes were also located, one which was bound by dual contacts, N-H \cdots O and O-H $\cdots\pi$, with PAm serving both as a proton donor through its

N-H bond and acceptor through the π electrons, and another involving an acetylenic C-H \cdots O interaction, similar to the structures observed in PA-H₂O systems. LMO-EDA analysis results have also been presented.

The 1:1 hydrogen bonded complexes of PAm with MeOH have also been studied. Experimental features corroborated by computations indicated that the global minimum PAm-MeOH complex was trapped in the matrix, with PAm serving as the proton acceptor through its nitrogen atom. NBO analysis revealed a strong n- σ^* interaction between the lone pair on nitrogen atom in PAm and the O-H bond in MeOH.

Chapter 6: Dimer studies in the Propargyl Systems

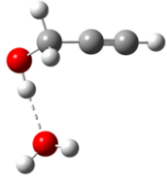
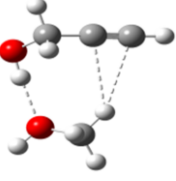
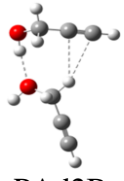
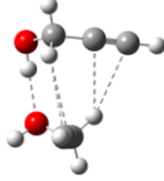
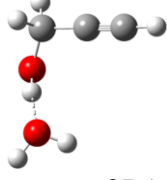
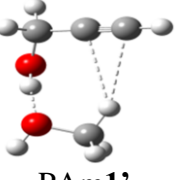
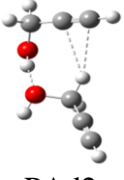
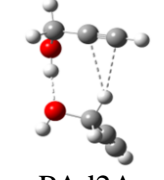
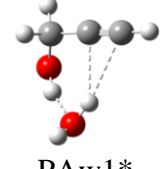
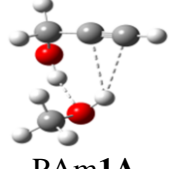
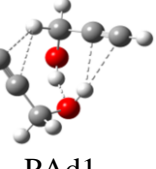
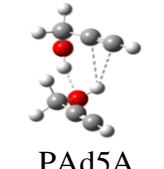

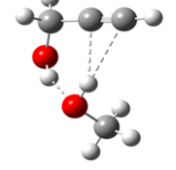
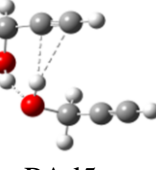
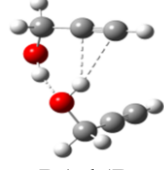
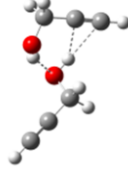
The results of the studies discussed in the earlier studies prompted us to look at possible trends in the structures of the various complexes. For example, the PA-MeOH structures appeared to be derived from the PA-H₂O structures, by the simple replacement of a hydrogen in H₂O with a methyl group. Likewise, replacing a hydrogen in the methyl group of a PA-MeOH complex gave rise to the PA dimer. We explored the possibility, if the structures of the complex systems could be derived from the simpler systems. If so, this could be a nice procedure to explore the potential surface from simpler systems.

There were three studies we could make from the earlier discussed PA and PAm systems, 1) PA Homodimers, 2) PA-PAm complexes, and 3) PAm Homodimers.

PA Homodimers. When the concentration of PA was gradually increased, features corresponding to the formation of PA dimers were observed in the FTIR spectra. These features were assigned to the computed modes of PA dimers 1 and 5. A triply tethered, dimer 1 involves an O-H \cdots O, an O-H $\cdots\pi$ and a C-H $\cdots\pi$ interaction, while in dimer 5, the two PA subunits were bound by dual contacts, an O-H \cdots O and an O-H $\cdots\pi$ interaction. These isomers were the two most stable and nearly isoenergetic PA dimers. In the microwave experiments

by Mani and Arunan, only dimer 1 was observed; while from our matrix isolation experiments, we have trapped both dimers 1 and 5 in the matrix. A spectral deconvolution and peak fitting using Lorentzian profile, gave the intensity of the experimental peaks, lending credence to our vibrational assignments of dimers 1 and 5.

Table S.1. Correlation between the structures of PA-H₂O, PA-MeOH and PA Homodimers, with their interaction energies $\Delta E_{\text{RAW}}/\Delta E_{\text{ZPC}}/\Delta E_{\text{BSSE}}$, in kcal/mol, at the MP2/aug-cc-pVDZ level.

PA-H ₂ O	PA-MeOH	PA Homodimers		
 Precursor of PAm1'A (Not optimized)	 PAm1'A (-7.7/-6.4/-5.7)	 PAd2B (-7.8/-6.7/-5.4)	 PAd3 (-8.9/-7.7/-6.3)	
 Precursor of PAm1' (Not optimized)	 PAm1' (-8.2/-6.8/-6.3)	 PAd2 (-8.4/-7.1/-6.1)	 PAd2A (-8.3/-7.1/-6.1)	
 PAw1* (-7.7/-5.7/-6.1)	 PAm1A (-9.2/-7.6/-6.8)	 PAd1 (-10.0/-8.5/-7.2)	 PAd5A (-9.3/-7.9/-6.5)	
 PAw1 (-7.9/-5.9/-6.2)	 PAm1 (-9.3/-7.6/-7.0)	 PAd5 (-9.9/-8.4/-7.1)	 PAd5B (-8.8/-7.5/-6.5)	 <i>gauche-trans</i> PAd6 (-9.8/-8.3/-7.1)

As discussed earlier, a common thread was observed between the earlier studied PA-H₂O, PA-MeOH and PA dimer systems. It was found that starting from simpler PA-H₂O complexes, the systematic replacement of each of the hydrogen atom in H₂O with methyl group, resulted into different PA-MeOH structures. Similarly, in PA-MeOH complexes, when

each of the methyl hydrogen atoms was replaced by an acetylenic group, different PA-dimers were systematically evolved. This scheme therefore presented a method, where starting from simpler PA-H₂O system, structures of the PA-dimers were systematically derived.

PA-PAm complexes. Similar to computing several PA Homodimer structures starting from simpler PA-H₂O complexes, we can also generate possible structures of hydrogen bonded complexes between PA and PAm. Thus, in PAm-H₂O, systematic replacement of hydrogen atom in water molecule with a methyl group, result in PAm-MeOH complex structures, which in turn, will lead to generation of PA-PAm complexes by replacing each of the hydrogen atom in methyl group in MeOH with an acetylenic group. Matrix isolation infrared experiments were performed to observe the shifts in the O-H and C-O stretch of the computed most stable PA-PAm dimer, however, features corresponding to the formation of dimer were not observed.

PAm Homodimers. In addition, we have also computationally constructed different PAm homodimers by systematic replacement of each methyl hydrogen atom in methylamine (MeNH₂) of PAm-MeNH₂ complexes, which in turn was deduced from the hydrogen bonded complexes between PAm and ammonia.

Chapter 7: Conclusions

The PA conformational landscape was well understood in our work and we inferred that the vicinal orbital interactions were majorly responsible for the stabilization of ground state conformer, which was trapped in our matrix isolation experiments. When 1:1 PA-H₂O complexes were studied experimentally and computationally, global minimum cyclic complex involving dual interactions, an O-H...O and an O-H... π was trapped in the matrix, as evident from the large red shift in PA subunit on complex formation. The two interactions in the complex operated in an antagonistic manner. The two nearly isoenergetic PA-MeOH

structures constituting the global minimum, were distinguishably identified and trapped in our matrix experiments. These complexes showed a relatively strong primary interaction and greater vibrational shift compared with PA-H₂O complex.

In Propargyl amine conformations, the formation of dominantly populated gg form was observed, with no evidence for the higher energy form. It was found that global minimum structure in PAm-H₂O complexes, in which the O-H group of H₂O interacts with the nitrogen atom of PAm, forming an O-H...N interaction, was formed in the matrix. In addition, the computed features for the global minimum structure in PAm-MeOH complex having an O-H...N interaction, were in agreement with the experimental results.

Starting from simpler PA-H₂O structures, we systematically derived different PA homodimers, thus PA-MeOH complexes served as a bridge between the PA-H₂O and PA homodimers. This scheme was used to predict the structures for PA-PAm dimers in a similar way. We have also computationally constructed PAm homodimers from PAm-MeNH₂ complexes, which were evolved systematically from the PAm-NH₃ complexes.

We have highlighted on antagonism where the optimum conditions when individual interactions were present, were sacrificed in forming dual interaction complex. An interesting correlation was made between the PA-H₂O, PA-MeOH and PA homodimers; which was useful in predicting the structures for PA-PAm complexes and PAm homodimers.

CHAPTER 1

INTRODUCTION

Hydrogen bonding is a class of non-covalent interactions, which plays a very important role in many chemical and biological processes.¹⁻³ The classical definition of hydrogen bonding, which states that hydrogen attached to an electronegative atom forms a bond with another electronegative atom, was first proposed by Latimer and Rodebush in 1920.⁴ One of the first examples which did not fit this definition was recognized when June Sutor proposed that the hydrogen attached to carbon could be involved in a hydrogen bond.⁵ In 2011,⁶ a modified definition of hydrogen bonding was presented which states that “the hydrogen bond is an attractive interaction between a hydrogen atom from a molecule or a molecular fragment X-H in which X is more electronegative than H, and an atom or a group of atoms in the same or a different molecule, in which there is evidence of bond formation”. The importance of directionality of the hydrogen bond has also been recognized which drives the structure and folding of proteins, and molecular recognition.⁷

Electronic structure calculations and the experimental techniques such as infrared, NMR spectroscopy, X-Ray diffraction and calorimetry have been widely used to study these interactions. In addition, molecular dynamics simulation has been used to understand the dynamics of formation and breaking of these weak bonds.⁸ Among the experimental techniques, infrared spectroscopy has been a very popular tool since it provides information on the non-covalent interactions present in weakly bound complexes.⁹ The presence, nature and strength of hydrogen bonded interactions are determined from the magnitude and direction (red or blue) of shifts in the vibrational features of the submolecules in the complex, relative to those observed in the uncomplexed molecules. To obtain a good estimate of the shifts, it is essential to have spectral features with small linewidths. Towards this end, matrix isolation spectroscopy and supersonic expansion techniques have been used because of the

small linewidths that these techniques offer.¹⁰ One of the earliest matrix isolation studies include hydrogen bonding in water reported by Pimentel and coworkers in 1957.¹¹ While the supersonic jet technique traps the system in the lowest energy, i.e. the global minimum structures, matrix isolation spectroscopy allows for trapping of both the global and local minima structures, thus offering a better perspective of the potential energy landscape.¹²⁻¹⁴

The strength of hydrogen bond ranges from ~1-40 kcal/mol.¹⁵ While strong hydrogen bonds which have interaction energies greater than 10 kcal/mol, play a significant role in determination of properties of many substances, the weak hydrogen bonds with interaction energies less than 10 kcal/mol are no less important in chemistry and biology.¹⁶ In fact, some of the unique characteristics of hydrogen bonding interactions originate rather ironically from the weakness of these bonds. The small interaction energies of these interactions provide the hydrogen bonds, the flexibility to associate and dissociate quickly at ambient temperatures and on short time scales.

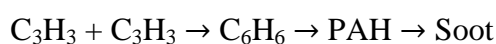
Not infrequently, a molecule can act as a proton donor, a proton acceptor or both. This can result in the formation of different types of hydrogen bonding interactions which fall into the n- σ^* complexes involving O-H \cdots O, O-H \cdots N, \equiv C-H \cdots O, C-H \cdots O, etc. and into the H- π complexes involving O-H $\cdots\pi$, N-H $\cdots\pi$, C-H $\cdots\pi$, etc. Few examples of molecules which have more than one functional group to participate in hydrogen bonding are pyrrole,¹⁷ C₂H₂,¹⁸ phenylacetylene PhAc,¹⁹ o-fluorophenol,²⁰ etc. In the study of complexes of C₂H₂ with water, *only* the global minimum complex having \equiv C-H \cdots O interaction was experimentally observed.¹⁸ In this n- σ^* complex, C₂H₂ served as a proton donor to the oxygen atom of H₂O. Further, when C₂H₂ is complexed with methanol, in addition to the similar n- σ^* complex, the O-H $\cdots\pi$ complex in which C₂H₂ played the role as a proton acceptor through its π bond to the hydroxyl hydrogen of methanol, was also observed in the N₂ matrix.²¹ A recent study of C₂H₂ with propargyl alcohol PA, also showed the formation of both the n- σ^* complex involving a

$\equiv\text{C-H}\cdots\text{O}$ interaction between the acidic hydrogen of C_2H_2 and oxygen atom of PA and the $\text{O-H}\cdots\pi$ complex.²² Thus, in these multifunctional molecules, there is a competition between different types of hydrogen bonding interactions such as $n\text{-}\sigma^*$ or $\text{H-}\pi$. In addition, such molecules can also simultaneously serve the role of a proton donor as well as a proton acceptor in a complex.^{23,24} For example, o-fluorophenol complex with water forming a $\text{O-H}\cdots\text{O-H}\cdots\text{F}$ intermolecular hydrogen bond linkage, has been observed in which o-fluorophenol served as a proton donor through its O-H group and as a proton acceptor through the fluorine atom.²⁰ Similarly, the global minimum for PhAc-water system has a primary $\text{O-H}\cdots\pi$ interaction with PhAc serving as a proton acceptor through its π bond, together with a secondary $\text{C-H}\cdots\text{O}$ hydrogen bond between the C-H of phenyl ring (proton donor) and the oxygen atom of water.¹⁹ Thus, the motivation of the present work is to study the two multifunctional propargyl systems, propargyl alcohol PA and propargyl amine PAm, which can act as a proton donor (through an O-H or N-H group, $\equiv\text{C-H}$ and C-H groups) and a proton acceptor (through acetylenic π electron cloud and lone pairs on oxygen or nitrogen atom), thereby offering a wide spectrum of structures from $n\text{-}\sigma^*$ to $\text{H-}\pi$ contacts. Using matrix isolation spectroscopy, we set out to observe different 1:1 hydrogen bonded complexes of propargyl alcohol and propargyl amine with a variety of precursors, to study the competition between the various isomers of the hydrogen bonded complexes.

In addition to serving as an interesting model system of multifunctional hydrogen bond precursor, propargyl alcohol is also an interesting molecule as it has been considered as a possible candidate for detection in interstellar medium, ISM and has therefore been a subject of intense study.^{25,26} It has also been popular as a probe for the study of both gas phase ion chemistry and surface chemistry on dust grains. The structural isomer of PA, propenal, $\text{H}_2\text{C}=\text{CH-C(O)H}$, has already been detected in the interstellar region.^{25,27} In this regard, PA ice under astrochemical conditions is studied for the first time by Sivaraman et

al.²⁸ The IR spectra of reported amorphous (85 K) and crystalline (180 K) PA ices, thus can be used to detect its presence in the ISM. Another recent study investigated the formation of PA along with its deuterated isomer HCCCH₂OD in a dense molecular cloud, which showed that the gaseous PA can most likely be detected in hot cores or in collections of hot cores such as the star forming region Sagittarius Sgr B2(N).²⁹ Further, theoretical investigations showed that most of the observed astromolecules have the C-C-O backbone, thus rendering PA likely to be detected in ISM.³⁰

PA also finds applications as a corrosion inhibitor and anti-scaling agent.³¹ In organic synthesis, it is used as an intermediate. In addition, PA plays an important role in combustion chemistry.³²⁻³⁴ Recombination of two propargyl radicals yields benzene³⁵⁻³⁸ which is considered one of the key reactions in the production of polycyclic aromatic hydrocarbons (PAH). Sivaraman et al. reported the formation of benzene as the major product, by irradiating the icy layers of PA grown at 85 K by 2 keV electrons, at astrochemical conditions in the laboratory and probed using FTIR spectrometer in 4000-500 cm⁻¹ region.²⁸ Their experiments, thus, confirmed the role of propargyl radicals formed from propargyl alcohol dissociation to effectively synthesize benzene in the interstellar icy mantles.



The infrared and Raman spectra of normal and deuterated liquid PA were recorded and compared with the vapour phase spectrum, which were then subsequently used for the vibrational assignments of PA.³⁹ Recently, for the first time Mani et al.⁴⁰ recorded the mass-selective infrared spectra of PA in 1600-560 cm⁻¹ range using the helium nanodroplet setup which is coupled with free electron lasers. The observed vibrational bands were assigned to the gauche conformer of PA. Earlier microwave studies on PA were performed for the first time by Hirota and Bolton et al. in 1968.⁴¹⁻⁴³ The rotational spectrum of PA has also confirmed the presence of only the gauche form. The gauche conformer was about 1.6

kcal/mol more stable than the trans form at CCSD(T)-F12/VDZ-F12 level of theory and dominated the population at room temperature (~96%).⁴⁴ While the trans form is non-degenerate, the gauche form has two equivalent minima separated by a small barrier corresponding to the orientation of hydroxyl hydrogen on either side of the C-C-C-O plane of PA.⁴³ Theoretical investigations suggested that gauche PA conformer is not stabilized by intramolecular hydrogen bond between the OH group and π electrons.⁴⁵ Later, it was found that the conformational stability was caused by electron repulsion between the oxygen lone pairs and the π -electrons associated with the C \equiv C triple bond.⁴⁴ Clearly, the reason for conformational preference in PA has not been well explained.

In chapter 3, we have addressed the problem of conformers in PA through experiments, AIM calculations and NBO analysis.⁴⁶ In a similar matrix isolation infrared study and DFT calculations using 6-311++G(d,p) basis set, the vibrational wavenumbers of the matrix-isolated spectra of PA in Ar, N₂ and Xe matrices were compared with the DFT calculations, which clearly revealed that only the gauche conformer was trapped and identified in the experiment.²² However, there was no explanation for the conformational stability of gauche form. Therefore, we have revisited the conformational landscape of PA in order to deduce the reason for stability of gauche PA over the other form. As a result of this work, we have shown that the conformational stability resulted from the interplay of electron delocalization interactions, particularly the remote and vicinal orbital interactions as revealed from NBO analysis. The importance of such interactions in the conformations of molecules has been reported in many other systems in the literature.^{47,48} For example in a recent work,⁴⁷ using matrix isolation infrared and *ab initio* study on threonine, the importance of such interactions has been discussed.

Following the study of PA conformers, we studied the weak complexes of PA. The first experimental and theoretical study on weakly bound complex of PA was conducted in

2013.⁴⁹ Mani and Arunan reported the pure rotational spectra of Ar \cdots PA complex and its two deuterated forms (Ar \cdots PA (-OD)) and Ar \cdots PA (\equiv CD)). They confirmed the occurrence of cyclic PA \cdots Ar complex, in which gauche PA interacts with Ar to form O-H \cdots Ar and Ar $\cdots\pi$ interactions as revealed by AIM and electrostatic potential (ESP) calculations, and thus enjoys the proximity of both the O-H group and π electron density. The 1:1 complexes of PA-C₂H₂ have also been studied.²² Four minima corresponding to complexes A (C-H \cdots O), B (O-H $\cdots\pi$), C and D (C-H $\cdots\pi$) were located. The IR spectra of PA and C₂H₂ codeposited in the Ar matrix together with DFT computations indicated that both the global minimum complex A, where oxygen of PA subunit served as the proton acceptor and the local minimum complex B, where the hydroxyl hydrogen of PA subunit acts as a proton donor, were generated in low temperature matrix.

We have studied 1:1 complexes of PA with H₂O using matrix isolation infrared spectroscopy and *ab initio* computations.⁴⁶ We have also compared the computed PA-H₂O complexes with reported complexes of PhAc-H₂O system,¹⁹ in which the structure having primary O-H $\cdots\pi$ interaction together with a relatively weak C-H \cdots O interaction, constitutes the global minimum. It was found that a similar structure was computed as a global minimum for PA-H₂O system with dual interactions and we wished to note if the dual interactions act together in a synergistic manner.

In chapter 4, we have presented our experimental and computational work on PA-MeOH complexes which provides the possibility of C-H interactions involving the methyl group of MeOH, thus providing a richer landscape of non-covalently bonded complexes.⁵⁰ A comparison has also been made between PA-MeOH and PA-H₂O system in terms of their interaction energies, gas phase basicity values, geometrical parameters and vibrational shifts.

We next wished to explore the effect of replacing the O-H group in PA with an NH₂ group and hence study propargyl amine (PAm). PAm was studied using matrix isolation

infrared spectroscopy for the first time by Hamada et al. in 1984.⁵¹ They observed the IR spectra in gas phase and in low temperature Ar matrix which showed the presence of ggPAm conformer. Geometry optimization and vibrational analysis of the PAm conformers was performed with *ab initio* MO calculations using 4-31G(N*) basis set. They confirmed their vibrational assignments through isotopic experiments on two partially deuterated species DCCCH₂ND₂ and HCCCH₂ND₂. In addition, previous microwave^{42,52} and Raman⁵³ spectroscopic studies have also been performed on PAm.

Chapter 5 presents our experimental and computational work on the conformers of PAm and its 1:1 hydrogen bonded complexes with H₂O and MeOH. Study of PAm conformers and complexes, which has not been explored well before, provides a logical extension to our work on PA conformers. The most stable ggPAm conformer is non-degenerate and the higher energy gt form is doubly degenerate in contrary to the doubly degenerate gauche form and non-degenerate trans PA conformer. We therefore explored the possibility of observing the higher energy gtPAm conformer in our experiments, for which there has not been any experimental evidence. In the 1:1 hydrogen bonded complexes of PAm with H₂O and MeOH, we were motivated to see how a relatively poor proton donor PAm, compared with PA, will interact with these precursors and whether the most stable structure would be similar or not, to that observed for PA-H₂O and PA-MeOH system.

In addition, we have also computed the 1:1 hydrogen bonded complexes of PA and PAm with diethylether (DEE), similar to a recent matrix isolation infrared and *ab initio* study on hydrogen bonded interactions of pyrrole with different precursors like H₂O, MeOH and dimethylether to understand the effect of successive methyl substitution on hydrogen atom of water, on hydrogen bond strength and vibrational shifts.¹⁷

In chapter 6, we have discussed a scheme through which we can predict the structures of complex systems starting from the structures of simple systems. In this way, we have

computed different PA homodimers by systematic replacement of each of the methyl hydrogens in PA-MeOH complexes with an acetylenic group. Similarly, we arrived at different PA-MeOH complexes by systematically replacing each hydrogen atom in H₂O with a methyl group. In addition, for the first time, we have presented the matrix isolation infrared experimental results on PA homodimers.⁵⁴ Earlier, Mani and Arunan had reported the rotational spectra of the most stable structure of PA homodimer and its two mono-deuterated and one bi-deuterated isotopologues.⁵⁵ AIM analysis showed that the two monomer entities in the observed dimer were in a three point contact involving an O-H···O, O-H··· π and C-H··· π hydrogen bond interaction. Computationally, a number of isomers were indicated for the PA dimers, though only the most stable structure was observed in the gas phase study. From our experimental work, we wished to possibly trap the other computed PA homodimers together with the most stable dimer, thereby providing an explanation for the reported changes in observed IR spectra of PA ices.²⁸

We were also interested to compute the structures of PA-PAm heterodimers and the PAm homodimers implementing the same scheme that was used for deriving the structures of PA homodimers.

The conclusions drawn from our work have been presented in chapter 7.

1.1. Scope of Present Work

The principal aim of this work is to understand the interplay of different hydrogen bonding interactions in the stabilization of PA or PAm complexes, both of which are multifunctional molecules. In the matrix isolation infrared study on C₂H₂-H₂O complex by Engdahl and Nelander,¹⁸ the global minimum n- σ^* structure where C₂H₂ served as a proton donor forming a \equiv C-H···O interaction, was observed. Computations did indicate a weak local minimum corresponding to the C₂H₂-H₂O complex having an O-H··· π interaction.⁵⁶ Similarly, the global minimum n- σ^* complex was also observed experimentally in the C₂H₂-

MeOH complex.²¹ When phenylacetylene PhAc, containing a phenyl ring in place of an acetylenic hydrogen, was complexed with H₂O, it is the H- π structure that was computed to be the global minimum and not the n- σ^* complex.¹⁹ The greater stability of cyclic PhAc-H₂O complex having a primary O-H $\cdots\pi$ interaction between the acetylenic π cloud of PhAc and O-H group of H₂O, is attributed to the presence of a secondary C-H \cdots O interaction. Gas phase studies observed the O-H $\cdots\pi$ complex, while the matrix isolation experiments observed the n- σ^* complex, which was the local minimum.

In this thesis work, we have examined the effect of -OH and a relatively poor proton donor -NH₂ group, replacing the phenyl group in PhAc, in the formation of 1:1 hydrogen bonded complexes. We have discussed that depending on the relative strengths of hydrogen bonding interactions, the stability of complexes on potential energy surface is altered. We wished to explore, whether an H- π complex wins over n- σ^* complex, in the case of PA-H₂O and PAm-H₂O system, and which complex will be observed in our experiments.

We have also explored whether in a 1:1 PA-H₂O complex having more than one hydrogen-bonding interaction, the interactions operate together in a cooperative manner to increase the overall stabilization of the complex, implying that the interaction energy of the complex having multiple contacts ought to be *greater* than the sum of the interaction energies of complexes where each of the interactions were present individually. This cooperative effect will then be confirmed from the spectral shifts, change in the geometrical parameters and the orbital interactions.⁵⁷ Thus, cooperativity effects in hydrogen bonded complexes are important, which we have studied in this thesis work.

Interestingly, as a result of our work, we were able to observe a trend between PA-H₂O, PA-MeOH complexes and PA homodimers through computations. It was found that different complex structures could be constructed progressively from the simpler systems by replacing one group with the other group. This scheme of deriving the structures of

complexes presents a simpler method which we have employed to systematically derive the structures of different PA-PAm complexes and PAm homodimers easily without the trouble of optimizing the complex structures by guessing the input geometry.

In short, our thesis presents the matrix isolation infrared studies on molecular conformations and hydrogen bonded complexes of two propargyl systems, which is well supported by the computational results.

References

1. Espinoza, C.; Szczepanski, J.; Vala, M.; Polfer, C. N. Glycine and its Hydrated Complexes: a Matrix Isolation Infrared Study. *J. Phys. Chem. A* **2010**, *114*, 5919-5927.
2. Nishio, M. The CH/ π Hydrogen Bond in Chemistry: Conformation, Supramolecules, Optical Resolution and Interactions involving Carbohydrates. *Phys. Chem. Chem. Phys.* **2011**, *13*, 13873-13900.
3. Altnöder, J.; Lee, J. J.; Otto, K. E.; Suhm, M. A. Molecular Recognition in Glycoaldehyde, the Simplest Sugar: Two Isolated Hydrogen Bonds Win Over One Cooperative Pair. *ChemistryOpen* **2012**, *1*, 269-275.
4. Latimer, W. M.; Rodebush, W. H. Polarity and Ionization from the standpoint of the Lewis Theory of Valence. *J. Am. Chem. Soc.* **1920**, *42*, 1419-1433.
5. Sutor, D. J. The C-H \cdots O Hydrogen Bonds in Crystals. *Nature* **1962**, *195*, 68-69.
6. Arunan, E.; Desiraju, G. R.; Klein, R. A.; Sadlej, J.; Scheiner, S.; Alkorta, I.; Clary, D. C.; Crabtree, R. H.; Dannenberg, J. J.; Hobza, P.; Kjaergaard, H. G.; Legon, A. C.; Mennucci, B.; Nesbitt, D. J. Definition of the Hydrogen Bond. *Pure Appl. Chem.* **2011**, *83*, 1637-1641.
7. Hubbard, E. R.; Kamran, M. John Wiley & Sons, **2010**.
8. Mori, Y.; Masuda, Y. Effect of Solvent on Proton Location and Dynamic Behaviour in Short Intramolecular Hydrogen Bonds Studied by Molecular Dynamics Simulations and NMR Experiments. *Chem. Phys.* **2015**, *458*, 18-29.
9. Dubey, P.; Saini, J.; Verma, K.; Karir, G.; Mukhopadhyay, A.; Viswanathan, K. S. "Matrix Isolation: A window to Molecular Processes" in *Molecular and Laser Spectroscopy: Advances and Applications*. Elsevier, **2017**, 317-340.
10. Khriachtchev, L. Matrix-Isolation Studies of Noncovalent Interactions: More Sophisticated Approaches. *J. Phys. Chem. A* **2015**, *119*, 2735-2746.
11. Thiel, M. V.; Becker, E. D.; Pimentel, G. C. Infrared studies of Hydrogen bonding of Water by the Matrix Isolation Technique. *J. Chem. Phys.* **1957**, *27*, 486-490.
12. Karir, G.; Viswanathan, K. S. The elusive $\equiv\text{C}-\text{H}\cdots\text{O}$ complex in the Hydrogen bonded systems of Phenylacetylene: A Matrix Isolation Infrared and *Ab Initio* Study. *J. Chem. Sci.* **2016**, *128*, 1557-1569.
13. Verma, K.; Viswanathan, K. S.; Sathyamurthy, N.; Majumder, M. How different is the Borazine-Acetylene Dimer from the Benzene-Acetylene Dimer? A Matrix Isolation Infrared and *Ab Initio* Quantum Chemical Study. *Mol. Phys.* **2017**, *115*, 2637-48.
14. Goswami, M.; Arunan, E. Microwave Spectroscopic and Theoretical Studies on the Phenylacetylene \cdots H₂O complex: C-H \cdots O and O-H \cdots π Hydrogen Bonds as Equal Partners. *Phys. Chem. Chem. Phys.* **2011**, *13*, 14153-14162.
15. Desiraju, G. R.; Steiner, T. *The Weak hydrogen Bond in Structural Chemistry and Biology*. **1999**, Oxford University Press Inc., New York.

-
16. Steiner, S. Weak H-bonds. Comparisons of CH \cdots O to NH \cdots O in Proteins and PH \cdots N to Direct P \cdots N Interactions. *Phys. Chem. Chem. Phys.* **2011**, *13*, 13860-13872.
17. Sarkar, S.; Ramanathan, N.; Sundararajan, K. Effect of Methyl Substitution on the N–H \cdots O Interaction in Complexes of Pyrrole with Water, Methanol, and Dimethyl Ether: Matrix Isolation Infrared Spectroscopy and *Ab Initio* Computational Studies. *J. Phys. Chem. A* **2018**, *122*, 2445-2460.
18. Engdahl, A.; Nelander, B. The Acetylene-Water Complex. a Matrix Isolation Study. *Chem. Phys. Lett.* **1983**, *100*, 129-132.
19. Karir, G.; Viswanathan, K. S. Phenylacetylene-water complex: Is it n- σ or H- π in the matrix? *J. Mol. Struct.* **2016**, *1107*, 145-156
20. Banerjee, P.; Bhattacharya, I.; Chakraborty, T. Cooperative effect on Phenolic vO–H frequencies in 1:1 Hydrogen bonded complexes of o-Fluorophenols with Water: A Matrix Isolation Infrared Spectroscopic study. *Spectrochim. Acta, Part A* **2017**, *181*, 116-121.
21. Sundararajan, K.; Viswanathan, K. S. A Matrix Isolation and *Ab initio* study of the C₂H₂-MeOH complex. *J. Mol. Struct.* **2006**, *798*, 109-116.
22. Sundararajan, K.; Gopi, R.; Ramanathan, N. Conformations of Propargyl Alcohol and its Interaction with Acetylene: a Matrix Isolation Infrared and DFT Computations. *J. Mol. Struct.* **2016**, *1121*, 26-34.
23. Jemmis, E. D.; Giju, K. T.; Sundararajan, K.; Sankaran, K.; Vidya, V.; Viswanathan, K. S.; Leszczynski, J. An *Ab initio* and Matrix Isolation Infrared study of the 1:1 C₂H₂-CHCl₃ adduct. *J. Mol. Struct.* **1999**, *510*, 59-68.
24. Heger, M.; Schargez, T.; Suhm, M. A. From Hydrogen bond donor to acceptor: the effect of Ethanol Fluorination on the first solvating water molecule. *Phys. Chem. Chem. Phys.* **2013**, *15*, 16065-16073.
25. <http://science.gsfc.nasa.gov/691/cosmicice/interstellar.html>.
26. Pearson, J. C.; Drouin, B. J. The Ground State Torsion-Rotation Spectrum of Propargyl Alcohol (HCCCH₂OH). *J. Mol. Spectrosc.* **2005**, *234*, 149-156.
27. Hollis, J. M.; Jewell, P. R.; Lovas, F. J.; Remijan, A.; Møllendal, H. Green Bank Telescope Detection of New Interstellar Aldehydes: Propenal and Propanal. *ApJL* **2004**, *610*, 21-24.
28. Sivaraman, B.; Mukherjee, R.; Subramanian, K. P.; Banerjee, S. B. Benzene Formation on Interstellar Icy Mantles containing Propargyl Alcohol. *ApJL* **2015**, *798*, 1-4.
29. Gorai, P.; Das, A.; Majumdar, L.; Chakrabarti, S. K.; Sivaraman, B.; Herbst, E. The Possibility of Forming Propargyl Alcohol in the Interstellar Medium. *Molecular Astrophysics* **2017**, *6*, 36-46.
30. Etim, E. E.; Gorai, P.; Das, A.; Arunan, E. Theoretical investigation of Interstellar C–C–O and C–O–C bonding backbone molecules. *Astrophys. Space Sci.* **2018**, 363:6.
31. http://pubchem.ncbi.nlm.nih.gov/compound/propargyl_alcohol.
32. Miller, J. A.; Melius, C. F. Kinetic and Thermodynamic issues in the formation of Aromatic compounds in flames of Aliphatic fuels. *Combust. Flame* **1992**, *91*, 21-39.

-
33. Frenklach, M. Reaction mechanism of Soot formation in Flames. *Phys. Chem. Chem. Phys.* **2002**, *4*, 2028-2037.
34. Sharath, N.; Reddy, K. P. J.; Arunan, E. Thermal Decomposition of Propargyl Alcohol: Single Pulse Shock Tube Experimental and *Ab Initio* Theoretical Study. *J. Phys. Chem.* **2014**, *118*, 5927-5938.
35. Schüßler, T.; Roth, W.; Gerber, T.; Alcaraz, C.; Fischer, I. The VUV photochemistry of Radicals: C_3H_3 and C_2H_5 . *Phys. Chem. Chem. Phys.* **2005**, *7*, 819-825.
36. Zhang, X.; Sander, S. P.; Chaimowitz, A.; Ellison, G. B.; Stanton, J. F. Detection of Vibrational Bending Mode ν_8 and Overtone Bands of the Propargyl Radical, $HCCCH_2 \tilde{X}^2B_1$. *J. Phys. Chem. A* **2010**, *114*, 12021-12027.
37. Zhang, X.; Sander, S. P.; Stanton, J. F. Detection of the far-IR ν_{12} bending level in Propargyl: a complete set of fundamentals for an important radical. *J. Phys. Chem. A* **2012**, *116*, 10338-10343.
38. Wilson, E. H.; Atreya, S. K.; Coustenis, A. Mechanisms for the formation of Benzene in the atmosphere of Titan. *J. Geophys. Res.* **2003**, *108* (E2), 5014.
39. Nyquist, R. A. Vibrational Assignments of $H-C\equiv C-CH_2OH$ and its Deuterium Analogs. *Spectrochim. Acta Part A* **1971**, *27*, 2513-2523.
40. Mani, D.; Fischer, T.; Schwan, R.; Dey, A.; Redlich, B.; Van der Meer, A. F. G.; Schwaab, G.; Havenith, M. A Helium Nanodroplet setup for mid and far Infrared Spectroscopy using Pulsed-free-electron Lasers: Vibrational spectra of Propargyl Alcohol. *RSC Adv.* **2017**, *7*, 54318-54325.
41. Hirota, E. Internal Rotation in Propargyl Alcohol from Microwave Spectrum. *J. Mol. Spectrosc.* **1968**, *26*, 335-350.
42. Bolton, K.; Owen, N. L.; Sheridan, J. Molecular Structure of Propargyl Alcohol and Propargyl Amine from Microwave Spectra. *Nature* **1968**, *217*, 164-164.
43. Pearson, J. C.; Drouin, B. J. The Ground state Torsion–Rotation spectrum of Propargyl Alcohol ($HCCCH_2OH$). *J. Mol. Spectrosc.* **2005**, *234*, 149-156.
44. Miller, B. J.; Lane, J. R.; Kjaergaard, H. G. Intramolecular $OH\cdots\pi$ interactions in alkenols and alkynols. *Phys. Chem. Chem. Phys.* **2011**, *13*, 14183-14193.
45. Stewart, E. L.; Mazurek, U.; Bowen, J. P. *Ab Initio* and Molecular Mechanics (MM3) Calculations on Propargyl Alcohol and Derivatives. *J. Phys. Org. Chem.* **1996**, *9*, 66-78.
46. Saini, J.; Viswanathan, K. S. Does a Hydrogen bonded complex with Dual contacts show Synergism? A Matrix Isolation Infrared and *Ab initio* study of Propargyl Alcohol-Water complex. *J. Mol. Struct.* **2016**, *1118*, 147-156.
47. Dubey, P.; Mukhopadhyay, A.; Viswanathan, K. S. Do Amino acids prefer only certain backbone structures? Steering through the Conformational maze of L-Threonine using Matrix isolation Infrared spectroscopy and *Ab initio* studies. *J. Mol. Struct.* **2019**, *1175*, 117-129.

-
48. Ramanathan, N.; Sundararajan, K.; Kar, B. P.; Viswanathan, K. S. Conformations of Trimethyl Phosphite: A Matrix Isolation Infrared and *Ab Initio* Study. *J. Phys. Chem. A* **2011**, *115*, 10059-10068.
49. Mani, D.; Arunan, E. Microwave Spectroscopic and Atoms in Molecules Theoretical Investigations on the Ar \cdots Propargyl Alcohol Complex: Ar \cdots H-O, Ar \cdots π , and Ar \cdots C Interactions. *Chem. Phys. Chem.* **2013**, *14*, 754-763.
50. Saini, J.; Viswanathan, K. S. From Propargyl Alcohol-Water to the Propargyl Alcohol Dimer: Where does the Propargyl Alcohol-Methanol fit in? *New J. Chem.* **2019**, *43*, 3969-3980.
51. Hamada, Y.; Tsuboi, M.; Nakata, M.; Tasumi, M. Infrared Spectrum of Propargylamine. *J. Mol. Spectros.* **1984**, *107*, 269-283.
52. Cervellati, R.; Caminati, W.; Esposti, C. D.; Mirri, A. M. Structure and Dipole Moment of Trans Propargyl Amine by Microwave Spectroscopy. *J. Mol. Spectrosc.* **1977**, *66*, 389-398.
53. Verma, A. L.; Bernstein, H. J. Rotational Isomerism in Propargyl Amine studied by Raman Spectroscopy. *J. Chem. Soc. Faraday Trans 2* **1973**, *69*, 1586-1589.
54. Saini, J.; Viswanathan, K. S. Discerning Near-Isoergic Isomers. A Matrix Isolation Infrared and *Ab Initio* Study of the Propargyl Alcohol Dimers. *J. Phys. Chem. A* **2017**, *121*, 1448-1459.
55. Mani, D.; Arunan, E. Rotational Spectra of Propargyl Alcohol Dimer: a Dimer Bound with Three Different Types of Hydrogen Bonds. *J. Chem. Phys.* **2014**, *141*, 164311.
56. Rovira, M. C.; Novoa, J. J.; Whangbo, M. H.; Williams, J. M. *Ab initio* computation of the potential energy surfaces of the water-hydrocarbon complexes H₂O \cdots C₂H₂, H₂O \cdots C₂H₄ and H₂O \cdots CH₄: minimum energy structures, vibrational frequencies and hydrogen bond energies. *Chem. Phys.* **1995**, *200*, 319-335
57. Samanta, A. K.; Banerjee, P.; Bandyopadhyay, B.; Pandey, P.; Chakraborty, T. Antagonistic Interplay between an Intermolecular CH \cdots O and an Intramolecular OH \cdots O Hydrogen Bond in a 1:1 Complex between 1,2-Cyclohexanedione and Chloroform: A Combined Matrix Isolation Infrared and Quantum Chemistry Study. *J. Phys. Chem. A* **2017**, *121*, 6012-6020.

CHAPTER 2

EXPERIMENTAL AND COMPUTATIONAL DETAILS

2.1. Introduction

The experimental technique of matrix isolation involves the isolation of analyte molecules in an inert gas matrix. The inert gases usually employed for isolation are Ar, N₂, Ne or Xe. The gas mixture, consisting of the analyte at high dilution in the matrix gas, is then deposited as a solid film on to a cold substrate which is maintained at a very low temperature of ~ 10 K. The dilutions employed are usually 1:1000 or better of the analyte:matrix mixture. This technique together with the spectroscopic tools is useful in investigating and understanding the chemical structure, bonding and reactivity of the trapped species. It is also popularly employed in the study of highly reactive species, reaction intermediates, exotic molecules, non-covalently bonded complexes and molecular conformations.

In the study of free radicals and other unstable substances, the inherent difficulty is the maintenance of suitable concentration of the reactive species under study, due to their high reactivity and fleeting lifetimes. The matrix isolation technique was first used to prepare such highly reactive free radicals and atoms through photolysis of a substance dissolved in glassy matrices and obtain their UV spectra.^{1,2} In 1954, Whittle, Dows and Pimentel for the first time, used matrix isolation technique for the infrared investigation of free radicals by studying the unstable products of decomposition of hydrazoic acid.^{3,4}

In the work described in this thesis, the molecules of interest, sample was isolated in a large excess of an inert gas, such as Ar or N₂. This gas mixture containing the inert gas and the vapours of sample molecules in the ratios of 1000:1, respectively, is effused through a nozzle into a vacuum system, which houses a cryostat onto which KBr window is mounted. The high

dilutions employed in our experiments causes the sample molecules to be isolated from each other, resulting in negligible intermolecular interactions between the sample molecules.

The important characteristic of matrix material is its chemical inertness, to avoid any reaction between the matrix and trapped species. In addition, the matrix gas must be free from impurities and transparent in the range where sample molecules absorb to prevent any spectral interference. Other rare gases besides Ar, which could be used as matrix gases are Ne, Kr and Xe. N₂ gas has also been popularly used. Alkanes have also been used as matrix material (Shpol'skii matrices) to detect matrix isolated species using fluorescence spectroscopy. CH₄, O₂, CO₂, SF₆, CO etc. can also be employed as matrix materials however they suffer from the disadvantage of reactivity to the sample molecules and spectral absorptions in the region of interest.

In the solid lattice formed by the inert matrix gas, there are broadly two possible sites for trapping the guest molecules: a) substitutional sites and b) interstitial sites. Both N₂ (below 35 K) and Ar crystallize in face centred cubic (f.c.c.) lattice.⁵ In f.c.c. arrangement, a species is most likely to be trapped in a substitutional site, which will be equally surrounded by 12 nearest matrix molecules. Thus, most species will occupy a "cage" consisting of more than one substitutional site. Removal of two matrix atoms gives rise to a site with 18 nearest matrix molecules.⁶ The substitutional site formed by removal of 3 matrix atoms in a triangle will make a site with 22 nearest neighbours and loss of 3 atoms in a row will give rise to 24 nearest neighbours.

In such lattices, there are two different interstitial sites: a tetrahedral site and an octahedral site. An octahedral site is less than half the size of surrounding spheres⁵ and could

only entrap species of small sizes. A tetrahedral site is less than one quarter the size of matrix molecule and is unlikely to be a trapping site unless seriously distorted.

As a rule of thumb, temperature of cold window should be kept at 30% below the melting point of matrix material used, to ensure rigidity of matrix material. Below this temperature, essentially no diffusion of isolated species is expected to occur. The need for rigid matrix requires low temperature which is provided by the cryogenic technology, which in turn work efficiently only under high vacuum conditions. In our experiments, the gas mixture is deposited as a solid thin film on the KBr window maintained at very low temperatures of ~ 12 K. After deposition, the infrared spectra are recorded for the matrix-isolated species at ~ 12 K, in the range of $4000-400\text{ cm}^{-1}$. The cryogenic temperature ensures that only lowest rovibronic and electronic levels of the sample are populated, thus resulting in significant reduction of spectral congestion. Rigidity of matrix at low temperature is also essential to prevent diffusion of sample molecules.

The immobilization of sample molecules in inert matrix at cryogenic temperatures ensures the absence of broadenings due to collision and Doppler effects. Furthermore, small linewidths of $2-4\text{ cm}^{-1}$ are obtained in matrix-isolated spectra due to isolation of sample molecules in the cage of inert matrix, minimizing the intermolecular interactions between sample molecules, as compared with the $40-60\text{ cm}^{-1}$ linewidths typical of condensed phase spectra. Sharp linewidths are useful for detecting very weak hydrogen bonded complexes showing frequency shift of a few to a few tens of wavenumbers.

This technique coupled with the spectroscopic probes such as UV/visible,⁷ Infrared, Fluorescence,⁸ ESR⁹ and Raman spectroscopy,¹⁰ have been used to study and characterize the matrix-isolated species. The choice of cold window, which acts as a substrate for deposition of matrix, depends on the spectroscopic method used for analysis. KBr or NaCl windows can be

used for infrared spectroscopy for the range of 4000-400 cm^{-1} , while for the analysis below 400 cm^{-1} , CsBr or CsI windows are used. For UV/Visible spectroscopy, quartz is used, while for ESR, copper or sapphire tipped copper rods are used as matrix substrates.

While the inert gases are minimally perturbing, it must be recognized that the trapped species are perturbed by the matrix gas and leads to matrix effects.

It must also be noted that sample to be studied should have sufficient vapour pressure at easily attainable temperatures which can be deposited on the cold substrate so as to obtain a detectable signal. Non-volatile substances having negligible vapour pressure pose problems as it is difficult to deposit them onto the matrix. The use of high temperature is resorted to, for depositing such species, but one must be careful not to decompose the sample during deposition.

Thus, the matrix isolation technique which involves trapping of analyte molecules in an inert environment provides for small linewidths and uncongested spectral features for the molecule under study. Our experiments, conducted using matrix isolation technique probed by infrared spectroscopy and the home-built setup have been discussed in the following section.

2.2. Matrix Isolation Infrared Setup

Our matrix isolation infrared spectroscopy (Fig. 2.1) consists of the following components: a) Cryogenic Assembly, b) Vacuum System, c) FTIR Spectrometer, and d) Sample Introduction.

a) Cryogenic Assembly: We have used the cryostat CH-202W Model, cooled by closed-cycle-Helium compressor Sumitomo Heavy Industries Ltd. (SHI) Model HC-4E1, to attain the temperature of ~ 12 K, required for our experiments.

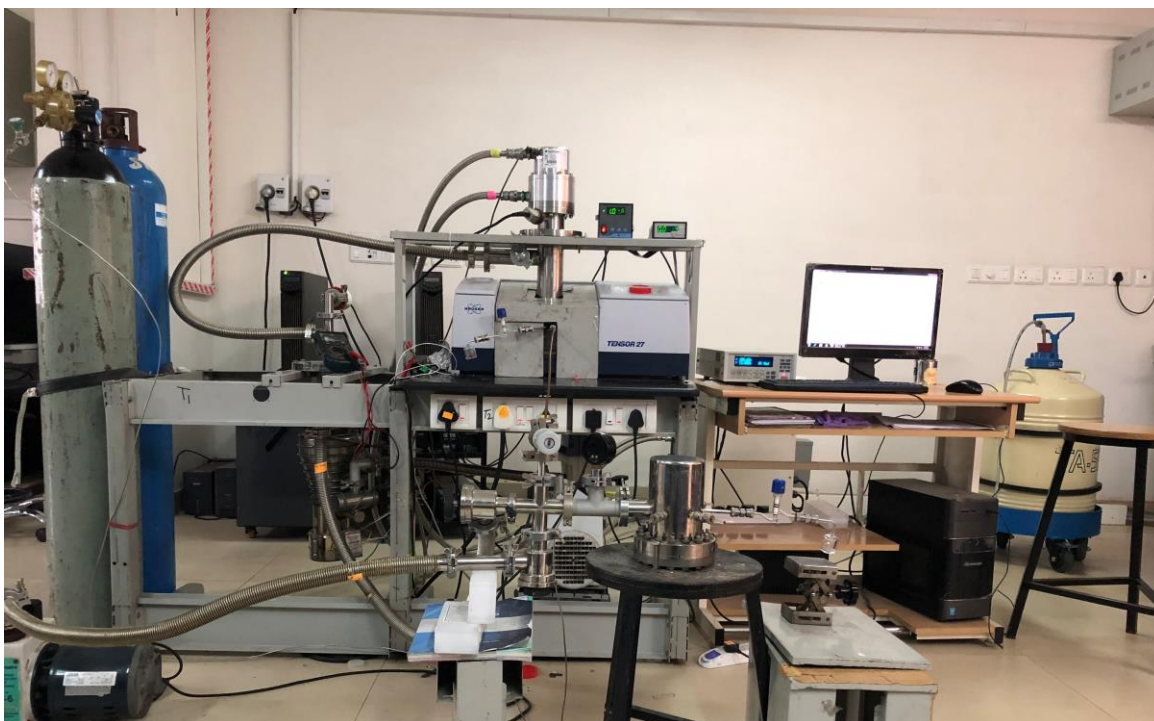


Fig. 2.1. Home-built Matrix Isolation Infrared Spectroscopy Setup

An electronically controlled temperature controller unit, Lakeshore Instruments-Model No. 335 helps to maintain the temperature of the cryotip between 12 K and 300 K. The temperature controller regulates the temperature by a closed loop PID (Proportional-Integral-Derivative) controller coupled to a heater unit. A silicon diode was used as sensor for monitoring the temperature. Temperature variation was required 1) to anneal the matrix, thus promoting diffusion of the trapped species leading to formation of complex and 2) to study the effect of multiple sites on the vibrational features of the trapped species. Annealing temperatures of 27 K for N_2 and 32 K for Ar were used and the matrix was kept at this temperature for about 1 hr after which the window was recooled to 12 K and a spectrum recorded. A 25 mm diameter and 2 mm thick KBr window is mounted on the cryotip. The distance of this KBr window from the effusive nozzle is ~50 mm. Two KBr windows of diameter ~40 mm and thickness ~4 mm were placed coaxial with KBr mounted on the cryotip. Barnes and Hallam⁵ have provided a schematic

diagram of the cryostat and matrix isolation cell together with gas injection system, which is shown in Fig. 2.2.

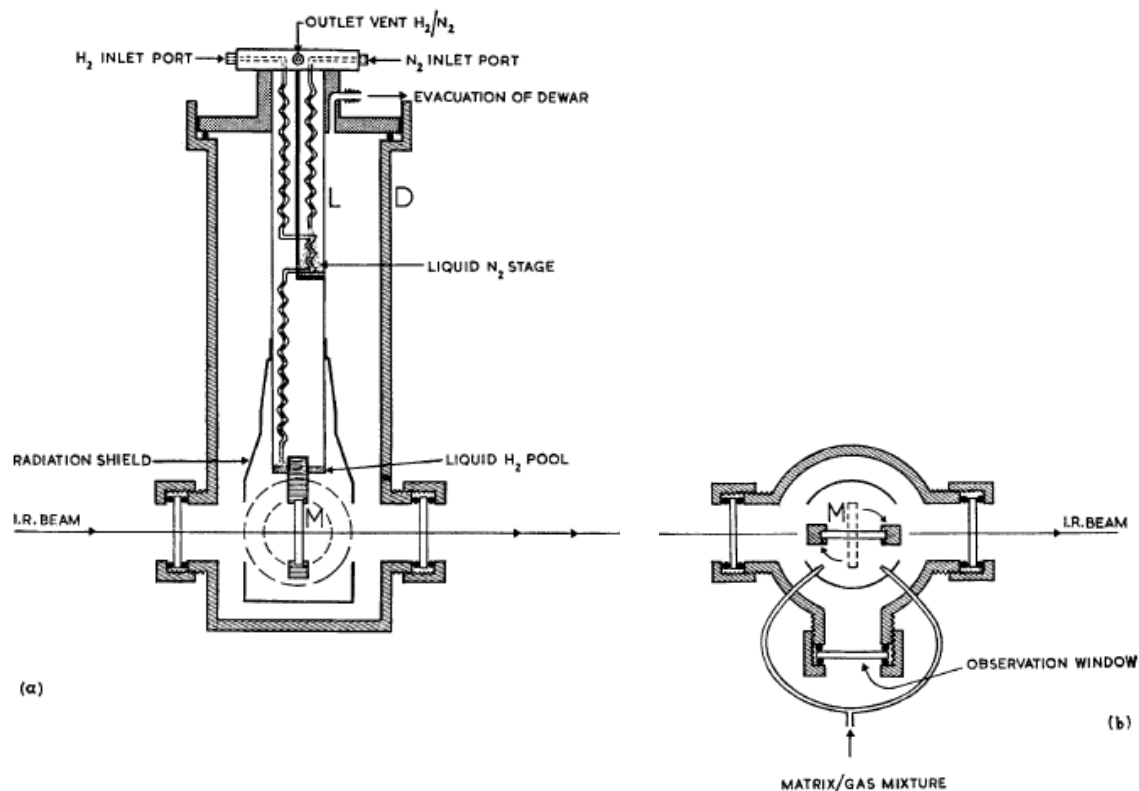


Fig. 2.2. a) Cryostat and Matrix Isolation cell, D = vacuum shroud, L = liquefier, M = matrix support window; b) Gas Injection System.

b) Vacuum System: The cryosystem was kept under high vacuum, the base pressure in the system being of $\sim 10^{-6}$ mbar or lower, achieved using a vapour diffusion pump (Edwards, Diffstak MK2 series 100/300) operating at a pumping speed of 300 L/sec. This diffusion pump is backed by a mechanical rotary pump (Hind Hivac, ED6) operating at a pumping speed of 200 L/min, providing rough vacuum of about 10^{-2} mbar. The vacuum is measured through two gauges: a digital Penning Gauge (Hind Hivac) and a Pirani Gauge 26 (Edwards APG 100 Active Pirani Gauge). A 2 kW water chiller system (Werner Finley) circulates water to the compressor and the diffusion pump at an approximate temperature of 15.0°C .

c) Fourier Transform Infrared (FTIR) Spectrometer: The Bruker-Tensor 27 FTIR Spectrometer was used for our experiments, operating at a resolution of 0.5 cm^{-1} . Typically eight scans were coadded to obtain a spectrum (in transmittance) with a good signal-to-noise ratio. A zero-filling factor of 8 and a triangular apodization function was used for the fourier transformation. The interferogram was sampled sufficiently to meet the Nyquist's sampling criterion to enable a correct identification of the wavenumbers after fourier transform without any problem of aliasing.

To begin with, a reference spectrum is recorded once the cryostat temperature reaches $\sim 12\text{ K}$. The sample is then deposited onto the KBr window mounted on the cryotip, as shown in Fig. 2.1. After deposition, which lasts typically for 1 hr, an infrared spectrum is recorded at $\sim 12\text{ K}$. The matrix is then annealed at an elevated temperature as mentioned earlier, recooled back to $\sim 12\text{ K}$ and finally, the annealed spectrum is recorded.

d) Sample Introduction: The matrix gas and sample mixture was prepared using manometric techniques and this mixture was deposited onto the cryostat by a controlled flow of the gas mixture. For this purpose, a vacuum line was built that incorporates a stainless steel storage chamber of 1 L capacity having four ports for attachment of glass containers. The vacuum system have pressure gauges to monitor the pressure in the mixing chamber, a fine-flow needle valve that allows controlled effusion of the gas mixture and interfaces to the inlet system attached to the vacuum shroud of the cryostat.

Initially, the cryostat and the mixing chamber were pumped down to a pressure less than $\sim 1 \times 10^{-6}$ mbar. The compressor was turned on to bring the temperature of the KBr window to $\sim 12\text{ K}$ from $\sim 300\text{ K}$. Using a liquid nitrogen and ethanol slush bath, the sample was maintained at an appropriate temperature for about 30 min to obtain the desired vapour pressure of the

sample. A PRT (HTA Instrumentation (P) Ltd., Resistance temperature detector, RTD with temperature range -100 to 200 °C) was used to determine temperatures of the slush bath. The temperature required to maintain the vapour pressure was obtained from the vapour pressure data of the sample and the use of Clausius Clayperon equation. The chamber was then topped with the matrix gas to about 1000 mbar, to obtain desired sample-to-matrix ratio. A needle valve (Model: EVN 116, Pfeiffer Vacuum) was used to control the rate of flow of mixture, through the effusive nozzle to the vacuum system. The rate of deposition was typically 3 mmol/hr of the matrix gas contained in 1 L volume of mixing chamber. In our experiments, roughly, the concentration of sample molecules that were deposited, was about 1×10^{19} molecules/cm³ in a cylindrical thin film of thickness of ~20 µm.

In few experiments, a double jet nozzle was used, in which one of the samples was effused through one nozzle, and the second precursor together with the matrix gas from the other nozzle, in order to codeposit two precursors. In addition, we always perform the concentration dependence studies which confirmed the features arising due to complex formation.

2.3. Hot Nozzle Source

A home-built hot nozzle source assembly was used in few experiments (Fig. 2.3) in order to observe the features corresponding to the higher energy conformer through the use of elevated temperatures. The main components of this assembly were the effusive nozzle and the sample holder. A nichrome wire was coiled around the stainless steel nozzle and the sample holder to heat it. A thermocouple was coiled onto the nozzle to measure the temperature of the nozzle. This hot nozzle assembly was mounted on a stainless steel flange.

Before starting deposition, the hot nozzle was heated to the required temperatures. The hot sample/matrix gas mixture coming from the hot nozzle was allowed to deposit on KBr window at 12 K at a rate of ~ 3 mmol/hr of the matrix gas.

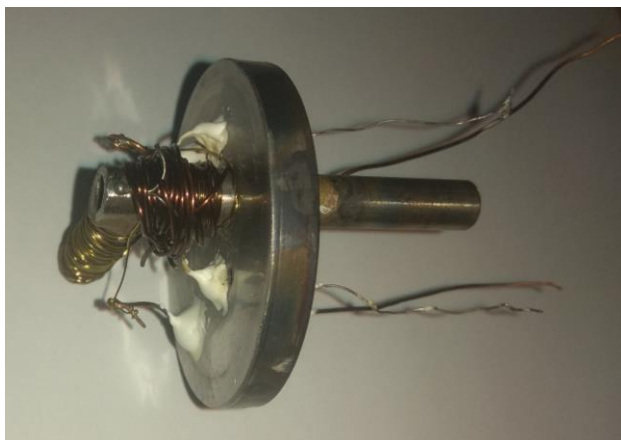


Fig. 2.3. Hot Nozzle Source assembly used

2.4. Supersonic Expansion

Supersonic Expansion experiments were also conducted using a pulsed valve (Parker Hannifin, United States; Part Number 009-1668-900) shown in Fig. 2.4.



(a)



(b)

Fig. 2.4. Supersonic assembly used: (a) IOTA ONE Pulse Driver, (b) Supersonic Solenoid Valve

It consists of a nozzle of 0.004" (0.10 mm) diameter orifice, with a PTFE poppet material. The pulsed valve operates at a voltage (VDC) of 28 V. This solenoid valve is capable of near 100% duty cycle over the temperature range of 277 K to 378 K and can operate at

pressures from 1×10^{-5} torr to 85 atmospheres. Combining high speed, ultra-low leak rate, high flow and high temperature capability in a small size; this valve operates with extreme repeatability and is constructed of non-corroding, passivated stainless steel. This valve was driven using IOTA ONE accessory (Parker Hannifin, United States; Pulse Driver).

2.5. Computational Details

Computations were carried out using Gaussian 09¹¹ and GAMESS suite of programs.¹² GaussView 5.0¹³ was used to visualize the structures. The procedure followed was a) Geometry optimization and vibrational frequency calculations, b) Interaction energy calculations, c) Isotopic calculations wherever required, d) Electron density topology analysis using Atoms in Molecules (AIM), e) Natural Bond Orbital (NBO) analysis for orbital interactions and f) Localized Molecular Orbital-Energy Decomposition analysis (LMO-EDA) for partitioning of the interaction energy of complex.

a) Geometry Optimization and Vibrational Frequency Calculations: Optimization refers to finding a set of geometrical parameters such as bond length, bond angles and dihedral angles for the molecule corresponding to the stationary point (either a minimum or saddle point) on the potential energy surface. The minimum energy structure of molecule is achieved when the forces, the root mean square of forces, the calculated displacement and the root mean square of displacement for the subsequent step reach values below specified threshold values. For a minimum on the potential surface, all vibrational frequencies must be positive, while for the saddle point, there could be imaginary frequencies for one or more modes of vibration. In our work, the computed structures of monomers and complexes were ensured to be minima on the potential energy surface.

Computations were conducted at the Møller-Plesset second order perturbation (MP2) and the density functional method M06-2X using 6-311++G(d,p) and aug-cc-pVDZ basis sets. For the M06-2X calculations, opt=tight and int=ultrafine options were used in Gaussian 09 as suggested by Vincent et al.¹⁴

Single point calculations at MP2/aug-cc-pVTZ, MP2/aug-cc-pVQZ, CCSD(T)/aug-cc-pVDZ levels were also performed using the optimized geometries at MP2/aug-cc-pVDZ level of computation.

Vibrational frequency calculations were performed at the above levels both to ensure that the computed structures corresponded to minima on the potential surface and also to assign the vibrational features in our experiments. The computed spectra were scaled using appropriate scaling factors which will be explained in detail in each of the chapters.

All the computed spectra have been plotted using SYNSPEC using a Lorentzian lineshape and a full width at half maximum (FWHM) of 1.0 cm^{-1} .¹⁵

The spectral decomposition method has also been used to fit a particular region of the experimental spectrum, having an overlap of features, into its individual Gaussian profiles. This method uses the Fityk software¹⁶ which incorporates the Levenberg-Marquardt algorithm of weighted least squares. In this peak fitting routine, each Gaussian was centered at the experimentally observed peak position as the initial guess. Then, the fit was done allowing the peak center, FWHM and the height of the Gaussian to be optimized as free parameters. Area under each fitted Gaussian profile gives the experimental intensity of each peak.

b) Interaction Energy Calculations: Interaction energy, $E = E_{AB} - (E_A + E_B)$ (eq. 1)

where E_{AB} , E_A and E_B represents the energies for the complex AB and the monomers A and B,

respectively. Negative value of interaction energy signifies complex to be more stable than its precursors.

$$\text{The interaction energy corrected for zero-point energy, } E_{ZPE} = E + ZPC \quad (\text{eq. 2})$$

where ZPC is the zero-point correction (in Hartree/Particle) obtained from the Gaussian output file of the frequency calculation.

Further, interaction energy is also corrected for the basis set superposition error (BSSE). When the energy of complex, E_{AB} is computed, it uses basis functions of both monomer subunits, while for computing the energies of individual precursors (E_A and E_B), the basis functions correspond to only one of the precursors used. As the number of basis functions becomes larger in computation of the complex, the energy obtained will be lower from the large basis sets, thus the interaction energies will be overestimated due to basis set superposition errors. Commonly used method to correct for BSSE is the counterpoise method proposed by Boys and Bernardi,¹⁷ in which energies E_{AB} , E_A and E_B are computed in the same basis set spanned by the functions of complex AB.

$$\text{Interaction energy corrected for BSSE, } E_{BSSE} = E_{AB}(AB) - \{E_A(AB) + E_B(AB)\} \quad (\text{eq. 3})$$

where $E_{AB}(AB)$ = Energy of complex AB using the basis set of AB,

$E_A(AB)$ = Energy of monomer A using the basis set of AB,

$E_B(AB)$ = Energy of monomer B using the basis set of AB.

Simultaneously correcting the interaction energy for the ZPE and BSSE was not performed, as such simultaneous correction is known to overcorrect the interaction energies.^{18,19}

Interaction energies were also computed at the MP2 and CCSD(T) method using CBS limit. The MP2/CBS calculations were done by two point extrapolation method by Helgaker et

al.²⁰ which employs MP2/aug-cc-pVXZ level where X represents triple and quadruple zeta basis sets.

$$\Delta E_{MP2/CBS} = \frac{4^3 \times \Delta E(pVQZ) - 3^3 \times \Delta E(pVTZ)}{4^3 - 3^3} \quad (\text{eq. 4})$$

The interaction energies were calculated at the CCSD(T)/CBS level as given by Bettinger et al.²¹

$$\Delta E_{CCSD(T)/CBS} = \Delta E_{MP2/CBS} + (\Delta E_{CCSD(T)/aug-cc-pVDZ} - \Delta E_{MP2/aug-cc-pVDZ}) \quad (\text{eq. 5})$$

b) Isotopic Calculations: Harmonic frequency calculations by Gaussian 09 do not only depend on the computed force constants but also on the atomic masses. Isotopic substitution therefore leads to dramatic changes in the computed vibrational frequencies. As the Hessian is not affected by the changes in the masses, the same Hessian can be used for all isotopomers. In order to read the Hessian matrix out of the checkpoint file and compute the vibrational frequency for different masses, we have used the keyword "freq=(ReadIso, ReadFc)" in combination with the additional information of the atomic masses of the various atoms in the molecule, arranged in the same order as they appeared in the molecular specification. ReadIso specifies the alternate isotope replacing the default most abundant isotope in Gaussian. ReadFc requests the force constants from previous frequency calculation to be read from the checkpoint file, and the normal modes and thermochemical analysis to be repeated using different isotope. We also used additional keyword "Geom=AllCheck" to take the molecular specification (including variables), the charge and multiplicity and the title section from the checkpoint file.

The mass of isotopes have been specified as integer values, since Gaussian automatically takes the exact mass of the respective isotope for the calculation, such as for deuterium, mass is input as 2, while for the calculation Gaussian uses exact value of 2.01410 a.u.

d) AIM analysis: AIM theory of Bader and coworkers,²² is used to identify and characterize hydrogen bonded interaction through topological analysis of electronic charge density, $\rho(\mathbf{r})$. In this analysis, the critical points are located where the gradient of $\rho(\mathbf{r})$ vanishes, $\nabla\rho(\mathbf{r}_c) = 0$.

Characteristics of these critical points are determined from the second derivative $\nabla^2\rho(r_c)$ and the Hessian of ρ . Diagonalization of this Hessian, which is a (3x3) symmetric matrix of partial second derivatives, yields three eigen values referred as the principal axis of curvature $\lambda_1 < \lambda_2 < \lambda_3$. Their sum given by $\sum_{i=1}^3 \lambda_i$ is called the Laplacian of ρ , at the bond critical point. The critical points are labelled as (ω, σ) using rank and signature of Hessian matrix, respectively. In our AIM calculations, wavefunction file (with .wfn extension) were generated using Gaussian 09, adding the keyword output=wfn, which were then used as input for the AIM2000²³ software. The bond critical point BCP given by (3,-1) corresponding to a bond between two atoms, the ring critical point given by (3,+1) corresponding to the presence of ring and the cage critical point given by (3,+3) corresponding to the presence of cage, have been located in our studies.

According to Koch and Popelier,²⁴ for a hydrogen bonded interaction, the $\rho(r)$ values should fall in the range 0.002-0.034 a.u. and the Laplacian values within 0.024-0.139 a.u. at the BCP. The sign of $\nabla^2\rho(r_c)$ at BCP, in our analysis, is positive indicative of the closed shell interactions (ionic, hydrogen bonded, van der Waal) where the electronic charge is locally depleted between the pair of atoms.

We have also calculated the interaction energy of each hydrogen bonded contact, E_{HB} through the use of local kinetic energy density $G(r_c)$ and local potential energy density $V(r_c)$ as described by Espinosa et al.²⁵

e) NBO analysis: NBO analysis developed by Weinhold and coworkers, is useful in understanding the donor-acceptor orbital interactions in hydrogen bonded structures.²⁶ NBO analysis is based on a method for transforming a given wavefunction into localized form, corresponding to the one-center (lone pair) and two-center (bond pair) elements of the Lewis

structure picture. The input atomic orbital basis set is thus transformed via natural atomic orbitals (NAOs) and natural hybrid orbitals (NHOs) into natural bond orbitals (NBOs).

In Gaussian 09, NBO analysis is performed by incorporating pop=nbo keyword. It provides the second-order perturbative estimates of ‘donor-acceptor’ (bond-antibond) interaction in the NBO basis. The stabilization energy $E(2)$ associated with delocalization (“2e-stabilization”) $i \rightarrow j$ is estimated as $E(2) = q_i [F(i,j)]^2 / (E(j) - E(i))$, where q_i is the donor orbital occupancy, $F(i,j)$ is the off-diagonal Fock matrix element, and $E(j)$ and $E(i)$ are the diagonal elements (orbital energies). Thus, $E(2)$ depends on $F(i,j)$ and is inversely proportional to the energy difference between donor (i) and acceptor (j) NBO orbitals. The electron occupancies in the acceptor orbitals were also used to explain the different vibrational shifts in isoenergetic complexes.

The reason for the conformational preferences was decided by systematic deletion of geminal, vicinal and remote interactions and computing the effect of deletion of these orbital interactions on the total energy of each conformer. In Gaussian 09, we have performed deletions in NBO by adding the keyword "pop=nbodel", and listing the donor (i) and acceptor (j) NBO orbital interactions to be deleted at the M06-2X/aug-cc-pVDZ level of theory. The relative contribution of geminal, vicinal and remote interactions towards stabilization of one conformer over the other, was thus quantitatively estimated. In addition, the effect of deleting all interactions (geminal, vicinal and remote) was also studied.

f) LMO-EDA analysis: In LMO-EDA²⁷ analysis performed using GAMESS, the interaction energy between two fragments A and B in molecule AB is partitioned into energy components such as electrostatic ΔE_{es} , exchange ΔE_{ex} , repulsion ΔE_{rep} , dispersion ΔE_{disp} and polarization ΔE_{pol} , thus giving an insight into the dominant terms characterizing an intermolecular interaction.

$$\Delta E_{\text{MP2}} = \Delta E_{\text{es}} + \Delta E_{\text{ex}} + \Delta E_{\text{rep}} + \Delta E_{\text{pol}} + \Delta E_{\text{disp}} \quad (\text{eq. 6})$$

where ΔE_{es} is the classical electrostatic interaction between occupied molecular orbitals, which does not cause any mixing of molecular orbitals, ΔE_{ex} is the interaction between occupied molecular orbitals which causes electron exchange and delocalization between molecules, ΔE_{rep} is the repulsive interaction due to Pauli's exclusion principle, ΔE_{pol} is the interaction which causes the mixing between the occupied and vacant molecular orbitals within each molecule, ΔE_{disp} is the interaction due to instantaneous dipole-induced dipole interactions.

References

1. Lewis, G. N.; Lipkin, D. Reversible Photochemical Processes in Rigid Media: The Dissociation of Organic Molecules into Radicals and Ions. *J. Am. Chem. Soc.* **1942**, *64*, 2801.
2. Norman, I.; Porter, G. Trapped Atoms and Radicals in a Glass 'Cage'. *Nature*, **1954**, *174*, 508.
3. Whittle, E.; Dows, D. A.; Pimentel, G. C. Matrix Isolation Method for the Experimental Study of Unstable Species. *J. Chem. Phys.* **1954**, *22*, 1943.
4. Dows, D. A.; Pimentel, G. C.; Whittle, E. Infrared Spectra of Intermediate Species in the Formation of Ammonium Azide from Hydrazoic Acid. *J. Chem. Phys.* **1955**, *23*, 1606.
5. Barnes, A. J.; Hallam, H. E. Infrared Studies of Matrix-isolated Species. *Q. Rev. Chem. Soc.* **1969**, *23*, 392-409.
6. Cradock, S.; Hinchcliffe, A. J. *Matrix Isolation*, Chap. 2, Cambridge University Press, London, **1975**.
7. Hobe, M. V.; Stroh, F.; Beckers, H.; Benter, T.; Willner, H. The UV/Vis Absorption Spectrum of Matrix-Isolated Dichlorine Peroxide, ClOOCl. *Phys. Chem. Chem. Phys.* **2009**, *11*, 1571-1580.
8. Bondybey, V. E.; English, J. H. Spectroscopy and Relaxation of Pb₂ in Rare Gas Solids. *J. Chem. Phys.* **1977**, *67*, 3405.
9. Costa, P.; Sander, W. Hydrogen Bonding Switches the Spin State of Diphenylcarbene from Triplet to Singlet. *Angew. Chem. Int. Ed.* **2014**, *53*, 1-5.
10. Majkut, A. O.; Ahokas, J.; Lundell, J.; Petterson, M. Raman Spectroscopy of Formic Acid and its Dimers Isolated in Low Temperature Argon Matrices. *Chem. Phys. Lett.* **2009**, *468*, 176-183.
11. Frisch, M. J.; Trucks, G. W.; Schlegel, H. B.; Scuseria, G. E.; Robb, M. A.; Cheeseman, J. R.; Scalmani, G.; Barone, V.; Mennucci, B.; Peterson, G. A.; *et al.* GAUSSIAN 09, Revision C.01, Gaussian Inc., Wallingford CT, **2010**.
12. Schmidt, M. W.; Baldridge, K. K.; Boatz, J. A.; Elbert, S. T.; Gordon, M. S.; Jensen, J. H.; Koseki, S.; Matsunaga, N.; Nguyen, K. A.; Su, S.; *et al.* General Atomic and Molecular Electronic Structure System. *J. Comp. Chem.* **1993**, *14*, 1347-1363.
13. Dennington II, R. D.; Keith, T. A.; Millam, J. M. GaussView version 5.0, Gaussian Inc., Wallingford, CT.
14. Vincent, M. A.; Hillier, I. H. The Structure and Interaction Energies of the Weak Complexes of CHClF₂ and CHF₃ with HCCH: A Test of Density Functional Theory Methods. *Phys. Chem. Chem. Phys.* **2011**, *13*, 4388-4392.
15. The Spectra were Simulated using SYNSPEC made Available by Irikura, K. National Institute of Standards and Technology, Gaithersburg, MD 20899, USA, **1995**.
16. Wojdyr, M. Fityk: a general-purpose peak fitting program. *J. Appl. Cryst.* **2010**, *43*, 1126-1128.

-
17. Boys, S. F.; Bernardi, F. The Calculation of Small Molecular Interactions by the Differences of Separate Total Energies. Some Procedures with Reduced Errors. *Mol. Phys.* **1970**, *19*, 553-566.
 18. Turi, L.; Dannenberg, J. J. Molecular Orbital Studies of the Nitromethane-Ammonia Complex. An Unusually Strong CH \cdots N Hydrogen Bond. *J. Phys. Chem.* **1995**, *99*, 639-641.
 19. Wong, N. B.; Cheung, Y. S.; Wu, D. Y.; Ren, Y.; Wang, X.; Tian, A. M.; Li, W. K. A Theoretical Study of the C-H \cdots N Hydrogen Bond in the Methane-Ammonia Complex. *J. Mol. Struct.* **2000**, *507*, 153-156.
 20. Helgaker, T.; Klopper, W.; Koch, H.; Noga, J. Basis-Set Convergence of Correlated Calculations on Water. *J. Chem. Phys.* **1997**, *106*, 9639-9646.
 21. Bettinger, H. F.; Kar, T.; Sánchez-García, E. Borazine and Benzene Homo- and Heterodimers. *J. Phys. Chem. A* **2009**, *113*, 3353-3359.
 22. Bader, R. F. W. *Atoms in Molecules. A Quantum Theory*, Clarendon Press, Oxford, **1994**.
 23. Bliieger-König, F.; Bayles, D.; Schönbohn, J. AIM2000 (Version 1.0); Chemical Adviser: Bader, R. F. W.
 24. Koch, U.; Popelier, P. L. A. Characterization of C-H \cdots O Hydrogen Bonds on the Basis of the Charge Density. *J. Phys. Chem.* **1995**, *99*, 9747-9754.
 25. Espinosa, E.; Molins, E.; Lecomte, C. Hydrogen Bond Strengths Revealed by Topological Analyses of Experimentally Observed Electron Densities. *Chem. Phys. Lett.* **1998**, *285*, 170-173.
 26. Glendening, E. D.; Reed, A. E.; Carpenter, J. E.; Weinhold, F. NBO (Version 3.1).
 27. Su, P.; Li, H. Energy Decomposition Analysis of Covalent Bonds and Intermolecular Interactions. *J. Chem. Phys.* **2009**, *131*, 014102-15.

CHAPTER 3
PROPARGYL ALCOHOL CONFORMATIONS AND
ITS HYDROGEN BONDED COMPLEXES WITH WATER

3.1. Introduction

The conformations of propargyl alcohol PA arise from the internal rotation of its C-OH group which results in two conformations: the gauche (gPA) and the trans (tPA) form with respect to the carbon chain of the molecule, as shown in Fig 3.1.^{1,2} Calculations at the CCSD(T)-F12/VDZ-F12 level of theory indicated that the gPA is 1.6 kcal/mol more stable than the non-degenerate trans structure (tPA).^{2,3} The gauche form having a degeneracy of 2, dominated the Boltzmann population at room temperature with ~96%. It is also reported that the ground state gPA has two equivalent minima separated by a small barrier of ~1.1 kcal/mol, corresponding to orientation of hydroxyl hydrogen on either side of CCCO plane of PA, subtending a dihedral angle of $\pm 60^\circ$ at the MP2/6-311+G(d,p) level.^{2,4} The trans form with a CCOH dihedral angle of exactly 180° , was computed as a saddle point at this level of calculation and separates two equivalent minima with CCOH dihedral angles of 160° and 200° . The energy barrier for interconversion of these two equivalent forms is a mere 0.04 kcal/mol.

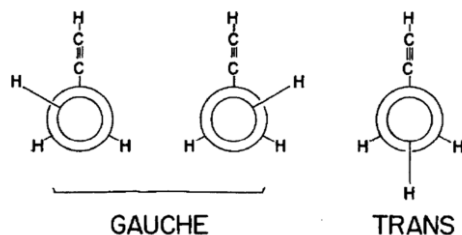


Fig. 3.1. Schematic diagram of Conformers of PA.¹

The gauche conformer of PA has been recently observed using the helium nanodroplet setup coupled with free electron lasers, by recording the mass-selective infrared spectra of PA in $1600\text{-}560\text{ cm}^{-1}$ range.⁵ Earlier microwave studies on PA performed by Hirota and Bolton et al.

has also confirmed the presence of only the gauche form.^{1,4,6} The vibrational wavenumbers of the matrix-isolated spectra of PA in Ar, N₂ and Xe matrices compared with the DFT calculations using 6-311++G(d,p) basis set, clearly revealed that only the more stable gauche conformer was trapped and identified in the experiment.⁷

Preliminary results on matrix isolation infrared spectroscopy and computations for PA have been reported elsewhere.⁸ The experimental work was performed at resolutions insufficient for matrix isolation work and computations were also reported at lower levels of calculations such as B3LYP, M06 and MP2 using 6-311++G(d,p) basis set. In addition, there was no explanation for the conformational stability of gauche form, as detailed NBO calculations were not performed.

The present study has addressed those deficiencies. The matrix isolation experiments on PA were performed at a resolution of 0.5 cm⁻¹. Computations were performed at higher levels of theory in an effort to understand the reasons for the conformational preference of gPA over tPA using Natural bond orbital NBO analysis. These levels of theory were also used to explore the 1:1 hydrogen bonded complexes of PA-H₂O using matrix isolation infrared spectroscopy and *ab initio* computations, which revealed new insights that will be discussed in this chapter.

3.2. Experimental Details

The experimental details have been elaborated in Chapter 2. Specifically in this experiment, N₂ (Sigma Gases and Services, Grade I: 99.999% purity) and Ar (Sigma Gases and Services, Grade I: 99.999% purity) have been used as the matrix gases. Propargyl alcohol, HC≡CCH₂OH (Sigma-Aldrich, 99% assay) and Milli-Q® Type 1 Ultrapure H₂O (with purity typically 18.2 MΩ.cm at 25 °C) were used without further purification. These compounds have

been subjected to several freeze-pump-thaw cycles prior to use. Isotopic experiments were also performed using D₂O (Sigma-Aldrich, isotopic purity of 99.9 atom % D).

In our experiments, firstly PA was equilibrated at appropriate temperatures (of -24 °C and -6 °C for 0.8 and 3 mbar, respectively) and allowed to enter the mixing chamber, then the matrix gas was filled into the mixing chamber upto 1 atm, maintaining the sample-to-matrix ratios. The sample (PA) together with the matrix gas was then effused out through needle valve onto the cold substrate at ~12 K. A similar procedure was followed when PA and H₂O were codeposited, implying that firstly PA was equilibrated at respective temperatures and after passing the vapours of PA into mixing chamber, H₂O was equilibrated at appropriate temperatures (of -29 °C and -20 °C for 0.4 and 1 mbar, respectively) and allowed to enter into the mixing chamber. After filling the mixing chamber with sample (PA and H₂O), matrix gas was filled in and deposition to the cold window was taking place through a single jet containing the sample vapours and the matrix gas.

3.3. Computational Details

The Gaussian 09 suite of programs⁹ was used to optimize the structures of PA conformers as well as the hydrogen bonded complexes of PA with H₂O. Computations were performed at the M06-2X and MP2 level of theory, using 6-311++G(d,p) and aug-cc-pVDZ basis sets. The M06-2X calculations were performed together with opt=tight and int=ultrafine commands. The PA-H₂O complex structures were obtained using the optimized geometries of both the monomers, PA and H₂O.

The MP2 level frequencies matched very closely with the experimental frequencies and hence we have used the frequencies computed at the MP2/aug-cc-pVDZ level to compare with

our experiments. AIM2000¹⁰ software was used in identifying and characterizing different hydrogen bonded interaction in PA-H₂O complexes.

In this chapter, we will first present our results on PA conformers, followed by discussion on PA-H₂O complexes using matrix isolation infrared spectroscopy and *ab initio* computations.

3.4. Results- Conformations of PA

Experiments were performed in both N₂ and Ar matrices, however the spectral features were sharper in the N₂ matrix than that obtained in the Ar matrix. Such variations in linewidths of spectral features in different matrices arising primarily from site effects have also been observed earlier.^{11,12}

3.4.1. Experimental

Fig. 3.2 shows the IR spectra of PA with N₂ as the matrix gas (with sample-to-matrix ratio of 3:1000), as deposited at 12 K and after the matrix was annealed for 30 min. at 27 K. The spectral region between 3750-2850 cm⁻¹ corresponds to the O-H, ≡C-H and CH₂ stretch, 1420-1370 cm⁻¹ corresponds to the coupled mode of CH₂ wag and O-H bend, 1060-1020 cm⁻¹ corresponds to the C-O stretch and 690-620 cm⁻¹ where the bending modes of PA occur. Table 3.1 shows the the experimentally observed features recorded at 12 K, when PA was deposited in the N₂ matrix.

A feature at 3727.5 cm⁻¹, which corresponds to the asymmetric O-H stretch in H₂O was observed in the infrared spectra, since water is always present in our experiments.¹³ Strong features were observed at 3641.9 and 3311.0 cm⁻¹ in the spectral range 3750-2850 cm⁻¹, when PA was deposited in the N₂ matrix. In addition to these bands, we also observed weak features at 2926.1/2881.2 cm⁻¹. Another feature appeared at 1389.8 cm⁻¹ in the 1420-1370 cm⁻¹ region. The

strong feature occurring at 1040.8 cm^{-1} have also been marked in the spectra. In the bending region, features at 669.4 and 644.0 cm^{-1} were observed in our experiments.

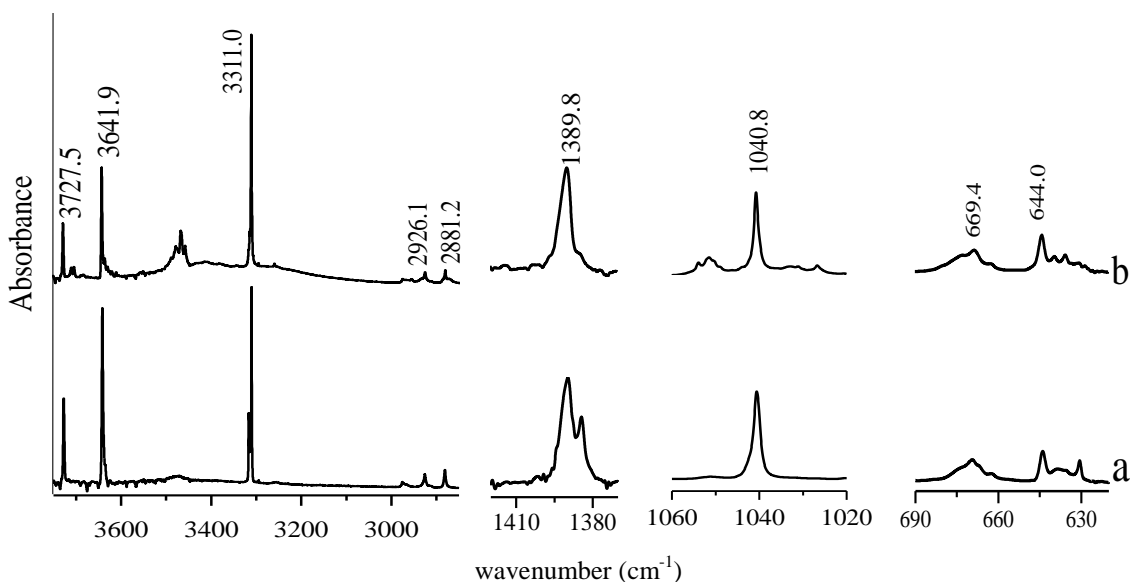


Fig. 3.2. Infrared spectra of PA in N_2 matrix, over the regions $3750\text{-}2850\text{ cm}^{-1}$, $1420\text{-}1370\text{ cm}^{-1}$, $1060\text{-}1020\text{ cm}^{-1}$ and $690\text{-}620\text{ cm}^{-1}$, a) Recorded at 12 K after deposition of PA (sample-to-matrix ratio 3:1000) and b) Spectra of (a) after annealing the matrix at 27 K .

Infrared spectra of PA in the Ar matrix, with the sample-to-matrix ratio of 1.5:1000, deposited at 12 K and after the matrix was annealed at 32 K , have also been shown in the spectral regions $3800\text{-}3200\text{ cm}^{-1}$ and $1070\text{-}1010\text{ cm}^{-1}$ (Fig. 3.3).

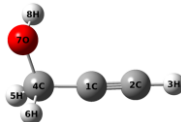
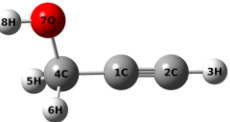
A feature at 3731.5 cm^{-1} corresponds to the asymmetric stretch of H_2O monomer in the Ar matrix.¹³ Features at 3650.0 , 3320.2 and 1042.8 cm^{-1} were observed when PA was deposited in Ar matrix.

3.4.2. Computational

In addition to the experimentally observed features, Table 3.1 also shows the optimized structures of gauche and trans conformer of PA, with their computed vibrational modes at MP2/aug-cc-pVDZ level. It was ensured that all the frequency values were positive, corresponding to the minimum on potential energy surface. These computed vibrational features

of PA conformers were then, scaled to bring them to agreement with the experimental features. Scaling factors in different regions were calculated using the experimental and computed features of PA, for instance, for the region 3750-2850 cm^{-1} , scaling factor 0.9548 was calculated by dividing the experimental feature, 3641.9 cm^{-1} corresponding to the O-H stretch, by the computed feature for the same mode at 3814.4 cm^{-1} . Similarly, the C-O stretch and $\equiv\text{C-H}$ bend \perp to CCO plane were used to obtain the scaling factors 0.9852 and 1.139, respectively for the relevant regions of the spectra.

Table 3.1. Experimental (N_2 matrix at 12 K) and scaled computed wavenumbers (cm^{-1}) at MP2/aug-cc-pVDZ level for the gauche and trans conformers of PA and vibrational assignments. IR intensities (in km/mole) given in parenthesis.

Experimental	Computed ^a		Assignment
	Gauche (g-PA)	Trans (t-PA)	
			
3641.9	3642.0 (38)	3644.6 (35)	O-H stretch
3311.0	3326.5 (54)	3329.6 (52)	$\equiv\text{C-H}$ stretch
2975.6	3007.1 (7)	2956.5 (17)	CH_2 asymmetric stretch
2926.1/2881.2	2926.5 (32)	2910.4 (38)	CH_2 symmetric stretch
1389.8	1384.7 (56)	1229.8 (64)	CH_2 wag and O-H bend (Out of phase)
1281.5	1319.7 (2)	1411.1 (28)	CH_2 wag and O-H bend (In phase)
1040.8	1040.8 (102)	1039.4 (115)	C-O stretch
669.4	683.3 (47)	682.5 (33)	$\equiv\text{C-H}$ bend in the CCO plane
644.0	644.1 (53)	640.1 (47)	$\equiv\text{C-H}$ bend \perp to CCO plane

^aScaling factors: (3750-2850 cm^{-1} , 0.9548); (1420-1020 cm^{-1} , 0.9852); (690-620 cm^{-1} , 1.139).

The uncorrected and zero-point energy (ZPE) corrected stabilization energies were calculated by subtracting the energy of gauche conformer from the energy of trans form of PA, at all the above levels of computation, as listed in Table 3.2. Single point energy calculation was

also done at the CCSD(T)/aug-cc-pVDZ level, resulting in an uncorrected stabilization energy of 1.5 kcal/mol, using the optimized geometries of PA conformers at MP2/aug-cc-pVDZ level.

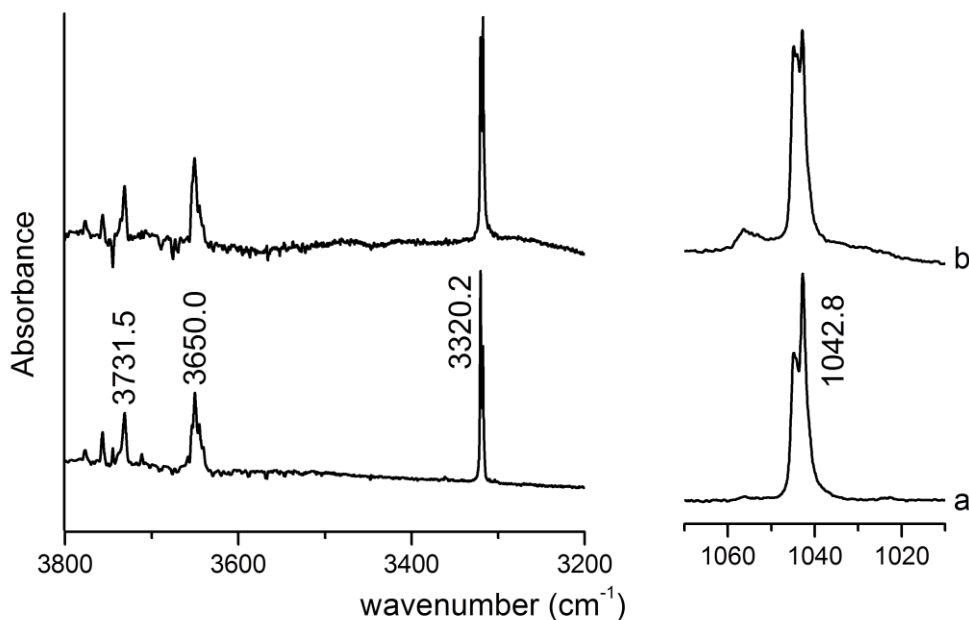


Fig. 3.3. Infrared spectra of PA over the region 3800-3200 cm^{-1} and 1070-1010 cm^{-1} , a) recorded at 12 K after deposition of PA in the Ar matrix (sample:matrix ratio 1.5:1000) and b) Spectra of (a) after annealing the matrix at 32 K.

Table 3.2. Uncorrected/Zero-point energy (ZPE) corrected stabilization energies between PA conformers computed at different levels of theory.

Level of Theory	Stabilization energies in kcal/mol	
	6-311++G(d,p)	aug-cc-pVDZ
M06-2X	2.1/1.6	1.8/1.6
MP2	2.0/1.6 ^a	1.5/1.4
CCSD(T)	-	1.5

^aThis structure was near-trans.

It was found that at all the above levels of theory, gPA optimized as the most stable conformer, with two equivalent minima (g and g'), corresponding to the CCOH dihedral angles of nearly $\pm 52^\circ$, as shown in Fig. 3.4. The trans conformer with CCOH dihedral angle of $\pm 180^\circ$, optimized to a minimum at all levels of computation, except at the MP2/6-311++G(d,p), where

the trans form existed as the saddle point, connecting the local minima with CCOH dihedral angles of $\pm 162^\circ$, which were referred to as the near-trans structures. At the MP2/aug-cc-pVDZ level, the interconversion barrier from gauche to trans form ($g \rightarrow t$) was calculated to be 2.2 kcal/mol, by locating the structure of transition state TS, having CCOH dihedral angle of 130° , as shown in Fig. 3.4.

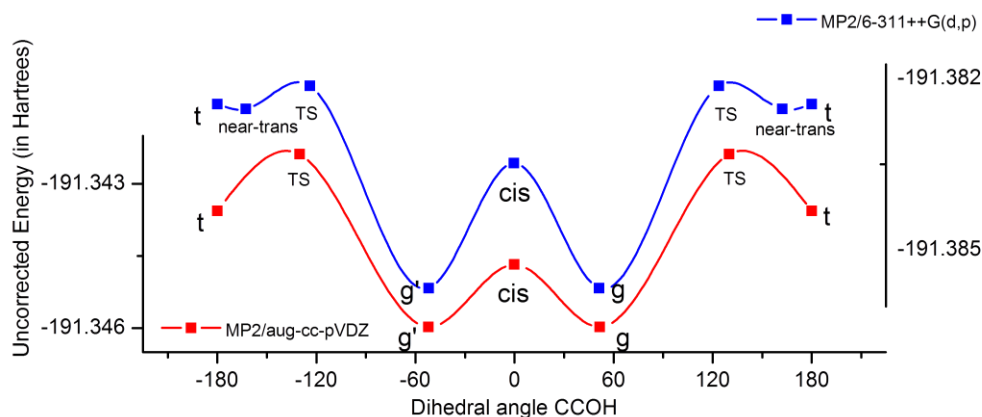


Fig. 3.4. Plot of Uncorrected energy of different structures of PA (in Hartrees) with the change in dihedral angle CCOH (in degrees) at the MP2 level using 6-311++G(d,p) and aug-cc-pVDZ basis sets.

3.5. Discussions - Conformations of PA

3.5.1. Vibrational Assignments

The experimental features observed for PA in both N_2 and Ar matrices, have been assigned to the dominantly populated gauche conformer. In the N_2 matrix, the experimental features at 3641.9 and 3311.0 cm^{-1} have been assigned to the O-H and $\equiv\text{C-H}$ stretch of gauche PA, respectively, as shown in Table 3.1. The features occurring at 2926.1 and 2881.2 cm^{-1} , corresponds to the CH_2 symmetric stretches of PA, which might have been trapped in two different matrix sites for the same mode of vibration. CH_2 wag coupled with O-H bend was observed at 1389.8 and 1281.5 cm^{-1} for the in phase and out of phase vibrations, respectively.

The feature observed at 1040.8 cm^{-1} has been assigned to the C-O stretch of gauche PA. The observed bending modes, 669.4 and 644.0 cm^{-1} have been assigned to the $\equiv\text{C-H}$ bend in CCO plane and perpendicular to CCO plane, respectively, for the gauche conformer of PA.

It is discernible from Table 3.1 that the O-H, $\equiv\text{C-H}$ and C-O stretch, and the $\equiv\text{C-H}$ bending modes do not show significant differences in their computed IR frequencies for the two conformers. However, the CH_2 symmetric stretch was computed at 2926.5 cm^{-1} for gPA and 2910.4 cm^{-1} for tPA, and the CH_2 wag coupled with O-H bend, computed at 1384.7 cm^{-1} for gPA and 1411.1 cm^{-1} for tPA. These features occurring experimentally at $2926.1/2881.2$ and 1389.8 cm^{-1} , respectively, points to the presence of only the gauche conformer in the matrix.

Similarly from Fig. 3.3, features at 3650.0 cm^{-1} corresponds to the O-H stretch, 3320.2 cm^{-1} to the $\equiv\text{C-H}$ stretch and 1042.8 cm^{-1} to the C-O stretch of gauche PA conformer in the Ar matrix.

Further to examine if a conformational interconversion could take place from the ground state (gPA) form to the higher energy trans conformer, we exposed the deposited N_2 matrix to the infrared beam from the FTIR for 2-4 hrs at 12 K and 27 K, in order to observe any interconversion to the trans form of PA. In an earlier work, features corresponding to the higher energy cis conformer of formic acid, were observed with the tunable IR radiation of an optical parametric oscillator.^{14, 15} However, no such interconversion could be observed in our experiments.

3.5.2. AIM Analysis

Our AIM analysis performed at MP2/aug-cc-pVDZ level, also did not reveal any intramolecular hydrogen bonding, ruling out the role of intramolecular hydrogen bonding in conformational landscape of PA, an observation reported earlier.³ The geometrical parameters

for the O-H $\cdots\pi$ distance in the gauche PA were computed as 2.54 and 3.43 Å for the H₈C₁ and H₈C₂ bond distances, respectively, at the MP2/aug-cc-pVDZ level, rather large for an interaction of this type to be of any consequence.

3.5.3 NBO Analysis

In order to understand the reason for the conformational preference of gPA over tPA based on electron delocalization, we performed NBO analysis for both conformers at the M06-2X/aug-cc-pVDZ level, as shown in Table 3.3. NBO analysis indicated that in PA, the delocalization interactions (geminal, remote and vicinal) were important in stabilizing both conformers. A detailed list of these interactions has been given in Table 3.4. The relative contribution of these delocalization interactions were quantitatively estimated by a systematic deletion of these interactions between the donor and acceptor orbitals, within each PA conformer, and then computing the energy of the conformers after deletions, at M06-2X/aug-cc-pVDZ level. The relative change in the energies of gauche and trans conformer after systematic deletions of various orbital interactions have also been presented graphically in Fig. 3.5.

Table 3.3. NBO analysis showing the energies obtained after deletion of the different delocalization interactions in conformers of PA, computed at M06-2X/aug-cc-pVDZ level.

	Energy (Hartrees) ^a	Interactions deleted	Deletion energy (Hartrees)	Change in energy		Relative contribution for stabilization (%)
				Hartrees	kcal/mol	
gPA	-191.810948630	Remote	-191.807424085	0.003525	2.2	1.8
		Geminal	-191.770233535	0.040715	25.6	20.5
		Vicinal	-191.656582171	0.154366	96.9	77.7
		All	-191.620647188	0.190301	119.4	
tPA	-191.808124967	Geminal	-191.762811979	0.045313	28.4	23.2
		Vicinal	-191.658211712	0.149913	94.1	76.8
		All	-191.624012657	0.184112	115.5	

^aEnergies have not been corrected for ZPE.

Table 3.4. NBO analysis of some of the significant geminal, vicinal and remote delocalization interactions, showing the donor and acceptor orbitals and the second order perturbation energies, E(2), in PA Conformers, calculated at the M06-2X/aug-cc-pVDZ level.

Donor orbital	Acceptor orbital	Second Order Perturbation Energies, E(2) (in kcal/mol)	
		gauchePA	transPA
Geminal			
σ C1C2	σ^* C1C4	5.3	5.7
σ C1C2	σ^* C2H3	3.2	3.2
σ C1C4	σ^* C1C2	8.7	8.8
σ C2H3	σ^* C1C2	6.8	6.8
σ C4H5	σ^* C1C4	-	0.6
σ C4H6	σ^* C1C4	-	0.6
Vicinal			
π_1 C1C2	σ^* C4H6	2.6	2.4
π_1 C1C2	σ^* C4H5	2.2	2.4
π_2 C1C2	σ^* C4O7	7.2	7.2
π_2 C1C2	σ^* C4H5	1.1	0.8
π_2 C1C2	σ^* C4H6	0.5	0.8
σ C1C4	σ^* C2H3	3.2	3.1
σ C1C4	σ^* O7H8	-	1.9
σ C2H3	σ^* C1C4	6.5	6.6
σ C4H5	π_1^* C1C2	5.1	5.6
σ C4H5	σ^* C1C2	3.7	3.8
σ C4H5	σ^* O7H8	3.4	-
σ C4H5	π_2^* C1C2	2.0	1.6
σ C4H6	π_1^* C1C2	6.2	5.6
σ C4H6	σ^* C1C2	3.9	3.8
σ C4H6	π_2^* C1C2	0.9	1.6
σ C4O7	π_2^* C1C2	2.3	2.4
σ C4O7	σ^* C1C2	2.1	2.2
σ O7H8	σ^* C4H5	2.5	-
σ O7H8	σ^* C1C4	-	3.9
n_1 O7	σ^* C4H5	2.5	1.0
n_1 O7	σ^* C1C4	1.5	1.4
n_1 O7	σ^* C4H6	1.5	1.0
n_2 O7	σ^* C4H6	7.4	7.2
n_2 O7	σ^* C4H5	-	7.2
n_2 O7	σ^* C1C4	7.2	-
Remote			
n_2 O7	π_2^* C1C2	1.4	-

When all the delocalization interactions were present, gauche conformer was 1.8 kcal/mol more stable than the trans form, at M06-2X/aug-cc-pVDZ level. A remote interaction,

between the lone pair on oxygen and the antibonding π orbital of $C\equiv C$ bond, was present only in gauche PA conformer. On deletion of this interaction, a small change of ~ 2.2 kcal/mol ($\sim 2\%$) was observed in energy of gauche form, with an inversion in the conformational ordering.

It was found that when geminal interactions were deleted, keeping the vicinal interactions intact, energies of both conformers raised, and the conformational ordering was the same as when all delocalization interactions were present, thus indicating that the geminal interactions were about equally operative in both conformers.

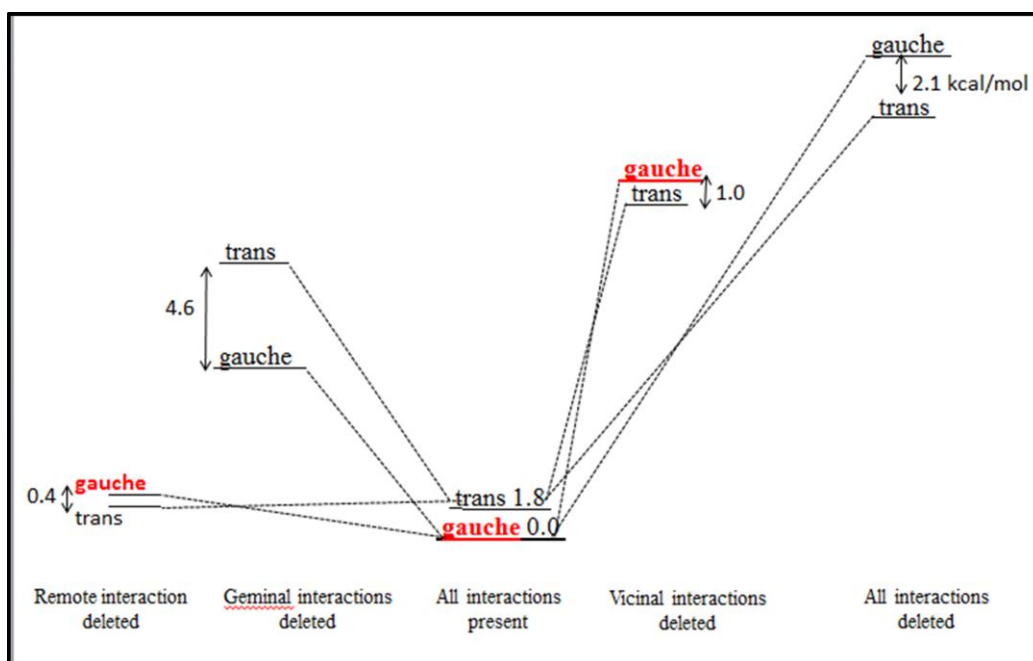


Fig. 3.5. Correlation diagram showing the relative change in energies (in kcal/mol) of the gauche and trans conformer of PA, when orbital interactions were systematically deleted. Calculations were done at the M06-2X/aug-cc-pVDZ level. (The energy axis is not to scale.)

Similar procedure was repeated with vicinal interactions deletions keeping geminal interactions intact, the energies of conformers further increased, however the conformational

ordering is reversed from the situation when all interactions were present, implying that gauche form, which was the global minimum, turned out to be less stable than trans conformer. Deletion of vicinal interactions increased the energy of gauche conformer by ~96.9 kcal/mol (~78%) and that of trans conformer by ~94.1 kcal/mol (~77%), indicating that vicinal interactions majorly play an important role in deciding the conformational ordering in PA. The importance of such interactions in the conformations of molecules has been reported in many other systems in the literature.^{16,17}

When all interactions were deleted, further increase in energies was observed with conformational ordering reverse of that obtained when all interactions were present. This inversion was being dictated due to absence of remote and vicinal interactions. Thus, it is clear that remote and vicinal interactions play important role in deciding the conformational preference in PA.

3.6. Results- PA-H₂O Complexes

Matrix isolation infrared experiments were performed, with co-deposition of PA and H₂O using both N₂ and Ar matrices.

3.6.1. Experimental

When PA and H₂O were co-deposited into N₂ matrix and the matrix then annealed at 27 K for ~ 30 min., new features were observed in the IR spectra at 3703.4, 3467.2 and 1053.4 cm⁻¹, in Fig. 3.6. Similarly, in the Ar matrix, on co-deposition of PA and H₂O, new features at 3489.4 and 1056.3 cm⁻¹ were observed after annealing the matrix at 32 K, shown in Fig. 3.7. As mentioned earlier, the features in the N₂ matrix are sharper and have been used for the assignments to the PA-H₂O complexes.

3.6.2. Computational

Fig. 3.8 displays the optimized structures of different complexes of gauche PA with H₂O, computed at the MP2/aug-cc-pVDZ level. For a comparison of our experimental data, we have considered only the complexes of H₂O with gauche PA, as the population of trans conformer was too small to be observed.

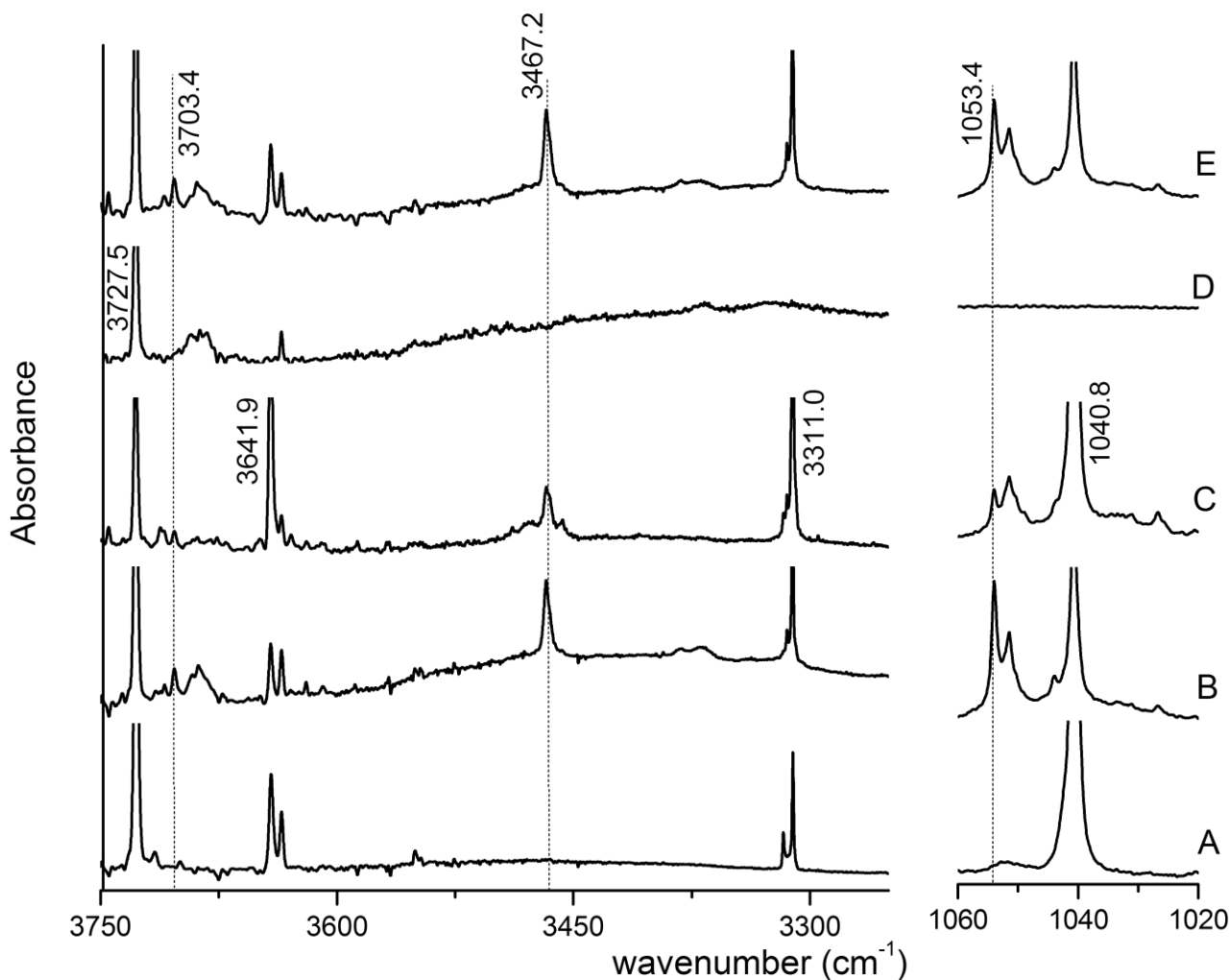


Fig. 3.6. Infrared spectra of PA-H₂O in N₂ matrix over the regions 3750-3250 cm⁻¹ and 1060-1020 cm⁻¹, of A) PA: H₂O: N₂ (0.8: 1.0:1000) at 12 K, B) PA: H₂O: N₂ (0.8: 1.0:1000) annealed at 27 K, C) PA: H₂O: N₂ (0.8: 0.0: 1000) annealed at 27 K, D) PA: H₂O: N₂ (0.0: 0.5: 1000) annealed at 27 K and E) PA: H₂O: N₂ (3.0: 0.4:1000) annealed at 27 K.

We did few concentration dependence experiments and it was found that these product features increased in intensity when concentration of either of the two monomers (PA or H₂O) was increased, clearly implying that these features were due to complex formation between PA and H₂O. Since H₂O was a ubiquitous impurity in matrix isolation experiments, features due to PA-H₂O complex were observed even when only PA was deposited. It must be recognized that these features were observed even at very low concentrations, pointing to the formation of 1:1 complex between PA and H₂O.

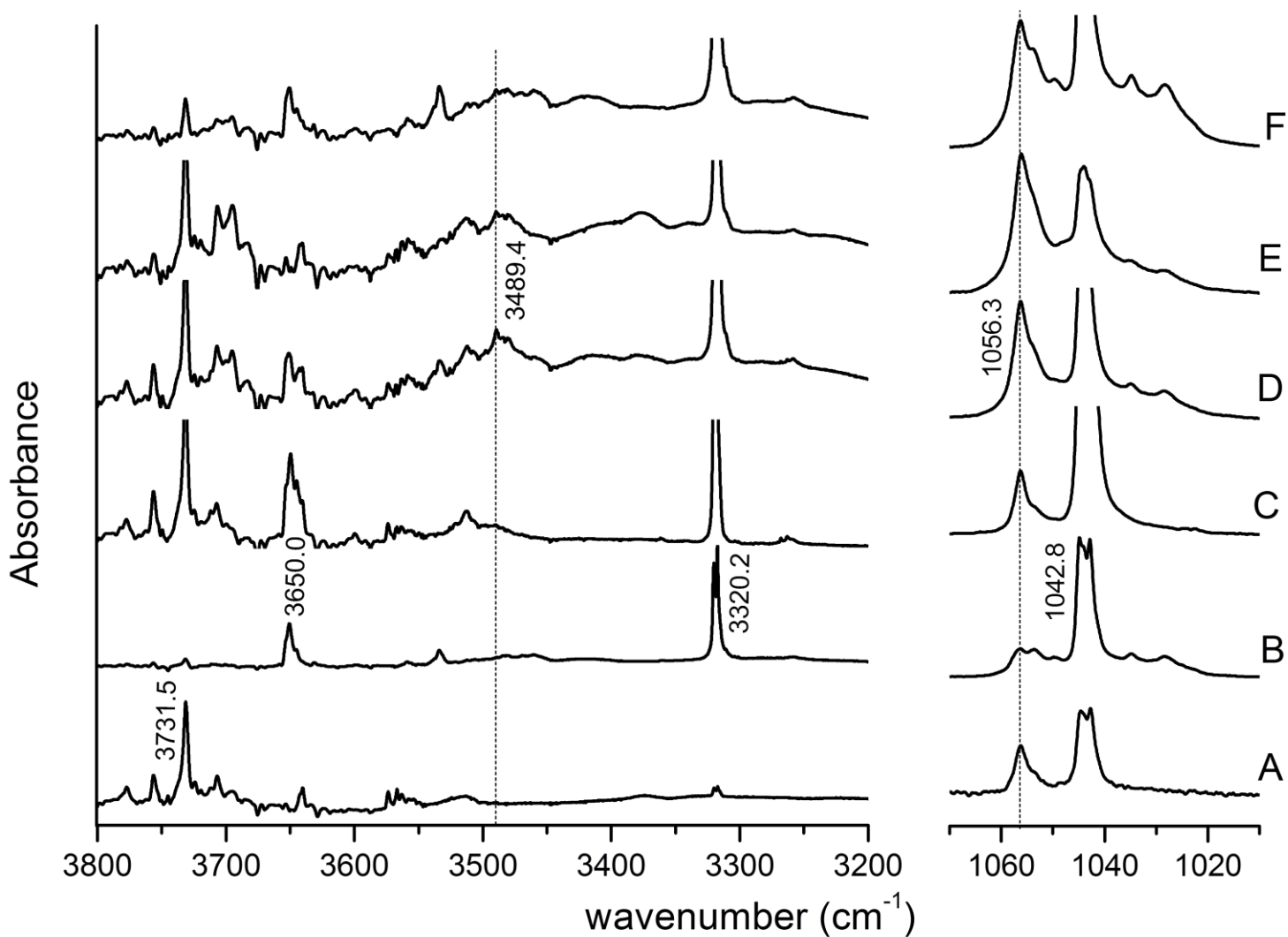


Fig. 3.7. Infrared spectra of PA-H₂O in an Ar matrix over the regions 3800-3200 cm⁻¹ and 1070-1010 cm⁻¹, of A) H₂O: Ar (5:1000) annealed at 32 K, B) PA: Ar (5:1000) annealed at 32 K, C) PA: H₂O: Ar (5:5:1000) at 12 K, D) PA: H₂O: Ar (5:5:1000) annealed at 32 K, E) PA: H₂O: Ar (5:10:1000) annealed at 32 K and F) PA: H₂O: Ar (10:5:1000) annealed at 32 K.

Complexes 1 and 1*, were bound by two hydrogen bonded contacts- an O-H \cdots O and an O-H \cdots π interaction, with PA acting as a proton donor through its O-H bond and as a proton acceptor through its C \equiv C π cloud. It must also be noted that in both these complexes, H₂O serves both as a proton donor and a proton acceptor. These two distinct isomeric structures having same hydrogen bonded interactions (O-H \cdots O and O-H \cdots π), only differ in the orientation of water molecule.

Complex 2 is the structure in which PA serves as a proton acceptor through its oxygen atom forming an O-H \cdots O contact. Complex 3 is bound by a \equiv C-H \cdots O interaction, with PA serving as the proton donor through its acetylenic hydrogen to the oxygen atom of H₂O. In complex 4, π cloud of PA interacts with the hydrogen atom of H₂O, thus forming an O-H \cdots π interaction.

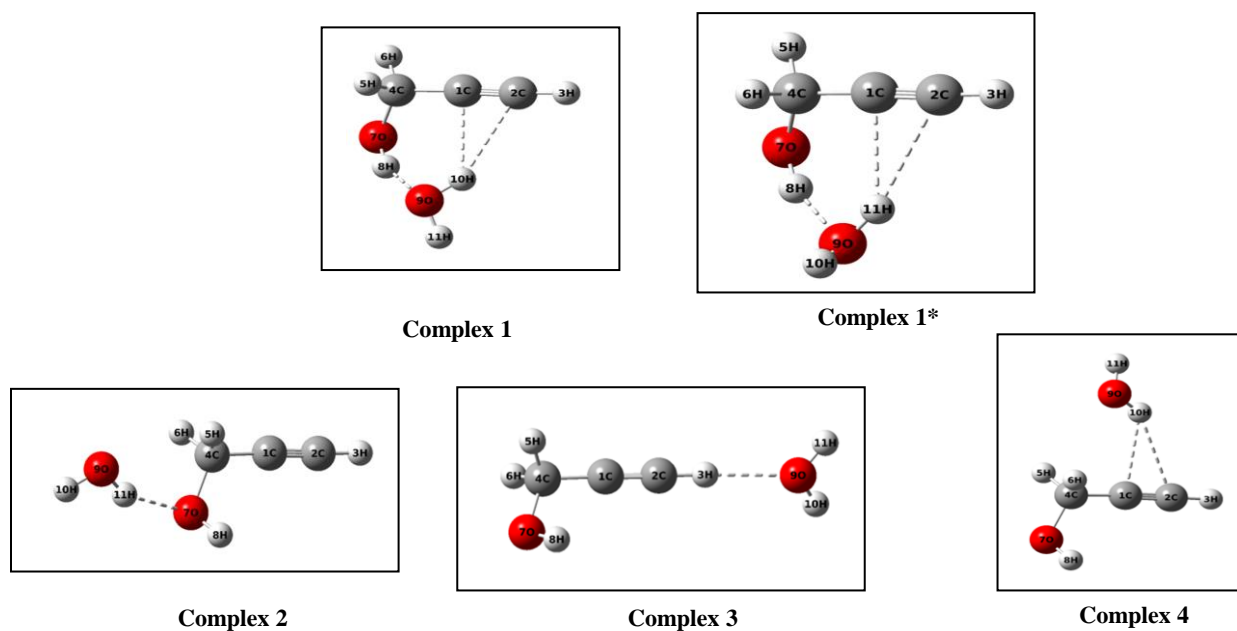


Fig. 3.8. Optimized geometries of the complexes of gauche-PA and water, computed at the MP2/aug-cc-pVDZ level (*Dotted lines do not imply bond paths; these lines are drawn just to indicate the interaction in the complex*).

Table 3.5 provides the uncorrected, ZPE corrected and BSSE corrected interaction energies for different gauche PA-H₂O complexes. It can be seen that structures 1 and 1* were the two nearly isoenergetic complexes with energy difference of ~0.1 kcal/mol, thus, it would not be possible to distinguish between these two minima experimentally. Hence for discussions on this structure 1* of PA-H₂O complex, we will use complex 1. Both these complexes were computed to be the most stable among all other structures at all levels of theory.

Some important geometrical parameters for each of the complexes have been listed in Table 3.6, indicating the hydrogen bonded distances, bond angles and dihedral angles computed at the MP2/aug-cc-pVDZ level.

Table 3.5. Uncorrected/ZPE corrected/BSSE corrected interaction energies (in kcal/mol) for the PA-H₂O complexes computed at the M06-2X and MP2 level using a 6-311++G(d,p) and aug-cc-pVDZ basis set. Single point calculations were also done at CCSD(T)/aug-cc-pVDZ level. Interaction energies using the CBS limit were computed at MP2 and CCSD(T) levels.

	M06-2X		MP2			CCSD(T)	
	6-311++G(d,p)	aug-cc-pVDZ	6-311++G(d,p)	aug-cc-pVDZ	CBS	aug-cc-pVDZ	CBS
1	-9.1/-7.1/-8.2	-8.2/-6.2/-7.7	-7.9/-6.0/-5.6	-7.9/-5.9/-6.2	-7.9	-7.8	-7.8
1*	Not Optimized	-8.0/-6.1/-7.6	-7.7/-5.8/-5.4	-7.7/-5.7/-6.1	-7.8	-7.6	-7.7
2	-6.5/-4.8/-5.9	-5.8/-4.0/-5.3	-6.0/-4.3/-4.5	-6.1/-4.2/-4.7	-5.9	-6.0	-5.9
3	-3.9/-2.7/-3.2 ^a	-3.3/-2.2/-2.8 ^a	-4.0/-2.4/-2.5	-3.7/-2.7/-2.7	-3.4	-3.7	-3.4
4	-4.4/-3.1/-4.0	-4.2/-2.9/-3.7	-3.6/-2.5/-2.3	-4.1/-2.9/-2.8	-4.0	-4.0	-3.9

^aThe tight convergence criteria has been relaxed while optimizing this geometry.

Table 3.6. Some important geometrical parameters for the different PA-H₂O hydrogen bonded complexes computed at the MP2/aug-cc-pVDZ level, showing bond lengths (in Å), bond angles and dihedral angles (in degrees).

	O₉H₈	O₇H₈O₉	H₁₀C	H₁₀C₂	O₉H₁₀C₁	O₉H₁₀C	O₇H₈O₉H₁₀	
complex 1	1.95	154.0	2.45	2.56	121.5	149.9	-28.5	
complex 1*	1.95	155.8	2.43	2.53	125.0	152.0	-4.4	
	O₉H₈	O₇H₈O₉	H₁₀C₁	H₁₀C₂	O₉H₁₀C₁	O₉H₁₀C₂	C₄C₁H₁₀O₉	
complex 4	-	-	2.44	2.68	120.4	147.2	8.4	
	O₇H₁₁	O₇H₁₁O₉	C₄O₇H₁₁O₉		O₉H₃	O₉H₃C₂	C₂H₃O₉H₁₀	
complex 2	1.94	153.0	-10.8		complex 3	2.17	178.5	27.1

The optimized geometries of the complexes of trans PA with water, computed at the MP2/aug-cc-pVDZ level have also been shown in Fig. 3.9.

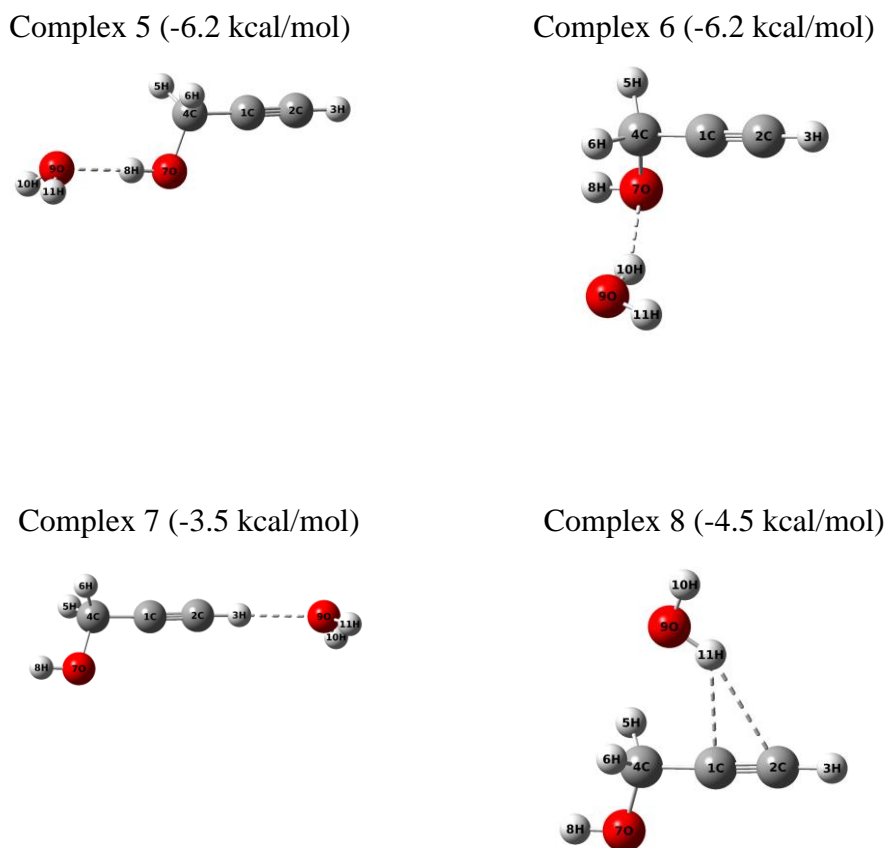


Fig. 3.9. Optimized geometries of the complexes of trans-PA with water, with their uncorrected interaction energies, computed at the MP2/aug-cc-pVDZ level.

3.7. Discussion - PA-H₂O Complexes

3.7.1. Vibrational Assignments in the N₂ matrix

a) O-H Stretch of PA subunit in PA-H₂O Complex: Complex 1 was computed to show the largest red shift of 133.2 cm⁻¹ from the same mode in uncomplexed PA computed at 3642.0 cm⁻¹. Complexes 2 and 4 were computed to show red shifts of 11.0 and 0.7 cm⁻¹, respectively. In complex 3, this mode computed at 3642.1 cm⁻¹, with a blue shift of 0.1 cm⁻¹. In our experiments, a strong feature due to complex formation between PA and H₂O was observed at 3467.2 cm⁻¹,

red shifted by 174.7 cm^{-1} from the same mode in uncomplexed PA at 3641.9 cm^{-1} . The observed experimental shift was in agreement with the computed shift for only complex 1, suggesting its formation in the matrix, as indicated in Table 3.7.

Table 3.7. Experimental (in N_2) and scaled computed vibrational wavenumbers (cm^{-1}) for PA, H_2O , D_2O , the different PA- H_2O and PA- D_2O complexes in N_2 matrix at MP2/aug-cc-pVDZ level.

Experimental		Computed ^a						
PA	Complex	PA	Complex1	Complex1*	Complex2	Complex3	Complex4	modes
3641.9	3467.2 -174.7 ^b	3642.0	3508.8 -133.2	3510.7 -131.3	3631.0 -11.0	3642.1 0.1	3641.3 -0.7	O-H stretch
1040.8	1053.4 12.6	1040.8	1054.0 13.2	1056.1 15.3	1022.3 -18.5	1037.4 -3.4	1036.6 -4.2	C-O stretch
Water	Complex	Water	Complex1	Complex1*	Complex2	Complex3	Complex4	
3727.5	3703.4 -24.1	3760.3	3723.9 -36.4	3722.9 -37.4		3756.1 -4.2	3737.0 -23.3	O-H asym. stretch
3635.0	-	3631.9	3575.1 -56.8	3573.0 -58.9		3629.8 -2.1	3600.2 -31.7	O-H sym. stretch
					3727.0 -33.3 ^c			non-bonded O-H stretch
					3519.7 -240.6 ^c			bonded O-H stretch
D_2O	Complex	D_2O	Complex1	Complex1*	Complex2	Complex3	Complex4	
2765.9	2748.9 -17.0	2765.7	2737.0 -28.7	2736.2 -29.5		2762.8 -2.9	2747.9 -17.8	O-D asym. stretch
2655.7	-	2629.4	2588.9 -40.5	2587.7 -41.7		2627.9 -1.5	2607.7 -21.7	O-D sym. stretch
					2734.9 -30.8 ^c			non-bonded O-D stretch
					2556.3 -209.4 ^c			bonded O-D stretch

^aScaling factors: (2780-2500 cm^{-1} , 0.9587); For other regions, scaling factors have already been given in Table 3.1.

^bShifts, $\Delta v = v(\text{complex}) - v(\text{monomer})$. ^cShifts for bonded and non-bonded O-H and O-D stretch in complex 2, calculated from asymmetric stretch of O-H and O-D stretch in monomer, respectively. On complex formation, the O-H vibrations in water occurred as bonded and non-bonded O-H stretches in complex 2, as opposed to the antisymmetric and symmetric stretches in free H_2O .

b) C-O Stretch of PA subunit in PA- H_2O Complex: Experimentally, product feature appeared at 1053.4 cm^{-1} for the complex, with a blue shift of 13.2 cm^{-1} from the same feature in uncomplexed PA (1040.8 cm^{-1}). Complex 1 showed a blue shifted feature at 1054.0 cm^{-1} , while the same mode was red shifted by 18.5, 3.4 and 4.2 cm^{-1} for complexes 2, 3 and 4, respectively.

This observation of blue shifted feature in our experiments for the C-O stretch, unequivocally points to the formation of complex 1 in matrix.

c) Asymmetric O-H Stretch of H₂O subunit in PA-H₂O Complex: The experimental feature corresponding to this mode in complex was observed at 3703.4 cm⁻¹, red shifted by 24.1 cm⁻¹ from the same mode in uncomplexed H₂O, occurring at 3727.5 cm⁻¹. This shift is consistent with the computed shifts of 36.4, 33.3 and 31.7 cm⁻¹ for complexes 1, 2 and 4, respectively. However, based on earlier assignments using other modes, we assigned 3703.4 cm⁻¹ to the computed feature for complex 1, with a red shift of 36.4 cm⁻¹. It must be recognized that the shift of 36.4 cm⁻¹ in complex 1, results from the dual role water plays in this complex as a proton donor and a proton acceptor. In a later section, we will discuss if the two combined interactions imply cooperativity.

d) Symmetric O-H Stretch of H₂O subunit in PA-H₂O Complex: The experimental feature for complex corresponding to this mode was not observed.

e) PA-D₂O Complexes: In order to confirm our assignments for PA-H₂O complexes, we also performed experiments when PA and D₂O were codeposited. The frequencies of the vibrational modes of PA subunit in the PA-H₂O and PA-D₂O complexes are not very different, as indicated both by our experiments and computations. Hence, we discuss only the modes of D₂O in the PA-D₂O complex.

D₂O Asymmetric Stretch: Experimentally, this feature occurs at 2765.9 cm⁻¹ for the uncomplexed D₂O. Product bands corresponding to complex occurred at 2748.9 cm⁻¹, with a red shift of 17.0 cm⁻¹. This shift was consistent with earlier conclusion that complex 1 was trapped in the matrix.

3.7.2. Vibrational Assignments in the Ar matrix

Similarly, in the Ar matrix, feature at 3489.4 cm^{-1} corresponds to the O-H stretch of PA subunit in the PA-H₂O complex, shown in Fig. 3.7. In the spectral region $1070\text{-}1010\text{ cm}^{-1}$, feature at 1056.3 cm^{-1} , corresponds to the C-O stretch of PA subunit in the complex. Therefore, the experimentally observed features agreed best with the computed feature for complex 1 (and 1*). Specifically, the O-H and C-O stretching vibrations of PA subunit clearly point to the formation of complex 1 (and 1*) in the matrix.

3.7.3. AIM Analysis

Based on electron density topologies, we have also presented the bond and ring critical points for different gauchePA-H₂O complexes at MP2/aug-cc-pVDZ level (Fig. 3.10). In addition, the values of electron density, Laplacian, $G(r_c)$, $V(r_c)$ and the hydrogen bonded energies for each interaction have been listed in Table 3.8. In all PA-H₂O complexes, values of electron density and Laplacian fall in the range as proposed by Koch and Popelier.¹⁸ It was found that in complex 1, O-H...O interaction was relatively strong than the O-H... π contact, which thus served as the secondary interaction.

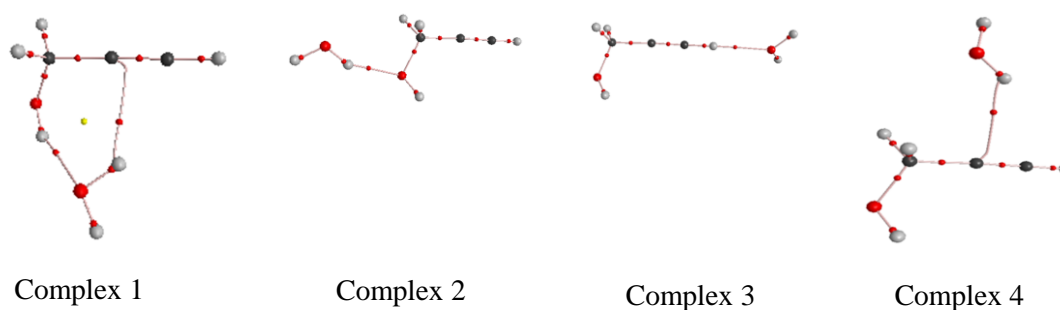


Figure 3.10. Charge density topologies for the different structures of gauchePA-H₂O complexes computed at the MP2/aug-cc-pVDZ level.

Table 3.8. AIM calculations showing the charge densities $\rho_b(r_c)$ and Laplacian $\nabla^2\rho_b(r_c)$ at the bond critical point for various gauchePA-water complexes at MP2/aug-cc-pVDZ level. The values of $\rho_b(r_c)$, $\nabla^2\rho_b(r_c)$, $G(r_c)$ and $V(r_c)$ are expressed in a.u. and E_{HB} in kcal/mol.

Complex		$\rho_b(r_c)$	$\nabla^2\rho_b(r_c)$	$G(r_c)$	$V(r_c)$	E_{HB}	Total
Complex 1	O-H...O	0.0250	0.0851	0.0204	-0.0194	-6.1	-8.2
	O-H... π	0.0119	0.0358	0.0078	-0.0066	-2.1	
Complex 2	O-H...O	0.0258	0.0899	0.0215	-0.0205	-6.4	-6.4
Complex 3	\equiv C-H...O	0.0146	0.0498	0.0108	-0.0092	-2.9	-2.9
Complex 4	O-H... π	0.0111	0.0356	0.0075	-0.0062	-1.9	-1.9

3.7.4. NBO Analysis

At MP2/aug-cc-pVDZ level, NBO analysis revealed that in complex 1, there was a strong orbital interaction between the lone pair of oxygen of H₂O, serving as the electron donor, and σ^* orbital of O-H of PA, serving as electron acceptor, with the second order perturbation energy of 11.4 kcal/mol. The O-H... π interaction between the donor orbital of C \equiv C bond and the σ^* of the O-H of H₂O was only 0.8 kcal/mol, implying the former interaction to be the dominant in this complex.

3.7.5. LMO-EDA Analysis

It was found that in all the gauchePA-H₂O complexes, the electrostatic energy and exchange energy components have an important role to play in stabilization of the complexes, as seen in Table 3.9. LMO-EDA analysis at the MP2/aug-cc-pVDZ level showed that the ΔE_{MP2} of complex 1 was the largest among all complexes, with a value of -8.2 kcal/mol. Polarization and dispersion energy makes minor contribution to the total interaction energy.

Table 3.9. Energy decomposition analysis for the various PA-H₂O complexes computed using the LMO-EDA method at the MP2/aug-cc-pVDZ level. All energies are in kcal/mol.

Complex	ΔE_{es}	ΔE_{ex}	ΔE_{rep}	ΔE_{pol}	ΔE_{disp}	ΔE_{MP2}
Complex 1	-12.9 (35%)	-16.0 (43%)	28.5	-4.2 (11%)	-3.7 (11%)	-8.2
Complex 2	-8.9 (37%)	-10.2 (41%)	18.4	-2.8 (11%)	-2.7 (11%)	-6.2
Complex 3	-4.6 (39%)	-4.4 (38%)	8.0	-1.6 (13%)	-1.1 (10%)	-3.8
Complex 4	-5.2 (30%)	-7.5 (43%)	13.0	-1.7 (11%)	-2.8 (16%)	-4.3

3.8. Does a Hydrogen Bonded Complex with Dual Contacts exhibit Synergism?

In order to probe if the two interactions in complex 1, an O-H...O and an O-H... π contacts, behave synergistically, we have compared the uncorrected interaction energies of complex 1 with those of complexes 5 and 8, as shown in Fig. 3.11, at the MP2/aug-cc-pVDZ level. The same conclusions are reached if ZPE or BSSE corrected interaction energies are used. Choice of trans PA-H₂O complexes 5 and 8 was prompted by the fact that complex 5 consist of only the O-H...O interaction, while complex 8 has only the O-H... π interaction, both these interactions together present in complex 1. Conformation of PA is unlikely to make any substantial influence on the interaction energies of the complexes.

Complex 1 has the interaction energy of -7.9 kcal/mol, while complexes 5 and 8 have interaction energies of -6.2 and -4.5 kcal/mol, respectively. Complex 1 with two interactions operating simultaneously has larger interaction energy than either of the complexes 5 or 8. However, the sum of interaction energies of complexes 5 and 8 was more than that for complex 1. Thus, both interactions do not even seem to occur in an additive manner, however, these interactions operated in an antagonistic way.

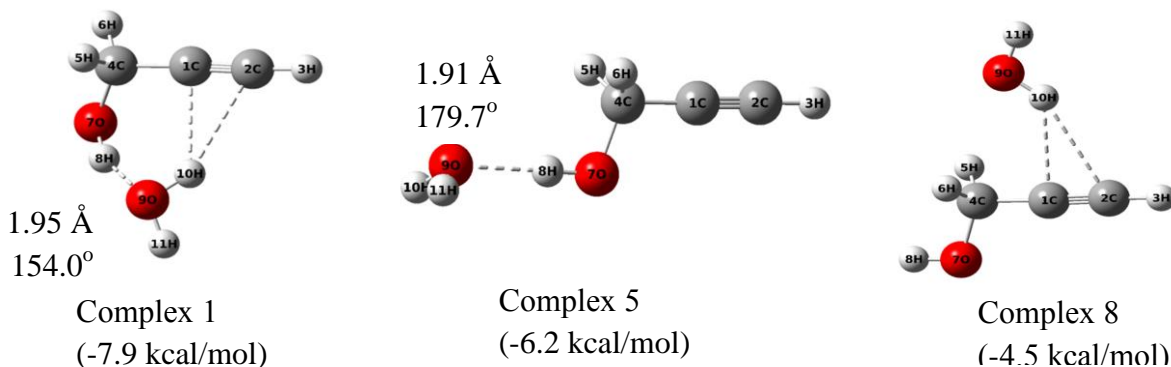


Fig. 3.11. Optimised geometries of the transPA-water complexes 5 and 8, with their O...H bond length and O-H...O bond angle and interaction energies, computed at the MP2/aug-cc-pVDZ level (*Dotted lines do not imply bond paths; these lines are drawn just to indicate the interaction in the complex*).

We have also examined the structures of the three complexes 1, 5 and 8, and it was found that the O₉H₈ bond in complex 5 is shorter (1.91 Å) than that in complex 1 (1.95 Å). Furthermore, the O₇H₈O₉ angle is linear (179.7°) in complex 5, whereas it is bent (154.0°) in complex 1. It is known that hydrogen bonds prefer linear geometries, which therefore implies that complex 5 adopts the best geometrical parameters for hydrogen bonding. In complex 1, both distances and angles have been compromised. Thus, a certain attempt by the two precursors to sacrifice the optimum conditions for each of the two interactions, O-H...O and O-H...π, in order to maximize the stabilization by allowing the two interactions to operate simultaneously. This structural compromise thus resulted into antagonism.

To further examine the point of antagonism, we fixed the O₉H₈ bond length and O₇H₈O₉ angle at the values obtained in complex 5, scanned the dihedral angle O₇H₈O₉H₁₀ and computed the energies for various structures. The best stabilization was found to be -6.3 kcal/mol, which was less than that obtained when a full geometry optimization was done to obtain complex 1, meaning that with these frozen parameters, the O-H...π interaction could not set in.

It must also be recognized that the frequency shift in complex 1 was 36.4 cm⁻¹, while those in complexes 5 and 8 were 15.5 and 25.0 cm⁻¹, respectively. Again, the combined shift, in complexes 5 and 8, of 40.5 cm⁻¹ was more than that of complex 1. Thus, in complex 1, water was involved with two interactions, showing greater frequency shift than either complex 5 or 8, the two interactions lacked additivity or synergism in complex 1.

3.9. Conclusions

Infrared spectra of matrix-isolated PA clearly indicate the presence of dominantly populated gauche conformer. The experimental features are corroborated by computations. NBO analysis of PA conformers revealed that the remote and vicinal interactions are important in

deciding the conformational preference, with vicinal interactions playing a major role. Furthermore, AIM analysis indicated that the intramolecular hydrogen bonding was not responsible for the gauche conformer to be the lower energy form in PA.

FTIR spectra of the matrix isolated PA-H₂O complex, together with *ab initio* computations, indicate that the global minima (Complexes 1 and 1*) involves two interactions; one between the O-H group of PA and O atom of water, and another between the hydrogen of water and C≡C π system of PA. Convincing evidence for formation of complex 1 was indicated by the large red shift of the O-H stretching vibration of the PA subunit. The cyclic geometry of the complex was confirmed by the AIM theory, which showed a ring critical point, consistent with the dual interactions. NBO analysis on this complex indicated the existence of a strong interaction between the lone pair of oxygen of water, which serves as the electron donor, and σ* orbital of O-H of PA which serves as the electron acceptor orbital. Three other local minima at MP2 level of theory were also located with an O-H...O interaction (in complex 2), a ≡C-H...O interaction (in complex 3) and an O-H...π interaction (in complex 4); however no experimental evidence was found in the matrix for these complexes. For all the complexes, electrostatic and exchange interactions are dominant contributors to the stabilization energy at the MP2/aug-cc-pVDZ level.

It was also recognized that where dual interactions were present, as in complex 1, the two precursors adopt a geometry that is not necessarily the one that is found when each of the interactions: O-H...O and O-H...π, were present individually. This results in antagonism, where the optimum geometries when individual interactions are present are in fact sacrificed when forming the dual interaction complex.

It is worth mentioning that the global minimum computed for the PA-H₂O system was structurally similar to the global minimum computed for the phenylacetylene-H₂O system.¹² In the PA-H₂O complex, we see a strong O-H...O interaction together with a relatively weaker O-H... π , resulting in BSSE corrected interaction energy of -6.2 kcal/mol at the MP2/aug-cc-pVDZ level. In the phenylacetylene-H₂O the global minimum was an O-H... π interaction together with a marginally weaker C-H...O interaction, having BSSE corrected interaction energy of -3.2 kcal/mol, computed at the same level of theory. However, while in the PA-H₂O system, this global minimum was observed and the only one observed in the matrix, the computed global minimum was not observed in the matrix isolation experiments of phenylacetylene-H₂O system. Rather in that experiment, an n- σ^* complex, which was a local minimum involving the interaction between the acetylenic hydrogen of phenylacetylene and the oxygen of H₂O was observed. Interestingly, the energy difference (BSSE corrected) between the global minimum and n- σ^* in the phenylacetylene-H₂O system was 0.7 kcal/mol only, while the energy difference between similar systems in PA-H₂O was 3.5 kcal/mol. Clearly the two strong interactions in PA-H₂O (i.e. O-H...O and O-H... π) direct the global minimum to be dominantly stronger than the corresponding global minimum in phenylacetylene-water. Interestingly acetylene, which lacks the secondary interaction, shows the n- σ^* complex as the global minimum.¹⁹ Clearly these systems highlight the importance of multiple interactions in the stabilization of complexes.

References

1. Hirota, E. Internal Rotation in Propargyl Alcohol from Microwave Spectrum. *J. Mol. Spectrosc.* **1968**, *26*, 335-350.
2. Mani, D.; Arunan, E. Microwave Spectroscopic and Atoms in Molecules Theoretical Investigations on the Ar \cdots Propargyl Alcohol Complex: Ar \cdots H-O, Ar $\cdots\pi$, and Ar \cdots C Interactions. *Chem. Phys. Chem.* **2013**, *14*, 754-763.
3. Miller, B. J.; Lane, J. R.; Kjaergaard, H. G. Intramolecular OH $\cdots\pi$ Interactions in Alkenols and Alkynols. *Phys. Chem. Chem. Phys.* **2011**, *13*, 14183-14193.
4. Bolton, K.; Owen, N. L.; Sheridan, J. Molecular Structures of Propargyl Alcohol and Propargyl Amine from Microwave Spectra. *Nature* **1968**, *217*, 164.
5. Mani, D.; Fischer, T.; Schwan, R.; Dey, A.; Redlich, B.; Van der Meer, A. F. G.; Schwaab, G.; Havenith, M. A Helium Nanodroplet setup for mid and far Infrared Spectroscopy using Pulsed-free-electron Lasers: Vibrational spectra of Propargyl Alcohol. *RSC Adv.* **2017**, *7*, 54318-54325.
6. Pearson, J. C.; Drouin, B. J. The Ground state Torsion-Rotation spectrum of Propargyl Alcohol (HCCCH₂OH). *J. Mol. Spectrosc.* **2005**, *234*, 149-156.
7. Sundararajan, K.; Gopi, R.; Ramanathan, N. Conformations of Propargyl Alcohol and its Interaction with Acetylene: a Matrix Isolation Infrared and DFT Computations. *J. Mol. Struct.* **2016**, *1121*, 26-34.
8. Saini, J. Conformations of Propargyl Alcohol and its Hydrogen Bonded Complexes with Water Studied using Matrix Isolation Infrared Spectroscopy and Computations, Master's Thesis, IISER Mohali, **2014**.
9. Frisch, M. J.; Trucks, G. W.; Schlegel, H. B.; Scuseria, G. E.; Robb, M. A.; Cheeseman, J. R.; Scalmani, G.; Barone, V.; Mennucci, B.; Peterson, G. A.; *et al.* GAUSSIAN 09, Revision C.01, Gaussian Inc., Wallingford CT, **2010**.
10. Blieger-König, F.; Bayles, D.; Schönbohn, J. AIM2000 (Version 1.0); Chemical Adviser: Bader, R. F. W.
11. George, L.; Viswanathan, K. S.; Singh, S. *Ab Initio* Study of Trimethyl Phosphate: Conformational Analysis, Dipole Moments, Vibrational Frequencies, and Barriers for Conformer Interconversion. *J. Phys. Chem. A* **1997**, *101*, 2459-2464.
12. Karir, G.; Viswanathan, K. S. Phenylacetylene-Water Complex: Is it n- σ or H- π in the Matrix? *J. Mol. Struct.* **2016**, *1107*, 145-156.
13. Bentwood, R. M.; Barnes, A. J.; Orville-Thomas, W. J. Studies of Intermolecular interactions by Matrix Isolation Vibrational Spectroscopy: Self-association of Water. *J. Mol. Spectros.* **1980**, *84*, 391-404.
14. Maçôas, E. M. S. Vibrational Spectroscopy of cis- and trans-Formic Acid in Solid Argon. *J. Mol. Spectrosc.* **2003**, *219*, 70-80.

-
15. Pettersson, M.; Lundell, J.; Khriachtchev, L.; Räsänen, M. IR Spectrum of the Other Rotamer of Formic Acid, cis-HCOOH. *J. Am. Chem. Soc.* **1997**, *119*, 11715-11716.
16. Dubey, P.; Mukhopadhyay, A.; Viswanathan, K. S. Do Amino acids prefer only certain backbone structures? Steering through the Conformational maze of L-Threonine using Matrix isolation Infrared spectroscopy and *Ab initio* studies. *J. Mol. Struct.* **2019**, *1175*, 117-129.
17. Ramanathan, N.; Sundararajan, K.; Kar, B. P.; Viswanathan, K. S. Conformations of Trimethyl Phosphite: A Matrix Isolation Infrared and *Ab Initio* Study. *J. Phys. Chem. A* **2011**, *115*, 10059-10068.
18. Koch, U.; Popelier, P. L. A. Characterization of C-H...O Hydrogen Bonds on the Basis of the Charge Density. *J. Phys. Chem.* **1995**, *99*, 9747-9754.
19. Engdahl, A.; Nelander, B. The Acetylene-Water Complex: A Matrix Isolation Study. *Chem. Phys. Lett.* **1983**, *100*, 129-132.

CHAPTER 4
HYDROGEN BONDED COMPLEXES BETWEEN
PROPARGYL ALCOHOL AND METHANOL

4.1. Introduction

In this chapter, the 1:1 hydrogen bonded complexes of PA with methanol (MeOH) have been investigated for the first time using matrix isolation infrared spectroscopy and *ab initio* computations. As opposed to PA-H₂O complexes discussed in the previous chapter, PA-MeOH complexes give rise to the possibility of C-H interactions involving the methyl group of MeOH, thereby offering a richer landscape of non-covalently bonded complexes, which we wished to explore. A comparison between the most stable complexes of PA-MeOH and those of PA-H₂O has been made in terms of their interaction energies, strength of individual hydrogen bonded contact, infrared features, vibrational shifts and the gas-phase basicity values. Thus, this work attempts to study the effects of methyl substitution on water subunit in PA-H₂O complexes.

Further, we have also explored the computational study on the PA-Diethylether (DEE) system, which is constrained to form only an O-H...O contact with PA, with suppression of the O-H... π interaction.

4.2. Experimental Details

Ar and N₂ (Grade-I, Sigma Gases and Services 99.999%) were used as matrix gases. PA (Sigma Aldrich 99%) and MeOH (Sigma Aldrich 99%) were used without further purification. However, both precursors were subjected to several freeze-pump-thaw cycles before use. MeOH was maintained at approximate temperatures of -49 °C and -36 °C, to obtain vapour pressures of ~1 and ~3 mbar, respectively, which when mixed with the matrix gas, yielded the required sample-to-matrix ratios. PA was injected into the vacuum system through a second nozzle of a double jet assembly. The concentration of PA in the matrix was controlled by maintaining the

sample at temperatures of $-80\text{ }^{\circ}\text{C}$ and $-70\text{ }^{\circ}\text{C}$ to obtain PA to matrix ratios of 1:1000 and 3:1000, respectively. Specifically, the concentration of each precursor in the matrix was varied over the range 1:1000 to 3:1000 for PA and MeOH.

Experiments were also done using CD_3OD (Cambridge Laboratories, 98%), which contained some CD_3OH due to isotopic exchange of the O-D, to confirm our assignments made for PA-MeOH system.

4.3. Computational Details

Initially, the structure of the precursor molecules, gauchePA and MeOH were optimized using Gaussian 09 suite of programs¹. Starting from these optimized geometries of PA and MeOH, structures of different gauchePA-MeOH complexes were optimized. To enable us to make the vibrational assignments for the experimentally observed features, the computed harmonic frequencies of PA-MeOH complexes were scaled using the appropriate scaling factors of 0.9548 for the O-H and 0.9852 for the C-O stretch region, as used in chapter 3. Interaction energies for each of the PA-MeOH complexes were calculated by subtracting the sum of energies of the submolecules from the energy of complex. Single-point energy calculations were also performed at the CCSD(T)/aug-cc-pVDZ level using the optimized geometries of PA-MeOH complexes at the MP2/aug-cc-pVDZ level. AIM, NBO and LMO-EDA analysis were done on all the PA-MeOH complexes.

The computed features of O-H and C-O stretch for PA-MeOH complexes were simulated in vibrational spectrum using SYNSPEC program,² assuming a Lorentzian line profile with FWHM of 1.0 cm^{-1} .

4.4. Results

Experiments were performed in both Ar and N_2 matrices. The spectral features showed a richer structure in the N_2 matrix than in the Ar matrix.

4.4.1. Experimental

Fig. 4.1 shows the infrared spectra of matrix-isolated precursors, PA and MeOH, and that recorded when both were codeposited in the N₂ matrix, over the regions 3740-3600, 3480-3410 and 1065-1015 cm⁻¹. Features at 3641.9 and 1040.8 cm⁻¹ corresponds to the O-H and C-O stretch of PA monomer. Since water was always present in our experiments, feature at 3727.5 cm⁻¹ corresponding to the asymmetric stretch of H₂O monomer was observed.³ We also observed features at 3467.2 and 1053.4 cm⁻¹, which had been assigned to the PA-H₂O complexes in the N₂ matrix, in chapter 3.

Strong features at 3664.2 and 1034.6 cm⁻¹ corresponds to the O-H and C-O stretch, respectively, of MeOH monomer, as shown in Fig. 4.1. In the C-O stretching region (1065-1015 cm⁻¹), a weak feature occurring at 1048.1 cm⁻¹ had been assigned to the hydrogen-bonded MeOH-H₂O complex reported by Bakkas et al. in 1993.⁴ Two features at 1051.0 and 1032.1 cm⁻¹ have also been observed, only when the concentration of MeOH was high, implying them to be due to presence of MeOH dimers or clusters.⁵

When PA and MeOH were codeposited in the N₂ matrix, new features in the O-H stretch region 3480-3410 cm⁻¹, were observed at 3445.1, 3439.6, 3433.1 and 3424.9 cm⁻¹ after the matrix was annealed. Similarly, in the C-O stretch region, after the matrix was annealed, new features at 1058.7, 1052.9, 1027.8 and 1019.7 cm⁻¹ were observed. Concentration dependence experiments were done by varying the concentration of either of the two precursors, PA or MeOH, in order to ensure that the product features, 3445.1, 3439.6, 3433.1, 3424.9, 1058.7, 1052.9, 1027.8 and 1019.7 cm⁻¹, are due to the complex formation between PA and MeOH. Specifically, these features have been observed at low concentration of precursors such as with sample-to-matrix ratios of 1:1000 for MeOH and 3:1000 for PA, thus, we have attributed these features clearly to

the 1:1 complexes of PA-MeOH. As has been mentioned earlier, the features due to binary complexes PA-H₂O, MeOH dimer and MeOH-H₂O are very weak under the conditions of our experiments and hence it is very unlikely that the product features are due to the presence of any ternary complexes involving any of the above mentioned binary complexes.

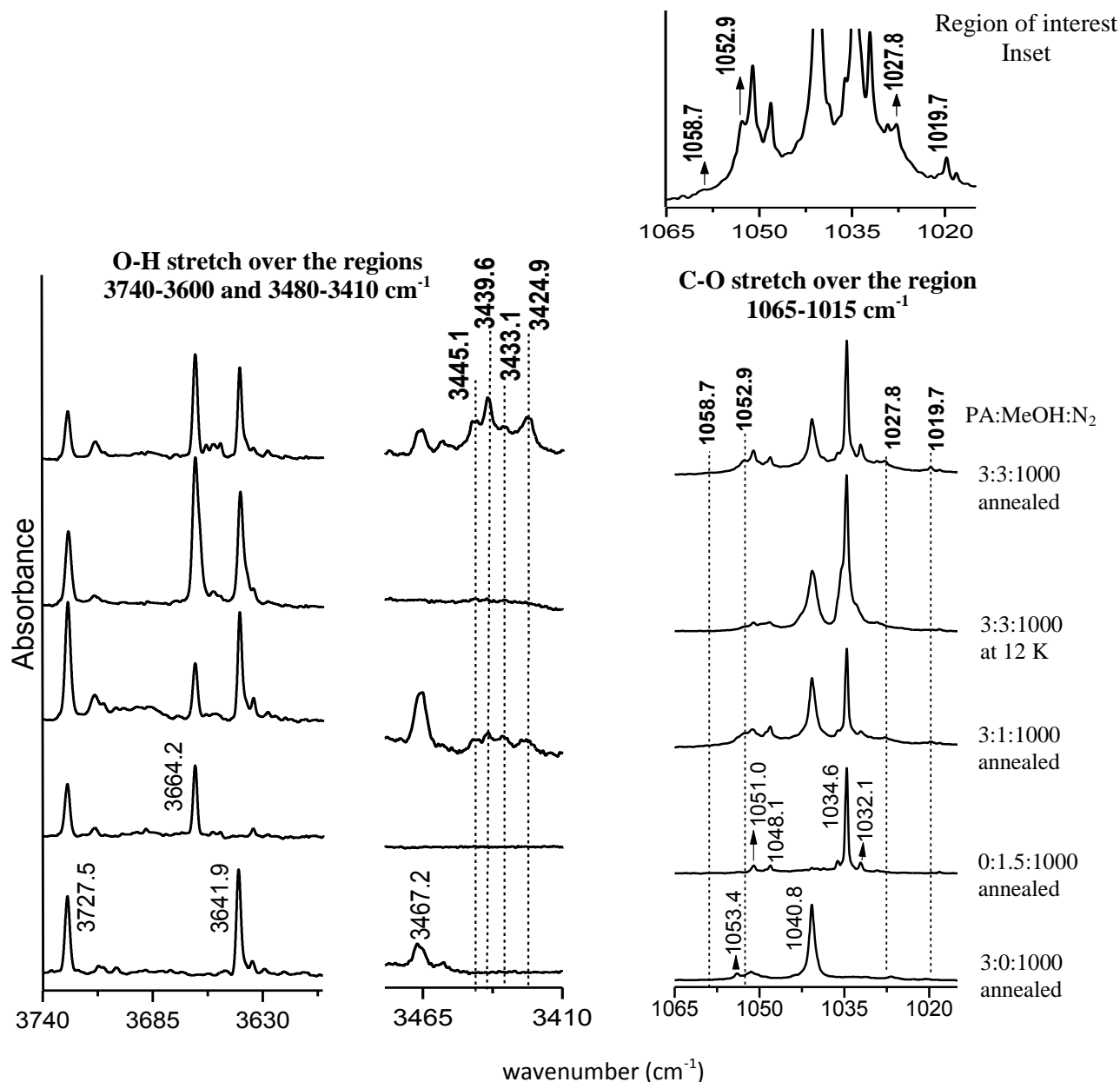


Fig. 4.1. Matrix Isolation Infrared spectra showing the monomers (PA and MeOH) and the PA-MeOH complexes. An inset has been shown for PA:MeOH:N₂(3:3:1000) annealed spectra in 1065-1015 cm⁻¹ spectral region. Dotted lines are drawn to show the features of PA-MeOH complexes observed.

We also performed few experiments with codeposition of PA and MeOH in the Ar matrix. In Fig. 4.2, we have shown the annealed spectra for the regions 3460-3410 and 1065-1015 cm^{-1} for both the N_2 and Ar matrix, when PA and MeOH were codeposited. Similar to the experimentally observed features in the N_2 matrix, new features due to PA-MeOH complex formation were observed after the matrix was annealed. As mentioned earlier, the spectral features, were however sharper in N_2 matrix in comparison with the Ar matrix.

4.4.2. Computational

Fig. 4.3 shows the different optimized structures of gauchePA-MeOH complexes computed at the MP2/aug-cc-pVDZ level. Complexes 1, 1A, 1' and 1'A, have PA serving as the proton donor through its hydroxyl hydrogen as well as a proton acceptor through its acetylenic π electron cloud. Both complexes 1 and 1A have MeOH acting as the proton donor through its hydroxyl hydrogen and acceptor through its oxygen atom. These PA-MeOH complexes were bound by an O-H \cdots O and an O-H $\cdots\pi$ interaction. Complexes 1 and 1A, were only different in the orientation of MeOH submolecule about the O-H $\cdots\pi$ bond, which corresponds to a change in the dihedral angle $\text{H}_8\text{H}_{14}\text{O}_{13}\text{C}_9$, given in Table 4.1. In complexes 1' and 1'A, MeOH interacts with PA forming a C-H $\cdots\pi$ contact through its methyl group, together with the O-H \cdots O interaction. Complex 1' can be obtained from complex 1, by a rotation around the O-H \cdots O bond, which brings the O-H in MeOH nearly trans to the O-H group in PA. Complexes 1' and 1'A were different in orientation of MeOH in the complex.

Complexes 2, 2' and 2'A, have PA serving as the proton acceptor through its O atom. In complex 2, in addition to the O-H \cdots O contact, MeOH forms a C-H $\cdots\pi$ interaction with PA. Complexes 2 and 2' are related by a rotation of the methyl group around the O-H \cdots O bond as indicated by the dihedral angle $\text{C}_2\text{C}_4\text{O}_7\text{H}_{14}$ in Table 4.1. Likewise, complexes 2 and 2'A are

related by a rotation about the O-H group of MeOH, given by dihedral angle $O_7H_{14}O_{13}C_9$. Both complexes 2' and 2'A were bound by an O-H...O contact, while differing only in the orientation of MeOH subunit.

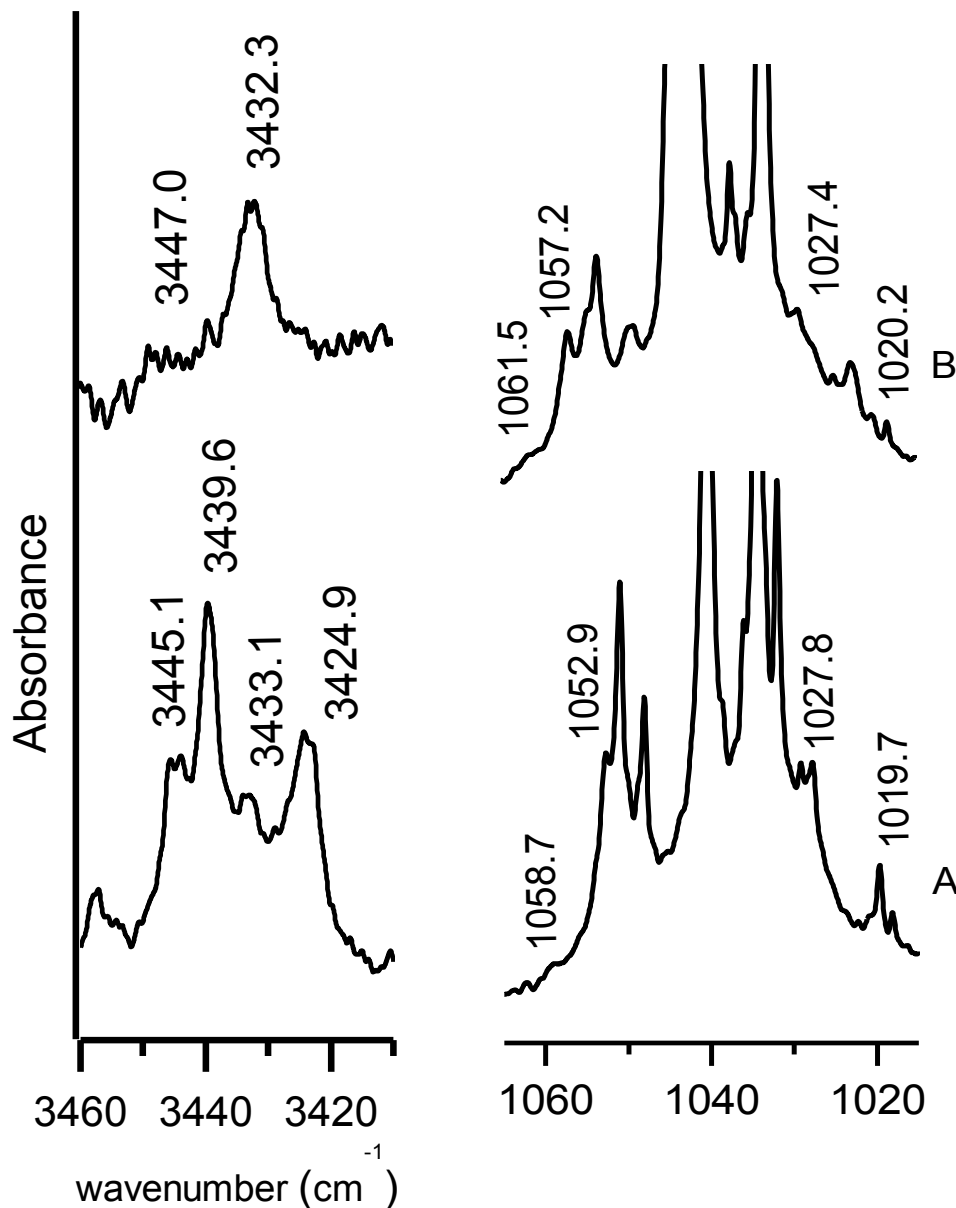


Fig. 4.2. Matrix isolation infrared spectra of PA codeposited with CH₃OH over the region 3460-3410 cm⁻¹ and 1065-1015 cm⁻¹, with PA:CH₃OH in (A) N₂ matrix (3:3:1000) annealed at 27 K and (B) Ar matrix (10:5:1000) annealed at 32 K.

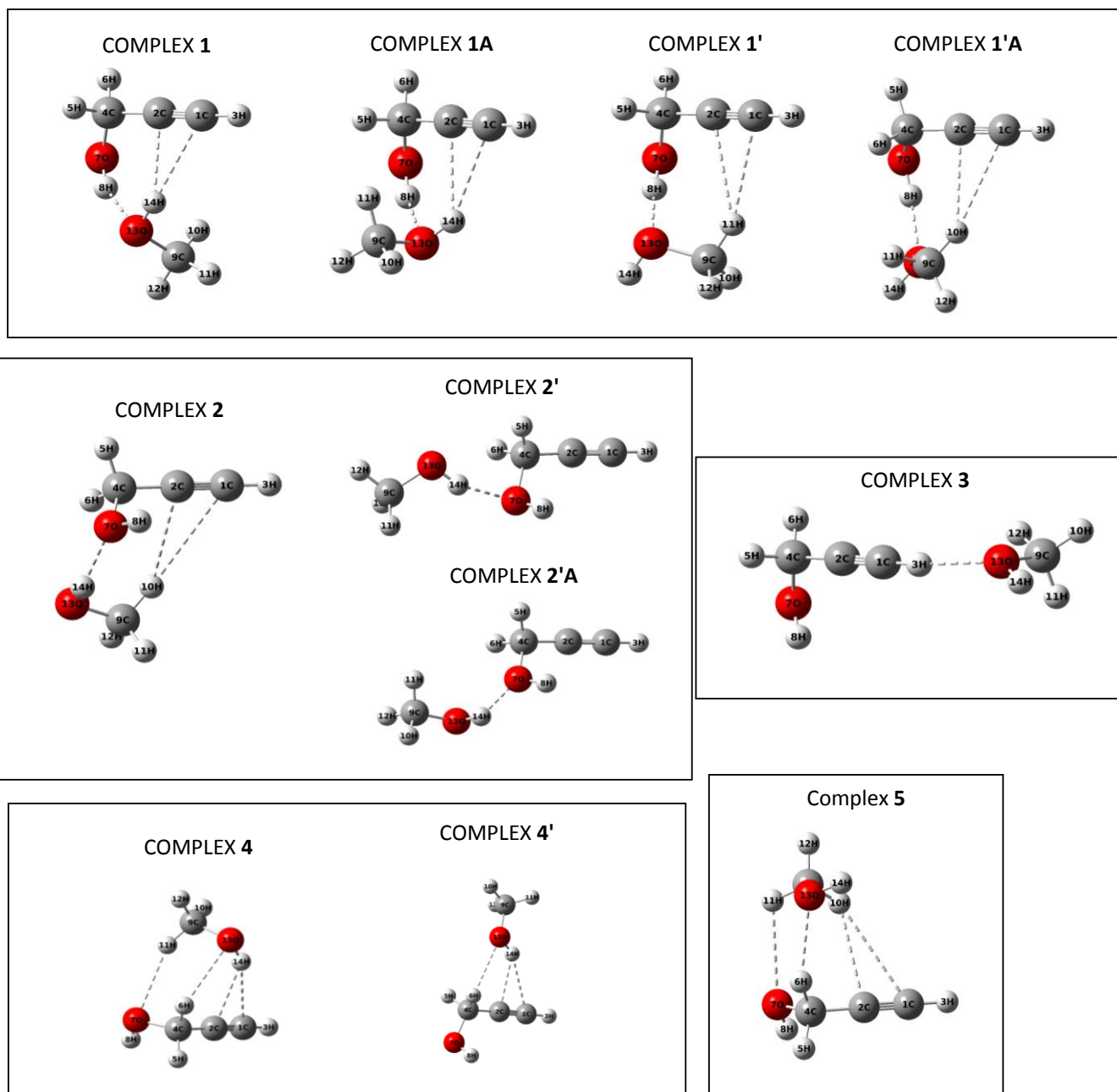


Fig. 4.3. Different optimized gauchePA-MeOH complexes computed at the MP2/aug-cc-pVDZ level, with their hydrogen bonded contacts indicated by dashed line.

In complex 3, PA interacts with MeOH through its acetylenic hydrogen atom, thus forming a $\equiv\text{C}-\text{H}\cdots\text{O}$ contact. In both complexes 4 and 4', PA interacts with MeOH through an $\text{H}\cdots\pi$ and a $\text{C}-\text{H}\cdots\text{O}$ contact (C-H of PA as the proton donor). Complex 4 has an additional $\text{C}-$

H...O contact formed with C-H of MeOH acting as the proton donor to the O atom of PA. Complex 5 was bound by a C-H... π interaction and two C-H...O contacts, one in which C-H of PA interacts with MeOH and other in which C-H of MeOH serves as the proton donor to the oxygen atom of PA.

Table 4.1. Some of the important geometrical parameters for different hydrogen bonded PA-MeOH complexes computed at MP2/aug-cc-pVDZ level. Bond distances given in Å and angles in degrees.

	O...H	O-H...O	H...C ₁	H...C ₂	O-H...C ₁	O-H...C ₂	C ₄ O ₇ C ₉ O ₁₃	O ₇ H ₈ O ₁₃ H ₁₄	O ₇ H ₈ O ₁₃ C ₉	H ₈ H ₁₄ O ₁₃ C ₉
1	1.88	158.7	2.53	2.43	148.7	125.9	+59.3	+28.9	-79.0	+103.2
1A	1.89	158.6	2.56	2.48	146.7	119.4	-124.0	-30.2	+79.7	-114.6
	O...H	O-H...O	H...C ₁	H...C ₂	C-H...C ₁	C-H...C ₂	C ₂ C ₄ O ₇ H ₁₄	O ₇ H ₈ O ₁₃ H ₁₄	O ₇ H ₈ O ₁₃ C ₉	O ₇ H ₁₄ O ₁₃ C ₉
1'	1.83	173.7	2.83	2.90	157.5	132.8	+69.2	-161.2	-38.9	-121.4
1'A	1.88	169.9	2.91	2.77	155.5	131.3	+80.3	+103.0	-27.9	+130.6
2	1.97	151.6	3.25	2.86	157.0	139.7	-97.2	-91.5	+133.8	+78.0
2'	1.92	159.5	-	-	-	-	+172.1	+51.8	+69.7	+139.9
2'A	1.95	152.0	-	-	-	-	-99.2	-153.0	-51.9	-68.7
	O...H	\equiv C-H...O	H...C ₁	H...C ₂	C-H...C ₁	C-H...C ₂	C ₁ H ₃ O ₁₃ H ₁₄	C ₁ H ₃ O ₁₃ C ₉		
3	2.11	165.8	-	-	-	-	-150.9	-14.2		
	O ₇ ...H ₁₁	C ₉ H ₁₁ ...O ₇	H...C ₁	H...C ₂	O-H...C ₁	O-H...C ₂	C ₄ H ₆ O ₁₃ H ₁₄	O ₁₃ H ₁₄ C ₁ H ₃		
4	2.64	151.2	2.59	2.41	160.7	133.6	-28.8	+156.0		
	O ₁₃ ...H ₆	C ₄ H ₆ ...O ₁₃								
	2.64	120.1								
	O...H	C-H...O	H...C ₁	H...C ₂	O-H...C ₁	O-H...C ₂	C ₄ H ₆ O ₁₃ H ₁₄	C ₄ H ₆ O ₁₃ C ₉	O ₁₃ H ₁₄ C ₁ H ₃	
4'	2.72	101.7	2.35	2.59	127.9	156.2	-46.6	+71.2	-172.5	
	O ₇ ...H ₁₁	C ₉ H ₁₁ ...O ₇	H...C ₁	H...C ₂	C-H...C ₁	C-H...C ₂	C ₄ H ₆ O ₁₃ H ₁₄	O ₁₃ H ₁₄ C ₁ H ₃		
5	2.81	113.8	3.25	2.87	141.8	122.2	-76.3	+157.2		
	O ₁₃ ...H ₆	C ₄ H ₆ ...O ₁₃								
	2.35	144.3								

The uncorrected, zero-point energy corrected and BSSE corrected interaction energies calculated for all the gauchePA-MeOH complexes, have been listed in Table 4.2, at the M06-2X and MP2 methods using 6-311++G(d,p) and aug-cc-pVDZ basis sets. Single-point energy calculations were performed at the MP2 method using the aug-cc-pVTZ and aug-cc-pVQZ, and at the CCSD(T)/aug-cc-pVDZ level, using the optimized structures of PA-MeOH complexes at the MP2/aug-cc-pVDZ level of theory. The uncorrected interaction energies at the MP2 and

CCSD(T) method employing CBS limit, were thus deduced for different PA-MeOH complexes, using the optimized geometries computed at the MP2/aug-cc-pVDZ level. Complex 1 is near-isoenergetic to complex 1A at all levels of theory and together they constitute the most stable isomers of PA-MeOH complexes.

Table 4.2. Uncorrected ΔE_{RAW} , zero-point energy corrected ΔE_{ZPC} and BSSE corrected ΔE_{BSSE} interaction energies (in kcal/mol) for different PA-MeOH hydrogen bonded complexes at M06-2X and MP2 methods using 6-311++G(d,p) and aug-cc-pVDZ basis sets. Uncorrected interaction energies computed at MP2 and CCSD(T) methods at the CBS limit, using optimized geometries at MP2/aug-cc-pVDZ level.

	M06-2X		MP2			CCSD(T)	
	6-311++G(d,p)	aug-cc-pVDZ	6-311++G(d,p)	aug-cc-pVDZ	CBS	aug-cc-pVDZ	CBS
1	-9.4/-7.7/-8.6	-9.0/-7.3/-8.4	-8.7/-7.2/-6.0	-9.3/-7.6/-7.0	-8.8	-9.1	-8.6
1A	-9.4/-7.8/-8.6	-8.9/-7.3/-8.3	-8.5/-7.1/-5.9	-9.2/-7.6/-6.8	-8.7	-9.0	-8.4
1'	-8.3/-7.0/-7.6	-7.2/-5.9/-6.7	Not Optimized	-8.2/-6.8/-6.3	-7.8	-8.0	-7.6
1'A	Not Optimized	Not Optimized	Not Optimized	-7.7/-6.4/-5.7	-7.3	-7.6	-7.1
2	-7.2/-5.8/-6.5	-6.4/-5.0/-5.8	-6.6/-5.4/-4.5	-6.8/-5.6/-5.0	-6.4	-6.7	-6.3
2'	-6.3/-5.1/-5.8	-5.7/-4.4/-5.2	Not Optimized	-6.3/-5.1/-4.8	-6.0	-6.2	-6.0
2'A	-6.6/-5.3/-5.9	-5.8/-4.6/-5.3	-6.3/-5.1/-4.4	-6.2/-5.1/-4.7	-6.0	-6.2	-5.9
3	-4.2/-3.3/-3.8 ^a	-3.8/-2.9/-3.3 ^a	-4.3/-3.1/-2.9	-4.4/-3.6/-3.2	-4.0	-4.3	-4.0
4	-5.4/-4.2/-4.8	-5.3/-4.1/-4.7	-4.8/-3.8/-2.8	-5.6/-4.6/-3.6	-5.0	-5.4	-4.8
4'	-4.4/-3.6/-4.0	-4.2/-3.3/-3.7	Not Optimized	-4.6/-3.9/-3.1	-4.3	-4.5	-4.2
5	Not Optimized	Not Optimized	Not Optimized	-4.6/-3.8/-2.8	-3.9	-4.5	-3.8

^a Opt=tight convergence criteria was relaxed for this PA-MeOH complex geometry.

The experimentally observed PA-MeOH features in the N₂ matrix together with the scaled computed features at the MP2/aug-cc-pVDZ level have been listed in Table 4.3, showing the O-H and C-O stretch, of PA and MeOH subunits in the four most stable PA-MeOH complexes 1, 1A, 1' and 1'A, likely to be observed experimentally. The computed features for the other PA-MeOH complexes are provided in Table 4.4.

Table 4.3. Experimental (in N₂) and computed scaled vibrational features (in cm⁻¹) for the PA, MeOH and PA-MeOH hydrogen bonded complexes 1, 1A, 1' and 1'A. Scaling factor for the O-H stretching region is 0.9548 and for the C-O stretching region is 0.9851. IR intensities (km/mole) have been indicated in brackets.

Experimental		Computed scaled at MP2/aug-cc-pVDZ				
Monomers						
PA	MeOH	PA		MeOH		
3641.9	3664.2	3642.0 (38)		3667.3 (34)		O-H stretch
1040.8	1034.6	1040.8 (102)		1027.5 (112)		C-O stretch
Complexes						
PA	MeOH	Complex 1	Complex 1A	Complex 1'	Complex 1'A	Modes
3424.9 -217.0 ^a		3426.0 (359) -216.0				O-H stretch in PA subunit
3439.6 -202.3			3440.1 (342) -201.9			
3433.1 -208.8				3438.7 (546) -203.3		
3445.1 -196.8					3469.3 (446) -172.7	
	-	3584.4 (157) -82.9	3591.9 (128) -75.4	3657.0 (46) -10.3	3658.9 (48) -8.4	O-H stretch in MeOH subunit
1052.9 +12.1		1053.5 (93) +12.7	1056.9 (92) +16.1			C-O stretch in PA subunit
-				1054.9 (99) +14.1	1056.5 (86) +15.7	
	1019.7 -14.9	1014.8 (93) -12.7				C-O stretch in MeOH subunit
	1027.8 -6.8		1022.6 (92) -4.9			
	-			1012.1 (91) -15.4	1016.4 (64) -11.1	

^aShifts, $\Delta\nu$, in cm⁻¹, calculated as $\nu_{\text{complex}} - \nu_{\text{monomer}}$

4.5. Discussion

4.5.1. Vibrational assignments in N₂ matrix

a) O-H stretch of PA subunit in complex: In our codeposition experiments, four product features were observed in this region: two strong features at 3424.9 and 3439.6 cm⁻¹, with weaker satellites at 3433.1 and 3445.1 cm⁻¹. Feature at 3424.9 cm⁻¹ showed the largest red shift

of 217.0 cm^{-1} from the feature occurring at 3641.9 cm^{-1} for the same mode in uncomplexed PA. This feature was thus assigned to the computed feature for complex 1 at 3426.0 cm^{-1} , red-shifted by 216.0 cm^{-1} . Another feature at 3439.6 cm^{-1} , observed experimentally was assigned to the computed feature at 3440.1 cm^{-1} , showing a red shift of 201.9 cm^{-1} . Similarly, another feature occurring at 3433.1 cm^{-1} , red-shifted by 208.8 cm^{-1} , has been assigned to the computed feature for complex 1', red-shifted by 203.3 cm^{-1} . The least red-shifted O-H stretch feature in experiments, observed at 3445.1 cm^{-1} was assigned to the computed feature at 3469.3 cm^{-1} for complex 1'A. The computed scaled features for the complexes 1, 1A, 1' and 1'A have been shown using Synspec spectrum and corroborated with experiments in Fig. 4.4.

Table 4.4. Computed scaled vibrational features (in cm^{-1}) for the PA, MeOH and higher energy PA-MeOH hydrogen bonded complexes. Scaling factor for the O-H stretching region is 0.9548 and for the C-O stretching region is 0.9851. IR intensities (km/mole) have been indicated in brackets.

Computed scaled at MP2/aug-cc-pVDZ							
Monomers							
PA				MeOH			
3642.0 (38)				3667.3 (34)			O-H stretch
1040.8 (102)				1027.5 (112)			C-O stretch
PA-MeOH Complexes							
2	2'	2'A	3	4	4'	5	Modes
3637.6 (42) -4.4	3630.5 (43) -11.5	3637.8 (40) -4.2	3641.8 (35) -0.2s	3637.6 (39) -4.4	3642.7 (38) +0.7	3638.0 (36) -4.0	O-H st. in PA subunit
3572.0 (222) -95.3	3534.0 (466) -133.3	3563.1 (294) -104.2	3665.5 (43) -1.8	3620.0 (112) -47.3	3615.1 (161) -52.2	3661.2 (34) -6.1	O-H st. in MeOH subunit
1025.9 (79) -14.9	1021.7 (130) -19.1	1025.3 (95) -15.5	1037.1 (100) -3.7	1037.0 (141) -3.8	1039.7 (24) -1.1	1032.6 (112) -8.2	C-O st. in PA subunit
1038.8 (90) +11.3	1045.4 (90) +17.9	1041.6 (96) +14.1	1020.3 (104) -7.2	1023.8 (32) -3.7	1031.6 (234) +4.1	1015.1 (69) -12.4	C-O st. in MeOH subunit

b) C-O stretch of PA subunit in complex: The product feature for C-O stretch in the complex was observed at 1052.9 cm^{-1} , which corresponds to a blue shift of 12.1 cm^{-1} from the feature of uncomplexed PA (1040.8 cm^{-1}). Computations for complexes 1 and 1A yielded

features at 1053.5 and 1056.9 cm^{-1} , which can both be assigned to the experimental feature at 1052.9 cm^{-1} . The small difference between the computed features for 1 and 1A renders it difficult for them to be resolved. In fact, the computed features for 1' and 1'A also occur within a couple of wavenumbers of those computed for 1 and 1A. However, given that complexes 1' and 1'A had only shown weak satellites in the O-H region, alluded to earlier, we do not hazard an assignment for these complexes. It must also be noted that the features for C-O stretch of PA in complexes 1 and 1A occur to the blue of the feature for the uncomplexed PA, both in our experiments and computations.

c) O-H stretch of MeOH subunit in complex: This mode computed to occur at 3584.4 cm^{-1} with a red shift of 82.9 cm^{-1} for complex 1, at 3591.9 cm^{-1} with a red shift of 75.4 cm^{-1} for complex 1A, at 3657.0 cm^{-1} with red shift of 10.3 cm^{-1} for complex 1' and 3658.9 cm^{-1} with red shift of 8.4 cm^{-1} for complex 1'A. The corresponding red shifts were calculated from the same mode in uncomplexed MeOH computed at 3667.3 cm^{-1} at the MP2/aug-cc-pVDZ level. In our experiments, we did not observe the feature for O-H stretch in MeOH subunit. It may be noted that the intensity of O-H stretch of the proton acceptor, MeOH is smaller than that of the O-H stretch in the proton donor, PA, which was clearly observed. At the small concentrations of complex, that were prepared in the matrix, MeOH features in the complex were not observed. The complex concentration could only have been increased by increasing the concentration of the precursors, which then would have given rise to the formation of homodimers, which we wanted to avoid.

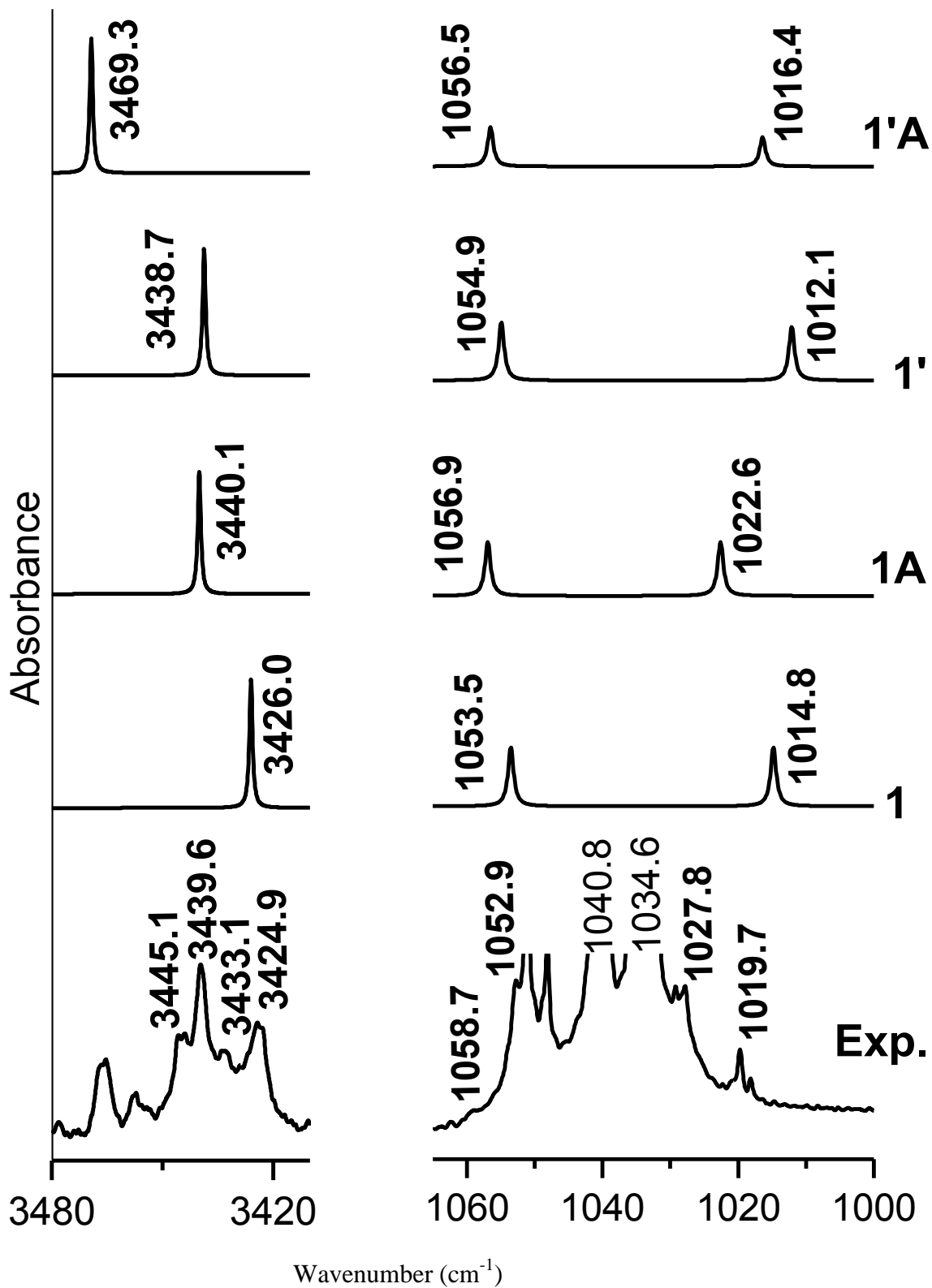


Fig. 4.4. Experimental IR spectrum of PA:MeOH:N₂ (3:3:1000) annealed and computed spectra of PA-MeOH complexes 1, 1A, 1' and 1'A with their respective scaled wavenumbers.

It must be noted that complexes 1 and 1A show large red shifts for the O-H stretch in MeOH, while complexes 1' and 1'A shows a very small red shift for the same mode. This results from the dual role MeOH plays as a proton acceptor and a proton donor, in complexes 1 and 1A; while it serves only as a proton acceptor in complexes 1' and 1'A. The absence of this O-H $\cdots\pi$ interaction involving the O-H group of MeOH, also leads to complexes 1' and 1'A to be less stable by ~ 1.0 kcal/mol relative to complexes 1 and 1A, at CCSD(T)/CBS level.

d) C-O stretch of MeOH subunit in complex: Two features (1019.7 and 1027.8 cm^{-1}) were observed in the codeposition experiments for this mode. Feature occurring at 1019.7 cm^{-1} showed a red shift of 14.9 cm^{-1} from the same mode in uncomplexed MeOH (1034.6 cm^{-1}). This feature was assigned to the computed features for complex 1. Similarly, experimental feature at 1027.8 cm^{-1} , red shifted by 6.8 cm^{-1} was in excellent agreement with the computed feature for complex 1A at 1022.6 cm^{-1} with the red shift of 4.9 cm^{-1} .

The computed features for complexes 1' and 1'A occur at 1012.1 and 1016.4 cm^{-1} respectively. While it may be tempting to assign the 1019.7 cm^{-1} feature multiply to complexes 1' and 1'A, in addition to complex 1, given the evidence, or rather the lack of it based on earlier arguments, for the presence of 1' and 1'A, we deem it unlikely that we are seeing these two complexes in the matrix. It must be noted that in computations, while the C-O stretch in PA subunit in complexes 1 and 1A shows a blue shift, that in MeOH subunit shows a red shift, which is consistent with our experimental observations. It can therefore be concluded that in our experiments, the most strongly bound complexes 1 and 1A are clearly produced in the nitrogen matrix.

e) Complexes of PA with CD₃OD and CD₃OH: Experiments were performed with isotopic species, CD₃OD, to confirm the vibrational assignments we had made earlier. However, the

sample of CD₃OD also contained some CD₃OH, due to exchange. When PA was codeposited with CD₃OD in a N₂ matrix, features were observed for the O-H stretch of PA in the region 3480-3410 cm⁻¹ (Fig. 4.5). Computations were performed for both PA-CD₃OD and PA-CD₃OH at MP2/aug-cc-pVDZ level for comparison, which are shown in Table 4.5.

It can be seen that the O-H stretch in PA occurs at nearly the same region in these complexes, for both CD₃OD and CD₃OH as it was in the case of CH₃OH. However, since two different complexes 1 and 1A, and two isotopic species, CD₃OD/CD₃OH, were involved, the multiplicity of peaks that resulted over a small wavenumber region presents only a broad feature that prevented us from making individual assignments to each species. However, it is still reassuring that the features of the O-H of PA in the complex, agree with computed values for the PA-CD₃OD and PA-CD₃OH systems.

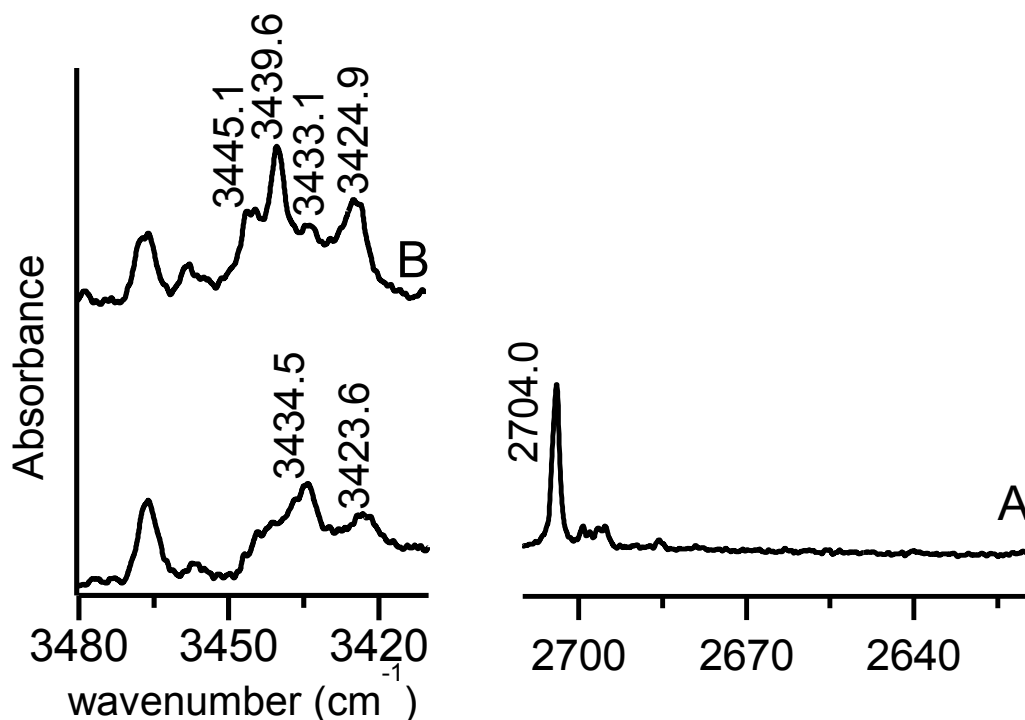


Fig. 4.5. Matrix Isolation Infrared spectra of PA:CD₃OD:N₂ (6:1:1000) in Trace A, over the region 3480-3410 cm⁻¹ (O-H stretch region of PA) and 2710-2620 cm⁻¹ (O-D stretch region of CD₃OD). The spectrum was recorded after annealing the matrix. For comparison, the spectra corresponding to the PA-CH₃OH system is also shown in Trace B for the region 3480-3410 cm⁻¹.

Table 4.5. Experimental (in N₂) and computed scaled vibrational features for the PA, CD₃OD, CD₃OH and hydrogen bonded complexes 1, 1A, 1' and 1'A of PA-CD₃OD and PA-CD₃OH at the MP2/aug-cc-pVDZ level. Scaling factor for the O-H stretching region taken as 0.9548, for the C-O stretching region as 0.9851, for O-D stretch as 0.9668. IR intensities (km/mole) have been indicated in brackets.

Experiment	Computed Scaled wavenumbers (cm ⁻¹)				Modes
Monomers					
	CD ₃ OD		CD ₃ OH		
3664.8			3667.1 (35)		O-H stretch
2704.0	2704.1 (22)				O-D stretch
981.3	971.2 (34)				C-O stretch
986.1			976.7 (39)		C-O stretch
PA subunit in PA-CD ₃ OD and PA-CD ₃ OH					
	Complex 1	Complex 1A	Complex 1'	Complex 1'A	
3423.6, 3434.5	3429.9 (390)	3441.7 (370)	3438.8 (542)	3469.2 (444)	O-H stretch for PA-CD ₃ OD
	3428.3 (355)	3440.5 (343)	3438.7 (548)	3469.2 (447)	O-H stretch for PA-CD ₃ OH
1053.0, 1058.5	1053.3 (86)	1057.0 (94)	1055.0 (95)	1056.2 (99)	C-O stretch for PA-CD ₃ OD
	1053.2 (89)	1056.2 (82)	1054.4 (101)	1055.8 (92)	C-O stretch for PA-CD ₃ OH
CD ₃ OD subunit for PA-CD ₃ OD					
-	2641.1 (69)	2647.1 (57)	2696.3 (32)	2697.8 (31)	O-D stretch
-	961.9 (43)	966.2 (43)	961.4 (41)	964.0 (32)	C-O stretch
CD ₃ OH subunit for PA-CD ₃ OH					
-	3584.1 (159)	3591.9 (128)	3656.9 (47)	3658.8 (48)	O-H stretch
-	967.0 (46)	971.3 (46)	966.6 (44)	969.9 (34)	C-O stretch

In particular, these experiments were used to see if perturbation in the O-D region could be observed for the deuterated methanol submolecule. It may be recalled that perturbations in the O-H stretch of MeOH in the PA-MeOH complex could not be observed. As in the case of the PA-CH₃OH experiments, here too, we were unable to observe the perturbations in the O-D stretch, which were computed to occur near 2645 cm⁻¹ (Table 4.5), while the features due to the O-H stretch of PA could be clearly observed. Both CH₃OH and CD₃OD experiments failed to present features resulting from the perturbations in the O-H(O-D) stretches in the respective

submolecule, indicating that these modes probably carried intensities that were too low to be observed.

4.5.2 Vibrational assignments in Ar matrix

PA and MeOH codeposition experiments were also performed in the Ar matrix and the spectra presented in Fig. 4.2, did not show as rich a structure as in the N₂ matrix. Only one strong feature was seen in the O-H stretching region of PA, which could be assigned to complex 1 (Table 4.6).

Table 4.6. Experimental (in Ar matrix) and computed scaled vibrational features (in cm⁻¹) for the PA, MeOH and PA-MeOH hydrogen bonded complexes 1, 1A, 1' and 1'A. Scaling factor for the O-H stretching region is 0.9570 and for the C-O stretching region is 0.9872. IR intensities (km/mole) have been indicated in brackets.

Experimental		Computed scaled at MP2/aug-cc-pVDZ					
Monomers							
PA	MeOH	PA		MeOH			
3650.2	3667.0	3650.4		3675.7		O-H stretch	
1042.9	1033.6	1042.9		1029.6		C-O stretch	
Complexes							
PA	MeOH	Complex 1	Complex 1A	Complex 1'	Complex 1'A	Modes	
3432.3		3434.0 (359)				O-H stretch in PA subunit	
			3448.1 (342)				
				3446.7 (546)			
					3477.3 (446)		
	-	3584.4 (157)	3591.9 (128)	3657.0 (46)	3658.9 (48)	O-H stretch in MeOH subunit	
1057.2		1055.7 (93)		1057.1 (99)		C-O stretch in PA subunit	
				1059.2 (92)			1058.7 (86)
1020.2		1016.9 (93)		1014.2 (91)	1018.6 (64)	C-O stretch in MeOH subunit	
			1024.8 (92)				

No clear evidence was obtained for complex 1A, which was observed in the N₂ matrix.

Likewise, data in the C-O stretching region of PA and MeOH also showed evidence for the

formation of complex 1 only. It appears that the N₂ matrix was aiding the formation of complex 1A together with complex 1. Matrices have been shown to selectively stabilize isomers of complexes. In an earlier work on C₂H₂-MeOH complex,⁶ the O-H···π complex was observed only in the N₂ matrix and not in Ar matrix. Based on computational evidence, it was argued in their work that interaction with N₂ matrix increased the basicity of π cloud of C₂H₂ which thus stabilizes the complex. Such subtle interactions of the matrix with the precursors have thus been shown to selectively stabilize isomers of complexes. It may also be possible that complex 1A readily relaxes to complex 1 in the Ar matrix.

4.5.3. AIM analysis

We performed AIM analysis on all the optimized PA-MeOH complexes at the MP2/aug-cc-pVDZ level, showing the bond and ring critical points (Fig. 4.6), thus identifying and characterizing the hydrogen bonded contacts. The values of electron density $\rho_b(\mathbf{r}_c)$, Laplacian $\nabla^2\rho_b(\mathbf{r}_c)$, local electronic kinetic energy density $G(\mathbf{r}_c)$, local electronic potential energy density $V(\mathbf{r}_c)$ and the hydrogen bonded energy E_{HB} for each contact, for the *gauche* PA-MeOH complexes, at the MP2/aug-cc-pVDZ level, have been listed in Table 4.7. In the four most stable and experimentally observed PA-MeOH complexes, 1, 1A, 1' and 1'A, the O-H···O interaction was being the dominant contact.

4.5.4. NBO analysis

We performed NBO analysis on *gauche*PA-MeOH complexes 1, 1A, 1' and 1'A to understand the contribution of orbital interactions. The significant orbital interactions in these complexes between the donor and acceptor orbitals computed at MP2/aug-cc-pVDZ level, have been provided in Table 4.8. In all these complexes, a greater second order perturbation energy was computed when one of the lone pairs of O atom of MeOH donated its electron density to the

antibonding orbital of O-H bond in PA ($\sigma^*_{\text{O}_7\text{H}_8}$), which is also consistent with the larger value of occupancy in the acceptor orbital $\sigma^*_{\text{O}_7\text{H}_8}$.

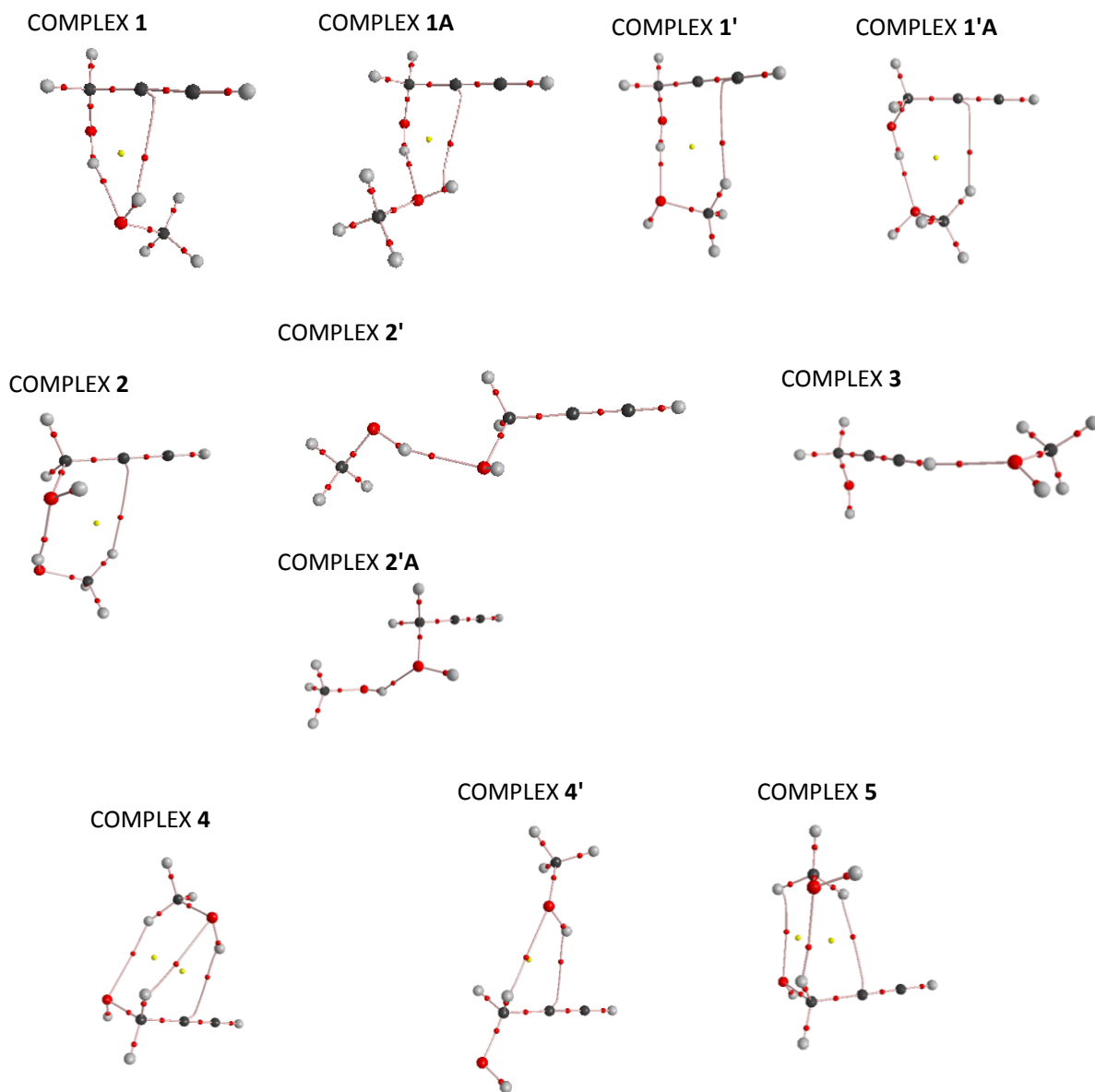


Fig. 4.6. AIM analysis for PA-MeOH complexes at MP2/aug-cc-pVDZ level showing the bond and ring critical points.

Table 4.7. Electron density $\rho_b(\mathbf{r}_c)$, Laplacian $\nabla^2\rho_b(\mathbf{r}_c)$, local electronic kinetic energy density $G(\mathbf{r}_c)$, local electronic potential energy density $V(\mathbf{r}_c)$ and the hydrogen bonded energy E_{HB} values for *gauche*PA-MeOH complexes, at the MP2/aug-cc-pVDZ level. The $\rho_b(\mathbf{r}_c)$, $\nabla^2\rho_b(\mathbf{r}_c)$, $G(\mathbf{r}_c)$, $V(\mathbf{r}_c)$ values given in atomic units and E_{HB} in kcal/mol. Values for *trans*PA-MeOH complex 6 involving O-H...O interaction, with PA serving as proton donor, has also been shown.

	Interaction	$\rho_b(\mathbf{r}_c)$	$\nabla^2\rho_b(\mathbf{r}_c)$	$G(\mathbf{r}_c)$	$V(\mathbf{r}_c)$	E_{HB}	total E_{HB}
<i>gauche</i> PA-MeOH Complexes							
complex 1	O-H...O	0.0309	0.0998	0.0254	-0.0259	-8.1	-10.4
	O-H... π	0.0132	0.0377	0.0084	-0.0074	-2.3	
complex 1A	O-H...O	0.0302	0.0985	0.0249	-0.0251	-7.9	-10.1
	O-H... π	0.0125	0.0377	0.0082	-0.0070	-2.2	
complex 1'	O-H...O	0.0324	0.1160	0.0288	-0.0287	-9.0	-9.9
	C-H... π	0.0067	0.0192	0.0039	-0.0030	-0.9	
complex 1'A	O-H...O	0.0282	0.1043	0.0249	-0.0238	-7.5	-8.5
	C-H... π	0.0071	0.0202	0.0041	-0.0032	-1.0	
	O-H... π	0.0119	0.0358	0.0077	-0.0066	-2.1	
complex 2	O-H...O	0.0229	0.0836	0.0193	-0.0176	-5.5	-6.2
	C-H... π	0.0052	0.0165	0.0032	-0.0023	-0.7	
complex 2'	O-H...O	0.0273	0.0959	0.0231	-0.0223	-7.0	-7.0
complex 2'A	O-H...O	0.0260	0.0836	0.0205	-0.0201	-6.3	-6.3
complex 3	\equiv C-H...O	0.0173	0.0585	0.0131	-0.0116	-3.6	-3.6
complex 4	C-H...O ^a	0.0083	0.0288	0.0058	-0.0044	-1.4	-4.8
	C-H...O ^b	0.0074	0.0243	0.0049	-0.0037	-1.1	
	O-H... π	0.0127	0.0393	0.0085	-0.0073	-2.3	
complex 4'	C-H...O ^a	0.0066	0.0291	0.0055	-0.0038	-1.2	-3.6
	O-H... π	0.0132	0.0397	0.0087	-0.0076	-2.4	
complex 5	C-H...O ^a	0.0131	0.0388	0.0086	-0.0074	-2.3	-3.9
	C-H...O ^b	0.0054	0.0211	0.0040	-0.0027	-0.9	
	C-H... π	0.0054	0.0174	0.0034	-0.0024	-0.8	
	O-H... π	0.0119	0.0358	0.0077	-0.0066	-2.1	
<i>trans</i> PA-MeOH Complexes							
complex 6	O-H...O	0.0309	0.1131	0.0276	-0.0270	-8.5	-8.5

^aC-H involving the PA. ^bC-H involving the MeOH.

It must also be noted that the larger electron occupancy in the σ^* acceptor orbital of O-H in MeOH for both complexes 1 and 1A resulted in a greater red shift of 85.9 and 75.4 cm^{-1} respectively in comparison to the red shift of 10.3 and 8.4 cm^{-1} for complexes 1' and 1'A, respectively, where MeOH serves only as a proton acceptor.

Table 4.8. NBO Analysis showing the significant orbital interactions between the donor and acceptor orbitals among the two subunits in PA-MeOH complexes 1, 1A, 1' and 1'A, their corresponding second order perturbation energies E(2) in kcal/mol, difference in energy between donor and acceptor orbitals E(j)-E(i) and the off-diagonal NBO Fock matrix element F(i,j), computed at the MP2/aug-cc-pVDZ level. E(j)-E(i) and F(i,j) in atomic units.

		Donor NBO(i)	Acceptor NBO (j)	E(2)	E(j)-E(i)	F(i,j)
COMPLEXES	1	n1 O ₁₃	σ^* O ₇ H ₈	1.4	1.6	0.042
		n2 O ₁₃	Occupancy 0.02502	13.6	1.3	0.118
		π 1 C ₁ C ₂	σ^* O ₁₃ H ₁₄	0.5	1.1	0.021
		π 2 C ₁ C ₂	Occupancy 0.00982	2.6	1.1	0.048
	1A	n1 O ₁₃	σ^* O ₇ H ₈	2.0	1.5	0.049
		n2 O ₁₃	Occupancy 0.02415	12.5	1.3	0.114
		π 1 C ₁ C ₂	σ^* O ₁₃ H ₁₄	0.3	1.1	0.016
		π 2 C ₁ C ₂	Occupancy 0.00915	2.4	1.1	0.046
	1'	n1 O ₁₃	σ^* O ₇ H ₈	2.6	1.5	0.056
		n2 O ₁₃	Occupancy 0.02564	15.1	1.4	0.129
		π 1 C ₁ C ₂	σ^* C ₉ H ₁₁	0.2	1.1	0.012
		π 2 C ₁ C ₂	Occupancy 0.00959	1.2	1.1	0.033
		σ O ₇ H ₈	σ^* O ₁₃ H ₁₄ Occupancy 0.00543	0.1	1.6	0.009
	1'A	n1 O ₁₃	σ^* O ₇ H ₈	3.5	1.5	0.065
		n2 O ₁₃	Occupancy 0.02222	11.5	1.4	0.113
		π 1 C ₁ C ₂	σ^* C ₉ H ₁₀	1.0	1.1	0.030
		π 2 C ₁ C ₂	Occupancy 0.00978	0.4	1.1	0.018
		σ O ₇ H ₈	σ^* O ₁₃ H ₁₄ Occupancy 0.00544	0.1	1.6	0.009

4.5.5. LMO-EDA analysis

Table 4.9 lists the contribution of each energy component, such as the electrostatic energy ΔE_{es} , the exchange energy ΔE_{ex} , the repulsion energy ΔE_{rep} , the polarization energy ΔE_{pol}

and the dispersion energy ΔE_{disp} , towards the total interaction energy of all the PA-MeOH complexes computed at the MP2/aug-cc-pVDZ level, using LMO-EDA analysis. In complexes 1, 1A, 1' and 1'A, the electrostatic and exchange energy contributes significantly while polarization and dispersion energy have a minor contribution of $\sim 11\%$ to ΔE_{MP2} . Similarly, in the higher energy complexes 2, 2', 2'A and 3, the electrostatic and exchange energy were the major contributors to the total interaction energy. It can also be seen that in complexes 4, 4' and 5, major contributing component was the exchange energy (44%), with the electrostatic and dispersion energy being the second largest contributors to the total interaction energy.

Table 4.9. LMO-EDA results on PA-MeOH complexes at MP2/aug-cc-pVDZ level. All energies given in kcal/mol.

	ΔE_{es}	ΔE_{ex}	ΔE_{rep}	ΔE_{pol}	ΔE_{disp}	ΔE_{MP2}
1	-15.1(32%)	-21.0(45%)	37.4	-5.2(11%)	-5.6(12%)	-9.5
1A	-14.7(32%)	-21.0(45%)	37.3	-5.1(11%)	-5.9(12%)	-9.4
1'	-12.6(33%)	-16.7(44%)	29.7	-4.5(12%)	-4.4(11%)	-8.5
1'A	-11.2(32%)	-15.3(44%)	27.1	-4.1(11%)	-4.6(13%)	-8.0
2	-8.6(31%)	-11.8(43%)	20.6	-2.7(10%)	-4.5(16%)	-6.9
2'	-9.2(35%)	-11.0(42%)	19.8	-2.9(11%)	-3.1(12%)	-6.4
2'A	-8.3(33%)	-10.6(42%)	18.9	-2.8(11%)	-3.6(14%)	-6.4
3	-5.4(34%)	-6.4(41%)	11.2	-1.9(12%)	-2.0(13%)	-4.4
4	-5.9(26%)	-10.0(44%)	17.0	-2.0(9%)	-4.7(21%)	-5.6
4'	-5.7(29%)	-8.8(44%)	15.2	-1.9(10%)	-3.4(17%)	-4.7
5	-4.1(24%)	-7.8(44%)	12.9	-1.5(8%)	-4.2(24%)	-4.6

4.6. Comparison of PA-MeOH Complex studies with PA-H₂O system

It can be seen from Table 4.2 that the global minima on the PA-MeOH potential energy surface, complexes 1 and 1A, have BSSE corrected interaction energies of -7.0 and -6.8 kcal/mol at MP2/aug-cc-pVDZ level. At the same level of theory, PA-H₂O hydrogen-bonded complex 1, which is the global minimum, has interaction energy of -6.2 kcal/mol,⁷ which is less than that of PA-MeOH complexes 1 and 1A. PA-MeOH complexes 1 and 1A, which have higher interaction

energy relative to the PA-H₂O complex, also shows a larger shift in the O-H stretching mode of the PA subunit. The experimental red shift in the PA-MeOH complex was 217.0 cm⁻¹, which is larger than that for the PA-H₂O system with a red shift of 174.7 cm⁻¹.⁷

AIM analysis revealed that in PA-MeOH complexes 1 and 1A, there exists a much stronger O-H...O interaction with E_{HB} of -8.1 and -7.9 kcal/mol, respectively, as shown in Table 4.7. NBO results in Table 4.8 show that the lone pairs on oxygen of MeOH donates relatively a greater share of electron density into the σ* orbital of O-H bond of PA than H₂O in the PA-H₂O complex (11.4 kcal/mol).⁷

In PA-H₂O system, the two isoenergetic complexes 1 and 1*, both of which had an O-H...O and an O-H...π interaction, had similar vibrational spectra. Thus in our matrix experiments, these complexes could not be individually identified. However, the isoenergetic PA-MeOH complexes 1 and 1A, had infrared features that showed discernible differences in the O-H stretch region of PA subunit, which enabled us to individually identify these complexes in our experiments.

It must also be noted that MeOH is stronger base than H₂O in gas phase, since their gas phase basicity values are 724.5 and 660.0 kJ/mol, respectively.⁸ Thus, MeOH forms the stronger complex with PA than does H₂O. Further, the pK_a equalization principle,⁹ states that strength of D-H...:A bond increases with decrease in the value of ΔpK_a= pK_a(D-H) - pK_a(A-H⁺), where proton donor D-H is the O-H group in PA while the acceptor is the O atom in MeOH or H₂O. The ΔpK_a will be smaller with MeOH as the proton acceptor relative to H₂O. Hence the strength of O-H...O interaction will be greater in PA-MeOH complex as compared with PA-H₂O complex, which is in agreement with our results.

In our earlier work on PA-H₂O hydrogen bonded complexes,⁷ we had deduced that when dual interactions (O-H...O and O-H... π contacts) were present in the complex, the two precursors adopt a geometry where they sacrifice their optimum orientations for each of the two interactions, in order to maximize the overall stabilization. We explored if a similar situation prevailed in PA-MeOH hydrogen-bonded complexes 1 and 1A, which are the global minima with the two similar contacts: an O-H...O and an O-H... π , as in PA-H₂O. Since both complexes 1 and 1A are isoenergetic with uncorrected interaction energies of -9.3 and -9.2 kcal/mol, respectively, at MP2/aug-cc-pVDZ level; we present here the data for complex 1 alone.

It can be seen from Fig. 4.7 that in complex 6, which has *only* an O-H...O interaction, has a O₁₃H₈ hydrogen bonded distance of 1.85 Å that is shorter than that in complex 1 (1.88 Å) with dual interactions. Furthermore, the O₁₃H₈O₇ bond angle is close to linearity with a value of 167.9° in complex 6, while it is 158.7° in complex 1. It is therefore clear that when dual interactions were present as in complex 1, both the O-H...O bond distance and angle have been compromised in order to accommodate the secondary O-H... π contact, thus maximizing the overall stabilization.

This compromise is also reflected in the energies of the complexes. We compared the uncorrected interaction energy of PA-MeOH complex 1 with those of complexes 4' and 6 in a similar way as explained in our previous work on PA-H₂O complexes.⁷ Complexes 4' and 6 are chosen for the comparison, since the dual interactions O-H...O and O-H... π present in complex 1, were present individually in complexes 4' and 6. Complex 4' has a dominant O-H... π interaction, (together with a weaker secondary C-H...O interaction) with the PA subunit in *gauche* conformation, while complex 6 has *only* an O-H...O interaction, where a *trans* PA submolecule

interacts as a proton donor to MeOH, as shown in Fig. 4.7. Complex 1, with *both* an O-H \cdots π and an O-H \cdots O interaction has a larger interaction energy (-9.3 kcal/mol) than either complexes 4' or 6. However, the interaction energy of complex 1 is significantly less than the sum (-12.0 kcal/mol) of interaction energies of complexes 4' and 6, where each of the interactions were present individually. Even though, complex 4' has an extra C-H \cdots O interaction, it is unlikely that the difference between the sum of the energies of complexes 4' and 6 and the energy of complex 1, is due to this extra interaction. It is more due to the compromise adopted by complex 1 in its attempt to engage dual contacts.

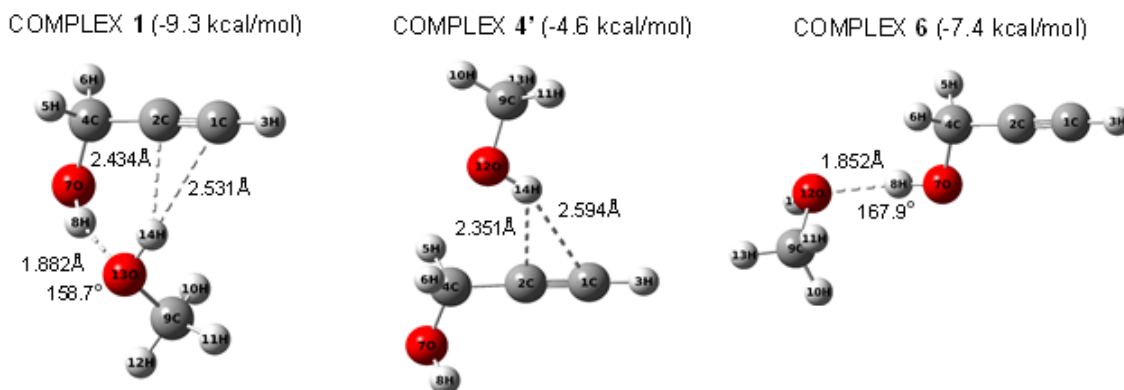


Fig. 4.7. PA-MeOH complexes 1, 4' and 6 computed at MP2/aug-cc-pVDZ level, with their uncorrected interaction energies in kcal/mol, indicated in brackets. Dashed lines represent the bond distances between atoms.

4.7. PA-DEE Complexes

An attempt was made to compare the strength of primary O-H \cdots O interaction in the global minima complexes of PA-H₂O and PA-MeOH having dual contacts, with a system, particularly PA-DEE in which the primary O-H \cdots O interaction existed with a complete suppression of the secondary O-H \cdots π interaction. We have thus optimized the structures of PA-

DEE hydrogen bonded complexes in which the most stable TTT conformation of DEE have been used, at the MP2/aug-cc-pVDZ level, shown in Fig. 4.8.

Only two geometries were possible, one in which a dominant O-H...O interaction was formed between the O-H group of PA and O atom of DEE, and other in which PA interacts with O atom of DEE through its acetylenic H atom, forming a $\equiv\text{C-H}\cdots\text{O}$ interaction. The interaction energies have been computed for these complexes and have been listed in Table 4.10.

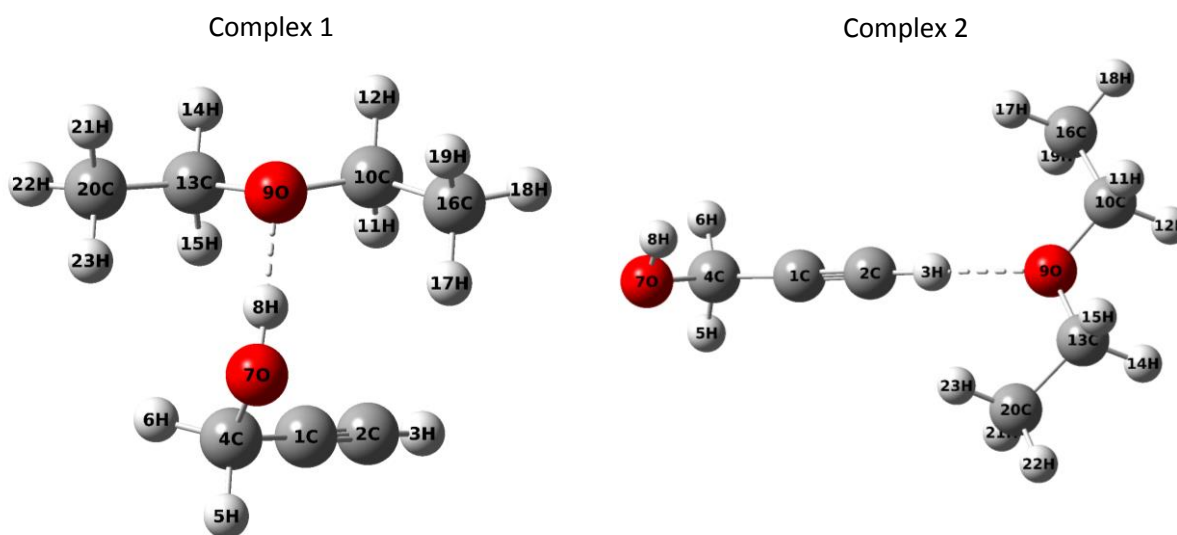


Fig. 4.8. Optimized structures of PA-DEE complexes at the MP2/aug-cc-pVDZ level.

Table 4.10. Uncorrected/ZPE corrected/BSSE corrected interaction energies for PA-DEE complexes computed at the MP2 level using 6-311++G(d,p) and aug-cc-pVDZ basis sets. Uncorrected interaction energies at CCSD(T)/aug-cc-pVDZ level have also been shown. All energy values are given in kcal/mol.

PA-DEE complexes			
	MP2/6-311++G(d,p)	MP2/aug-cc-pVDZ	CCSD(T)/aug-cc-pVDZ
Complex 1	-10.5/-9.2/-6.6	-11.7/-10.3/-7.8	-11.2
Complex 2	-4.9/-3.9/-3.4	-5.7/-4.9/-3.8	-5.5

The O...H hydrogen bond length in PA-DEE complex 1 was the shortest with a value of 1.82 Å, in comparison to the values in PA-H₂O and PA-MeOH. The O-H...O bond angle (169.0°) in PA-DEE complex 1 was much closer to linearity than that in PA-H₂O and PA-MeOH

complexes. AIM analysis on this PA-DEE complex revealed an E_{HB} value of -9.5 kcal/mol for the O-H...O interaction, much greater than E_{HB} values for same interaction in PA-H₂O and PA-MeOH complexes, implying a stronger O-H...O interaction for the PA-DEE complex 1, when O-H... π interaction has been completely suppressed. This was also accounted by a relatively greater red shift of 252.4 cm⁻¹ in the O-H stretch of PA subunit in PA-DEE complex 1 (Table 4.11). Thus, the geometrical parameters for the primary O-H...O interaction were compromised in both PA-H₂O and PA-MeOH complexes, in order to accommodate a secondary O-H... π interaction, in agreement with our results.

Table 4.11. Computed scaled wavenumbers (in cm⁻¹) with their vibrational mode assignments for PA-DEE complexes at MP2/aug-cc-pVDZ level. Scaling factors used are 0.9548 for the O-H and \equiv C-H stretch and 0.9799 for the C-O stretch. Shifts are calculated as $\Delta\nu = \nu$ (complex) - ν (monomer). The computed IR intensities in km/mole units are indicated in parenthesis.

Exp. (N ₂)	Computed Scaled at MP2/aug-cc-pVDZ level			
Monomer	Monomer	Complex		Mode of Assignment
PA	PA	Complex 1	Complex 2	
3641.9	3642.0 (38)	3389.6 (484) -252.4	3641.8 (33) -0.2	O-H stretch
3311.0	3326.5 (54)	3322.8 (50) -3.7	3228.8 (354) -97.7	\equiv C-H stretch
1040.8	1035.2 (102)	1052.8 (77) +17.6	1031.1 (100) -4.1	C-O stretch
DEE	DEE	Complex 1	Complex 2	
1128.0	1128.0 (190)	1105.8 (162) -22.2	1121.8 (186) -6.2	C-O asym. stretch
-	1054.8 (16)	1046.6 (24) -8.2	1052.1 (25) -2.7	C-O sym. stretch

4.8. Conclusions

Infrared spectrum of PA codeposited with MeOH in N₂ and Ar matrices, was studied for the first time. In N₂ matrix, presence of 1:1 PA-MeOH were revealed by occurrence of new product bands in the O-H and C-O stretch region after the matrix was annealed. This was evidenced by larger red shift of ~ 200 cm⁻¹ in the O-H stretch of PA subunit in complex.

Computationally, eleven structures were optimized. The two most stable and nearly isoenergetic complexes 1 and 1A with an energy difference of 0.2 kcal/mol at CCSD(T)/CBS level constituting the global minima, were bound by a primary O-H...O contact, together with a secondary O-H... π contact. Similarly, the second most stable isoenergetic complexes 1' and 1'A were bound by a primary O-H...O contact, together with a secondary C-H... π contact. Computations together with experiments confirm the formation of complexes 1 and 1A, with possibly complexes 1' and 1'A. Isotopic results with CD₃OD further strengthened our assignments. NBO results showed interaction to be between the lone pairs on O of MeOH, serving as electron donor and σ^* orbital of O-H bond in PA, as electron acceptor. From LMO-EDA, it was found that in complexes 1 and 1A, exchange and electrostatic energy were the major contributors to the total interaction energy. The other higher energy complexes showed an O-H...O contact along with a C-H... π contact in complex 2, an O-H...O contact in complexes 2' and 2'A with PA serving as a proton acceptor, a \equiv C-H...O contact in complex 3, an O-H... π as primary contact in complexes 4 and 4' and a C-H... π contact with two C-H...O contacts in complex 5.

It was noted that in PA-MeOH complexes 1 and 1A, the O...H bond distance was shorter and O-H...O bond angle close to linearity as compared with PA-H₂O global minimum complex. The interaction energies have greater values for these complexes in PA-MeOH relative to PA-H₂O. Further from the gas phase basicity values of MeOH and H₂O, the strength of O-H...O contact was greater for PA-MeOH complex with a lower value of ΔpK_a , relative to PA-H₂O complex. In PA-MeOH complexes 1 and 1A, a similar antagonistic behavior was observed, as in PA-H₂O complex.

Computations on PA-DEE complexes revealed a stronger primary O-H \cdots O contact where the O-H \cdots π contact was completely suppressed. The O \cdots H hydrogen bond length was the shortest and O-H \cdots O bond angle closest to linearity, in PA-DEE complex, clearly implying that in PA-H₂O and PA-MeOH complexes, these geometrical parameters were compromised in order to bring a secondary O-H \cdots π contact alongside.

References

1. Frisch, M. J.; Trucks, G. W.; Schlegel, H. B.; Scuseria, G. E.; Robb, M. A.; Cheeseman, J. R.; Scalmani, G.; Barone, V.; Mennucci, B.; Peterson, G. A.; *et al.* GAUSSIAN 09, Revision C.01, Gaussian Inc., Wallingford CT, **2010**.
2. The Spectra were Simulated using SYNSPEC made Available by Irikura, K. National Institute of Standards and Technology, Gaithersburg, MD 20899, USA, **1995**.
3. Bentwood, R. M.; Barnes, A. J.; Orville-Thomas, W. J. Studies of Intermolecular interactions by Matrix Isolation Vibrational Spectroscopy: Self-association of Water. *J. Mol. Spectros.* **1980**, *84*, 391-404.
4. Bakkas, N.; Bouteiller, Y.; Loutellier, A.; Perchard, J. P.; Racine, S. The Water-Methanol Complexes. I. a Matrix Isolation Study and an *Ab Initio* Calculation on the 1-1 species. *J. Chem. Phys.* **1993**, *99*, 3335-3342.
5. Schriver, L.; Burneau, A.; Perchard, J. P. Infrared spectrum of the Methanol dimer in Matrices. Temperature and irradiation effects in solid nitrogen, *J. Chem. Phys.* **1982**, *77*, 4926.
6. Jose, K. V. J.; Gadre, S. R.; Sundararajan, K.; Viswanathan, K. S. Effect of Matrix on IR Frequencies of Acetylene and Acetylene-Methanol complex: Infrared Matrix Isolation and *Ab initio* study. *J. Chem. Phys.* **2007**, *127*, 104501-10.
7. Saini, J.; Viswanathan, K. S. Does a Hydrogen bonded complex with Dual contacts show Synergism? A Matrix Isolation Infrared and *Ab initio* study of Propargyl Alcohol-Water complex. *J. Mol. Struct.* **2016**, *1118*, 147-156.
8. NIST, Nist Webbook, <http://webbook.nist.gov/chemistry>, **2008** (accessed 18 January 2008).
9. Gilli, P.; Pretto, L.; Bertolasi, V.; Gilli, G. Predicting Hydrogen-Bond Strengths from Acid-Base Molecular Properties. The pKa Slide Rule: Toward the Solution of a Long-Lasting Problem. *Accounts Chem. Res.* **2009**, *42*, 33-44.

CHAPTER 5
CONFORMATIONS OF PROPARGYL AMINE AND
ITS HYDROGEN BONDED COMPLEXES

5.1. Introduction

In this chapter, we discuss the conformations of propargyl amine (PAm), which is a logical extension of our earlier studies on propargyl alcohol. This study will throw light on the relative importance of OH and NH₂ groups, on the conformations of the acetylenic systems.

Based on the conformations of PA, one can expect PAm to have two possible forms: the gg and gt conformations, as has already been reported.^{1,2} The gg conformer is one in which the two NH bonds occupy gauche positions with the CCNH dihedral angle being $\sim \pm 60^\circ$, very similar to that observed in gPA. The gt form has one of the NH bond in the gauche orientation, while the other NH bond has a trans orientation with CCNH dihedral angle of 180° . The gg conformer was shown to be lower in energy relative to gt form. In contrast to the PA conformers where the gauche form was doubly degenerate and the trans form was non-degenerate; in the case of PAm, the gg conformer is non-degenerate and gtPAm form is doubly degenerate, as shown in Fig. 5.1².

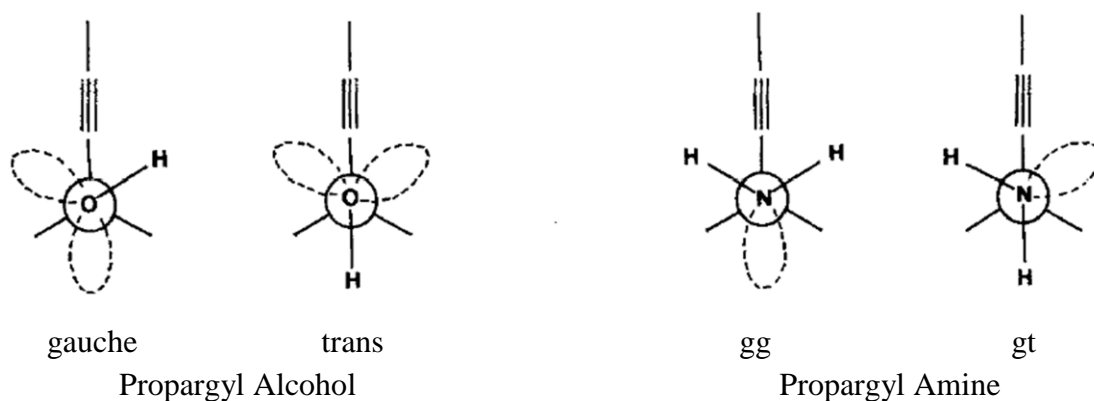


Fig. 5.1. Conformers of Propargyl Alcohol and Propargyl Amine.²

In this work, we have studied the conformations of PAm using matrix isolation infrared spectroscopy and *ab initio* computations at higher levels such as MP2/aug-cc-pVDZ. Specifically we looked for the presence of the higher energy *gt* form of PAm. In addition, we also looked at the 1:1 complexes of PAm with H₂O, MeOH and Diethylether DEE.

5.2. Experimental Details

Matrix isolation experiments were performed using N₂ (Sigma Gases and Services, Grade I: 99.999% purity). Propargyl amine, HC≡CCH₂NH₂, PAm was obtained from Sigma Aldrich with an assay of 98%. PAm, Milli-Q® Type 1 Ultrapure H₂O (with purity typically 18.2 MΩ.cm at 25 °C) and MeOH (Sigma Aldrich 99%) were used without further purification. Several freeze-thaw-pump cycles were performed prior to the use of chemicals.

In the matrix isolation experiments, appropriate concentrations of PAm vapour were mixed with the matrix gas, and passed through an effusive nozzle. This mixture was deposited on a KBr window maintained at ~12 K. To obtain the appropriate concentrations of PAm, the liquid sample of PAm was maintained at temperatures of ~ -58 °C and -47 °C to achieve vapour pressures of 1 and 2.5 mbar respectively, which when mixed with 1000 mbar of N₂, yielded sample to matrix concentrations of 1:1000 and 2.5:1000. Double-jet experiments were also employed for the study of hydrogen bonded complexes of PAm with H₂O, in which gas mixture of PAm/matrix gas was deposited through one nozzle while vapours of H₂O were separately deposited through a second nozzle, on the cold window. H₂O was equilibrated at -23 °C to obtain the vapour pressure of ~0.8 mbar and similarly, MeOH was equilibrated at -36 °C for obtaining the vapour pressure of ~3 mbar. Isotopic experiments were also performed using D₂O (Sigma-Aldrich, isotopic purity of 99.9 atom % D). The hydrogen bonded complexes of PAm with CH₃OH and CD₃OD (Cambridge Laboratories, 98%) were also studied.

5.3. Computational Details

The structures of the conformers of PAm were optimized using Gaussian 09,³ at the M06-2X and MP2 methods employing 6-311++G(d,p) and aug-cc-pVDZ basis sets. When performing the M06-2X calculations, keywords `opt=tight` and `int=ultrafine` were used.⁴ Relative energies of the two conformers were computed for the PAm conformers at all the levels mentioned above. These energies were then corrected for the zero-point energy. Single point energy calculations were performed to compute the uncorrected energies at the CCSD(T)/aug-cc-pVDZ level of theory, using the optimized geometries of PAm conformers at MP2/aug-cc-pVDZ level.

Vibrational harmonic frequencies of the PAm conformers were computed at the MP2/aug-cc-pVDZ level and scaled using 0.9508 for the stretching vibrations, and 0.9609 for the bending modes to make a comparison with experimental wavenumbers. The scaling factor 0.9508 was obtained by dividing the experimental feature by the computed feature for the NH₂ asymmetric stretch, while the scaling factor of 0.9609 was obtained by dividing the experimental feature for the NH₂ wagging mode with the computed feature for the same mode.

NBO analysis was done for the PAm conformers at the M06-2X/aug-cc-pVDZ level. A systematic deletion of specific orbital interactions was carried out using NBO deletions, at the same level of theory, to identify the role of the various orbital interactions in determining the stability of the conformers.

The optimized structures of PAm conformers were used to further optimize the structures of PAm hydrogen bonded complexes with H₂O/MeOH. The uncorrected interaction energies for the PAm-H₂O/MeOH were computed at the M06-2X and MP2 methods employing 6-311++G(d,p) and aug-cc-pVDZ basis sets. The uncorrected interaction energies for complexes of PAm with H₂O/MeOH, were also computed at the MP2 and CCSD(T) method at the CBS

limit,^{5,6} using single point energy calculations on the optimized geometries of complexes at the MP2/aug-cc-pVDZ level. In addition, interaction energies were also calculated at the CCSD(T)/aug-cc-pVDZ level from the optimized geometries of complexes at MP2/aug-cc-pVDZ level. The interaction energies separately corrected for zero-point energies and BSSE were also computed using the M06-2X and MP2 methods employing 6-311++G(d,p) and aug-cc-pVDZ basis sets. We also performed NBO analysis on the complexes of PAm with H₂O/MeOH to understand the orbital interactions between the two subunits in complex. AIM analysis helped in identifying and characterizing the hydrogen bonded interaction in these complexes. Total interaction energy of complexes, was partitioned into electrostatic, exchange, repulsion, polarization and dispersion using LMO-EDA analysis,⁷ done on GAMESS⁸.

5.4. Results-PAm Conformers

5.4.1. Experimental

Matrix isolation infrared experiments were performed at ~12 K, with the deposition of PAm in a N₂ matrix, with a sample-to-matrix ratio of 0.5:1000. Experimental features were observed at 3416.3, 3311.7, 2941.5 cm⁻¹ in the spectral range 3800-2900 cm⁻¹, and 1277.7, 1080.6, 929.7, 823.7, 808.5, 654.9, 651.2, 643.4, 633.9 and 536.6 cm⁻¹ in the spectral region 1300-520 cm⁻¹, as shown in Fig. 5.2 and listed in Table 5.1. Feature occurring at 3727.5 and 3635.0 cm⁻¹, corresponds to the asymmetric and symmetric stretch of H₂O, respectively, which is always present in any matrix isolation experiment, as an unavoidable impurity.

5.4.2. Computational

The computed structures of PAm conformers: gg and gt, have been optimized at the MP2/aug-cc-pVDZ level as shown in Fig. 5.3. The non-degenerate ggPAm conformer has both the N-H bonds, gauche to the C≡C bond with H₈NCC and H₉NCC dihedral angles of +57° and -

57° respectively. The gtPAm conformer is doubly degenerate with gt1 and gt2 structures. The gt1 structure has one N-H bond in a gauche orientation with the H₉NCC dihedral angle of +60° and the other N-H bond, trans (+176°) to the C≡C bond, while gt2 structure has H₈NCC dihedral angle of -60° and H₉NCC dihedral angle of -176°. Both the gg and gt PAm conformers were minima on the potential energy surface, at all levels of theory from the frequency calculations. The frequencies of the various normal modes of the two conformers were shown in Table 5.1. The interconversion barrier from gg to gt PAm form (gg→gt1) was calculated at MP2/aug-cc-pVDZ to be 2.8 kcal/mol, by locating the transition state (H₈NCC and H₉NCC dihedral angle of +125° and +8°, respectively), which is relatively greater than the g→t interconversion barrier of 2.2 kcal/mol for PA conformers.

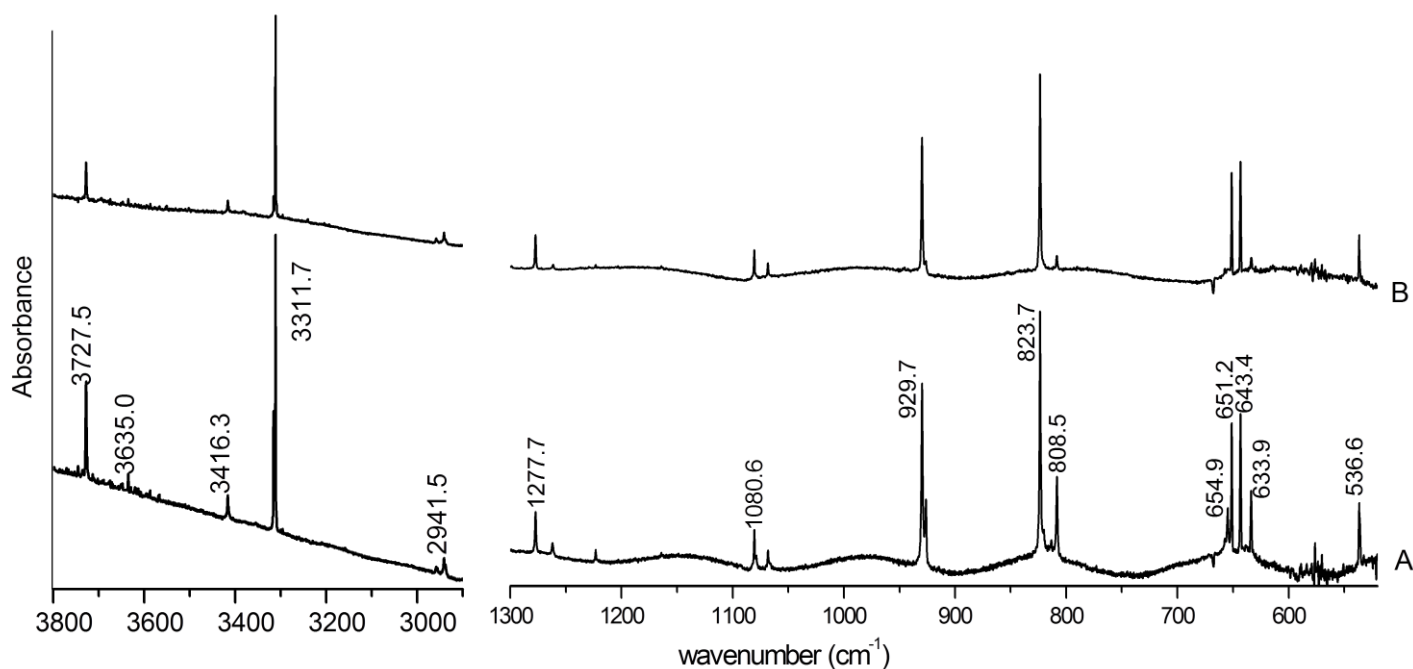


Fig. 5.2. Infrared spectrum over the spectral range 3800-2900 and 1300-520 cm⁻¹ of PAm:N₂ (0.5:1000) recorded after (A) depositing the matrix at 12 K and (B) annealing the matrix at 27 K.

Table 5.1. Experimental (N₂ matrix) and computed scaled vibrational wavenumbers (cm⁻¹) at MP2/aug-cc-pVDZ level for the PAm conformers. Scaling factors used are 0.9508 for the stretching vibrations and 0.9608 for the bending modes. Computed IR intensities (km/mole) given in brackets.

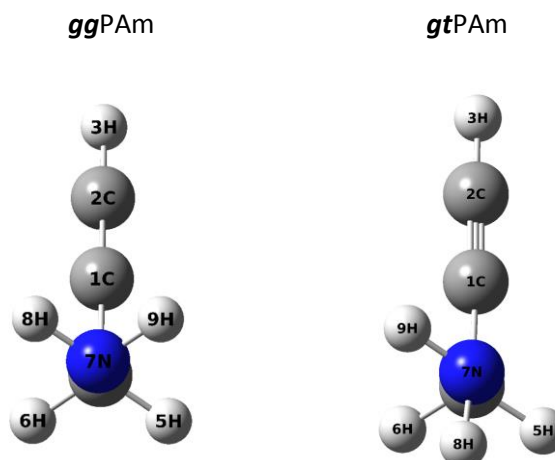
Vibrational modes	Experimental	Computed scaled	
		<i>gg</i>	<i>Gt</i>
NH ₂ asym. str.	3416.3	3416.5 (5)	3423.0 (4)
NH ₂ sym. str.	-	3325.6 (1)	3324.2 (1)
≡C-H str.	3311.7	3312.3 (55)	3314.6 (53)
CH ₂ asym. str.	-	2984.5 (7)	2957.6 (10)
CH ₂ sym. str.	2941.5	2935.6 (18)	2879.7 (43)
C≡C str.	-	1998.2 (0)	2014.7 (0)
NH ₂ sci.	-	1582.9 (20)	1569.9 (27)
CH ₂ sci.	-	1410.6 (3)	1433.9 (1)
NH ₂ twist.	-	1323.0 (0)	1240.9 (9)
CH ₂ wag.	1277.7	1290.7 (24)	1350.1 (24)
CH ₂ twist.	-	1134.0 (0)	1135.0 (1)
C-N str.	1080.6	1053.4 (11)	1039.8 (14)
NH ₂ wag.	929.7	929.7 (95)	
	808.5		813.9 (107)
CH ₂ rock.	-	850.2 (2)	971.1 (28)
C-C str.	823.7	813.1 (72)	848.5 (4)
≡C-H bend in NCCC plane	651.2	564.1 (58)	
	654.9		573.8 (40)
≡C-H bend ⊥ to NCCC plane	643.4	543.6 (52)	
	633.9		543.1 (47)
CCN bend	536.6	488.2 (8)	493.7 (6)

Table 5.2 showed the calculated values of relative energies for the PAm conformers. It was found that at all the levels of theory studied, the ggPAm conformer was lower in energy than the gt conformer. At the CCSD(T)/aug-cc-pVDZ level, ggPAm form was ~1.5 kcal/mol lower in energy than the gtPAm conformer.

5.5. Discussion- PAm Conformers

5.5.1. Vibrational Assignments

Table 5.1 presents the experimental infrared features recorded at ~12 K, together with the computed scaled features for the PAm conformers, at the MP2/aug-cc-pVDZ level. Assignments of the experimental features for the various modes have also been presented in the same Table.



	<i>ggPAm</i>	<i>gtPAm</i> (or <i>gt1</i>)
H ₈ N ₇ C ₄ C ₁	+57	+176
H ₉ N ₇ C ₄ C ₁	-57	+60

Fig. 5.3. Optimized structures of *gg* and *gt* PAm conformers with some important dihedral angles (in degrees), computed at the MP2/aug-cc-pVDZ level.

In the N₂ matrix, feature at 3416.3 cm⁻¹ was assigned to NH₂ asymmetric stretch in the dominantly populated *ggPAm* conformer. A strong feature occurring at 3311.7 cm⁻¹ was assigned to the ≡C-H stretch in *ggPAm* conformer. Similarly, features at 2941.5, 1277.7, 1080.6, 823.7 and 536.6 cm⁻¹ were assigned to CH₂ symmetric stretch, CH₂ wag, C-N stretch, C-C stretch and CCN bend, respectively for the *gg* PAm conformer.

A strong feature occurring at 929.7 cm⁻¹ was assigned to the NH₂ wagging mode for *ggPAm*. The features at 651.2 and 643.4 cm⁻¹ corresponds to the ≡C-H bend in the NCCC plane and ≡C-H bend ⊥ to NCCC plane, respectively, for the *gg* PAm conformer. In the spectra

recorded after the matrix was annealed at 27 K (Fig. 5.2), features at 808.5, 654.9 and 633.9 cm^{-1} were found to decrease in intensity, which could therefore possibly be the features due to the higher energy gt-PAm conformer. Hence, the features at 808.5, 654.9 and 633.9 cm^{-1} could be assigned to the NH_2 wagging, $\equiv\text{C-H}$ bend in NCCC plane and $\equiv\text{C-H}$ bend \perp to NCCC plane, respectively for the gt PAm conformer. Alternatively, these features could be due to site effects. In order to resolve this point, we also performed heated nozzle and the supersonic experiments on PAm which is discussed in following section.

Table 5.2. The Uncorrected (ΔE_{RAW})/ ZPE corrected (ΔE_{ZPE}) relative energies of PAm conformers, *gg* and *gt*, computed at different levels of theory.

Level of computation	Relative energies in kcal/mol	
	6-311++G(d,p)	aug-cc-pVDZ
M06-2X	1.8 /1.6	1.6/1.5
MP2	1.6/1.4	1.4/1.3
CCSD(T)	-	1.5

5.5.2. Heated Nozzle Experiments

We performed the heated nozzle experiments, to see if the higher energy gt conformer of PAm could be observed in the matrix. Initially, PAm vapours maintained at the temperature of ~ -47 $^{\circ}\text{C}$ to attain a vapour pressure of 2.5 mbar which was mixed with 1000 mbar of the matrix gas (N_2) to obtain a sample-to-matrix ratio of 2.5:1000. This gas mixture was passed through an effusive nozzle for deposition onto a KBr window. During deposition, the effusive nozzle through which PAm/matrix gas was passed, was heated to a temperature of 393 K, over a length of about 25 mm, using a regulated DC Power supply. With increase in temperature of the nozzle, it is possible to populate the higher energy gtPAm conformer. An increase in temperature increases the population of the gt conformer from 16% at room temperature (300 K) to 25% at 393 K, calculated using the uncorrected energy difference between the two conformers at the

MP2/aug-cc-pVDZ level and their degeneracies. Hence, increase in intensity of any of the features of PAm can possibly be assigned to the higher energy gt form. However, we did not observe any increase in the intensity of the features in the spectrum recorded at the higher nozzle temperature, which could have been assigned to the gt form.

5.5.3. Supersonic Experiments

In addition, we also performed the supersonic nozzle experiments on PAm using N₂ as the matrix gas. Expansion in the beam causing cooling of the various modes, that can possibly depopulate the higher energy form, which is expected to be present to the extent of ~16% in a room temperature PAm/matrix gas mixture. We employed stagnation pressures of 680 and 720 torr. The pulsed solenoid valve was operated with a pulse width of 150 and 180 ms and a repetition rate 5 Hz, to deposit the matrix, which corresponded to duty cycle of 75% and 90%. However, deposition of PAm using the supersonic nozzle yielded spectra that showed no changes in the intensities of features compared with that observed with the effusive source at room temperature.

Thus, it was inferred from effusive, heated nozzle and supersonic experiments on PAm that the dominantly populated ggPAm conformer was unambiguously trapped in the matrix. No evidence was found for the formation of higher energy conformer in our matrix isolation experiments. The reduction in intensity of the 808.5, 654.9 and 633.9 cm⁻¹ after annealing the matrix deposited using a room temperature effusive source was likely due to site effects.

5.5.4. AIM Analysis

AIM analysis was performed on both the PAm conformers at the MP2/aug-cc-pVDZ level. It was found that in both conformers, no bond critical point was found between the hydrogen atom of NH₂ group and the acetylenic π cloud, indicating the absence of an

intramolecular hydrogen bond in PAm. The H_8C_1 and H_8C_2 distances were ~ 2.697 and 3.600 Å, respectively, which are rather large for an intramolecular hydrogen bond. The stability of the ggPAm conformer over the gtPAm structure was further investigated using NBO analysis.

5.5.5. NBO Analysis

NBO analysis was performed at the M06-2X/aug-cc-pVDZ level on the conformers of PAm, the results of which are shown in Table 5.3. The results presented show the different orbital delocalizations such as remote, geminal and vicinal, in each of the two conformers. Subsequently, calculations were performed after deletions of specific orbital interactions and the change in energy of each conformer after deletions are shown in Table 5.4.

When only the geminal interactions were deleted, while retaining the other interactions, energy of both conformers were raised, with the conformational ordering being still the same, i.e. ggPAm was more stable than the gtPAm conformer, which indicates that geminal interactions do not play a decisive role in conformer preference of PAm.

When the vicinal interactions were deleted, ggPAm conformer became less stable with an energy difference of 1.1 kcal/mol, in comparison to ggPAm being 1.6 kcal/mol more stable when all interactions were present. Clearly, the vicinal interactions also contribute in stabilizing the ggPAm form.

A remote interaction in which the lone pair on nitrogen atom of PAm was donated to the acetylenic π^* orbital, was present only in the ggPAm conformer, with the second-order perturbation energy of 2.0 kcal/mol. On deletion of this remote interaction, a slight increase in the energy of gg-PAm by 3.0 kcal/mol was observed, resulting in an inversion as shown graphically in Fig. 5.4. Thus, the $n-\pi^*$ remote interaction in ggPAm conformer is important since

on deletion of this remote interaction, we observe a switch in the conformational ordering meaning that ggPAm now becomes less stable than the gtPAm form.

Table 5.3. NBO analysis of significant geminal, vicinal and remote interactions in PAm conformers with their second order perturbation energies, E(2), computed at the M06-2X/aug-cc-pVDZ level.

Interactions	Donor orbital	Acceptor orbital	E(2) in kcal/mol	
			<i>gg</i>	<i>gt</i>
Geminal	σ_{C1C2}	σ^*_{C1C4}	5.4	5.8
	σ_{C1C2}	σ^*_{C2H3}	3.3	3.3
	σ_{C1C4}	σ^*_{C1C2}	8.6	8.8
	σ_{C2H3}	σ^*_{C1C2}	7.0	7.0
	σ_{C4N7}	σ^*_{C1C4}	0.5	0.6
	σ_{C4H5}	σ^*_{C1C4}	-	0.6
	σ_{C4H6}	σ^*_{C1C4}	-	0.6
Vicinal	π_1_{C1C2}	σ^*_{C4H5}	2.5	2.2
	π_1_{C1C2}	σ^*_{C4H6}	2.5	2.7
	π_2_{C1C2}	σ^*_{C4N7}	5.7	5.4
	π_2_{C1C2}	σ^*_{C4H5}	0.9	1.2
	π_2_{C1C2}	σ^*_{C4H6}	0.9	0.5
	σ_{C1C4}	σ^*_{C2H3}	3.3	3.2
	σ_{C1C4}	σ^*_{N7H9}	-	2.0
	σ_{C2H3}	σ^*_{C1C4}	6.7	6.8
	σ_{C4H5}	$\pi_1^*_{C1C2}$	5.5	4.9
	σ_{C4H5}	σ^*_{C1C2}	3.6	3.6
	σ_{C4H5}	σ^*_{N7H9}	3.5	-
	σ_{C4H5}	σ^*_{N7H8}	-	3.6
	σ_{C4H5}	$\pi_2^*_{C1C2}$	1.5	2.4
	σ_{C4H6}	$\pi_1^*_{C1C2}$	5.5	6.2
	σ_{C4H6}	σ^*_{C1C2}	3.6	3.9
	σ_{C4H6}	σ^*_{N7H8}	3.5	-
	σ_{C4H6}	$\pi_2^*_{C1C2}$	1.5	0.9
	σ_{C4N7}	$\pi_2^*_{C1C2}$	2.8	3.1
	σ_{C4N7}	σ^*_{C1C2}	2.5	2.7
	σ_{N7H8}	σ^*_{C4H6}	2.9	-
	σ_{N7H8}	σ^*_{C4H5}	-	2.7
	σ_{N7H9}	σ^*_{C4H5}	2.9	-
	σ_{N7H9}	σ^*_{C1C4}	-	4.0
	n_1_{N7}	σ^*_{C1C4}	9.9	0.8
	n_1_{N7}	σ^*_{C4H6}	1.4	8.7
n_1_{N7}	σ^*_{C4H5}	1.4	1.9	
Remote	n_1_{N7}	$\pi_2^*_{C1C2}$	2.0	-

Table 5.4. NBO analysis showing the energies obtained after deletion of different delocalization interactions in PAM conformers at M06-2X/aug-cc-pVDZ level of computation. Energies have not been corrected for ZPE.

	Energy (Hartrees)	Interactions deleted	Deletion energy (Hartrees)	Change in energy		Relative contribution for stabilization (%)
				Hartrees	kcal/mol	
gg	-171.945376651	Remote	-171.9405557	0.004821	3.0	2.5
		Geminal	-171.9029568	0.04242	26.6	21.8
		Vicinal	-171.7979583	0.147418	92.5	75.8
		All	-171.7595596	0.185817	116.6	
gt	-171.942917665	Geminal	-171.8951863	0.047731	30.0	24.6
		Vicinal	-171.7961548	0.146763	92.1	75.4
		All	-171.7605244	0.182393	114.5	

This is consistent with our NBO results on PA conformers as discussed earlier in chapter 3 that remote and vicinal orbital interactions play a deciding role in the conformational preference.

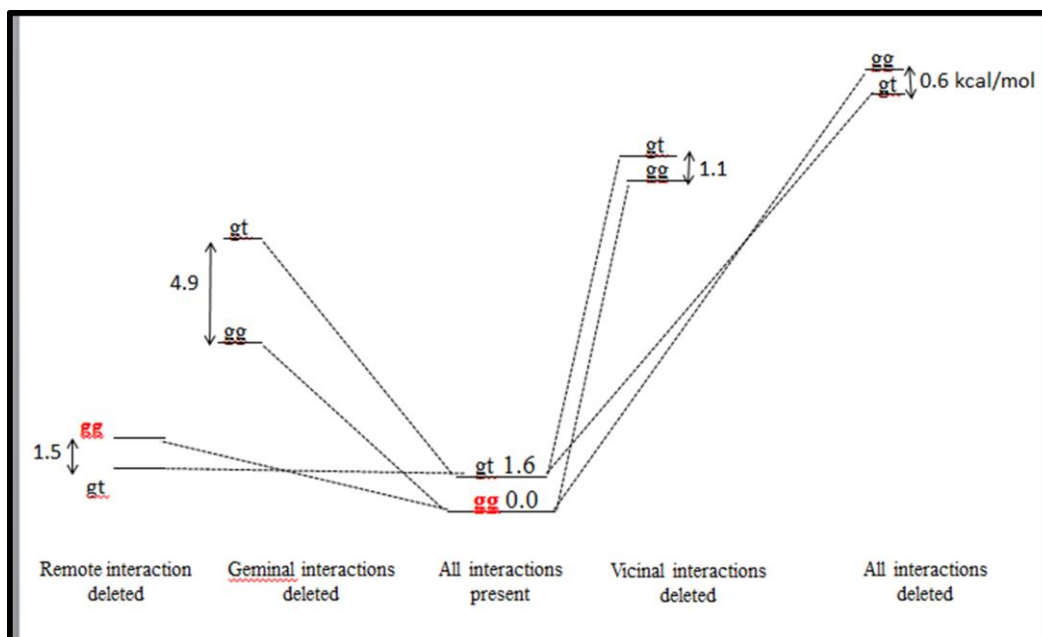


Fig. 5.4. Correlation diagram showing the relative energies (kcal/mol) of **gg** and **gt** PAM, when orbital interactions were systematically deleted at M06-2X/aug-cc-pVDZ level.

5.6. Results- PAm-H₂O Complexes

5.6.1. Experimental

To study the complexes of PAm with H₂O, PAm and H₂O were codeposited in a N₂ matrix and the infrared spectra were recorded at 12 K. The matrix was then annealed at 27 K, to promote complex formation. The spectra are shown in Fig. 5.5. Trace A showed the annealed infrared spectrum of PAm in N₂ matrix with sample-to-matrix ratio of 1:1000. Features at 3416.3 and 3311.7 cm⁻¹, in the 3425-3250 cm⁻¹ region, correspond to the NH₂ asymmetric and ≡C-H stretch, respectively of the PAm submolecule. Similarly, a strong feature occurring at 929.7 cm⁻¹ corresponds to the NH₂ wagging mode of PAm. The feature at 3727.5 cm⁻¹ is due to the antisymmetric O-H stretch of the H₂O submolecule.⁹

In trace G of Fig. 5.5, recorded after annealing the matrix, we observed new product features at 3694.6, 3381.5 and 960.0 cm⁻¹. These features were obtained only after the matrix was annealed. These new features were also only observed when *both* PAm and H₂O were codeposited, implying that these product features must be due to the PAm-H₂O complex.

5.6.2. Computational

To help in the assignment of the product features, we performed *ab initio* computations for the PAm-H₂O complex. The optimized structures of hydrogen bonded complexes of PA with H₂O computed at the MP2/aug-cc-pVDZ are shown in Fig. 5.6. Three complexes were optimized for each of the ggPAAm- and gtPAAm- complexes with H₂O. Complex 1 in both ggPAAm-H₂O and gtPAAm-H₂O complexes, was bound by dual interactions, a N-H...O contact where N-H of PAm serves as proton donor to the O atom of H₂O and an O-H...π contact, where the C≡C of PAm serves as the proton acceptor to the O-H group of H₂O. In complex 2, PAm interacts with the hydroxyl hydrogen of H₂O through its nitrogen atom, forming an O-H...N contact. The PAm in

this case serves as a proton acceptor. Complex 3 has PAm serving as the proton donor through its acetylenic hydrogen atom to the O atom of H₂O, with a $\equiv\text{C}-\text{H}\cdots\text{O}$ contact.

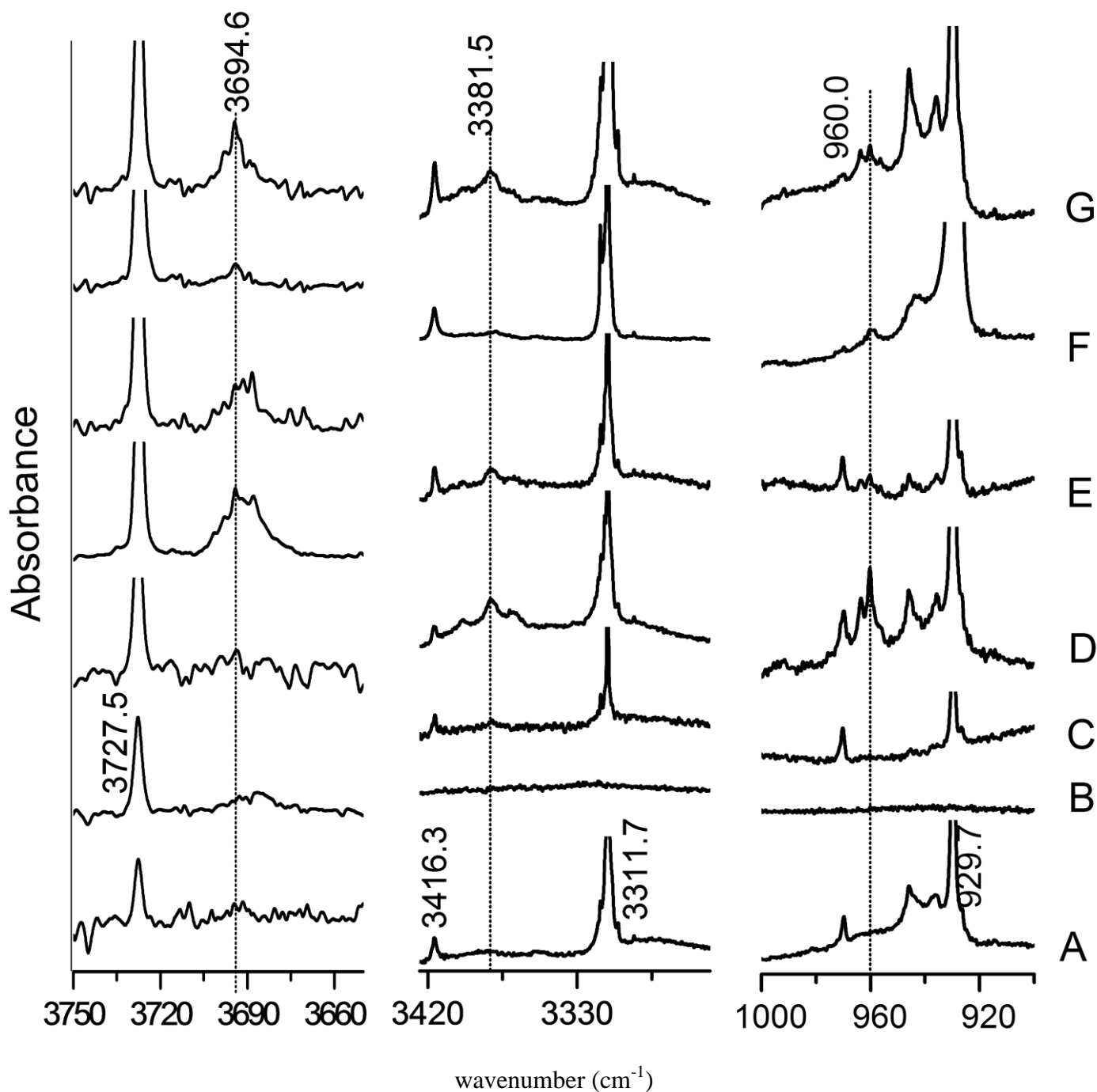
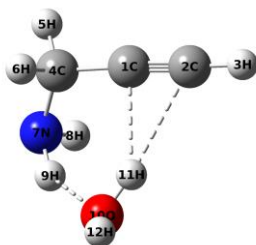


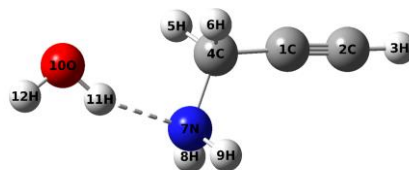
Fig. 5.5. Infrared spectra of PAm : H₂O : N₂ in the regions 3750-3650, 3425-3250 and 1000-900 cm⁻¹ annealed at 27 K (A) 1: 0: 1000 (B) 0: 0.2: 1000 (C) 0.5: 0.2: 1000 (D) 1: 0.8: 1000 (E) 1: 0.2: 1000 (F) 2.5: 0.2: 1000 and (G) 2.5: 0.2: 1000. Spectrum F is recorded at 12 K.

ggPAm-H₂O

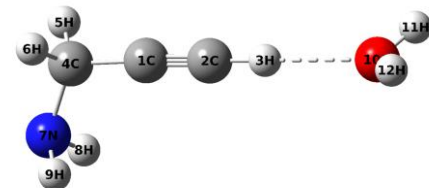
Complex 1 (-6.0/-4.4/-4.5)



Complex 2 (-7.9/-5.7/-6.3)

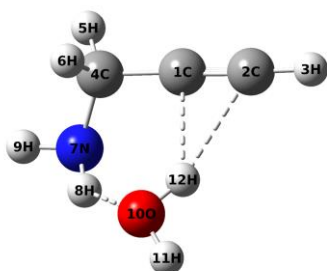


Complex 3 (-3.4/-2.4/-2.4)

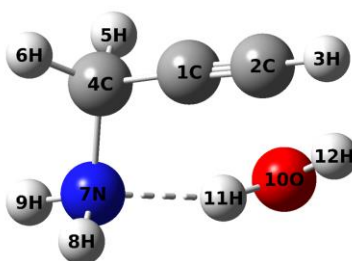


gtPAm-H₂O

Complex 1 (-6.2/-4.5/-4.6)



Complex 2 (-8.0/-5.9/-6.4)



Complex 3 (-3.3/-2.3/-2.3)

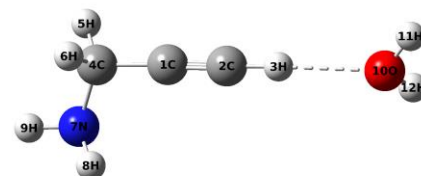


Fig. 5.6. Optimized structures of various hydrogen bonded complexes of gg and gt PAm with H₂O and their uncorrected/ZPE corrected/BSSE corrected interaction energies, computed at MP2/aug-cc-pVDZ level.

Some of the important geometrical parameters for the different ggPAm-H₂O complex computed at the MP2/aug-cc-pVDZ level have been listed in Table 5.5.

The uncorrected, zero-point energy corrected and BSSE corrected interaction energies have been calculated for ggPAm-H₂O complexes at the M06-2X and MP2 methods employing 6-311++G(d,p) and aug-cc-pVDZ basis sets. Single point energy calculations were also performed at the MP2/aug-cc-pVTZ and MP2/aug-cc-pVQZ levels, using the optimized geometries of

ggPAm-H₂O complexes at the MP2/aug-cc-pVDZ level, to compute the uncorrected interaction energies at the MP2/CBS. In addition, single point energy calculations were done at the CCSD(T)/aug-cc-pVDZ level using the optimized geometries of ggPAm-H₂O complexes at the MP2/aug-cc-pVDZ level, which further led to obtaining interaction energies at the CCSD(T)/CBS. Table 5.6 presents the interaction energies of all the complexes at various levels of theory employed. It can be seen that complex 2 bound by an O-H...N contact was the most stable amongst all the ggPAm-H₂O complexes and where PAm serves the role of a proton acceptor at the N atom.

This observation is at variance with the PA-H₂O complexes, where the structure corresponding to the O-H group of PA serving as the proton donor was the most stable.

Table 5.5. Some important geometrical parameters for different ggPAm-H₂O complexes computed at MP2/aug-cc-pVDZ level, showing bond lengths (in Å), bond angles and dihedral angles (in degrees).

ggPAm-H ₂ O	
Complex 1	
H ₉ O ₁₀	2.24
C ₁ H ₁₁	2.37
C ₂ H ₁₁	2.48
N ₇ H ₉ O ₁₀	144.7
C ₁ H ₁₁ O ₁₀	133.2
C ₂ H ₁₁ O ₁₀	159.5
C ₄ N ₇ H ₉ O ₁₀	-16.7
N ₇ H ₉ O ₁₀ H ₁₁	-17.6
Complex 2	
N ₇ H ₁₁	1.93
N ₇ H ₁₁ O ₁₀	157.1
C ₄ N ₇ H ₁₁ O ₁₀	0.0
Complex 3	
H ₃ O ₁₀	2.19
C ₂ H ₃ O ₁₀	179.9
C ₁ C ₂ H ₃ O ₁₀	-75.6

Table 5.6. Interaction energies RAW/ZPE/BSSE (in kcal/mol) for different PAm-H₂O complexes calculated at M06-2X, MP2 and CCSD(T) level using aug-cc-pVDZ basis set and CBS limit. CCSD(T) values are the uncorrected interaction energies obtained using single point energy calculations on geometries optimized at MP2/aug-cc-pVDZ level.

ggPA_m-H₂O							
	M06-2X		MP2			CCSD(T)	
	6-311++G(d,p)	aug-cc-pVDZ	6-311++G(d,p)	aug-cc-pVDZ	CBS	aug-cc-pVDZ	CBS
1	-6.7/-4.8/-6.2	-6.2/-4.6/-5.7	-5.8/-4.2/-3.9	-6.0/-4.4/-4.5	-5.5	-5.8	-5.3
2	-8.3/-6.0/-7.6	-7.5/-5.4/-6.9	-7.7/-5.7/-6.0	-7.9/-5.7/-6.3	-7.1	-7.7	-6.9
3	-3.6/-2.2/-2.9 ^a	-2.9/-1.8/-2.5 ^a	-3.7/-2.1/-2.2	-3.4/-2.4/-2.4	-2.6	-3.5	-2.7

^aThe tight convergence criteria has been relaxed while optimizing this geometry.

5.7. Discussion- PAm-H₂O Complexes

5.7.1. Vibrational Assignments

a) NH₂ wag. in PAm subunit in complex: Experimentally, this mode in the complex was observed at 960.0 cm⁻¹ which amounts to a blue shift of 30.3 cm⁻¹ from the corresponding mode in uncomplexed PAm which occurs at 929.7 cm⁻¹ (Table 5.7). This mode was computed to occur at 927.8 cm⁻¹ in complex 1, which corresponds to a red shift of 1.9 cm⁻¹. In complex 2, this mode occurs at 958.2 cm⁻¹, which amounts to a blue shift of 28.5 cm⁻¹. In complex 3, the same mode is computed to occur at 936.9 cm⁻¹ which is a blue shift of 7.2 cm⁻¹. Clearly the computed wavenumber for complex 2 is in excellent agreement with the experimental observation, implying the formation of complex 2 in matrix.

b) O-H stretch in H₂O subunit in complex: The features occurring at 3694.6 and 3381.5 cm⁻¹ were observed experimentally in the O-H stretch spectral region when both PAm and H₂O were codeposited. These features showed red shift of 32.9 and 346.0 cm⁻¹, respectively, calculated from the O-H asymmetric stretch at 3727.5 cm⁻¹ in uncomplexed H₂O.

Table 5.7. Experimental (in N₂ matrix) and computed scaled wavenumbers (cm⁻¹) at MP2/aug-cc-pVDZ level for different vibrational modes in PAm-H₂O complexes. Scaling factors used are 0.9508 for NH₂ and ≡C-H stretch, 0.9608 for NH₂ wag., 0.9465 for O-H stretch and 0.9588 for O-D stretch. Computed IR intensities (km/mole) are given in brackets.

Experimental		Computed scaled wavenumbers (cm ⁻¹)				
Monomers	Complex	Monomer	Complexes			Assignment
PAm		PAm	Complex 1	Complex 2	Complex 3	Assignment
3416.3	-	3416.5 (5)	3416.0 (26) -0.5 ^a	3412.8 (9) -3.7	3412.9 (4) -3.6	NH ₂ asym. st.
-	-	3325.6 (1)	3322.1 (20) -3.5	3321.9 (13) -3.7	3323.0 (1) -2.6	NH ₂ sym. st.
3311.7	-	3312.3 (55)	3306.6 (59) -5.7	3312.3 (62) 0.0	3254.6 (248) -57.7	≡C-H st.
929.7	960.0 +30.3	929.7 (95)	927.8 (118) -1.9	958.2 (121) +28.5	936.9 (84) +7.2	NH ₂ wag
H ₂ O	Complex	H ₂ O	Complex 1	Complex 2	Complex 3	Assignment
3727.5		3727.6 (67)	3694.1 (129) -33.5		3723.3 (78) -4.3	O-H asym. st.
3635.0		3600.4 (4)	3538.6 (102) -61.8		3598.0 (10) -2.4	O-H sym. st.
	3694.6 -32.9			3684.9 (93) -42.7 ^b		non-bonded O-H st.
	3381.5 -346.0			3351.6 (592) -376.0 ^b		bonded O-H st.
D ₂ O	Complex	D ₂ O	Complex 1	Complex 2	Complex 3	Assignment
2765.9		2766.0 (40)	2738.8 (86) -27.2		2763.0 (45) -3.0	O-D asym. st.
2655.7		2629.7 (3)	2587.8 (43) -41.9		2628.0 (8) -1.7	O-D sym. st.
	2729.0 -36.9			2722.9 (77) -43.1 ^b		non-bonded O-D st.
	2490.3 -275.6			2462.1 (301) -303.9 ^b		bonded O-D st.

^aShifts are calculated as $\Delta v = v(\text{complex}) - v(\text{monomer})$.

^bShifts for bonded and non-bonded O-H and O-D st. in PAm-H₂O and PAm-D₂O complex 2, calculated from the asym. st. of O-H and O-D in monomer, respectively.

In complex 1, the O-H asymmetric stretch was computed to occur at 3694.1 cm⁻¹ with a red shift of 33.5 cm⁻¹ and the symmetric stretch at 3538.6 cm⁻¹, red-shifted by 61.8 cm⁻¹.

In complex 2, the non-bonded O-H stretch was computed at 3684.9 cm^{-1} , manifesting a red shift of 42.7 cm^{-1} relative to asymmetric stretch of uncomplexed H_2O . The bonded O-H stretch in the complex was computed at 3351.6 cm^{-1} , amounting to a red shift of 376.0 cm^{-1} from antisymmetric O-H stretch in uncomplexed H_2O . On complex formation, the O-H vibrations in water occurred as bonded and non-bonded O-H stretches in complex 2, as opposed to the antisymmetric and symmetric stretches in free H_2O .

The computed vibrational frequencies for these two modes are in good agreement with the experimental shifts of 32.9 and 346.0 cm^{-1} , thus confirming that complex 2 is probably observed in the matrix.

The O-H asymmetric and symmetric stretches in complex 3 were only slightly affected on complex formation. The O-H asymmetric stretch in was computed to occur at 3723.3 cm^{-1} with a red shift of 4.3 cm^{-1} from the same mode in uncomplexed H_2O (3727.6 cm^{-1}). Similarly, the O-H symmetric stretch in H_2O subunit in complex was computed at 3598.0 cm^{-1} with a red shift of 2.4 cm^{-1} from the symmetric stretch in uncomplexed H_2O . It may be noted that in complexes 1 and 3, the symmetric and antisymmetric modes of vibration in H_2O are retained in the complex, in contrast to what was computed for complex 2.

Thus, it was clear that the experimental features, 3694.6 , 3381.5 and 960.0 cm^{-1} , together with computations unambiguously indicate to the formation of complex 2 in the matrix.

c) O-D stretch in D_2O subunit in PAm- D_2O complex: In the co-deposition experiments, product features were observed at 2729.0 and 2490.3 cm^{-1} , red-shifted by 36.9 and 275.6 cm^{-1} , respectively from the asymmetric O-D stretch in uncomplexed D_2O (2765.9 cm^{-1}). Complex 1 was computed to show features at 2738.8 and 2587.8 cm^{-1} for the asymmetric and symmetric O-D stretch, respectively. In complex 2, non-bonded O-D stretch was computed at 2722.9 cm^{-1} with

a red shift of 43.1 cm^{-1} and bonded O-D stretch at 2462.1 cm^{-1} with red shift of 303.9 cm^{-1} . In complex 3, computed feature at 2763.0 cm^{-1} showed red shift of 3.0 cm^{-1} from the asymmetric O-D stretch while feature at 2628.0 cm^{-1} showed red shift of 1.7 cm^{-1} from the symmetric O-D stretch.

It can be inferred that in PAm-D₂O experiments, computed features for complex 2 matched with the experimental results, thus further confirming our assignments made for the PAm-H₂O complex.

5.7.2. AIM Analysis

The electron density, $\rho_b(r_c)$ and the Laplacian values, $\nabla^2\rho_b(r_c)$ computed at MP2/aug-cc-pVDZ level of theory, were in the range of hydrogen bonded interaction (0.002-0.034 for $\rho_b(r_c)$ and 0.024-0.139 for $\nabla^2\rho_b(r_c)$ as proposed by Koch and Popelier, listed in Table 5.8.

Table 5.8. AIM analysis showing electron density $\rho_b(r_c)$, laplacian $\nabla^2\rho_b(r_c)$, local electronic kinetic energy density $G(r_c)$, local electronic potential energy density $V(r_c)$ values, in atomic units, for different hydrogen-bonded interactions in ggPA_m-H₂O complexes computed at MP2/aug-cc-pVDZ level. The hydrogen bond energy E_{HB} for each interaction and Total E_{HB} values, are given in kcal/mol.

PA _m -H ₂ O							
Complexes	Interactions	$\rho_b(r_c)$	$\nabla^2\rho_b(r_c)$	$G(r_c)$	$V(r_c)$	E_{HB}	Total E_{HB}
Complex 1	N-H...O	0.0140	0.0444	0.0098	-0.0084	-2.6	-5.0
	O-H... π	0.0134	0.0389	0.0087	-0.0076	-2.4	
Complex 2	O-H...N	0.0306	0.0946	0.0244	-0.0251	-7.9	-7.9
Complex 3	$\equiv\text{C-H}\cdots\text{O}$	0.0141	0.0478	0.0103	-0.0087	-2.7	-2.7

Complex 1 was stabilized by dual contacts: a N-H...O with E_{HB} value of -2.6 kcal/mol and an O-H... π interaction with E_{HB} value of -2.4 kcal/mol. In the global minimum PAm-H₂O complex 2, the O-H...N interaction was relatively strong with E_{HB} value of -7.9 kcal/mol. In complex 3, the E_{HB} value of -2.7 kcal/mol was computed for the $\equiv\text{C-H}\cdots\text{O}$ interaction. The

electron density topologies indicating the bond and ring critical points as well as bond paths deduced from AIM analysis on ggPAm-H₂O complexes at the MP2/aug-cc-pVDZ level, have been shown in Fig. 5.7.

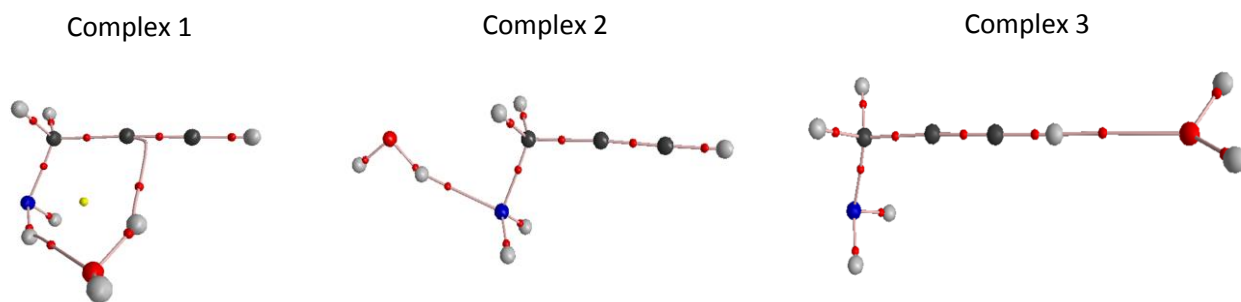


Fig. 5.7. Electron density topologies for various ggPAm-H₂O complexes at MP2/aug-cc-pVDZ level.

5.7.3. NBO Analysis

NBO analysis was performed for ggPAm-H₂O complexes at the MP2/aug-cc-pVDZ level, shown in Table 5.9. It was found that the complex 2 has the largest value for second order perturbation energy, E(2), 14.9 kcal/mol with the electron delocalization from the lone pair on nitrogen to the anti-bonding σ^* orbital of O-H bond of H₂O.

Table 5.9. NBO analysis on ggPAm-H₂O complexes, showing the significant interactions between the donor and acceptor orbitals and their corresponding second order perturbation energies E(2) in kcal/mol, difference in energy between acceptor and donor orbitals E(j)-E(i) and F(i,j) values given in atomic units, computed at MP2/aug-cc-pVDZ level.

	Donor orbital	Acceptor orbital	E(2)	E(j)-E(i)	F(i,j)
Complex 1	$\pi_2C_1C_2$	$\sigma^*O_{10}H_{11}$	3.1	1.2	0.054
	n_2O_{10}	$\sigma^*N_7H_9$	3.1	1.4	0.059
Complex 2	n_1N_7	$\sigma^*O_{10}H_{11}$	14.9	1.3	0.123
Complex 3	n_2O_{10}	$\sigma^*C_2H_3$	6.0	1.6	0.089

In complex 1, the π electron cloud of PAm donates the electron density to the σ^* orbital of O-H bond of H₂O, for the O-H... π interaction having E(2) as 3.1 kcal/mol. In addition, the N-

H \cdots O interaction in complex 1, donates electron density from the lone pair on oxygen of H₂O to the σ^* orbital of N-H bond in PAm with the delocalization energy of 3.1 kcal/mol. Complex 3 with E(2) value of 6.0 kcal/mol, donates electron density from the lone pair on oxygen of H₂O to the σ^* orbital of acetylenic C-H bond in PAm.

Thus, from NBO analysis, we found that it was the greater electron delocalization of lone pair on nitrogen of PAm to the σ^* orbital in O-H bond of H₂O, in complex 2, resulting in the formation of strong O-H \cdots N hydrogen bond, as located by the respective bond critical point in AIM results.

5.7.4. LMO-EDA Analysis

The LMO-EDA calculation was performed at MP2/aug-cc-pVDZ level to evaluate the contribution of different energy components towards the strength of hydrogen bonded interactions in ggPAm-H₂O complexes. The total interaction energy for each of the PAm-H₂O complexes, ΔE_{MP2} (or E_{TOTAL}) was decomposed into electrostatic energy ΔE_{es} , exchange energy ΔE_{ex} , repulsion energy ΔE_{rep} , polarization energy ΔE_{pol} and dispersion energy ΔE_{disp} , and results are listed in Table 5.10. It was found that complex 2 has the largest E_{TOTAL} value of -8.1 kcal/mol among the optimized PAm-H₂O complexes and the largest stabilization contribution of about 44%, was provided by exchange energy ($\Delta E_{\text{ex}} = -16.3$ kcal/mol), followed by 34% stabilization from electrostatic energy $\Delta E_{\text{es}} = -12.7$ kcal/mol. Polarization and dispersion energy make minor contribution of 12% and 10%, respectively, to E_{TOTAL} .

Similarly, complex 1 with total interaction energy of -6.1 kcal/mol has greater contribution from exchange (-12.0 kcal/mol) and electrostatic energy (-8.6 kcal/mol), while minor contribution from polarization and dispersion energy. Complex 3 with value of -3.4 kcal/mol for total interaction energy, has greater contribution from exchange and electrostatic

components (38%), while polarization and dispersion plays minor role in its stabilization. Thus, in all ggPAm-H₂O complexes, exchange and electrostatic energy contributes significantly in stabilization of complexes.

Table 5.10. LMOEDA analysis for ggPAm-H₂O complexes computed at MP2/aug-cc-pVDZ level. All energies are given in kcal/mol.

Complex	ΔE_{es}	ΔE_{ex}	ΔE_{rep}	ΔE_{pol}	ΔE_{disp}	ΔE_{MP2} (or E_{TOTAL})
Complex 1	-8.6 (32%)	-12.0 (44%)	20.9	-2.8 (11%)	-3.6 (13%)	-6.1
Complex 2	-12.7 (34%)	-16.3 (44%)	29.2	-4.6 (12%)	-3.6 (10%)	-8.1
Complex3	-4.2 (38%)	-4.2 (38%)	7.6	-1.4 (13%)	-1.2 (11%)	-3.4

5.7.5. Comparison of PAm-H₂O Complex studies with PA-H₂O system

In ggPAm-H₂O complexes, complex 2 having an O-H...N interaction was computed to be the global minimum with BSSE corrected interaction energy of -6.3 kcal/mol at MP2/aug-cc-pVDZ level. The local minimum structure ggPAm-H₂O complex 1 having a N-H...O and an O-H... π interaction, with -4.5 kcal/mol interaction energy, was indeed a global minimum for the gPA-H₂O as the weak N-H...O interaction was replaced by a strong O-H...O interaction for gPA-H₂O system. Thus, in co-deposition experiments of PAm and H₂O, complex 2 was experimentally observed, being computed as the global minimum.

We have also compared the geometrical parameters of both ggPAm-H₂O and gPA-H₂O complexes having dual contacts. The O...H bond length was longer with a value of 2.24 Å for ggPAm-H₂O complex 1, relative to 1.95 Å in gPA-H₂O complex, indicating to the weaker N-H...O interaction in ggPAm-H₂O complex. The N-H...O bond angle in ggPAm-H₂O complex 1 was 144.7°, while the O-H...O bond angle in gPA-H₂O was 154.0°. The O-H... π interaction is

slightly strong in ggPAm-H₂O complex with values of 2.37 and 2.48 Å for H...C, compared to 2.45 and 2.56 Å for H...C in gPA-H₂O complex.

In addition, from the AIM analysis at MP2/aug-cc-pVDZ level, it was found that in ggPAm-H₂O complex 1, the N-H...O interaction was much weaker with E_{HB} value of -2.6 kcal/mol, than O-H...O interaction with E_{HB} value of -6.1 kcal/mol in similar gPA-H₂O complex, while the E_{HB} value for the O-H...π interaction in both systems was nearly same. In complex 2 of ggPAm-H₂O system, the O-H...N interaction was stronger than the O-H...O interaction in similar complex of gPA-H₂O system, with their E_{HB} values of -7.9 and -6.4 kcal/mol, respectively. It can be inferred from this data that in the complex 2 of both systems, PAm/PA serving as the proton acceptor to the O-H group of H₂O, the basicity of PAm was greater as compared to the PA subunit in the complex. Further, the NBO analysis on complex 2 of both systems was consistent with the AIM results.

5.8. Results- PAm-MeOH Complexes

5.8.1. Experimental

We also conducted matrix isolation infrared experiments where PAm and MeOH were codeposited in a N₂ matrix. Fig. 5.8 (trace 'a') showed the matrix isolated infrared spectrum of PAm in N₂ matrix with sample-to-matrix ratio of 1:1000, in which features occurring at 3416.3, 3311.7 and 929.7 cm⁻¹ corresponds to N-H asymmetric stretch, ≡C-H stretch and NH₂ wagging mode, respectively in PAm monomer.

Trace 'b' of Fig. 5.8, showed peaks located at 3664.2 and 1034.6 cm⁻¹ for the O-H and C-O stretch, respectively in MeOH monomer. The feature occurring at 3727.5 cm⁻¹ corresponding to the O-H asymmetric stretch in H₂O, was also present in our experiments.

In experiments where both PAm and MeOH were codeposited, we observed new product bands at 3346.8, 1053.0 and 965.4 cm^{-1} .

These bands, which were observed only in the presence of both submolecules, increased in intensity when the concentration of the submolecules PAm and MeOH, were varied, implying that these product features were due to a complex involving both PAm and MeOH.

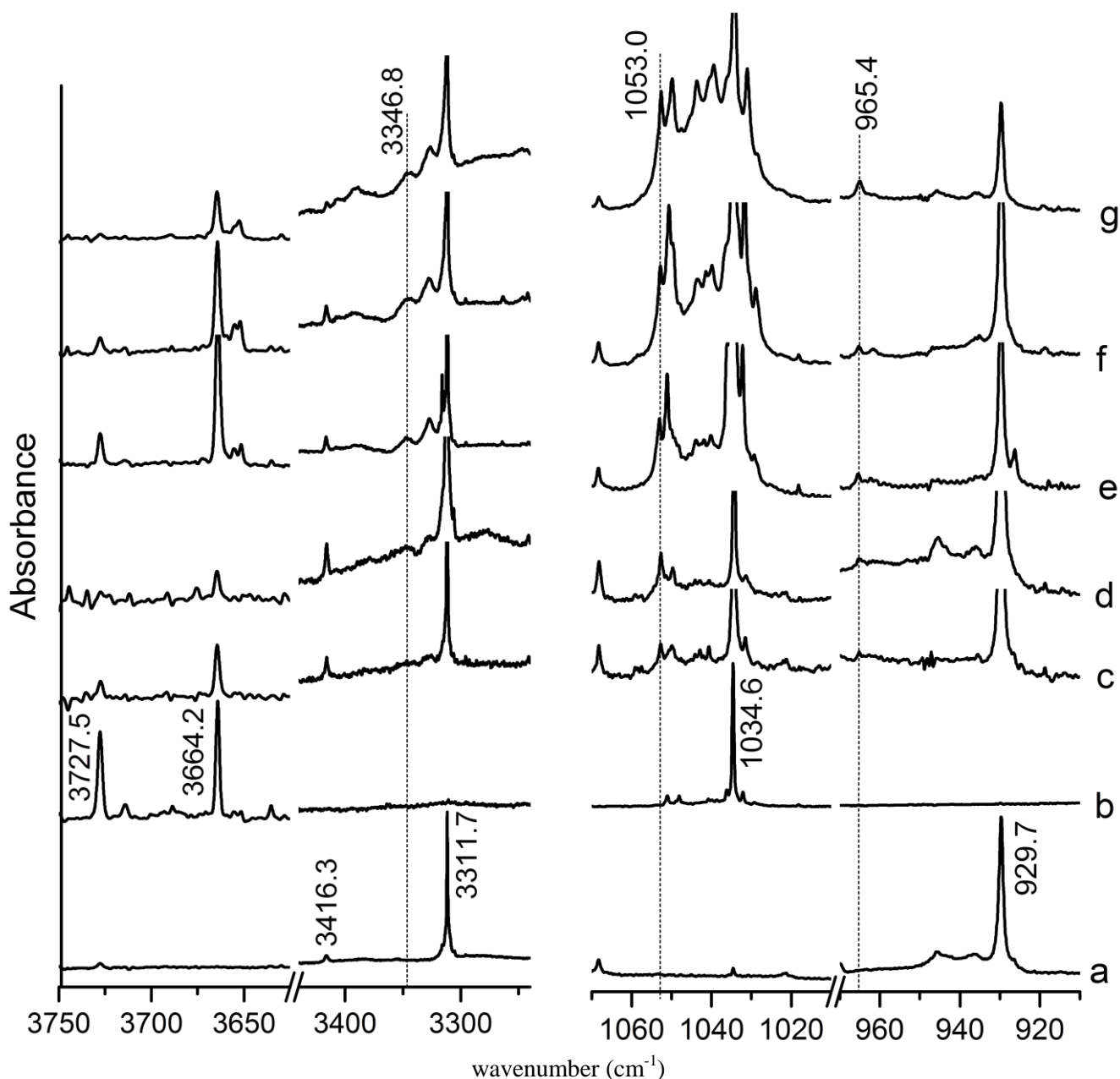


Fig. 5.8. Matrix isolation infrared spectra in the spectral range 3750-3625, 3440-3240, 1070-1010 and 970-910 cm^{-1} , for PAm:MeOH: N_2 a) 1.0:0.0:1000 annealed b) 0.0:1.5:1000 annealed c) 0.5:1.5:1000 annealed d) 1.0:1.5:1000 annealed e) 0.5:3.0:1000 annealed f) 1.0:3.0:1000 at 12 K and g) 1.0:3.0:1000 annealed.

5.8.2. Computational

Structures of different ggPAM-MeOH complexes were optimized at the MP2/aug-cc-pVDZ as shown in Fig. 5.9. Complex 1 was bound by dual interactions, one a N-H...O interaction in which the hydrogen atom of NH₂ group serves as a proton donor to the oxygen of MeOH and second, an O-H... π interaction with hydroxyl hydrogen of MeOH serving as proton donor to the acetylenic π cloud of PAM. In complex 2, PAM serves as a proton acceptor through its N atom, to the hydroxyl hydrogen of MeOH, forming an O-H...N interaction. Complex 3 involves a \equiv C-H...O interaction between the acetylenic hydrogen of PAM and the oxygen atom of MeOH.

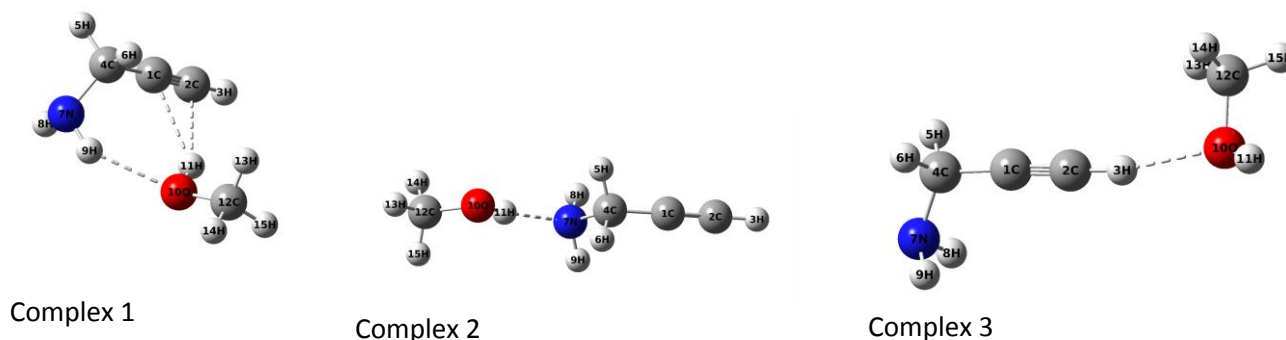


Fig. 5.9. Optimized geometries for ggPAM-MeOH complexes at MP2/aug-cc-pVDZ level.

Interaction energies were calculated for the ggPAM-MeOH complexes at M06-2X and MP2 employing 6-311++G(d,p) and aug-cc-pVDZ basis sets, as listed in Table 5.11. Single point energy calculation were performed at CCSD(T)/aug-cc-pVDZ level using the optimized geometries of complexes at the MP2/aug-cc-pVDZ level, which were further used to deduce the interaction energies at the MP2 and CCSD(T) methods using CBS limit. It was found that complex 2 was computed to be the most stable among all ggPAM-MeOH complexes with BSSE corrected interaction energy of -6.4 kcal/mol at MP2/aug-cc-pVDZ level.

Table 5.11. Interaction energies (Raw/ZPC/BSSE corrected) in kcal/mol for PAm-MeOH complexes at different levels of theory.

	M06-2X		MP2			CCSD(T)	
	6-311++G(d,p)	aug-cc-pVDZ	6-311++G(d,p)	aug-cc-pVDZ	CBS	aug-cc-pVDZ	CBS
Complex 1	-6.9/-5.6/-6.4	-6.7/-5.4/-6.1	-6.2/-5.2/-4.3	-6.9/-5.8/-4.9	-6.0	-6.7	-5.8
Complex 2	-8.1/-6.7/-7.4	-7.4/-6.1/-6.8	-7.8/-6.5/-6.1	-8.2/-6.8/-6.4	-7.3	-8.0	-7.1
Complex 3	-3.8/-2.9/-3.4 ^a	-3.4/-2.6/-3.0 ^a	-4.0/-2.8/-2.6	-4.1/-3.3/-2.9	-3.2	-4.1	-3.1

^aThe tight convergence criteria has been relaxed while optimizing this geometry.

Some important geometrical parameters for the hydrogen bond lengths, bond angles and dihedral angles for ggPAm-MeOH computed at the MP2/aug-cc-pVDZ level, have been shown in Table 5.12.

Table 5.12. Some important geometrical parameters for different ggPAm-MeOH complexes computed at MP2/aug-cc-pVDZ level, showing bond lengths (in Å), bond angles and dihedral angles (in degrees).

ggPAm-MeOH		
Complex 1	H ₉ O ₁₀	2.24
	C ₁ H ₁₁	2.36
	C ₂ H ₁₁	2.45
	N ₇ H ₉ O ₁₀	145.7
	C ₁ H ₁₁ O ₁₀	134.6
	C ₂ H ₁₁ O ₁₀	164.2
	C ₄ N ₇ H ₉ O ₁₀	-10.7
	N ₇ H ₉ O ₁₀ H ₁₁	-33.7
Complex 2	N ₇ H ₁₁	1.91
	N ₇ H ₁₁ O ₁₀	161.5
	C ₄ N ₇ H ₁₁ O ₁₀	-0.0
Complex 3	H ₃ O ₁₀	2.13
	C ₂ H ₃ O ₁₀	167.4
	C ₁ C ₂ H ₃ O ₁₀	-27.8

5.9. Discussion- PAm-MeOH Complexes

5.9.1. Vibrational Assignments

The experimentally observed features occurring at 3346.8, 1053.0 and 965.4 cm⁻¹ as shown in Fig. 5.8, were assigned to the computed features for ggPAm-MeOH complexes at

MP2/aug-cc-pVDZ level. In the PAm subunit in complex, NH₂ wagging mode was computed at 929.7 cm⁻¹ in complex 1, 958.0 cm⁻¹ in complex 2 and 936.1 cm⁻¹ in complex 3, listed in Table 5.13. The experimental feature 965.4 cm⁻¹, blue shifted by 35.7 cm⁻¹ from the same mode in uncomplexed PAm occurring at 929.7 cm⁻¹, matches closely with the computed blue shift of 28.3 cm⁻¹ for complex 2.

Table 5.13. Experimental (in N₂ matrix) and computed scaled wavenumbers (cm⁻¹) at MP2/aug-cc-pVDZ level for different vibrational modes in PAm-MeOH complexes. Scaling factors used are 0.9508 for NH₂ and ≡C-H stretch, 0.9608 for NH₂ wag., while for MeOH subunit: 0.9540 for O-H stretch and 0.9920 for C-O stretch. Computed IR intensities (km/mole) are given in brackets. Scaling factors for O-D stretch is 0.9668.

Experimental		Computed scaled wavenumbers (cm ⁻¹)				
Monomers	Complex	Monomer	Complexes			Assignment
PAm		PAm	Complex 1	Complex 2	Complex 3	
3416.3	-	3416.5 (5)	3407.4 (29) -9.1 ^a	3412.4 (10) -4.1	3413.0 (5) -3.5	NH ₂ asym. st.
-	-	3325.6 (1)	3308.0 (39) -17.6	3321.4 (16) -4.2	3323.0 (1) -2.6	NH ₂ sym. st.
3311.7	-	3312.3 (55)	3305.1 (53) -7.2	3312.1 (65) -0.2	3229.8 (289) -82.5	≡C-H st.
929.7	965.4 +35.7	929.7 (95)	929.7 (108) 0.0	958.0 (125) +28.3	936.1 (84) +6.4	NH ₂ wag
<hr/>						
MeOH	Complex	MeOH	Complex 1	Complex 2	Complex 3	Assignment
3664.2	3346.8 -317.4	3664.2 (34)	3579.3 (180) -84.9	3379.9 (792) -284.3	3660.9 (43) -3.3	O-H st.
1034.6	1053.0 +18.4	1034.6 (112)	1038.1 (89) +3.5	1058.0 (100) +23.4	1027.6 (105) -7.0	C-O st.
<hr/>						
CD ₃ OD	Complex	CD ₃ OD	Complex 1	Complex 2	Complex 3	Assignment
2704.0	2475.4 -228.6	2704.1 (22)	2641.1 (99) -63.0	2497.6 (441) -206.5	2701.7 (28) -2.4	O-D st.
981.3	987.7 +6.4	978.1 (34)	978.5 (38) +0.4	985.1 (92) +7.0	973.4 (36) -4.7	C-O st.

^aShifts are calculated as $\Delta v = v(\text{complex}) - v(\text{monomer})$.

For the MeOH subunit in the complex, the O-H stretch was computed to occur at 3579.3 cm⁻¹ for complex 1 with red shift of 84.9 cm⁻¹, at 3379.9 cm⁻¹ for complex 2 with large red shift of 284.3 cm⁻¹ and at 3660.9 cm⁻¹ for complex 3 with red shift of 3.3 cm⁻¹. Clearly, the feature

observed in experiments at 3346.8 cm^{-1} showing a large red shift of 317.4 cm^{-1} was unambiguously assigned to the O-H stretch upon formation of complex 2 in matrix. Similarly, the experimental feature at 1053.0 cm^{-1} in the C-O stretch region, blue shifted by 18.4 cm^{-1} , was assigned to the computed feature 1058.0 cm^{-1} for complex 2 with a blue shift of 23.4 cm^{-1} .

Thus, it was inferred that ggPAm-MeOH complex 2 was being trapped in our experiments.

To further confirm these assignments, we did few experiments in which CD_3OD was deposited with PAm in N_2 matrix. The O-D stretch was observed at 2704.0 cm^{-1} and C-O stretch at 981.3 cm^{-1} in CD_3OD monomer. The product bands on codeposition of PAm and CD_3OD were observed at 2475.4 cm^{-1} with a red shift of 228.6 cm^{-1} from the O-D stretch (2704.0 cm^{-1}) and 987.7 cm^{-1} , blue shifted by 6.4 cm^{-1} from the C-O stretch in uncomplexed CD_3OD .

Computations indicated O-D stretch in complex 1 to occur at 2641.1 cm^{-1} , in complex 2 at 2497.6 cm^{-1} and in complex 3 at 2701.7 cm^{-1} . The experimentally observed large shift of 228.6 cm^{-1} was in agreement to the computed red shift of 206.5 cm^{-1} for complex 2. Similarly, in the C-O stretch of CD_3OD subunit, experimental feature 987.7 cm^{-1} was assigned to the computed feature for complex 2 for same mode occurring at 985.1 cm^{-1} . Thus, experimental results together with computations clearly indicate to the formation of complex 2 in matrix.

5.9.2. AIM Analysis

AIM analysis was performed for the optimized structures of ggPAm-MeOH at the MP2/aug-cc-pVDZ level as shown in Fig. 5.10, indicating the bond and ring critical points, in order to identify the nature of hydrogen bonded interaction. The values of electron density, Laplacian at bond critical points for ggPAm-MeOH complexes have been provided in Table 5.14, which were further used to deduce the values of $G(r_c)$, $V(r_c)$ and E_{HB} . Complex 1 was

bound by an N-H...O and an O-H... π interaction with E_{HB} values of -3.1 and -2.7 kcal/mol, respectively, thus, forming a cyclic complex. Complex 2 showed an O-H...N interaction with E_{HB} of -8.5 kcal/mol. In complex 3, the $\equiv\text{C-H}\cdots\text{O}$ interaction was -3.5 kcal/mol. Thus, we found that the O-H...N interaction in complex 2 was much stronger than other interactions among ggPAm-MeOH complexes.

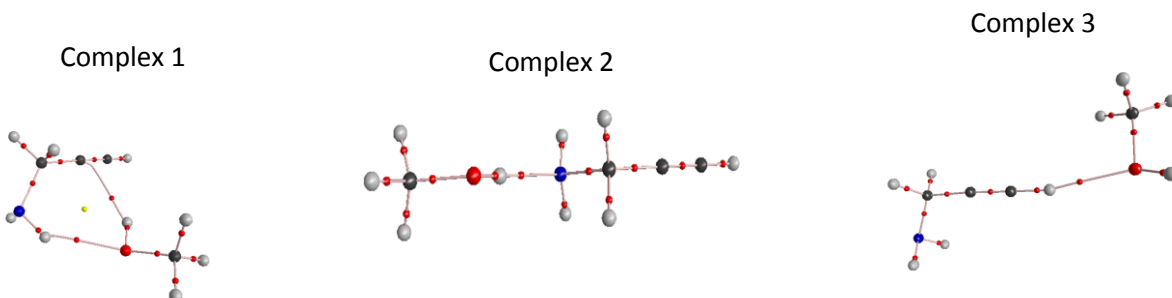


Fig. 5.10. AIM analysis of ggPAm-MeOH complexes at the MP2/aug-cc-pVDZ level.

Table 5.14. AIM analysis for PAm-MeOH complexes at MP2/aug-cc-pVDZ level. E_{HB} and E_{T} given in kcal/mol. The values of $\rho_{\text{b}}(r_{\text{c}})$, Laplacian, $G(r_{\text{c}})$ and $V(r_{\text{c}})$ are given in atomic units.

	Interaction	$\rho_{\text{b}}(r_{\text{c}})$	Laplacian	$G(r_{\text{c}})$	$V(r_{\text{c}})$	E_{HB}	E_{T}
Complex 1	N-H...O	0.0164	0.0444	0.0100	-0.0098	-3.1	-5.8
	O-H... π	0.0147	0.0417	0.0090	-0.0086	-2.7	
Complex 2	O-H...N	0.0324	0.0981	0.0260	-0.0271	-8.5	-8.5
Complex 3	$\equiv\text{C-H}\cdots\text{O}$	0.0171	0.0547	0.0120	-0.0111	-3.5	-3.5

5.9.3. NBO Analysis

Table 5.15 presents the NBO analysis for the PAm-MeOH complexes at the MP2/aug-cc-pVDZ level. In the global minimum complex 2, a greater value 17.7 kcal/mol, of delocalization energy $E(2)$ corresponded to the interaction between lone pair on N of PAm and the antibonding σ^* orbital of O-H group in MeOH. This implies greater electron donation and greater strength of O-H...N interaction in complex 2.

Table 5.15. NBO analysis for PAm-MeOH at MP2/aug-cc-pVDZ level.

	Donor NBO (i)	Acceptor NBO (i)	E(2) kcal/mol	E(j)-E(i) a.u.	F(i,j) a.u.
Complex 1	$\pi 1$ C ₁ C ₂	σ^* O ₁₀ H ₁₁	0.1	1.1	0.011
	$\pi 2$ C ₁ C ₂	σ^* O ₁₀ H ₁₁	4.1	1.1	0.061
	n_1 O ₁₀	σ^* N ₇ H ₉	0.8	1.6	0.033
	n_2 O ₁₀	σ^* N ₇ H ₉	3.6	1.2	0.060
Complex 2	n_1 N ₇	σ^* O ₁₀ H ₁₁	17.7	1.3	0.135
Complex 3	n_1 O ₁₀	σ^* C ₂ H ₃	2.8	1.6	0.060
	n_2 O ₁₀	σ^* C ₂ H ₃	4.1	1.3	0.066

5.10. PAm-DEE Complexes

In the 1:1 hydrogen bonded complexes of PAm with H₂O and MeOH, it was found that the most stable structure involves an O-H...N interaction with PAm serving as a proton acceptor to both precursors. Another structure having a N-H...O and an O-H... π interaction, was located as local minimum in both these systems. In this section, we have studied the complexes of PAm with DEE in which the formation of an O-H... π interaction is completely suppressed. Two PAm-DEE structures were optimized as minima at the MP2/aug-cc-pVDZ level, one in which a N-H...O interaction was formed between the N-H bond of PAm and O atom of DEE, and other in which PAm interacts with O atom of DEE through its acetylenic H atom, forming a \equiv C-H...O interaction, as shown in Fig. 5.11. The most stable TTT conformation of DEE subunit has been used in both complexes. The interaction energies have been computed for these complexes and listed in Table 5.16.

It is found that the global minimum PAm-DEE complex has a N-H...O interaction in contrary to the O-H...O interaction present in the global minimum PA-DEE complex.

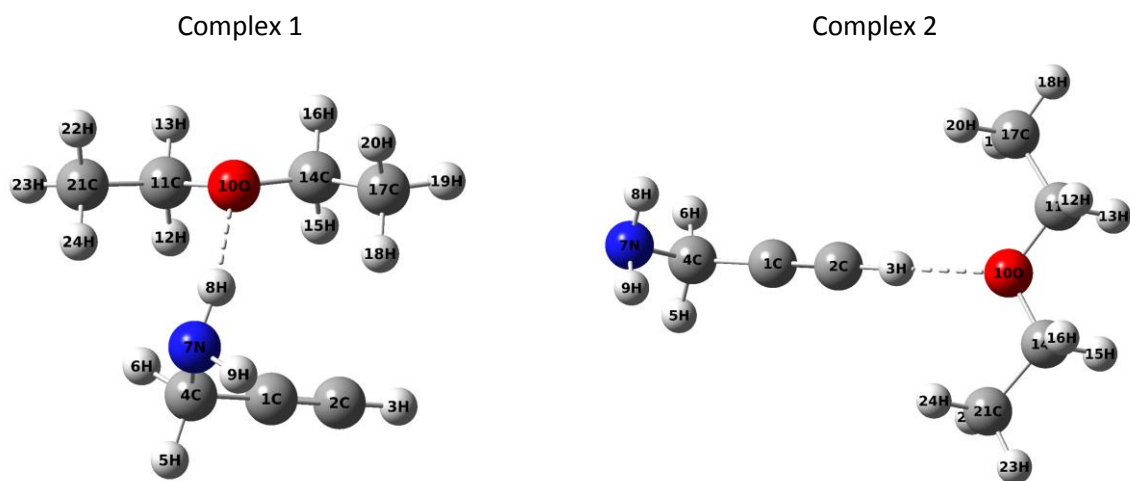


Fig. 5.11. Optimized structures of PAm-DEE complexes at the MP2/aug-cc-pVDZ level.

Table 5.16. Uncorrected/ZPE corrected/BSSE corrected interaction energies for PAm-DEE complexes computed at the MP2 level using 6-311++G(d,p) and aug-cc-pVDZ basis sets. Uncorrected interaction energies at CCSD(T)/aug-cc-pVDZ level have also been shown. All energy values are given in kcal/mol.

PAm-DEE complexes			
	MP2/6-311++G(d,p)	MP2/aug-cc-pVDZ	CCSD(T)/aug-cc-pVDZ
Complex 1	-7.2/-6.3/-4.2	-8.7/-7.8/-5.2	-8.2
Complex 2	-4.6/-3.6/-3.1	-5.4/-4.6/-3.6	-5.2

5.11. Conclusions

The conformational stability of ground state ggPAm over gtPAm was explored using NBO analysis. It was found that the remote and vicinal interactions play a deciding role in conformational landscape of PAm, consistent with results on PA conformations. Our matrix isolation infrared experiments showed the presence of ggPAm conformer, these features were corroborated with computations. We also attempt to trap the higher energy gtPAm form using

heated nozzle assembly and supersonic expansion experiments but did not observe any evidence for the higher energy conformer.

The 1:1 ggPAm-H₂O complex 2 was the most stable among the three computed structures at different levels of theory. In this complex, H₂O was the proton donor, where the O-H group of H₂O interacted with the lone pair of nitrogen in the NH₂ group of PAm. In our codeposition experiments of PAm and H₂O in N₂ matrix, features of complex 2 were observed. The convincing evidence was the large red shift of 346.0 cm⁻¹, experimentally in the bonded O-H stretch of H₂O subunit upon complex formation. The vibrational assignments were further confirmed through isotopic experiments using D₂O. AIM analysis revealed complex 2 being bound by a strong O-H...N interaction. There was a greater electron delocalization from lone pair on nitrogen of PAm to the σ*orbital of O-H in MeOH in complex 2. LMO-EDA results indicate exchange and electrostatic energy as the major contributors to the total interaction energy in PAm-H₂O complexes.

Matrix isolation infrared experiments were also performed with PAm and MeOH, in which the O-H and C-O stretch features in MeOH subunit corresponding to 1:1 complex, unambiguously point to the formation of complex, with the experimental shifts matching closely with the computed feature for complex 2. The complex 2 in PAm-MeOH was similar to complex 2 of PAm-H₂O. These assignments were confirmed through the matrix isolation experiments recorded, with codeposition of PAm and CD₃OD. Complex 2 bound by an O-H...N interaction, was computed as the global minimum among the three structures for ggPAm-MeOH complexes, at all levels of theory. It was the greater electron delocalization between lone pair of N of PAm and σ* orbital of O-H in MeOH.

Further, the structure having O-H...O interaction was computed as the global minimum for PA-DEE complex; while in the PAm-DEE complex, the global minimum was a similar looking structure involving a relatively weaker N-H...O interaction. In both these systems, the complex involving a $\equiv\text{C-H}\cdots\text{O}$ interaction was the local minimum. It was also found that the energy difference between the structures corresponding to the global and local minimum, was markedly different in the PA-DEE and PAm-DEE systems; it was 4.0 kcal/mol in case of PA-DEE system, while it was a mere 1.6 kcal/mol for PAm-DEE system.

It must also be recognized that in both PAm-H₂O and PAm-MeOH systems, the global minimum complex involving an O-H...N hydrogen bonded interaction in which PAm serves as the proton acceptor through its N atom, is experimentally observed. A similar complex, is however located as a less stable structure in the case of PA complexes with H₂O and MeOH. The experimentally observed and the computed global minimum complex for PA-H₂O and PA-MeOH systems, was the one having dual interactions, O-H...O with PA serving as the proton donor through its O-H group and a weaker O-H... π interaction. Therefore, relative stability of complexes changed with a change in -OH and -NH₂ group in propargyl system.

References

1. Verma, A. L.; Bernstein, H. J. Rotational Isomerism in Propargyl Amine studied by Raman Spectroscopy. *J. Chem. Soc. Faraday Trans 2* **1973**, *69*, 1586-1589.
2. Cervellati, R.; Caminati, W.; Esposti, C. D.; Mirri, A. M. Structure and Dipole Moment of Trans Propargyl Amine by Microwave Spectroscopy. *J. Mol. Spectrosc.* **1977**, *66*, 389-398.
3. Frisch, M. J.; Trucks, G. W.; Schlegel, H. B.; Scuseria, G. E.; Robb, M. A.; Cheeseman, J. R.; Scalmani, G.; Barone, V.; Mennucci, B.; Peterson, G. A.; *et al.* GAUSSIAN 09, Revision C.01, Gaussian Inc., Wallingford CT, **2010**.
4. Vincent, M. A.; Hillier, I. H. The Structure and Interaction Energies of the Weak Complexes of CHClF_2 and CHF_3 with HCCH : A Test of Density Functional Theory Methods. *Phys. Chem. Chem. Phys.* **2011**, *13*, 4388-4392.
5. Helgaker, T.; Klopper, W.; Koch, H.; Noga, J. Basis-Set Convergence of Correlated Calculations on Water. *J. Chem. Phys.* **1997**, *106*, 9639-9646.
6. Bettinger, H. F.; Kar, T.; Sánchez-García, E. Borazine and Benzene Homo- and Heterodimers. *J. Phys. Chem. A* **2009**, *113*, 3353-3359.
7. Su, P.; Li, H. Energy Decomposition Analysis of Covalent Bonds and Intermolecular Interactions. *J. Chem. Phys.* **2009**, *131*, 014102-15.
8. Schmidt, M. W.; Baldridge, K. K.; Boatz, J. A.; Elbert, S. T.; Gordon, M. S.; Jensen, J. H.; Koseki, S.; Matsunaga, N.; Nguyen, K. A.; Su, S.; *et al.* General Atomic and Molecular Electronic Structure System. *J. Comp. Chem.* **1993**, *14*, 1347-1363.
9. Bentwood, R. M.; Barnes, A. J.; Orville-Thomas, W. J. Studies of Intermolecular interactions by Matrix Isolation Vibrational Spectroscopy: Self-association of Water. *J. Mol. Spectros.* **1980**, *84*, 391-404.

CHAPTER 6

DIMER STUDIES IN THE PROPARGYL SYSTEMS

6.1. Introduction

The homodimers of propargyl alcohol and propargyl amine, and the PA-PAM heterodimers present an interesting system, as the multifunctionality of both submolecules can be expected to present a rich landscape of the isomers for the dimer. The rotational spectra of PA homodimer and its deuterium forms have been studied by Mani and Arunan¹ in a molecular beam, which confirmed that the two gPA units in the dimer were bound by a triple contact involving an O-H...O, an O-H... π and a C-H... π hydrogen bond interaction. Computationally, a number of isomers were indicated for the PA homodimers, though only one structure was observed in the gas phase study.

Sivaraman et al.² reported studies on the irradiation of PA ice matrices at 85 K with 2 KeV electrons, which resulted in the formation of benzene. They also studied the infrared spectra of PA ices, which was the first report on this molecule mimicking the low temperature astrochemical conditions. They observed changes in infrared spectra during phase transformation from the amorphous PA ice to a crystalline structure on annealing, which they took to indicate reorientation between the propargyl alcohol homodimers. This observation makes it important to understand the different isomers of the PA homodimers and their infrared spectra and have highlighted the use of this data in detecting PA in astrochemical environment. The need for a detailed study on the infrared spectroscopy of the PA dimers has also been explicitly indicated by Sivaraman et al. following their work on PA ices.

The motivation of the present work was therefore to study the homodimers of PA using matrix isolation infrared spectroscopy. To the best of our knowledge, no infrared data of the PA homodimer exists in the literature. Furthermore, while the gas phase studies

identified only one isomer,¹ matrix isolation experiments have the potential to locate local minima and it was therefore interesting to see if any of the other isomers of the dimer, could be identified in our experiments. This question is all the more relevant, given that there are many isomeric forms of the dimer having similar interaction energies, and structures in addition to the global minimum may have a role to play in the behavior of PA ices in astrochemical environments. Mani and Arunan¹ had alluded to the possibility that dimer structures corresponding to other minima may well be present, which we wanted to examine.

The results of the work discussed in the earlier studies prompted us to look at possible trends in the structures of the various complexes. For example, starting from the PA-H₂O structures, one can systematically evolve the structures of PA-MeOH, from which then, the structures of PA homodimers can be constructed.

This method, reminiscent of the retrosynthetic approach in organic chemistry, will be helpful in arriving at the structures of complex homo or hetero dimers using such a strategy. Similar to computing several PA Homodimer structures, we also explored possible structures of heterodimers between PA and PAm, together with homodimers of PAm.

6.2. Experimental Details

Matrix isolation experiments were performed using a closed cycle helium compressor-cooled cryostat (HC-4E1). The matrix was deposited on a KBr substrate maintained at a temperature of ~12 K. N₂ (Sigma Gases and Services 99.999%) and Ar (Sigma Gases and Services 99.999%) were used as matrix gases. PA (Sigma Aldrich 99%) and PAm (Sigma Aldrich with an assay of 98%) were used without further purification, though the sample was subjected to several freeze-pump-thaw cycles before use. In all the experiments, typical deposition rates of ~3 mmol/h of the matrix gas were employed. The experimental method has been described in detail in chapter 2. Spectra of the matrix-isolated

species were recorded using a Fourier Transform Infrared spectrometer, operating at a resolution of 0.5 cm^{-1} .

6.3. Computational Details

Gaussian 09 suite of programs³ was used to compute the structures of the various isomers of the PA, PAm homodimers as well as PA-PAm heterodimers. For the vibrational assignments, we have adopted a different procedure for scaling the computed features, for a better analysis of the data, which has been explained below.

We found that the scale factors from precursor data yielded scaled computed wavenumbers for the dimer, that do not agree well with those of the experimental product features, particularly for the hydrogen bonded O-H stretch. In the PA-dimer experiments, the multiplicity of peaks in the region of the O-H and C-O stretch of the PA submolecule requires that the vibrational shifts resulting from dimer formation, be better evaluated for a meaningful assignment. We therefore explored the possibility of computing the scaling factors for the dimer features differently. Instead of using the PA monomer features as the basis for scaling the PA-dimers, we tried to derive the scaling factors, by using the experimental and computed O-H and C-O stretch of the PA \cdots H₂O complex. Using our previous work on PA-H₂O,⁴ we used the experimental feature corresponding to the O-H stretch of PA submolecule in this complex, occurring at 3467.2 cm^{-1} and derived a scale factor of 0.9154 at the M06-2X/6-311++G(d,p) level, which could be employed to scale the computed O-H stretch in the PA homodimers. Likewise, we used the C-O stretch in the PA-H₂O complex occurring at 1053.4 cm^{-1} , to obtain the scaling factor for PA homodimers in this region, which was 0.9336. It can be seen that the scale factor for the O-H stretch (0.9154) was very different compared with that obtained when the PA monomer data was used (0.9341), while the scale factor for the C-O stretch does not change significantly. It was found that this method of scaling, where the PA-H₂O system was used as the calibrant for

scaling the computed features for the PA homodimers, yielded significantly better agreement between computations and experiments. It may be noted that the PA-H₂O features mentioned above appeared in all the spectra, as H₂O is an ever present impurity in the experiments and hence PA-H₂O system served as an internal calibrant for scaling.

Interaction energies for PA homodimers were calculated at both M06-2X and MP2 level of theory, using 6-311++G(d,p) and aug-cc-pVDZ as the basis sets. These interaction energies were then separately corrected for the zero point energies and basis set superposition error (BSSE) using the counterpoise method.⁵

AIM2000 program⁶ was used to identify and characterize different hydrogen bonded interactions based on their electron density topology. The Kohn-Sham orbitals required for this analysis were generated from Gaussian calculations performed at MP2/aug-cc-pVDZ level. We also used the topological parameters, $\rho_b(\mathbf{r}_c)$ and $\nabla^2\rho_b(\mathbf{r}_c)$, which are the electron density and Laplacian, respectively, at the bond critical points, to estimate the interaction energy corresponding to the hydrogen bond in question, as described by Espinosa et al.⁷

6.4. Results-PA Homodimer

6.4.1. Experimental

Fig. 6.1 shows the matrix isolation infrared spectra of PA in N₂ matrix with sample to matrix ratios of 0.8:1000, 3:1000 and 10:1000, over the spectral regions 3750-3400 cm⁻¹ and 1060-1020 cm⁻¹. The feature at 3727.5 cm⁻¹ is always present in our experiments which corresponds to the asymmetric stretch in H₂O monomer.⁸ The strong peaks at 3641.9 and 1040.8 cm⁻¹ are due to the O-H and the C-O stretch in PA monomer.

With the increase in PA concentration, new product bands appeared at 3488.6, 3477.9, 3457.4 and 3414.7 cm⁻¹ in the O-H stretch region and at 1050.6, 1049.1, 1033.0 and 1026.7 cm⁻¹ in the C-O stretch region, after the matrix was annealed. The product bands

occurring at 3467.2 and 1053.4 cm^{-1} had been assigned to the features corresponding to the 1:1 PA-H₂O hydrogen bonded complex, as discussed before, in chapter 3.

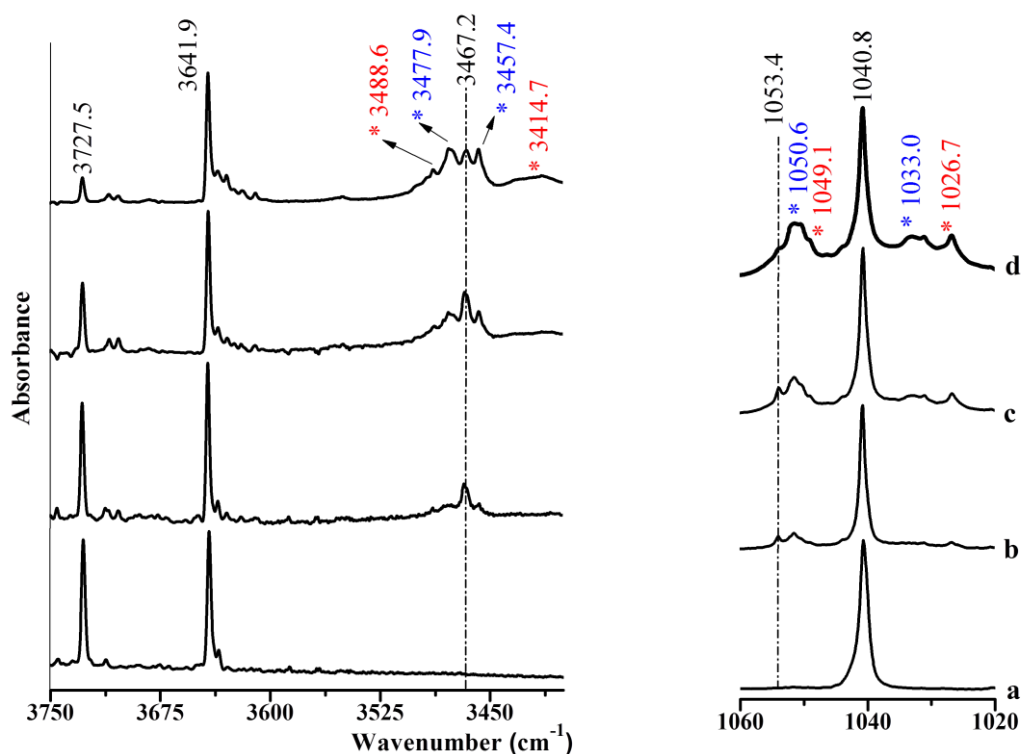


Fig. 6.1. Matrix isolation infrared spectra of PA over the regions 3750-3400 cm^{-1} and 1060-1020 cm^{-1} , with (a) PA:N₂ (0.8:1000) at 12 K, (b) PA:N₂ (0.8:1000), (c) PA:N₂ (3:1000) and (d) PA:N₂ (10:1000). Spectra of (b), (c) and (d) were recorded after annealing the matrix at 27 K. The product bands of PA-dimers highlighted in red and blue, are marked with an asterisk. PA-H₂O complex features are indicated by the dash-dotted line.

6.4.2. Computational

Optimized structures of PA homodimers 1, 2, 3, 4 and 5, in which both PA subunits were in gauche conformation had been reported by Mani and Arunan,¹ at the MP2/6-311+G(3df,2p) level. In the present work, we have computed different PA homodimers at the MP2/aug-cc-pVDZ level, which are shown in Fig. 6.2. As it can be seen, in addition to the earlier reported structures,¹ we have also computed the optimized structures of PA dimers 2A, 2B, 5A and 5B, at the MP2/aug-cc-pVDZ level, by employing the strategy of systematic

evolution of the structures of the complexes starting from the structures of simple complexes, which is elaborated in later section of this chapter.

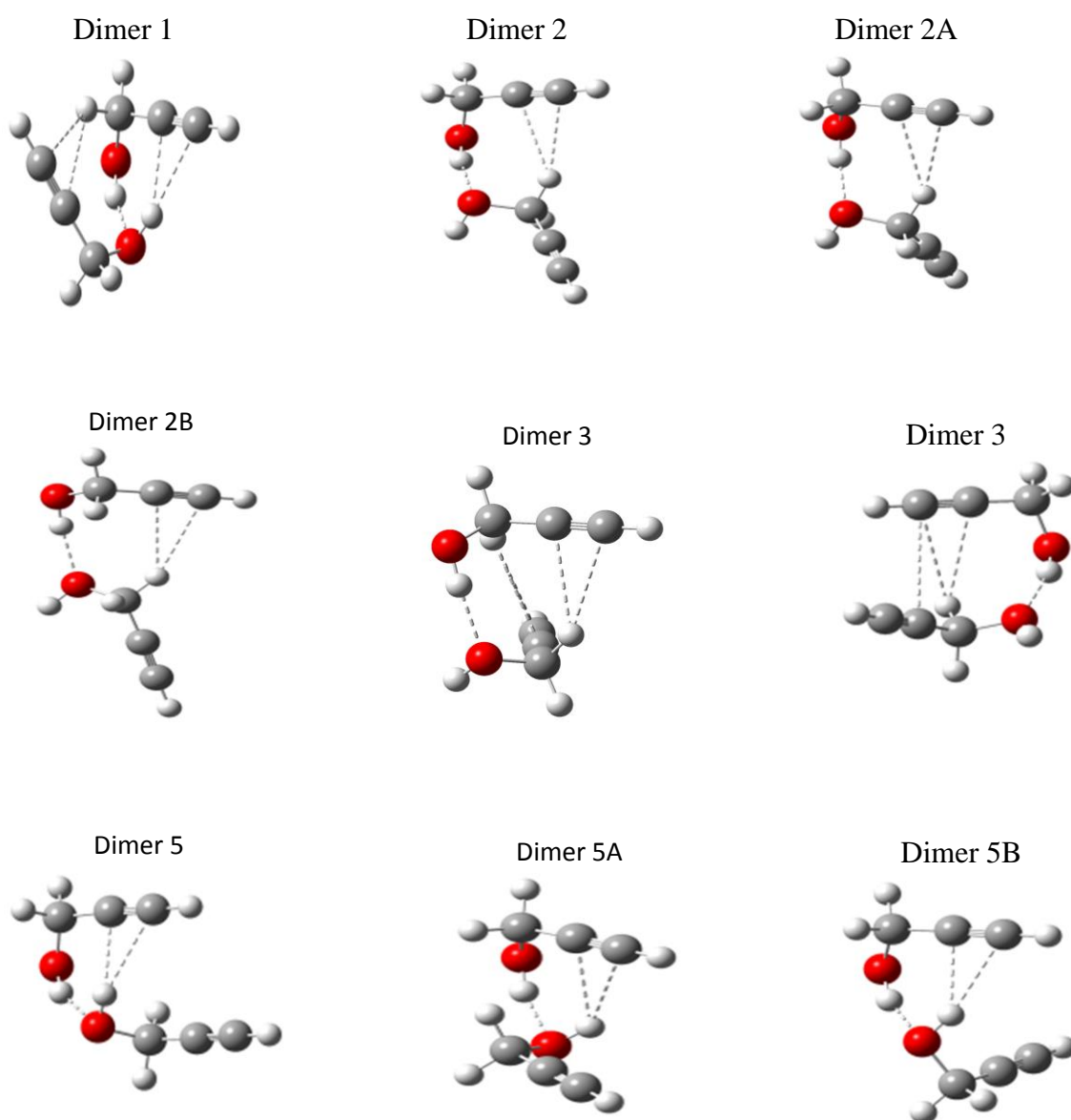


Fig. 6.2. Optimized structures of different PA homodimers having both PA subunits in gauche conformation, computed at the MP2/aug-cc-pVDZ level.

Structure 1 as reported by Mani and Arunan,¹ was bound by three hydrogen bonded interactions. One PA subunit serves as a proton donor to π cloud through its hydroxyl hydrogen forming an $O-H\cdots\pi$ interaction and also as a proton acceptor through its acetylenic π system from the $-CH_2$ group of other PA subunit, leading to a $C-H\cdots\pi$ interaction in

addition to the O-H \cdots O interaction. In structures 2, 2A and 2B, with O-H \cdots O and C-H \cdots π interactions, one PA subunit serves as the proton donor through the -CH₂ group to the π cloud of other PA subunit and as a proton acceptor at the oxygen atom to the hydroxyl hydrogen of the other PA subunit. Dimer 3 has three hydrogen bonded interactions similar to structure 1, but an O-H \cdots π contact in structure 1 is replaced by a weaker C-H \cdots π interaction (Fig. 6.3).

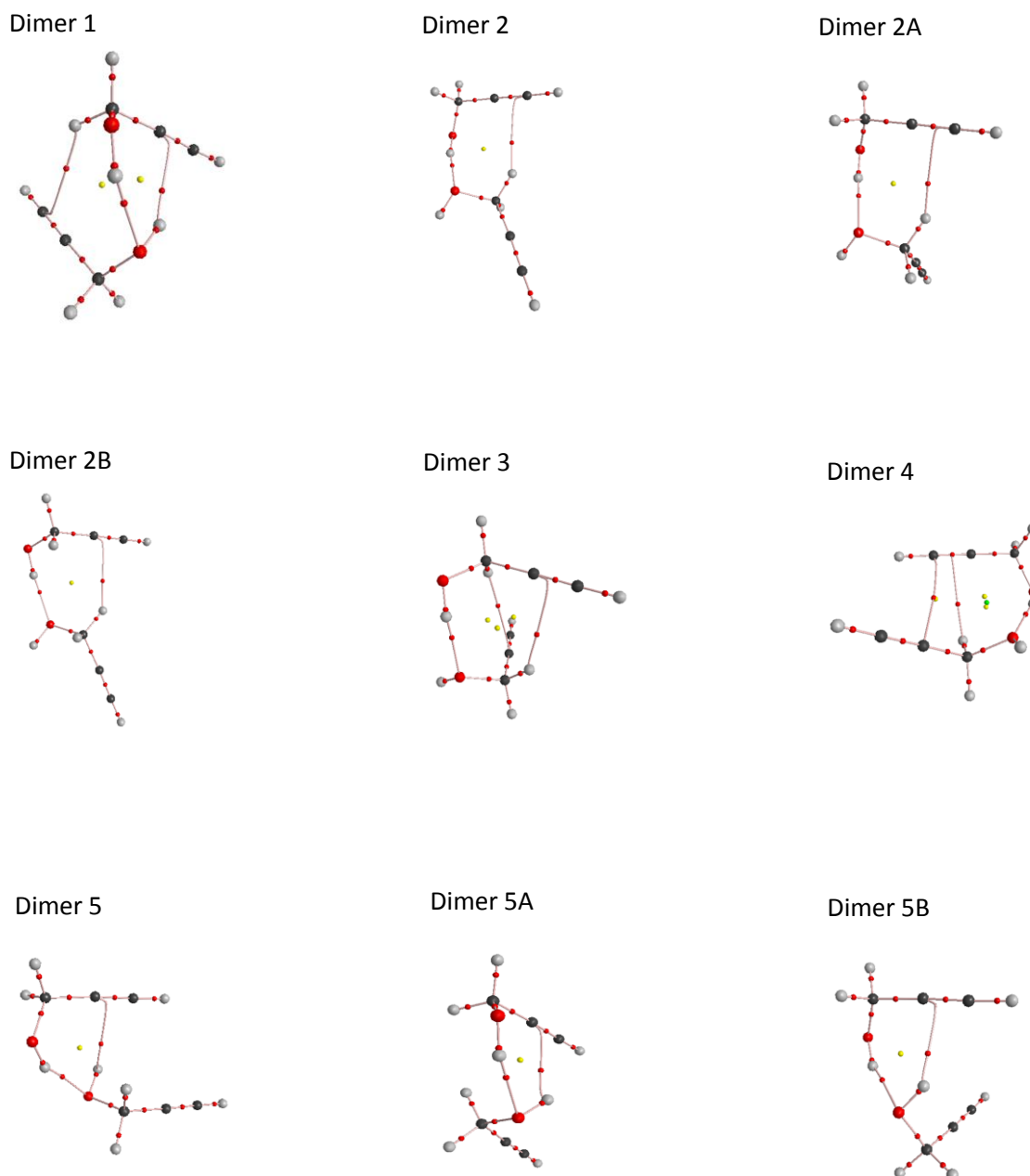


Fig. 6.3. Electron density topologies for different PA-dimers at MP2/aug-cc-pVDZ level with their bond, ring and cage critical points.

Structure 4 resembles structures 2, 2A and 2B, having an O-H \cdots O and a C-H \cdots π interaction. Incidentally, structure 4 is the only one with an additional $\pi\cdots\pi$ interaction, as indicated by our AIM calculations. Structures 5, 5A, 5B have an O-H \cdots O and an O-H \cdots π interaction. These isomers resembled structures 2, 2A and 2B, except that the weak C-H \cdots π interaction in structure 2 was replaced by an O-H \cdots π interaction in structures 5, 5A and 5B.

It must be noted that all the dimer structures of PA discussed above had an O-H \cdots O interaction as the primary interaction. Some of the important geometrical parameters for these PADimers computed at the MP2/aug-cc-pVDZ level, have been listed in Table 6.1. The variety in the structures of the dimers arise from a combination of additional O-H \cdots π and/or C-H \cdots π contacts. Other structures involving \equiv C-H \cdots O, C-H \cdots O, O-H \cdots π , C-H \cdots π and $\pi\cdots\pi$ interaction, were also obtained, but were significantly weaker than those involving an O-H \cdots O contact as the primary interaction and hence, have not been shown.

Interaction energies calculated for PADimers having both subunits in the gauche form, are listed in Table 6.2. These interaction energies were separately corrected for zero-point energy and basis set superposition error. We also performed single point energy calculation and calculated the uncorrected interaction energies at the MP2/CBS and CCSD(T)/CBS limit using the optimized geometries of PA dimers at MP2/aug-cc-pVDZ level.

6.5. Discussion- PA Homodimer

6.5.1. Vibrational Assignments

As shown in Table 6.2, dimers 1 and 5, exist as two structures with nearly equal interaction energies, being just ~ 0.2 kcal mol $^{-1}$ apart at the CCSD(T)/CBS level. Thus both these structures may be expected to be observed in the matrix and it was therefore interesting to see if these could be discerned in the matrix. It may be recalled that Mani and Arunan had seen only dimer 1 in their microwave experiments, but not the dimer 5.

Table 6.1. Important geometrical parameters of the PA-dimers, showing bond lengths (Å), and bond angles (degrees), computed at the MP2/aug-cc-pVDZ level.

Dimer	Geometrical parameters					
1	H ₁₆ O ₇	O ₁₅ H ₁₆ O ₇	H ₁₄ C ₁	H ₁₄ C ₂	C ₁₂ H ₁₄ C ₁	C ₁₂ H ₁₄ C ₂
	1.96	155.6	3.00	2.82	117.1	139.8
			H ₈ C ₉	H ₈ C ₁₀	O ₇ H ₈ C ₉	O ₇ H ₈ C ₁₀
2.33	2.42	131.0	160.0			
2	H ₁₆ O ₇	O ₁₅ H ₁₆ O ₇	H ₅ C ₉	H ₅ C ₁₀	C ₄ H ₅ C ₉	C ₄ H ₅ C ₁₀
	1.90	172.2	2.74	2.80	125.6	126.5
2A	H ₈ O ₁₅	O ₇ H ₈ O ₁₅	H ₁₃ C ₁	H ₁₃ C ₂	C ₁₂ H ₁₃ C ₁	C ₁₂ H ₁₃ C ₂
	1.87	168.5	2.74	2.71	137.9	159.8
2B	H ₈ O ₁₅	O ₇ H ₈ O ₁₅	H ₁₃ C ₁	H ₁₃ C ₂	C ₁₂ H ₁₃ C ₁	C ₁₂ H ₁₃ C ₂
	1.91	166.7	2.67	2.78	131.8	157.3
3	H ₁₆ O ₇	O ₁₅ H ₁₆ O ₇	H ₆ C ₉	H ₆ C ₁₀	C ₄ H ₆ C ₉	C ₄ H ₆ C ₁₀
	1.91	169.8	2.75	2.80	123.3	147.7
			H ₁₄ C ₁	H ₁₄ C ₂	C ₁₂ H ₁₄ C ₁	C ₁₂ H ₁₄ C ₂
2.91	3.04	120.6	143.7			
4	H ₁₆ O ₇	O ₁₅ H ₁₆ O ₇	H ₆ C ₉	H ₆ C ₁₀	C ₄ H ₆ C ₉	C ₄ H ₆ C ₁₀
	1.88	162.0	2.82	2.85	119.0	115.7
5	H ₁₆ O ₇	O ₁₅ H ₁₆ O ₇	H ₈ C ₉	H ₈ C ₁₀	O ₇ H ₈ C ₉	O ₇ H ₈ C ₁₀
	1.94	155.5	2.46	2.54	121.9	137.0
5A	H ₁₆ O ₇	O ₁₅ H ₁₆ O ₇	H ₈ C ₉	H ₈ C ₁₀	O ₇ H ₈ C ₉	O ₇ H ₈ C ₁₀
	1.94	157.1	2.48	2.52	118.6	141.2
5B	H ₈ O ₁₅	O ₇ H ₈ O ₁₅	H ₁₆ C ₁	H ₁₆ C ₂	O ₁₅ H ₁₆ C ₁	O ₁₅ H ₁₆ C ₂
	1.98	155.2	2.34	2.43	130.0	159.1

a) O-H Stretch: In our matrix-isolated infrared experiments (Fig. 6.1), the O-H stretch of the uncomplexed PA monomer occurred at 3641.9 cm⁻¹. Of the four product features of PA-dimers that appeared in infrared spectra shown in Fig. 6.1, the experimental feature at 3414.7 cm⁻¹ showed the largest red shift of 227.2 cm⁻¹ from the O-H feature of the uncomplexed PA monomer. The experimental features matched closely with the vibrational wavenumbers computed at the M06-2X/6-311++G(d,p) level, which are used for making our mode assignments for ggPA-dimers. Computations indicated that the in-phase O-H stretch of dimer 5 occurring at 3442.2 cm⁻¹ showed the largest red shift of 199.6 cm⁻¹ (Table 6.3). The experimental feature at 3414.7 cm⁻¹ may therefore be assigned to the in-phase O-H stretch of dimer 5. Likewise, the out-of-phase O-H stretch in the same dimer was computed to occur at 3518.8 cm⁻¹ manifesting the smallest red shift of 123.0 cm⁻¹ of the four features. The

experimental feature at 3488.6 cm⁻¹ which showed the smallest red shift of 153.3 cm⁻¹ can therefore be assigned to this mode. The other two product features at 3477.9 and 3457.4 cm⁻¹ were then assigned to the out-of-phase and the in-phase O-H stretches, respectively for dimer 1, which correlate well with the corresponding computed features at 3490.3 and 3461.7 cm⁻¹, thus strongly suggesting the formation of dimers 1 and 5 in the matrix. It may also be noted that dimers 5, 5A and 5B are similar in structure and even if they were formed in the matrix, it would be experimentally difficult to differentiate between them.

Table 6.2. Interaction energies for different PA-dimers given as uncorrected (ΔE_{RAW})/ZPE corrected (ΔE_{ZPC})/BSSE corrected (ΔE_{BSSE}) energies, at various levels of theory. Uncorrected energies at CCSD(T) level have also been shown, employing 6-311++G(d,p), aug-cc-pVDZ and complete basis set (CBS) limit. All energies are given in kcal/mol.

		6-311++G(d,p)	aug-cc-pVDZ	CBS
Dimer 1	M06-2X	-9.3/-8.0/-8.7	-8.9/-7.5/-8.3	
	MP2	-9.1/-7.9/-6.0	-10.0/-8.5/-7.2	-8.7
	CCSD(T)	-	-9.5	-8.2
Dimer 2	M06-2X	-7.7/-6.6/-7.0	-6.9/-5.9/-6.4	
	MP2	-8.1/-6.9/-5.4	-8.4/-7.1/-6.1	-7.1
	CCSD(T)	-	-7.8	-6.7
Dimer 2A	M06-2X	-7.8/-6.8/-7.2	-7.0/-6.0/-6.5	
	MP2	-8.1/-6.9/-5.4	-8.3/-7.1/-6.1	-7.1
	CCSD(T)	-	-8.1	-6.9
Dimer 2B	M06-2X	Not Optimized	Not Optimized	
	MP2	Not Optimized	-7.8/-6.7/-5.4	-6.5
	CCSD(T)	-	-7.6	-6.3
Dimer 3	M06-2X	-8.2/-7.0/-7.4	-7.4/-6.4/-6.8	
	MP2	-8.5/-7.3/-5.5	-8.9/-7.7/-6.3	-7.5
	CCSD(T)	-	-8.5	-7.1
Dimer 4	M06-2X	-8.3/-7.2/-7.7	-7.5/-6.5/-7.0	
	MP2	-8.3/-7.1/-5.5	-8.6/-7.6/-6.3	-7.5
	CCSD(T)	-	-8.1	-7.0
Dimer 5	M06-2X	-9.4/-7.9/-8.7	-9.3/-7.8/-8.6	
	MP2	-8.7/-7.5/-5.9	-9.9/-8.4/-7.1	-8.5
	CCSD(T)	-	-9.4	-8.0
Dimer 5A	M06-2X	-8.7/-7.3/-8.0	-8.5/-7.2/-7.8	
	MP2	-8.3/-7.1/-5.5	-9.3/-7.9/-6.5	-7.9
	CCSD(T)	-	-8.8	-7.4
Dimer 5B	M06-2X	-8.3/-7.1/-7.7	-7.9/-6.6/-7.4	
	MP2	-8.2/-7.0/-5.5	-8.8/-7.5/-6.5	-7.8
	CCSD(T)	-	-8.4	-7.4

Table 6.3. Experimental (in N₂ matrix) and computed scaled vibrational wavenumbers at the M06-2X/6-311++G(d,p) level for PA-dimers 1 and 5, given in cm⁻¹.

Experimental		Computed ^a				
PA	Dimer	PA	Dimer 1	Dimer 5	Mode	
3641.9	3477.9 <i>-164.0^b</i>	3641.8	3490.3 (275) <i>-151.5</i>		Out-of-phase O-H stretch	
	3488.6 <i>-153.3</i>			3518.8 (106) <i>-123.0</i>		
	3457.4 <i>-184.5</i>			3461.7 (140) <i>-180.1</i>		In-phase O-H stretch
	3414.7 <i>-227.2</i>				3442.2 (262) <i>-199.6</i>	
1040.8	1050.6 <i>+9.8</i>	1040.7	1050.5 (116) <i>+9.8</i>		C ₁₂ O ₁₅ stretch	
	1049.1 <i>+8.3</i>			1047.6 (102) <i>+6.9</i>		
	1033.0 <i>-7.8</i>			1034.6 (115) <i>-6.1</i>		C ₄ O ₇ stretch
	1026.7 <i>-14.1</i>				1021.5 (103) <i>-19.2</i>	

^a Scaling factors for PA-dimers: 0.9154 for the O-H stretch and 0.9336 for the C-O stretch. These were derived using the PA-H₂O features. See text for details.

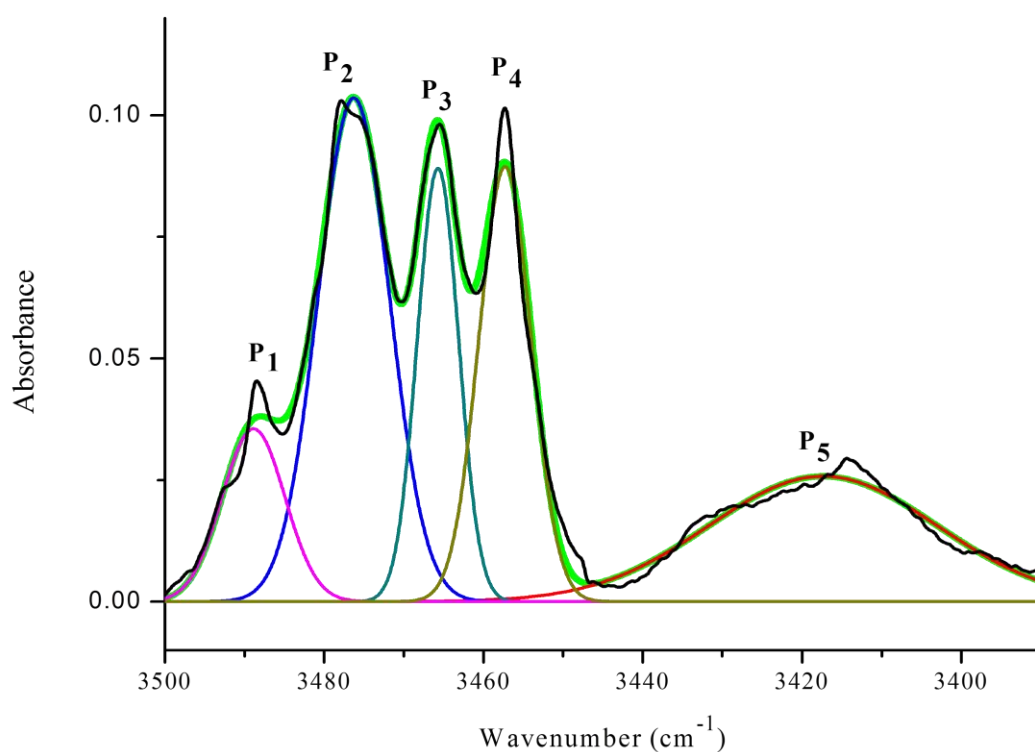
^b Vibrational shifts $\Delta v = v_{\text{dimer}} - v_{\text{monomer}}$ indicated in italics.

It must be mentioned that the scaling of PA-dimers using the PA-H₂O feature yielded a much better agreement between the computed and experimental values. Deriving scaling factors using the features of the PA monomer to scale the computed features of the dimers, yielded a poor agreement between experimental and computational wavenumbers.

b) C-O Stretch: This mode in dimer 1 corresponding to the C₁₂O₁₅ and C₄O₇ stretches were computed to occur respectively, at 1050.5 and 1034.6 cm⁻¹, the first being blue shifted and the second being red shifted from the feature of the monomer PA, which occurs at 1040.7 cm⁻¹. In dimer 5, the C₁₂O₁₅ stretch was computed to occur at 1047.6 cm⁻¹ and the C₄O₇ stretch at 1021.5 cm⁻¹, the first feature again being blue shifted while the second being red shifted from the monomer feature. In the annealed matrix, we observed strong blue-shifted product features at 1050.6, 1049.1 cm⁻¹ and red shifted features at 1033.0, 1026.7 cm⁻¹. The

experimental feature at 1026.7 cm^{-1} agrees well with the computed feature at 1021.5 cm^{-1} of dimer 5. The second red shifted experimental feature at 1033.0 cm^{-1} can be assigned to the computed feature at 1034.6 cm^{-1} of dimer 1. The experimental feature at 1050.6 cm^{-1} with a blue shift of 9.8 cm^{-1} showed excellent agreement with the computed feature at 1050.5 cm^{-1} of dimer 1. The experimental feature at 1049.1 cm^{-1} with a blue shift of 8.3 cm^{-1} is assigned to the computed feature at 1047.6 cm^{-1} of dimer 5. These assignments strongly confirm the formation of dimer 1 and 5 in the matrix.

The experimental spectrum over the region $3500\text{-}3390\text{ cm}^{-1}$ (d) from Fig. 6.1) was decomposed into its component features using a peak fitting routine. This spectral decomposition process was necessitated as there was overlap of the features in this region. The method of spectral decomposition used the Fityk software incorporating the Levenberg-Marquardt algorithm of weighted least squares, to fit the experimental spectrum to five individual Gaussian profiles. When performing the fit, as an initial guess, each Gaussian was centred at 3414.7 , 3457.4 , 3467.2 , 3477.9 and 3488.6 cm^{-1} to correspond to the experimentally observed peak positions. The fit was then done, allowing the peak position, FWHM and the height of the Gaussian, to be optimized as free parameters in the fit. Fig. 6.4 gives the experimental spectrum together with the Gaussian components derived from the fitting routine and the fitted spectrum obtained as the sum of the intensities in each Gaussian. Peaks P_1 and P_5 were assigned to the O-H stretch of dimer 5 while peaks P_2 and P_4 were assigned to dimer 1 for the same mode as discussed earlier. Peak P_3 was due to the O-H stretch in the PA-H₂O complex, assigned based on our earlier work.⁴ The table included in Fig. 6.4 gives the peak center, height, FWHM and the area under each individual spectral feature obtained from the fit.



Peak (P _n)	Peak center	Height	FWHM	Experimental intensities	Computed intensities
P ₁	3488.9	0.035	9.292	0.351	106
P ₂	3476.3	0.104	10.561	1.164	275
P ₃	3465.7	0.089	6.106	0.579	-
P ₄	3457.3	0.089	7.746	0.737	140
P ₅	3417.4	0.026	33.743	0.925	262

Fig. 6.4. Gaussian peak fitted infrared spectrum of PA:N₂ (10:1000) annealed at 27 K over the region 3500–3390 cm⁻¹. The experimental intensities are the areas under the respective features. The computed intensities given in km/mole, were obtained at the M06-2X/6-311++G(d,p) level of theory. See text for details. The experimental spectrum is shown in black and the total fitted spectrum in green.

While the area under each feature is a measure of the experimental intensities, the computed intensities at the M06-2X/6-311++G(d,p) level, for each of the corresponding

features of dimer 1 and 5, may be taken as a measure of absorptivity. Applying Beer-Lambert's law to each feature of the dimer, one can write

$${}^D\mathbf{A}_{P_n} = {}^D\boldsymbol{\varepsilon}_{P_n} \cdot \mathbf{c}_D \cdot l \quad (\text{eq. 1})$$

where ${}^D\mathbf{A}_{P_n}$ is the absorbance for peak P_n , measured as the area under this feature, corresponding to dimer D . ${}^D\boldsymbol{\varepsilon}_{P_n}$ is the corresponding absorptivity, a measure of which can be obtained from the computed vibrational intensity for the dimer D , and \mathbf{c}_D is the concentration of the dimer D , to which feature P_n corresponds to (eq 1). For example, for the feature P_1 occurring at 3488.9 cm^{-1} , corresponding to dimer 5, ${}^5\mathbf{A}_{P_1}$ was 0.351 and ${}^5\boldsymbol{\varepsilon}_{P_1}$ was 106. The ratio ${}^5\mathbf{A}_{P_1}/{}^5\boldsymbol{\varepsilon}_{P_1}$ was therefore a measure of the concentration, \mathbf{c}_5 of dimer 5.

Similarly, one can also deduce the concentration of dimer 5 using feature P_5 , which leads to a value very close to that obtained using feature P_1 . Likewise, the concentration of dimer 1, \mathbf{c}_1 , can be estimated using features P_2 and P_4 ; it was seen again that the two estimates agree quite well between themselves. The ratio of the concentrations of the two dimers 1 and 5, given by $\mathbf{c}_1/\mathbf{c}_5$, can be arrived at with the four different data sets as shown in Table 6.4. It can be seen that this ratio was fairly constant, ranging from 1.20 to 1.59, yielding an average value of 1.39 ± 0.18 , indicating that the concentration of dimer 1 was about 16% higher than that of dimer 5. This result was consistent with the computations at the CBS limit which indicated dimer 5 to be higher in energy than dimer 1 by about $0.2 \text{ kcal mol}^{-1}$. The intensity analysis lends credence to the vibrational assignments made for the two PA dimers.

6.5.2. AIM analysis

Table 6.5 lists the electron density and Laplacian of electron density values at the bond critical points for the ggPA-dimers computed at MP2/aug-cc-pVDZ level. In all the PA-dimer structures, values of $\rho_b(\mathbf{r}_c)$ and $\nabla^2\rho_b(\mathbf{r}_c)$ for the O-H \cdots O and O-H \cdots π contacts, fall in the range proposed by Koch and Popelier, while the $\nabla^2\rho_b(\mathbf{r}_c)$ values for the C-H \cdots π contacts

are marginally less than the lower limit. Of the O-H...O, O-H... π and C-H... π interactions, the O-H...O hydrogen bond was found to be the strongest, followed, in order, by O-H... π and C-H... π interactions, as can be inferred from the $\rho_b(\mathbf{r}_c)$ values in Table 6.5.

Table 6.4. Calculation showing the estimates of concentration of the PA-dimers 1 and 5 in the matrix.

	Feature of Dimer 1	${}^1A_{P_n}/{}^1\epsilon_{P_n}$ c_1	Feature of Dimer 5	${}^5A_{P_n}/{}^5\epsilon_{P_n}$ c_5	c_1/c_5
Case 1	P ₂	1.164/275 = 4.233 x 10 ⁻³	P ₁	0.351/106 = 3.311 x 10 ⁻³	1.28
Case 2	P ₂	1.164/275 = 4.233 x 10 ⁻³	P ₅	0.925/262 = 3.530 x 10 ⁻³	1.20
Case 3	P ₄	0.737/140 = 5.264 x 10 ⁻³	P ₁	0.351/106 = 3.311 x 10 ⁻³	1.59

We also used the topological parameters $\rho_b(\mathbf{r}_c)$ and $\nabla^2\rho_b(\mathbf{r}_c)$ to deduce the interaction energies of each contact, through the evaluation of the local kinetic energy density, $G(\mathbf{r}_c)$ and the local potential energy density, $V(\mathbf{r}_c)$,⁷ for the PA-dimers belonging to the 'gg' set. In dimer 1, which manifests three interactions, it can be seen that the O-H...O interaction contributed the largest stabilization of -4.8 kcal mol⁻¹, while the two weaker O-H... π and C-H... π interactions contributed -2.4 and -0.9 kcal mol⁻¹ respectively, as shown in the same table under the head 'E_{HB}'. The other near-isoenergetic dimer 5 with two interactions, O-H...O and O-H... π , has interaction energy of -5.2 and -2.1 kcal mol⁻¹, respectively.

Table 6.5. Electron density $\rho_b(\mathbf{r}_c)$, Laplacian $\nabla^2\rho_b(\mathbf{r}_c)$, local electronic kinetic energy density $G(\mathbf{r}_c)$, local electronic potential energy density $V(\mathbf{r}_c)$ and hydrogen bond energy E_{HB} values for different hydrogen bonded interactions in the 'gg' PA-dimer structures at MP2/aug-cc-pVDZ level. The values for $\rho_b(\mathbf{r}_c)$, $\nabla^2\rho_b(\mathbf{r}_c)$, $G(\mathbf{r}_c)$ and $V(\mathbf{r}_c)$ are given in atomic units and for E_{HB} , in kcal/mol.

Dimer	Interaction	$\rho_b(\mathbf{r}_c)$	$\nabla^2\rho_b(\mathbf{r}_c)$	$G(\mathbf{r}_c)$	$V(\mathbf{r}_c)$	E_{HB}	Total E_{HB}
1	O-H...O	0.0255	0.0825	0.0200	-0.0401	-4.8	-8.1
	O-H... π	0.0152	0.0433	0.0099	-0.0197	-2.4	
	C-H... π	0.0066	0.0186	0.0038	-0.0075	-0.9	
2	O-H...O	0.0306	0.1100	0.0269	-0.0537	-6.4	-7.5
	C-H... π	0.0081	0.0222	0.0046	-0.0093	-1.1	
2A	O-H...O	0.0301	0.1035	0.0255	-0.0511	-6.1	-7.2
	C-H... π	0.0085	0.0228	0.0048	-0.0096	-1.1	
2B	O-H...O	0.0262	0.0950	0.0224	-0.0448	-5.4	-6.6
	C-H... π	0.0087	0.0246	0.0051	-0.0103	-1.2	
3	O-H...O	0.0271	0.0944	0.0227	-0.0454	-5.4	-7.3
	C-H... $\pi(1)$	0.0081	0.0228	0.0047	-0.0095	-1.1	
	C-H... $\pi(2)$	0.0057	0.0171	0.0034	-0.0067	-0.8	
4	O-H...O	0.0268	0.1050	0.0243	-0.0487	-5.8	-7.6
	C-H... π	0.0073	0.0229	0.0046	-0.0092	-1.1	
	π ... π	0.0052	0.0148	0.0029	-0.0058	-0.7	
5	O-H...O	0.0277	0.0865	0.0216	-0.0433	-5.2	-7.3
	O-H... π	0.0133	0.0392	0.0087	-0.0173	-2.1	
5A	O-H...O	0.0270	0.0870	0.0214	-0.0428	-5.1	-7.1
	O-H... π	0.0129	0.0392	0.0086	-0.0171	-2.0	
5B	O-H...O	0.0250	0.0776	0.0190	-0.0380	-4.5	-6.8
	O-H... π	0.0153	0.0424	0.0098	-0.0195	-2.3	

6.5.3. NBO Analysis

NBO analysis at the MP2/aug-cc-pVDZ level was computed for PA dimers 1 and 5 to understand the role of some of the important orbital interactions between the two PA subunits (Table 6.6).

Table 6.6. NBO analysis showing the significant orbital interactions between the donor and acceptor orbitals in the two PA subunits, their corresponding second order perturbation energies, $E(2)$, difference in energy between acceptor and donor orbitals $E(j)-E(i)$, and $F(i,j)$ computed at MP2/aug-cc-pVDZ level in gg-PAdimers 1 and 5. $E(2)$ values are indicated in kcal/mol and values for $E(j)-E(i)$ and $F(i,j)$ are in atomic units.

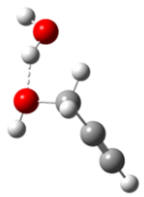
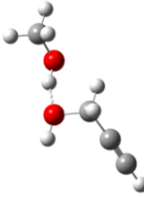
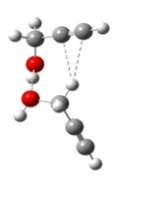

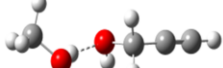
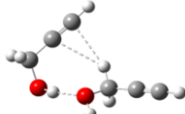
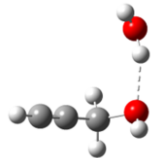
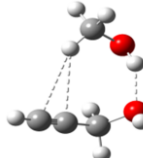
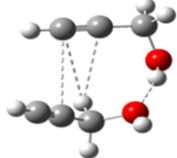
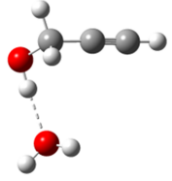
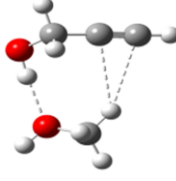

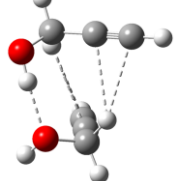
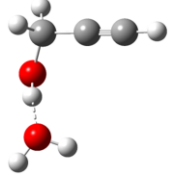
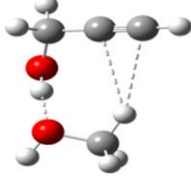
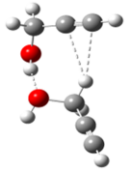
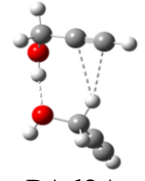
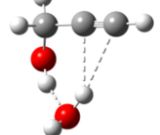
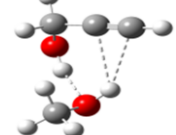
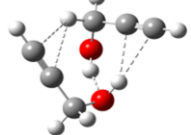
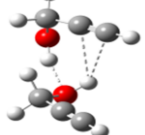
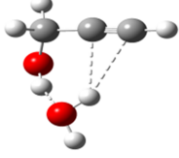
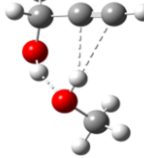
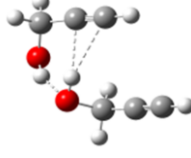
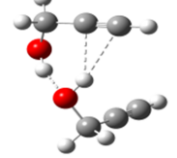
Dimer	Donor NBO (i)	Acceptor NBO (j)	$E(2)$	$E(j)-E(i)$	$F(i,j)$
1	n_1O_7	$\sigma^*O_{15}H_{16}$	2.9	1.6	0.060
	n_2O_7	$\sigma^*O_{15}H_{16}$	7.5	1.3	0.088
	$\pi_1C_1C_2$	$\sigma^*C_{12}H_{14}$	0.1	1.1	0.008
	$\pi_2C_1C_2$	$\sigma^*C_{12}H_{14}$	0.9	1.1	0.028
	$\pi_1C_9C_{10}$	$\sigma^*O_7H_8$	0.3	1.1	0.017
	$\pi_2C_9C_{10}$	$\sigma^*O_7H_8$	4.8	1.1	0.065
5	n_1O_7	$\sigma^*O_{15}H_{16}$	0.7	1.6	0.030
	n_2O_7	$\sigma^*O_{15}H_{16}$	11.1	1.3	0.107
	$\pi_1C_9C_{10}$	$\sigma^*O_7H_8$	0.8	1.1	0.026
	$\pi_2C_9C_{10}$	$\sigma^*O_7H_8$	2.0	1.1	0.042

It can be seen that there was a strong interaction between the lone pairs of oxygen of one PA subunit, serving as the electron donor to the σ^* orbital of O-H bond of the other PA subunit which serves as the electron acceptor, as can be seen from the relatively high values of second order perturbation energies, $E(2)$. In addition, dimers 1 and 5 manifests an O-H $\cdots\pi$ interaction between the donor orbital of the $C_9\equiv C_{10}$ π bond and the σ^* orbital of O_7-H_8 bond. Furthermore, in dimer 1, electron delocalization is observed from the acetylenic π bond to the σ^* acceptor orbital of the $C_{12}H_{14}$, resulting in a weak C-H $\cdots\pi$ interaction.

6.5.4. A Discernible trend in the Complexes of PA-H₂O, PA-MeOH and PA Dimer?

Table 6.7 shows the structures of PA-H₂O, PA-MeOH and PA homodimers, from which one can observe the systematic evolution of the structures of the complexes. For example, the PA-MeOH complex 1 can be obtained by replacing the non-hydrogen bonded H atom in water in PA-H₂O complex 1, with a methyl group. Likewise, PA-H₂O complex 1* can be correlated to the PA-MeOH complex 1A.

Table 6.7. Correlation between the structures of PA-H₂O, PA-MeOH and PA-dimers, with their interaction energies $\Delta E_{\text{RAW}}/\Delta E_{\text{ZPC}}/\Delta E_{\text{BSSE}}$, in kcal/mol, at the MP2/aug-cc-pVDZ level.

PA-H ₂ O	PA-MeOH	PA-dimers	
 Complex 2B (-5.8/-4.1/-4.6)	 Complex 2'A (-6.2/-5.1/-4.7)	 PAd2A (-8.3/-7.1/-6.1)	Not Optimized
 Complex 2 (-6.1/-4.2/-4.7)	 Complex 2' (-6.3/-5.1/-4.8)	 PAd2 (-8.4/-7.1/-6.1)	Not Optimized
 Complex 2A (-5.8/-4.0/-4.6)	 Complex 2 (-6.8/-5.6/-5.0)	 PAd4 (-8.6/-7.6/-6.3)	Not Optimized
 Precursor of Complex 1'A (Not Optimized)	 Complex 1'A (-7.7/-6.4/-5.7)	 PAd2B (-7.8/-6.7/-5.4)	 PAd3 (-8.9/-7.7/-6.3)
 Precursor of Complex 1' (Not Optimized)	 Complex 1' (-8.2/-6.8/-6.3)	 PAd2 (-8.4/-7.1/-6.1)	 PAd2A (-8.3/-7.1/-6.1)
 Complex 1* (-7.7/-5.7/-6.1)	 Complex 1A (-9.2/-7.6/-6.8)	 PAd1 (-10.0/-8.5/-7.2)	 PAd5A (-9.3/-7.9/-6.5)
 Complex 1 (-7.9/-5.9/-6.2)	 Complex 1 (-9.3/-7.6/-7.0)	 PAd5 (-9.9/-8.4/-7.1)	 PAd5B (-8.8/-7.5/-6.5)

The number of non-covalent interactions in both the sets of PA-H₂O and PA-MeOH complexes is the same and increased interaction energy in the PA-MeOH complexes result from the increased basicity of MeOH. From the PA-MeOH complexes, one can evolve the PA-dimer complexes, by progressively replacing each of the methyl hydrogen with a -C≡C-H group. For example, PA-MeOH complex 1 give rise to PAd5, PAd5B, PAd6 structures of the dimer. Incidentally, the PAd6 structure corresponding to a dimer where one PA submolecule is in a *trans*-geometry has been excluded from Table 6.7. It can be seen that structures of the PA-MeOH and the PA-dimer have similar hydrogen bonded architecture and hence manifest comparable interaction energies. Likewise, PA-MeOH complex 1A give rise to PAd1 and PAd5A dimer structures. In this correlation, it can be seen that PAd1 of the dimer has three hydrogen bonded contacts as opposed to two in PA-MeOH complex 1A and hence shows the largest interaction energy. This method of systematically constructing complex dimer structures starting from PA-MeOH, which in turn can be obtained from the simpler PA-H₂O structures is akin to the retrosynthetic approach of organic chemists, a method that can prove useful in arriving at structures of complex homo and heterodimers.

We have thus employed the strategy in which one can observe the systematic evolution of the structures of the complexes. Starting from the structures of PA-H₂O complex, we obtained the structures of PA-MeOH complexes, which were then used to obtain the different PA-PA complexes 1, 2, 2A, 2B, 3, 4, 5, 5A, 5B.

6.6. Results- PA-PAm dimers

6.6.1. Experimental

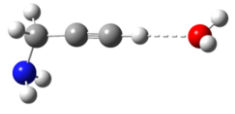
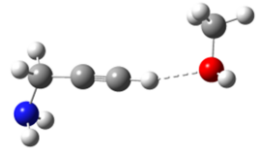
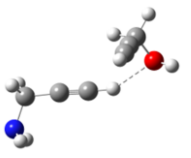
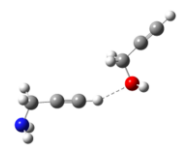
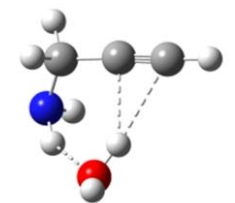
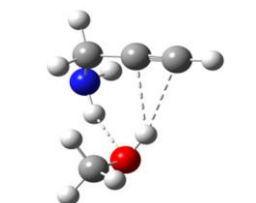

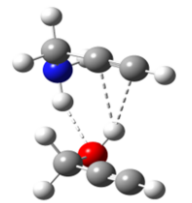
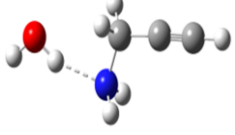
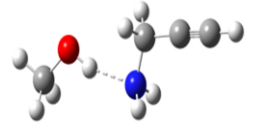
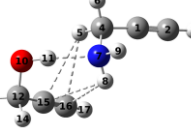
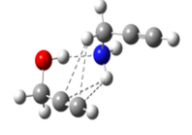
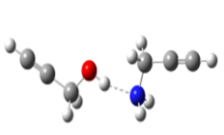
Matrix isolation infrared experiments were performed in the N₂ matrix, where the PAm/N₂ gas mixture was passed through the effusive nozzle together with the PA vapours maintained at appropriate temperatures. We observed the features for both the monomers PA and PAm in the spectrum recorded at 12 K. However, we did not observe any feature

corresponding to the formation of complex between PA and PAm, even after annealing the matrix at 27 K. This could be because when PA and PAm are deposited in matrix, they are likely to form their homodimers and hydrogen bonded complexes with water, making the IR spectra congested in the O-H stretch region. In order to observe complex between PA and PAm, concentrations of both precursor needs to be tuned favouring PA-PAm complexes and minimizing spectral interference from other complexes. Thus, we have to work under a small window by carefully tuning the concentrations of PA and PAm, making it difficult to observe their complex formation.

6.6.2. Computational

Different PAm-PA complexes were computed at the MP2/aug-cc-pVDZ level as shown in Table 6.8.

Table 6.8. Optimized structures of PAm-PA complexes with their interaction energies (in kcal/mol) computed at the MP2/aug-cc-pVDZ level.

PAm-H ₂ O	PAm-MeOH	PAm-PA		
 Complex 3 (-3.4/-2.4/-2.4)	 Complex 3 (-4.1/-3.3/-2.9)	 Dimer 4 (-4.3/-3.6/-2.9)	 Dimer 5 (-4.1/-3.3/-2.7)	
 Complex 1 (-6.0/-4.4/-4.5)	 Complex 1 (-6.9/-5.8/-4.9)	 Dimer 2 (-8.7/-7.8/-5.8)	 Dimer 3 (-7.5/-6.5/-5.0)	
 Complex 2 (-7.9/-5.7/-6.3)	 Complex 2 (-8.2/-6.8/-6.4)	 Dimer 1 (-11.6/-10.1/-8.7)	 Dimer 1A (-11.6/-10.1/-8.7)	 Dimer 6 (-9.3/-8.0/-7.3)

These structures were systematically derived from replacement of each methyl hydrogen in ggPAm-MeOH complex with an acetylenic group, in a similar way with which different PA homodimers were constructed. These ggPAm-MeOH complexes were computed starting from the simpler ggPAm-H₂O structures, by replacing each hydrogen atom in H₂O with a methyl group. The structures of six PA-PAm complexes 1, 1A, 2, 3, 4 and 5 were thus optimized, in which the PA subunit is in the gauche conformation. It must be noted here that on substituting the acetylenic group on the methyl hydrogen which is trans to the O-H group in MeOH subunit of ggPAm-MeOH complex, structures of *trans*PA-PAm complexes could be derived, for example dimer 6.

Dimers 1 and 1A, which are mirror images, are the most stable and isoenergetic structures, which are bound by an O-H...N, a N-H... π and C-H... π interaction, as revealed from AIM analysis (Fig. 6.5). These dimer structures were constructed from the most stable complex 2 of PAm-H₂O and PAm-MeOH system. Both dimers 1 and 1A are relatively more stable than complex 2 of PAm-H₂O and PAm-MeOH system. Dimer 2 involves four contacts, a N-H...O, N-H... π , C-H... π and O-H... π interaction. In dimer 3, PAm interacts with PA through its N-H bond forming an N-H...O interaction, together with an O-H... π interaction, thus having dual contacts.

In the nearly isoenergetic dimers 4 and 5, there is an interaction between the acetylenic hydrogen of PAm and oxygen atom of PA, thus bound by a \equiv C-H...O interaction. Table 6.9 lists some of the important geometrical parameters for the optimized PA-PAm complexes at the MP2/aug-cc-pVDZ level of computation. The computed scaled vibrational features for the most stable PA-PAm dimer 1 computed at the same level are shown in Table 6.10. AIM analysis was performed on PA-PAm dimers and results are listed in Table 6.11.

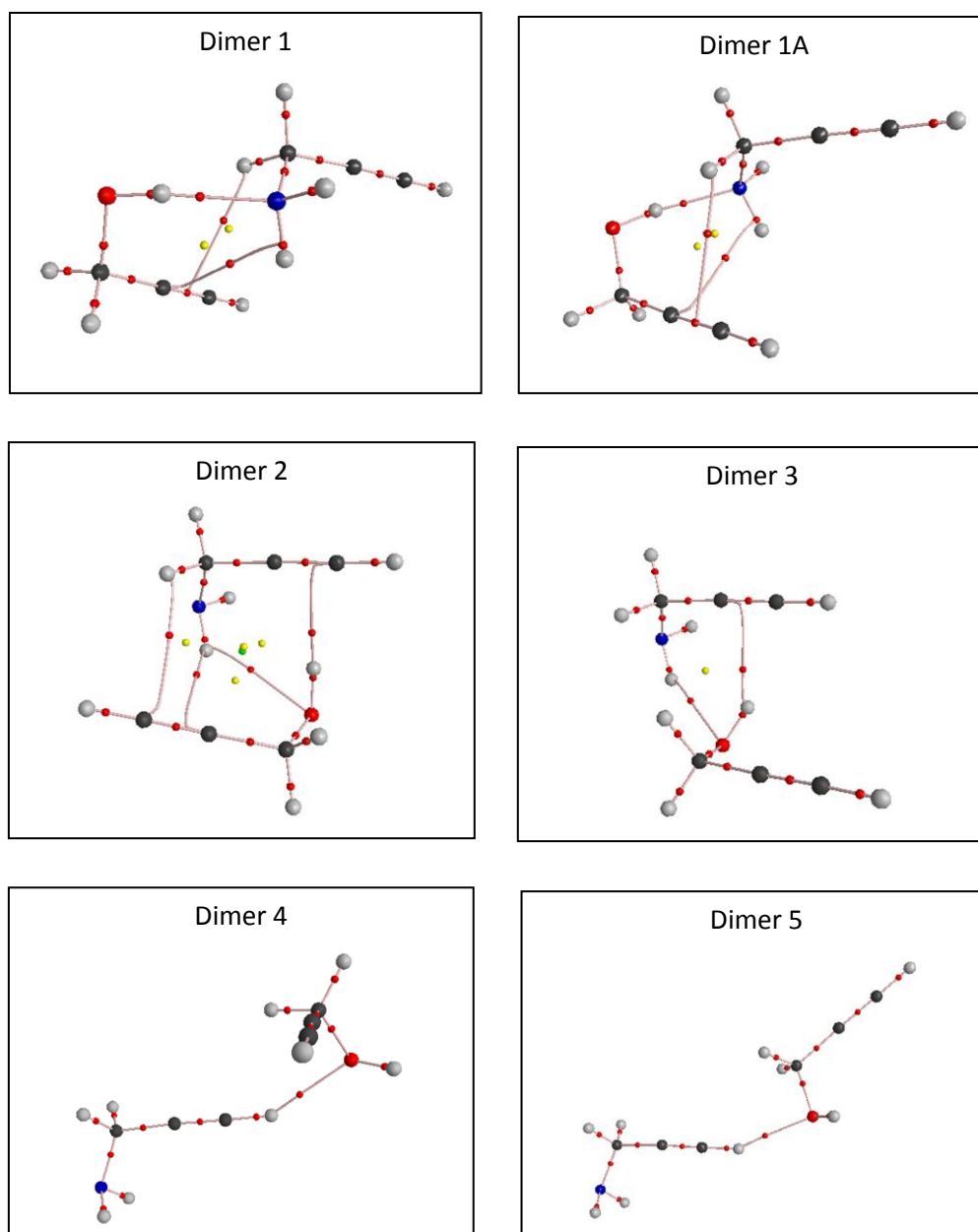


Fig. 6.5. Electron density topologies for different PA-PAM dimers at MP2/aug-cc-pVDZ level with their bond, ring and cage critical points.

Dimer 1 is dominantly stabilized by the O-H \cdots N interaction with E_{HB} value of -9.8 kcal/mol, followed by a N-H \cdots π and C-H \cdots π as secondary interactions. Dimer 2 has an O-H \cdots π as the primary interaction with E_{HB} value of -3.3 kcal/mol. Dimer 3 having a N-H \cdots O and an O-H \cdots π interaction, lacks the other two interactions present in dimer 2 which are N-H \cdots π and C-H \cdots π interaction.

Table 6.9. Some of the important geometrical parameters including bond lengths (in Å), bond angles and dihedral angles (in degrees) in PA-PAm complexes computed at MP2/aug-cc-pVDZ level.

Parameters	Dimer 1	Dimer 2	Dimer 3	Dimer 4	Dimer 5
N7H11	1.87				
O10H11N7	160.4				
O10H11N7H8	-57.2				
H8C15	2.74	2.66			
H8C16	2.86	2.74			
N7H8C15	105.2	138.7			
N7H8C16	119.2	124.1			
H5C15	2.84	3.18			
H5C16	2.86	2.83			
C4H5C15	119.1	101.4			
C4H5C16	119.5	118.5			
H8O10		2.74	2.33		
N7H8O10		133.1	143.8		
N7H8O10H11		+17.2	-32.5		
H11C1		2.33	2.36		
H11C2		2.28	2.40		
O10H11C1		156.1	131.9		
O10H11C2		160.5	151.4		
H3O10				2.19	2.19
C2H3O10				149.9	155.3
C2H3O10H11				137.2	118.9

Table 6.10. Vibrational scaled computed wavenumbers for PA-PAm dimer 1 at the MP2/aug-cc-pVDZ level. Scaling factors used are 0.9508 for NH₂ and ≡C-H stretch, 0.9608 for NH₂ wag., 0.9548 for O-H and 0.9852 for C-O stretch. Computed IR intensities (km/mole) are given in brackets.

Computed at MP2/aug-cc-pVDZ level		
PAm	Dimer 1	Assignment
3416.5 (5)	3406.5 (12) -10.0	NH ₂ asym. st.
3312.3 (55)	-	≡C-H st. of PAm
-	3312.5 (10) +0.2 ^a	NH ₂ sym. st. in-phase with ≡C-H st. of PAm
-	3310.6 (74) -1.7 ^a	NH ₂ sym. st. out-of-phase with ≡C-H st. of PAm
929.7 (95)	966.0 (106) +36.3	NH ₂ wag
PA	Dimer 1	Assignment
3642.0 (38)	3275.3 (688) -366.7	O-H st.
1040.8 (102)	1052.8 (96) +12.0	C-O st.

^aThese computed shifts were calculated by subtracting the complex feature from the ≡C-H st. of PAm monomer.

It must also be noted that even though the N-H...O interaction in dimer 3 is reasonably strong with E_{HB} value of -2.3 kcal/mol than that in dimer 2, it can be seen that dimer 3 is less stable than dimer 2, emphasizing to the role of weak secondary interactions towards stability of complex. Both dimers 4 and 5 involve a $\equiv\text{C-H}\cdots\text{O}$ interaction with E_{HB} value of -3.1 kcal/mol.

Table 6.11. AIM analysis on PA-PAm dimers computed at MP2/aug-cc-pVDZ level, with their electron density $\rho_b(\mathbf{r}_c)$, Laplacian $\nabla^2\rho_b(\mathbf{r}_c)$, local electronic kinetic energy density $G(\mathbf{r}_c)$ and local electronic potential energy density $V(\mathbf{r}_c)$ given in atomic units and hydrogen bond energy E_{HB} values in kcal/mol.

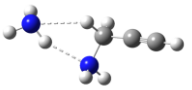
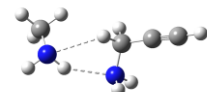
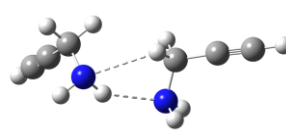
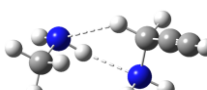
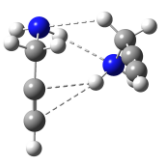
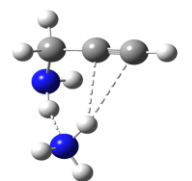
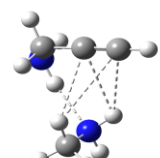
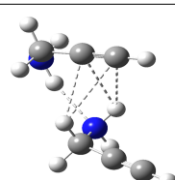
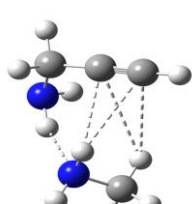
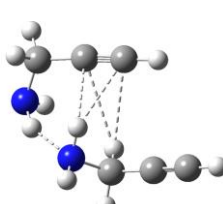
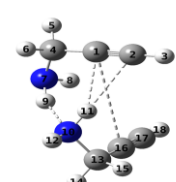
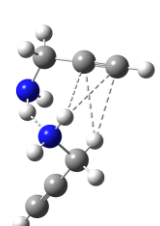
Dimer	Interaction	$\rho_b(\mathbf{r}_c)$	$\nabla^2\rho_b(\mathbf{r}_c)$	$G(\mathbf{r}_c)$	$V(\mathbf{r}_c)$	E_{HB}	Total E_{HB}
1	O-H...N	0.0360	0.1040	0.0286	-0.0313	-9.8	-12.3
	N-H... π	0.0084	0.0284	0.0057	-0.0044	-1.4	
	C-H... π	0.0073	0.0223	0.0045	-0.0035	-1.1	
2	N-H...O	0.0066	0.0241	0.0047	-0.0034	-1.1	-6.6
	O-H... π	0.0171	0.0470	0.0111	-0.0105	-3.3	
	N-H... π	0.0086	0.0262	0.0054	-0.0043	-1.3	
	C-H... π	0.0064	0.0199	0.0040	-0.0029	-0.9	
3	N-H...O	0.0133	0.0374	0.0084	-0.0074	-2.3	-5.3
	O-H... π	0.0157	0.0442	0.0102	-0.0094	-2.9	
4	$\equiv\text{C-H}\cdots\text{O}$	0.0156	0.0496	0.0111	-0.0098	-3.1	-3.1
5	$\equiv\text{C-H}\cdots\text{O}$	0.0158	0.0488	0.0110	-0.0098	-3.1	-3.1

6.7. Results- PAm Homodimers

6.7.1. Computational

We further wished to explore, if we can construct the geometries of PAm homodimers following the same scheme used to derive the structures of PA homodimers and PA-PAm complexes. For this we chose the simpler ggPAm-NH₃ system and located two structures as the minima on potential energy surface computed at MP2/aug-cc-pVDZ level, as shown in Table 6.12.

Table 6.12. Optimized structures of PAm Homodimers with their interaction energies, in kcal/mol, computed at the MP2/aug-cc-pVDZ level.

PAm-NH ₃	PAm-MeNH ₂	PAm Homodimers		
 Complex 2 (-4.6/-3.3/-3.3)	 Complex 2A (-5.4/-4.3/-3.6)	 Corresponding Dimer (Not Optimized)		
	 Complex 2 (-5.3/-4.2/-3.5)	 Dimer 2 (-6.9/-5.7/-3.9)		
 Complex 1 (-5.8/-4.4/-4.2)	 Complex 1A (-7.0/-5.9/-4.9)	 Dimer 1A (-7.5/-6.5/-5.0)		
	 Complex 1 (-7.1/-5.9/-5.0)	 Dimer 1 (-7.9/-6.9/-5.3)	 Dimer 3 (-7.5/-6.6/-5.1)	 Dimer 4 (-8.1/-7.2/-5.4)

The global minimum involves a N-H...N in which the N-H bond of PAm interacts with nitrogen atom of NH₃ and a N-H... π interaction, between the acetylenic π cloud of PAm and N-H bond of NH₃. In this PAm-NH₃ complex, when each of the hydrogen atoms in NH₃ are systematically replaced by a methyl group, keeping the dual interactions (N-H...N and N-H... π) intact, two most stable and nearly isoenergetic ggPAm-MeNH₂ complexes were computed. Both these complexes were bound by a N-H...N, N-H... π and C-H... π interaction.

It was found that when each of the methyl hydrogen atoms in ggPAm-MeNH₂ complex is replaced with an acetylenic group, we derived different PAm homodimer structures.

Table 6.13. AIM analysis on ggPAm homodimers computed at MP2/aug-cc-pVDZ level, with their electron density $\rho_b(\mathbf{r}_c)$, Laplacian $\nabla^2\rho_b(\mathbf{r}_c)$, local electronic kinetic energy density $G(\mathbf{r}_c)$ and local electronic potential energy density $V(\mathbf{r}_c)$ given in atomic units and hydrogen bond energy E_{HB} values in kcal/mol.

Dimer	Interaction	$\rho_b(\mathbf{r}_c)$	$\nabla^2\rho_b(\mathbf{r}_c)$	$G(\mathbf{r}_c)$	$V(\mathbf{r}_c)$	E_{HB}	Total E_{HB}
1	N-H...N	0.0172	0.0432	0.0105	-0.0102	-3.2	-6.0
	N-H... π	0.0099	0.0308	0.0065	-0.0052	-1.6	
	C-H... π	0.0076	0.0238	0.0048	-0.0037	-1.2	
1A	N-H...N	0.0175	0.0436	0.0107	-0.0104	-3.3	-6.0
	N-H... π	0.0091	0.0280	0.0058	-0.0046	-1.5	
	C-H... π	0.0079	0.0251	0.0051	-0.0039	-1.2	
2	N-H...N	0.0141	0.0406	0.0091	-0.0081	-2.6	-5.8
	N-H... π	0.0104	0.0309	0.0066	-0.0054	-1.7	
	C-H... π	0.0084	0.0346	0.0068	-0.0049	-1.5	

Dimer 1 was bound by the same interactions (a N-H...N, N-H... π and C-H... π interaction) as the precursor ggPAm-MeNH₂ complex 1, as revealed from AIM results listed in Table 6.13. In a similar way, another nearly isoenergetic isomeric structure having same hydrogen bonded interactions as dimer 1, was computed as dimer 1A from ggPAm-MeNH₂ complex 1A. Table 6.12 shows the structures of PAm homodimers, computed at MP2/aug-cc-pVDZ level in a similar manner, Dimer 2 less stable than dimers 1 and 1A, has the two PAm subunits interacting with each other forming a N-H...N, N-H... π and C-H...O interaction. It must be noted that dimers 1, 1A and 2 has both subunits in the ggPAm conformation and are bound by a primary N-H...N interaction followed by a N-H... π and C-H... π /C-H...O interaction. In addition, we can also compute the structures of PAm homodimers having one subunit in gg and other in gt form, as shown by dimers 3 and 4, which were obtained by systematic replacement of the other two methyl hydrogen atoms in MeNH₂ of ggPAm-

MeNH₂ complex 1. Such structures in which the gt PAm subunit is involved, is not shown in the table since the monomer itself is located at higher energy, their complexes are higher energy structures than the ggPAm homodimers.

Some of the important geometrical parameters for the ggPAm homodimers computed at MP2/aug-cc-pVDZ level, are listed in Table 6.14.

Table 6.14. Some important geometrical parameters including bond lengths (in Å), bond and dihedral angles (in degrees) in ggPAm homodimers computed at MP2/aug-cc-pVDZ level.

Parameters	Dimer 1	Dimer 1A	Dimer 2
N10H9	2.26	2.25	
N7H9N10	149.7	151.2	
N7H9N10H11	+26.0	-49.2	
H15C1	2.90	2.71	
H15C2	2.84	3.04	
C13H15C1	114.5	122.1	
C13H15C2	110.1	110.9	
H11C1	2.60	2.72	
H11C2	2.74	2.70	
N10H11C1	118.6	111.7	
N10H11C2	125.6	131.6	
N7H11			2.32
N10H11N7			139.6
N10H11N7H9			+57.9
H9C16			2.48
H9C17			2.78
N7H9C16			143.8
N7H9C17			162.7
H6N10			2.62
C4H6N10			123.1
N7C4H6N10			+19.7

6.8. Conclusions

The infrared spectra of PA indicated the formation of PA homodimers in the matrix, having both PA subunits in the gauche conformation. The FTIR spectra of the PA-dimers, together with the vibrational assignments at M06-2X/6-311++G(d,p) indicated that dimer 1 with three point contact, an O-H...O, an O-H... π and a C-H... π interaction, is the global minimum with another isomer, dimer 5, being nearly isoenergetic. At the CCSD(T)/CBS

limit, dimer 1 was marginally lower in energy than dimer 5 by about 0.2 kcal mol⁻¹. The presence of dimer 1 and 5 in the matrix was evidenced by the large red shift in the O-H stretching vibration of the PA subunits, which was also corroborated with the computational shift. NBO analysis showed dominant stabilization due to the strong orbital interaction between the lone pairs of oxygen and σ^* orbital of the O-H bond in all PA homodimers.

It is also worth mentioning that spectral deconvolution helped to resolve the experimental features of PA homodimers, since there was overlap of the features in the O-H stretch region, which was further confounded by the presence of the PA-H₂O feature. The ratio (c_1/c_5) indicated that the concentration of dimer 1 was about 16% larger than that of dimer 5. This result was consistent with the computations at the CCSD(T)/CBS limit which indicated dimer 5 to be higher in energy than dimer 1 by about 0.2 kcal mol⁻¹.

The presence of more than one dimer in low temperature matrices may in fact serve as an explanation for the reported changes in the infrared spectra of propargyl alcohol ices when the temperature of the ice was raised from 85 K to 180 K. Sivaraman et al.² observed that annealing of propargyl alcohol ices resulted in a red shift in the infrared features. It was speculated in that work that the changes in dimer structure could result in the observed spectral changes, when the amorphous propargyl alcohol ice at 85 K transformed to crystalline ice at 180 K. The identification of two lowest energy isomers, in our work, which are nearly isoenergetic (dimer 1 and 5) allows for the possibility of isomer interconversion. Furthermore, that dimer 5 of PA, which is slightly higher in energy than dimer 1, has a feature to the red, is consistent with the observation that annealing at higher temperatures causes a red shift in the ices spectrum. The other isomers of PA-dimers, not seen in our experiments, but indicated by the computations, may also have a role to play in the phase transformation.

It was also discerned that in PA-MeOH structures, when each of the methyl hydrogen atoms were replaced by an acetylenic group, different PA homodimers were systematically evolved at MP2/aug-cc-pVDZ level. Similarly, different PA-MeOH complexes can be arrived at from the PA-H₂O complexes, by a systematic replacement of each of the hydrogen atom in H₂O with methyl group.

In addition, starting from the simpler PAm-H₂O structures, we have systematically constructed the structures of hydrogen bonded complexes between PA and PAm, by replacing each of the methyl hydrogen atoms of PA subunit in PAm-MeOH complexes with an acetylenic group. Computations have located the mirror images PAm-PA dimers 1 and 1A, bound by a dominant O-H...N and relatively weaker N-H... π and C-H... π interactions, as the global minima. Matrix isolation infrared experiments were performed to observe the shifts in O-H and C-O stretch in PA subunit of dimer 1 or 1A, however we did not observe the features corresponding to formation of PA-PAm dimer in our experiments.

Computationally, we have also derived different PAm homodimer structures at the MP2/aug-cc-pVDZ level, by replacing each of the methyl hydrogen atoms in MeNH₂ subunit of PAm-MeNH₂ complexes with an acetylenic group, which in turn were systematically constructed from the simpler PAm-NH₃ complexes by replacing each hydrogen atom of H₂O with a methyl group. PAm homodimers 1 and 1A constituted the global minimum and were computed as the two nearly isoenergetic structures bound by three interactions, a primary N-H...N and relatively weaker N-H... π and C-H... π interactions.

This work therefore presents a method in which starting from simpler PA-H₂O, PAm-H₂O and PAm-NH₃ system; we can systematically derive different hydrogen bonded structures of complex systems like PA-PAm complexes, PA and PAm homodimers.

References

1. Mani, D.; Arunan, E. Rotational Spectra of Propargyl Alcohol Dimer: a Dimer Bound with Three Different Types of Hydrogen Bonds. *J. Chem. Phys.* **2014**, *141*, 164311.
2. Sivaraman, B.; Mukherjee, R.; Subramanian, K. P.; Banerjee, S. B. Benzene Formation on Interstellar Icy Mantles containing Propargyl Alcohol. *ApJL* **2015**, *798*, 1-4.
3. Frisch, M. J.; Trucks, G. W.; Schlegel, H. B.; Scuseria, G. E.; Robb, M. A.; Cheeseman, J. R.; Scalmani, G.; Barone, V.; Mennucci, B.; Peterson, G. A.; *et al.* *GAUSSIAN 09*, Gaussian Inc.; Wallingford, CT, **2010**.
4. Saini, J.; Viswanathan, K. S. Does a Hydrogen Bonded Complex with Dual Contacts show Synergism? a Matrix Isolation Infrared and *Ab Initio* Study of Propargyl Alcohol-Water Complex. *J. Mol. Struct.* **2016**, *1118*, 147-156.
5. Boys, S. F.; Bernardi, F. The Calculation of Small Molecular Interactions by the Differences of Separate Total Energies. Some Procedures with Reduced Errors. *Mol. Phys.* **1970**, *19*, 553-566.
6. Biegler-König, F.; Schönbohm, J. Update of the AIM2000-Program for Atoms in Molecules. *J. Comput. Chem.* **2002**, *23*, 1489-1494.
7. Espinosa, E.; Molins, E.; Lecomte, C. Hydrogen Bond Strengths Revealed by Topological Analyses of Experimentally Observed Electron Densities. *Phys. Lett.* **1998**, *285*, 170-173.
8. Bentwood, R. M.; Barnes, A. J.; Orville-Thomas, W. J. Studies of Intermolecular interactions by Matrix Isolation Vibrational Spectroscopy: Self-association of Water. *J. Mol. Spectros.* **1980**, *84*, 391-404.

CHAPTER 7

CONCLUSIONS

In this thesis, molecular conformations and hydrogen bonded complexes of two different propargyl systems have been explored. Experiments were performed using matrix isolation infrared spectroscopy and the results were corroborated with *ab initio* computations.

To begin with, propargyl alcohol (PA) was trapped in N₂ and Ar matrices and the observed infrared features were assigned to the dominantly populated gauche conformer. The assignments were done by a comparison with the infrared features computed using *ab initio* computations. AIM analysis indicated that intramolecular hydrogen bonding interactions were not responsible for stability of the gauche conformer over the trans form. The greater stability of the gauche structure was majorly due to the presence of vicinal orbital interactions together with some contribution from n- π^* remote interaction in gauche PA, as revealed from our NBO analysis.

The 1:1 hydrogen bonded complexes of PA with H₂O studied experimentally and corroborated by computations, indicated that the global minima were complexes 1 and 1* (Fig. 7.1). Both these nearly isoenergetic complexes involved an O-H \cdots O and an O-H $\cdots\pi$ interaction, resulting in a cyclic geometry of these complexes, as was evident from the AIM analysis, which yielded a ring critical point. The large red shift of 174.7 cm⁻¹ in the O-H stretch of PA subunit, was observed on formation of these complexes in the matrix. Isotopic results confirmed the vibrational assignments. Since the computed IR features of the two nearly isoenergetic complexes, 1 and 1*, were close lying, it was not possible to resolve the features of these complexes in our experiments. NBO indicated a strong electron delocalization between the lone pair of oxygen of water to the σ^* orbital of O-H bond in PA. LMO-EDA analysis showed that electrostatic and exchange energy contributed largest to the stabilization of these complexes. It was also recognized that in forming the dual interaction

PA-H₂O complex, the optimum geometries when each interaction was present individually, were sacrificed, resulting in antagonism.

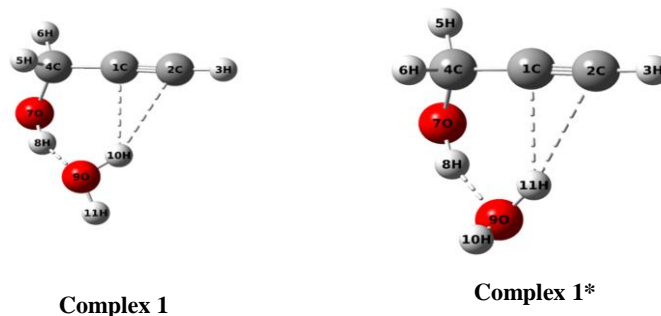


Fig. 7.1. Global minima PA-H₂O complexes 1 and 1*, computed at the MP2/aug-cc-pVDZ level.

We next studied the hydrogen bonded complexes of PA with MeOH experimentally and computationally. Our work revealed the formation of two most nearly isoenergetic complexes 1 and 1A, bound by a primary O-H...O together with a secondary O-H... π interaction. These two complexes were also indicated to correspond to the global minima by our computations. A relatively larger red shift of $\sim 200\text{ cm}^{-1}$ was observed as compared to that for PA-H₂O complex. The two nearly isoenergetic PA-MeOH complexes 1 and 1A were distinguishable in our experiments, since their IR features show discernible differences in their O-H and C-O stretch vibrations, which was unlike the case of PA-H₂O. It was found that the O...H bond distance was shorter ($\sim 1.88\text{ \AA}$) and O-H...O bond angle close to linearity (158°) as compared with PA-H₂O global minima complexes with respective values of $\sim 1.95\text{ \AA}$ and 154° . As with PA-H₂O complexes, antagonistic behaviour was observed in both PA-MeOH complexes 1 and 1A. The BSSE corrected interaction energy computed at MP2/aug-cc-pVDZ level, -7.0 and -6.8 kcal/mol for PA-MeOH complexes 1 and 1A, is greater than that computed for the PA-H₂O complexes, which was 6.0 kcal/mol . This observation was consistent with the gas phase basicity values of MeOH and H₂O, which indicated that the strength of O-H...O interaction should be greater in the PA-MeOH complexes which has the

lower value of ΔpK_a , compared to PA-H₂O complexes. LMO-EDA and NBO results for PA-MeOH global minima complexes are consistent with that of PA-H₂O complex.

Computational studies were then performed on PA-diethylether (DEE) complexes, in which the two subunits were bound by a dominant O-H...O interaction, in the complex corresponding to the global minimum. The BSSE corrected interaction energy (-7.8 kcal/mol) for the PA-DEE complex is largest as compared to the hydrogen bonded complexes of PA-H₂O and PA-MeOH, at MP2/aug-cc-pVDZ level. In addition, the geometrical parameters, O...H bond distance 1.82 Å, is the shortest and O-H...O bond angle closest to linearity 169° in PA-DEE global minimum complex, indicating to strongest O-H...O interaction in comparison with PA-H₂O and PA-MeOH complexes. It must be noted that PA-DEE complex lacks the secondary O-H... π interaction present in global minima 1:1 hydrogen bonded complexes of PA with H₂O and MeOH. Lack of the secondary O-H... π interaction results in the loss of antagonism, which in turn results in the O-H...O bond angle, being closer to linearity.

One of the highlights of this thesis is that starting from the structures of the simple PA-H₂O complexes, we could construct the structures of the different PA-MeOH complexes, by replacing the hydrogen atom in water with a methyl group. These PA-MeOH complex structures were then used to systematically derive different PA homodimer structures by replacing each of the methyl hydrogen in MeOH with the acetylenic group (-C \equiv C-H). The PA-MeOH complexes therefore served as a bridge between PA-H₂O and PA homodimers. Experiments and computations on PA homodimers indicated that structures corresponding to the global minima were dimer 1, bound by an O-H...O, an O-H... π and a C-H... π interaction, together with another nearly isoenergetic isomer dimer 5 involving dual contacts, O-H...O and O-H... π interactions.

In the second propargyl system, propargyl amine (PAm), it was found that the remote and vicinal orbital interactions played a deciding role in the conformational stability, similar to that in PA conformers. Matrix experiments trapped the most stable ggPAm conformer. In addition, the 1:1 hydrogen bonded complexes of PAm with H₂O were studied. It was interesting to note that PAm-H₂O complex 2, bound by an O-H...N interaction, where PAm serves as a proton acceptor, was computed as the global minimum. However, in the case of PA-H₂O and PA-MeOH complexes, similar structures involving an O-H...O interaction with PA serving as the proton acceptor, were computed to be local minimum. The convincing evidence for formation of complex 2 is the large red shift of 346.0 cm⁻¹ in the bonded O-H stretch of H₂O subunit from the O-H antisymmetric stretch in uncomplexed H₂O. Isotopic results confirmed our vibrational assignments.

The hydrogen bonded complexes PAm with MeOH were also explored. Computations together with experiments indicated to the formation of a similar complex 2 having an O-H...N interaction. It was found that this global minimum has nearly same BSSE corrected interaction energy (~ -6.4 kcal/mol) at MP2/aug-cc-pVDZ level, as PAm-H₂O complex 2. However, in PAm-MeOH complex 2, a greater n-σ* electron delocalization with second order perturbation energy E(2) of 17.7 kcal/mol was found as compared to 14.9 kcal/mol in PAm-H₂O complex 2.

Following the procedure that we adopted to generate the different PA homodimers, we constructed the different PA-PAm complexes starting from PAm-H₂O complexes. It was found that the most stable PA-PAm complex was bound by a dominant O-H...N interaction followed by secondary N-H...π and C-H...π interactions. Matrix isolation experiments were performed with codeposition of PA and PAm, however, features due to complex formation were not observed.

The structures of the PAm homodimers were also explored computationally by a systematic replacement of each of the methyl hydrogen of methylamine in PAm-MeNH₂ complexes, which in turn were constructed by replacing each hydrogen atom of NH₃ with methyl group in PAm-NH₃ complexes.

It would be appropriate at this point to compare the various hydrogen bonded systems involving PA and PAm with other systems such as acetylene and phenylacetylene (PhAc). Phenylacetylene-H₂O has been studied in an earlier work from this laboratory. C₂H₂ manifests a $\equiv\text{C}-\text{H}\cdots\text{O}$ interaction in its global minimum, while the other C₂H₂-H₂O complex involving O-H $\cdots\pi$ interaction, is only a weak local minimum. In PhAc-H₂O complex, the O-H $\cdots\pi$ isomer corresponds to the global minimum, which is prompted by a supporting weak C-H $\cdots\text{O}$ secondary interaction, with the C-H of the phenyl group being involved in this decisive secondary interaction. In the PA-H₂O complex, the global minimum is again the O-H $\cdots\pi$ complex; though in this case, the O-H $\cdots\pi$ interaction is the weaker interaction and the O-H $\cdots\text{O}$ contact is the stronger one. Our computational studies on PA-DEE, PAm-DEE and PhAc-DEE complexes at MP2/aug-cc-pVDZ level also present an interesting scenario. In the PA-DEE complex, the global minimum was computed to be a structure involving the O-H $\cdots\text{O}$ interaction, while in the PAm-DEE complex, the global minimum was a similar looking structure involving a relatively weaker N-H $\cdots\text{O}$ interaction. In both these systems, the complex involving a $\equiv\text{C}-\text{H}\cdots\text{O}$ interaction was the local minimum. It was also found that the energy difference between the structures corresponding to the global and local minimum, was markedly different in the PA-DEE and PAm-DEE systems; it was 4.0 kcal/mol in case of PA-DEE system, while it was a mere 1.6 kcal/mol for PAm-DEE system. In the PhAc-DEE system, the complex with the $\equiv\text{C}-\text{H}\cdots\text{O}$ interaction represents the global minimum.

This thesis has addressed some important questions on molecular conformations and dimer systems involving weak non-covalent interactions. It has been shown that orbital interactions, particularly the remote and vicinal interactions, play a very important role in deciding the conformation preferences in propargyl systems – propargyl alcohol and propargyl amine. The earlier assertion that intramolecular hydrogen bond involving the π system was the stabilising factor was found not to be correct. Another highlight of this thesis is that in dimers which involve more than one intermolecular interaction, a structural compromise is resorted to, such that each of the intermolecular interaction operates in less than its optimum orientation, but in a way that the overall stabilization is maximized. This was observed in many of the complexes, we studied and which has been discussed in detail. Finally, we have presented a scheme of deriving the structures of complex systems from simple systems in a systematic way by replacing one group with the other group. This method, reminiscent of the retrosynthetic approach of organic chemists, has been exploited in our work to compute several structures of homo- and hetero- dimers of the two propargyl systems.

LIST OF PUBLICATIONS

List of Publications included in the thesis

1. "Does a Hydrogen Bonded Complex with Dual Contacts show Synergism? a Matrix Isolation Infrared and *Ab Initio* Study of Propargyl Alcohol-Water Complex." *Jyoti Saini, K.S. Viswanathan, J. Mol. Struct.* **2016**, 1118, 147-156.
2. "Discerning Near-Isoergic Isomers. A Matrix Isolation Infrared and *Ab Initio* Study of the Propargyl Alcohol Dimers." *Jyoti Saini, K.S. Viswanathan, J. Phys. Chem. A* **2017**, 121, 1448-1459.
3. "From Propargyl Alcohol-Water to the Propargyl Alcohol Dimer: Where does the Propargyl Alcohol-Methanol fit in?" *Jyoti Saini, K.S. Viswanathan New J. Chem.* **2019**, 43, 3969-3980.

Manuscript in Preparation

1. Conformations and Hydrogen Bonded Complexes of Propargyl Amine: Matrix Isolation Infrared and *Ab Initio* Study. *Jyoti Saini, K.S. Viswanathan.*

Book Chapter

1. "Matrix Isolation: A window to Molecular Processes" in **Molecular and Laser Spectroscopy: Advances and Applications**. Pankaj Dubey, *Jyoti Saini, Kanupriya Verma, Ginny Karir, Anamika Mukhopadhyay, K.S. Viswanathan. Elsevier, 2017, 317-340.*